CIRCUITS AND SYSTEMS FOR ENERGY HARVESTING AND INTERNET OF THINGS APPLICATIONS

A Dissertation

by

JOHAN JAIR ESTRADA LOPEZ

Submitted to the Office of Graduate and Professional Studies of
Texas A&M University
in partial fulfillment of the requirements for the degree of

DOCTOR OF PHILOSOPHY

Chair of Committee,	Edgar Sánchez-Sinencio
Committee Members,	Kamran Entesari
	Shankar P. Bhattacharyya
	Erick Moreno-Centeno
Head of Department,	Miroslav M. Begovic

May 2019

Major Subject: Electrical Engineering

ABSTRACT

The Internet of Things (IoT) continues its growing trend, while new "smart" objects are constantly being developed and commercialized in the market. Under this paradigm, every common object will be soon connected to the Internet: mobile and wearable devices, electric appliances, home electronics and even cars will have Internet connectivity. Not only that, but a variety of wireless sensors are being proposed for different consumer and industrial applications. With the possibility of having hundreds of billions of IoT objects deployed all around us in the coming years, the social implications and the economic impact of IoT technology needs to be seriously considered.

There are still many challenges, however, awaiting a solution in order to realize this future vision of a connected world. A very important bottleneck is the limited lifetime of battery powered wireless devices. Fully depleted batteries need to be replaced, which in perspective would generate costly maintenance requirements and environmental pollution. However, a very plausible solution to this dilemma can be found in harvesting energy from the ambient. This dissertation focuses in the design of circuits and system for energy harvesting and Internet of Things applications.

The first part of this dissertation introduces the research motivation and fundamentals of energy harvesting and power management units (PMUs). The architecture of IoT sensor nodes and PMUs is examined to observe the limitations of modern energy harvesting systems. Moreover, several architectures for multisource harvesting are reviewed, providing a background for the research presented here. Then, a new fully integrated system architecture for multisource energy harvesting is presented. The design methodology, implementation, trade-offs and measurement results of the proposed system are described.

The second part of this dissertation focus on the design and implementation of low-power wireless sensor nodes for precision agriculture. First, a sensor node incorporating solar energy harvesting and a dynamic power management strategy is presented. The operation of a wireless sensor network for soil parameter estimation, consisting of four nodes is demonstrated. After that,

a solar thermoelectric generator (STEG) prototype for powering a wireless sensor node is proposed. The implemented solar thermoelectric generator demonstrates to be an alternative way to harvest ambient energy, opening the possibility for its use in agricultural and environmental applications.

The open problems in energy harvesting for IoT devices are discussed at the end, to delineate the possible future work to improve the performance of EH systems. For all the presented works, proof-of-concept prototypes were fabricated and tested. The measured results are used to verify their correct operation and performance.

DEDICATION

To God, my sovereign sustainer and savior. To my wonderful wife Liliana, and our daughters Natalia and Elizabeth. To my parents José and Lupita.

ACKNOWLEDGMENTS

First and foremost, I need to express my utmost gratitude toward God, my Lord and Savior. His sovereign and unmerited grace has sustained me all my life, and I know He will carry me all the way till the end. Without Him, I am nothing.

I would like to thank my advisor, Dr. Edgar Sánchez-Sinencio, for all the invaluable support and motivation he offered to me throughout my doctoral studies. I am also very grateful for all the guidance (both academic and in life), the professional advice and friendship he offered to me. In many ways, he always be to me an enduring example of how to cheerfully face life and work.

I would like to also thank my committee members, Dr. Kamran Entesari, Dr. Shankar P. Bhattacharyya, and Dr. Erick Moreno-Centeno, for all the suggestions that helped to improve the quality of this dissertation.

I wholeheartedly express my sincere gratitude and love to my wife, Liliana, for all the unconditional support and patience she always graciously extended to me. I wouldn't have been able to reach this goal without her. I am also deeply thankful for my daughters Natalia and Elizabeth, whose presence in my life (even without they realizing it) is a great motivation to always do my best.

I extend a very deep and special appreciation to Alfredo Costilla-Reyes and Amr Abuellil, great friends and colleagues. The work and discussions we developed together these years enriched not only this dissertation, but also my life.

Many thanks also go to my friends and colleagues in the AMSC research group: Kyoohyun Noh, Zizhen Zeng, Carlos Pech, Chao-Hsiuan Tsay, Sanghoon Lee, Sergio Soto, SungJun Yoon, Xiaosen Liu, Judy Amanor-Boadu, Adriana Sanabria, Fernando Lavalle, Mohamed Abouzied, Joseph Riad, Luis Tellez, Sylvester Ankamah-Kusi and Arihant Jain. Each one of you contributed to make my time at TAMU a great experience, with memories that will stay with me forever. I also have a special word of gratitude for Ms. Ella Gallagher, for all the help she provided to me every time I needed it.

Many people indirectly contributed to this achievement: Victor Trejo, Isaías Collí, Freddy Uicab, Alver Padilla, Daniel Hernández, Santiago Zapata and their families. Thanks to New Life Baptist Church for being an important part of my life these years, specially Allen Duty, Nathan and Rebeca Forbes, Micah Green, Sanil John and Jeremy Tarpley.

Finally, I give thanks to the National Council of Science and Technology (CONACYT) and to Universidad Autónoma de Yucatán for the economic support they provided throughout my doctoral studies.

CONTRIBUTORS AND FUNDING SOURCES

Contributors

This work was supported by a dissertation committee consisting of Professors Edgar Sánchez-Sinencio, Kamran Entesari and Shankar P. Bhattacharyya of the Department of Electrical and Computer Engineering and Professor Erick Moreno-Centeno of the Department of Industrial and Systems Engineering.

Design and layout of the MPPT control and Passive Start-Up circuits for the harvesting system presented in Chapter 4 were conducted in part by Alfredo Costilla-Reyes, Amr Abuellil and Sungjun Yoon. The soil quality estimation algorithm and the laboratory Phosphorus analysis that are presented in Chapter 5 were developed with the assistance of Alejandro Castillo-Atoche. The 3-D printing of the concentrating solar thermoelectric generator depicted in Chapter 6 was conducted by Alejandro Castillo-Atoche. The design and layout of the dual-input switched-capacitor converter discussed in Chapter 7 was mainly conducted by Carlos Pech.

All other work conducted for the dissertation was completed by the student independently.

Funding Sources

Graduate study was supported by the following fellowships: Silicon Labs Fellowship, TI J. Kilby Excellence Fellowship and Intel Fellowship, as well as the CONACYT scholarship.

NOMENCLATURE

ANN	Artificial Neural Network
BLE	Bluetooth Low-Energy
CMOS	Complementary metal-oxide-semiconductor
DPM	Dynamic Power Management
EH	Energy Harvesting
FOCV	Fractional Open Circuit Voltage
GSM	Global System for Mobile communications
IC	Integrated Circuit
IoT	Internet of Things
LDO	Low Drop-out Regulator
LoRa	Long Range
LPWA	Low Power Wide Area
MCU	Microcontroller Unit
MPPT	Maximum Power Point Tracking
MQTT	Message Queuing Telemetry Transport
M2M	Machine-to-Machine
NB-IoT	Narrowband IoT
OCC	Open Circuit Conditions
PA	Precision Agriculture
PCB	Printed Circuit Board
PG	Power Good
PMU	Power Management Unit

POR	Power-on Reset
P-SU	Passive Start-Up
PVC	Photovoltaic Cells
SC	Switched-Capacitor
SHM	Structural Health Monitoring
ULP	Ultra-Low-Power
UVLO	Under-voltage Lockout
RFID	Radio-Frequency Identification
WPT	Wireless Power Transfer
WSN	Wireless Sensor Network

TABLE OF CONTENTS

Page

LIST OF FIGURES

FIGURE Page

LIST OF TABLES

TABLE Page

1. INTRODUCTION

1.1 What is the Internet of Things?

The term '*Internet of Things*' was coined by Kevin Ashton in 1999 [1]. He originally used it in a presentation at the Procter & Gamble (P&G) company, where he talked about Radio-Frequency Identification (RFID) technology and its possible applications. Over the years, the term gradually gained academic popularity and even started to appear in mainstream publications [2, 3]. Today, the Internet of Things (IoT) is a well-known computing concept in which everyday objects are made 'smart' and connected. That is, these objects are embedded with hardware that enables them to gather information about the physical world, interact with the surrounding environment, and cooperate with each other through the Internet [4].

1.1.1 The present of the IoT

Enabled by advances in sensing and communication technologies [5], a considerable number of IoT-related products are being already commercialized in the market. For consumer applications, the most popular devices would be the smart phone, the smart watch and the fitness tracker, but other type of products can also be found. Some of them are listed in Table 1.1. For example, smart door locks[1] enable their users to conveniently lock or unlock their home doors from any location using an application in the cell phone. Smart batteries[2] retrofit into conventional smoke alarms, so they can send direct notifications over the Internet if the alarm has been activated. Smart power outlets[3] and home energy monitors allow the remote supervision of the energy usage at home, program the thermostat temperature, and also turn on/off lights and other appliances. Wireless key tags[4] allow us to locate any object with the pressing of a button. These products are designed to simplify our lives and save time in daily activities.

[1] https://august.com/products/august-smart-lock-connect
[2] http://www.getroost.com/product-battery.html
[3] http://www.ankuoo.com/products/
[4] https://www.thetileapp.com/en-us/products/mate

Table 1.1: Sample list of commercial IoT applications.

Product	Company	Battery Type	Battery Life
Smart door lock	August Home	4 AA cells	3 months
Smart battery	Roost Inc.	9 V Li cell	5 years
Smart AC outlet	Ankuoo Electronics Inc.	-	-
Key finder tag	Tile Inc.	1 CR1632 cell	1 year

Several companies also offer IoT wireless sensor systems for diverse applications, like environmental monitoring, vehicle detection and indoor parking in buildings. There are also systems designed to perform the supervision and control of industrial processes [6–8]. In Table 1.2 a brief survey and classification of these sensor products is presented. Other companies have made available a variety of open source development platforms, which a world-wide community of Do-it-Yourself (DIY) hobbyists and technology enthusiasts are using to continuously develop their own IoT devices and applications [9].

1.1.2 The future of the IoT

As shown in Figure 1.1, many opportunities are envisioned for the future of the IoT, with possible applications in urban infrastructure [10], wearable devices [11], healthcare [12], smart manufacturing [13], among others [14–16]. The most important opportunities and projected market shares for the future IoT are shown in Figure 1.2 [14]. With this perspective, and according to recent forecasts; it is expected that by the year 2025 the number of deployed IoT objects will surpass the 75 billion, with an annual economic impact of up to 6.2 trillion dollars [17]. If realized, the IoT paradigm will make almost every object at home or the office to be monitored and controlled over the Internet, enhancing almost every aspect of human activity.

Table 1.2: Survey of commercialized wireless sensor products.

Company	Sensor	Application	Battery	Connectivity
Banner Eng.	Ultrasonic	Indoor parking	D-cell	900 MHz ISM Band
Banner Eng.	Photoelectric	Industrial control	AA-cell	2.4 GHz radio
Phase IV	Temperature, Humidity	Industrial monitoring	Coin cell	IEEE 802.15.4
LORD Microstrain	Analog voltage	Monitoring	AA-cell	IEEE 802.15.4
Monnit	Temperature, Humidity	Buildings	Coin-cell	900 MHz ISM Band
Honeywell	Temperature	Industrial monitoring	AA-cell	IEEE 802.15.4
Advantech	Temperature, Humidity	Environment	-	3G Freq. Bands

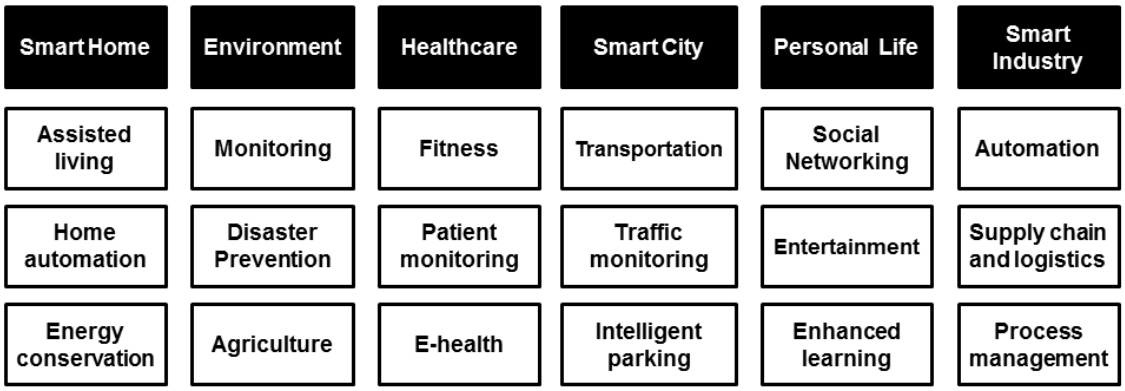

Figure 1.1: Some applications for the Internet of Things found in the literature.

However, in spite of all the recent progress that has been obtained, and the already existing solutions, the IoT vision of the future world is still a pending reality. There are many important challenges to deal with and open research problems in many disciplines [18]. These open areas

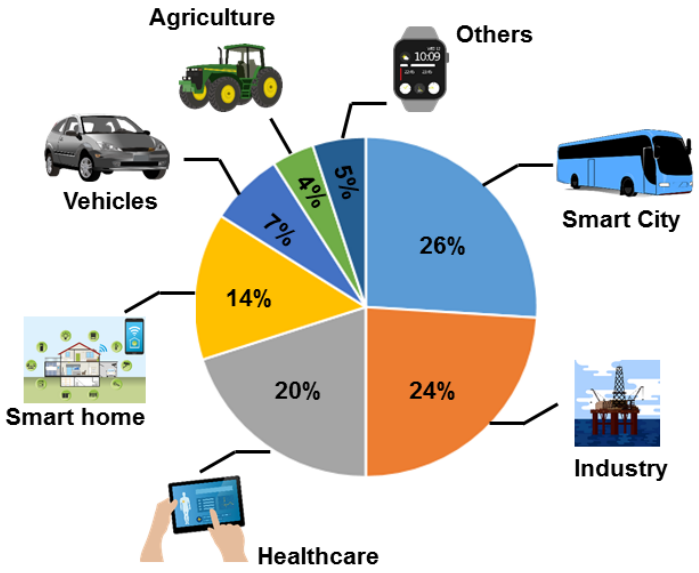

Figure 1.2: Market opportunities and perspective shares for the IoT by 2025 (adapted from [14]).

of opportunity can be better identified in the context of the IoT architecture, which is going to be discussed next.

1.2 The IoT Architecture: Areas of Opportunity

Over the years, several architecture models for the IoT have been proposed, with varying degrees of complexity. Still, there is no industrial or academic consensus about which model is more adequate to represent the Internet-of-Things [19]. For our purposes, we can refer to the 3-layer architecture that was introduced since the early stages of research in the area [15, 16]. This model defines the main idea of the IoT. The architecture shown in Figure 1.3 consists of the following layers:

1. The *perception layer* (also called the *objects* or *sensor layer*) represents the physical layer of the architecture. It contains the sensors that measure and gather information, the electronics that process, digitize and stores the associated data, and actuators performing different functions.

2. The *network layer* (also known as the *transmission layer*) is responsible of the interconnection of the smart things to other devices and servers in the network. The transfer of data is produced

Figure 1.3: The three-layer model of the IoT architecture.

in this layer through various devices (hub, gateway, etc.) and communication technologies such as Wi-Fi, Bluetooth, ZigBee, GSM, among others.

3. The *application layer* (also known as the *business layer*) is where the specific services or operations are provided to the user. This is the layer where the different market applications of Figures 1.1 and 1.2 are considered.

Due to its economic and social implications, the Internet of Things is in the present an important focus in different fields of knowledge. A taxonomy of the main areas of research for IoT technology is presented in Table 1.3 [16, 18]. As shown, there are many challenges and limitations that have been identified across all the levels of the network abstraction in terms of robustness, scalability and standardization. With the increased possibility of different types of attacks (like the injection of malicious code and of false data, signal interference and unauthorized access to data), how to provide network security and privacy of information are also becoming important concerns in the IoT development [14, 15]. To solve these problems, different solutions have been identified and are under active investigation.

In particular, it is important to observe that many of today's IoT applications are limited by hardware [20]. All of the mainstream consumer and industrial products listed in Table 1.1 and Table 1.2 are battery operated. However, most wireless IoT devices also have an active power consumption in the order of 10s to 100s of mW. Under that demand, typical batteries (like AA,

Table 1.3: A taxonomy of challenges and research areas in IoT technologies.

Limitations and Challenges		
Perception Layer	**Network Layer**	**Applications Layer**
Cost reduction	Standardization	Security
Miniaturization	Availability	Data privacy
Extended lifetime	Mobility	Reliability
Active Research Areas		
Sensor technology	Internet protocols	Big data and analytics
Data pre-processing	Networking technology	System identification
Sub-mW sensor nodes	Secure communications	Cloud/fog computing
Energy harvesting	Low-power communication	IoT secure software

AAA and coin cell sizes) can be completely depleted in months. Increasing the battery size is not an option where the application's cost and form factor are also particular driving concerns. To achieve low power consumption and extend the battery life over several years, many applications recur to duty cycling, i.e. the turning off of the device for large periods of time.

The shortcomings of powering up an IoT device with batteries become then immediately evident: they either impose a restricted functionality or a limited lifetime of operation. Not only that, but also over time batteries need to be replaced, which turns to be an inconvenience to the user, and a costly requirement for companies trying to massively adopt IoT technologies. The environmental impact of the possibly billions of discarded batteries over the coming years also have to be considered.

As an alternative, recent works indicate that modern Internet of Things devices and Wireless Sensor Networks can rely on energy harvesting techniques to extend their battery life, or even create a battery-less application [21–23]. Considering that in the environment there are different natural and man-made energy sources that can be harvested, the possibility of attaining an energy autonomous object turns out to be a very attractive solution. This dissertation focuses then on the

design of circuits and systems for energy harvesting (EH) and Internet of Things applications.

1.3 Research Contributions of this Dissertation

There are indeed many options to harvest energy from the environment. However, it has been noted that the energy coming from any of these ambient sources is in many times intermittent and display an unpredictable behavior [24]. In the end, this uncertainty can compromise the reliability of operation for any type of energy harvesting circuit, and in some cases will considerably limit their applicability. On the other hand, simultaneously harvesting energy from multiple sources will enable the collection of more power over time [25–27]. Therefore, a more stable supply can be created, and robust operation is achieved even in the presence of ambient intermittent sources.

In this dissertation, the implementation of a fully-integrated architecture for a multisource energy harvesting combiner system is introduced in Chapter 4. The proposed architecture, that is based on a switched-capacitor converter; incorporates a novel power-aware ranking strategy. This strategy is different from previous implementations, which are based only on the voltage level of the transducers. A passive start-up circuit is introduced, that eliminates the conduction losses of conventional implementations with diodes. Besides, a new control circuit for maximum power tracking is also introduced, that allows complete system integration, without the external sampling-and-hold capacitors commonly used in the literature. The performance of the converter is analyzed and experimentally demonstrated. Also, tests have been done with a small sensor system that validates the operation of the proposed combiner in a typical IoT system. The proposed circuit offers a cost and area effective solution, contributing to the state-of-the-art research on Power Management Units (PMUs) for energy harvesting, and to the miniaturization of IoT applications.

The performance of Internet of Things applications relying on EH is related to design decisions taken both at the circuit and system level. A careful selection of components and circuit design methods are critical to achieve the autonomous operation of a sensor node. Also, a number of techniques can be applied to extend the operation lifetime of sensor nodes, depending on their application [28]. In that regard, this dissertation also presents in Chapter 5 the design and implementation of a very low-power sensor node for precision agriculture (PA) applications. In this

sensor node, a dynamic power management (DPM) strategy was applied, considering the changing rate of phenomena in the soil along the day. This DPM strategy allows the system to establish an adaptive trade-off between the energy that is being consumed and the precision of its measurements. Four sensor node prototypes were used to form a wireless sensor network (WSN) for the smart estimation of soil parameters. The performance of the wireless system has been corroborated with experimental results.

This dissertation also introduces in Chapter 6 the design of a 3-D printed solar thermoelectric generator (STEG) prototype for powering wireless sensor nodes in agricultural and environmental applications. The focus was given to the design of an inexpensive system through the use of commercial TEG modules, together with an affordable manufacturing process. With this prototype, a different option for ambient EH is demonstrated. The two proposed WSN systems create opportunities for the implementation of low-cost PA infrastructure, with methodologies that can be adapted to various types of agricultural regions. Therefore, an important contribution has been made for the adoption of this type of technology in underdeveloped countries, where the cost of commercial WSN solutions is an important factor preventing its widespread use.

Finally, the design of a scalable multisource piezoelectric energy harvesting system is also presented in Chapter 7. The system is based on the well-known Synchronous Electric Charge Extraction technique that has been adapted to harvest power from multiple inputs. This has been previously done with discrete components but a highly integrated CMOS implementation is presented here. The scalability of the harvesting system is proposed to be performed through a multiple input switched-capacitor converter. With this architecture, the possibility of harvesting from multiple resonating piezoelectric transducers is created.

1.4 Dissertation Organization

This dissertation is organized as follows. The first part will present the fully integrated, switched capacitor based multisource power combiner with novel power ranking and maximum power tracking circuits, implemented in a standard CMOS 0.13-μm technology. For that purpose, this Chapter introduces the present and future expectations for the IoT, together with open research problems in

that area. Then, Chapter 2 describes the general architecture of IoT sensor nodes, and analyzes the power requirements of this type of system when it is implemented using off-the-shelf commercial components. The main aspects of power management unit design for energy harvesting will also be discussed in that chapter.

Then, Chapter 3 reviews several circuit architectures for multisource energy harvesting that have been proposed in the literature in recent years. Some open areas of opportunity in multisource energy harvesting are then discussed in that chapter. After that, Chapter 4 presents the design and fabrication of the proposed fully integrated, maximum power tracking combiner for energy harvesting IoT applications.

The second part of this dissertation focuses on the design of the autonomous sensor node for precision agriculture applications, which is presented in Chapter 5. A wireless network implemented with the proposed sensor node is also presented in Chapter 5. The experimental results of the wireless network used for a smart soil parameters estimation system are discussed. Chapter 6 describes the fabrication and experimental characterization of the STEG prototype. Measurement results demonstrate its potential to generate enough power to prolong the operation of a wireless sensor node application.

Chapter 7 presents the design of the scalable piezoelectric energy harvesting system. Simulation and measured results for its performance are shown. Finally, Chapter 8 summarizes and concludes this dissertation. Possible future work for research is presented in that chapter. All the published contributions derived from this work are listed in Appendix A.

2. ENERGY HARVESTING FOR IOT SENSOR NODES *

2.1 Lifetime prolonging techniques in wireless sensor networks

Due to the recent increase in popularity of the Internet of Things, common everyday objects are progressively being turned into "smart" devices and connected to the Internet. Wireless sensor systems are also frequently introduced in the literature, with applications in areas such as healthcare [29, 30], agriculture [31], environmental monitoring [32], smart industry [33] and structural health monitoring (SHM) [34], among others. If the IoT continues to grow as expected, by the year 2025 more than 50 billion of smart sensor nodes will be deployed around the world.

While trying to achieve this future scenario, an important practical problem that both designers and researchers alike are facing now is how to massively deploy this growing number of smart sensors in a cost-effective and sustainable manner. Indeed, if eventually billions of these devices will be deployed on houses, buildings and factories, what is going to be their source of energy? And, how are they going to be maintained?

Nowadays batteries are still commonly used as the main power source for Internet of Things devices. However, even when battery technology is progressing into much lighter and more energy dense storage devices [35], it has been shown that these improvements still don't follow the pace of growth in the power demands of modern electronic systems: processing power doubles approximately every two years, while the capacity of batteries double only in about ten years [36]. This means that the use of batteries imposes a limitation on the operating lifetime of an IoT device or sensor node. Over time, the batteries will require a replacement or to be recharged.

In many applications like implantable medical devices (IMDs) or wireless sensor nodes positioned on remote places, the replacement of batteries is costly and inconvenient, and in many times is not an option. To overcome this problem and prolong the lifetime of these type of systems, a number of techniques have been proposed and are under current research [37–40]. These are

*Portions of this chapter are reprinted with permission from "Technology Enabling Circuits and Systems for the Internet-of-Things: An Overview" by J. J. Estrada-López, A. Abuellil, A. Costilla-Reyes, and E. Sánchez-Sinencio. 2018 IEEE International Symposium on Circuits and Systems (ISCAS), Florence, 2018, pp. 1-5. ©IEEE 2018

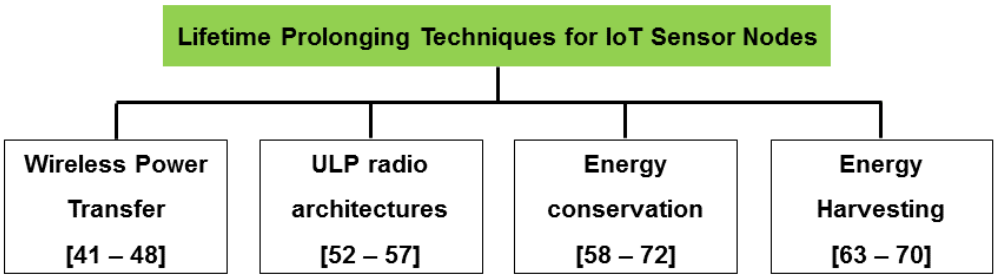

Figure 2.1: Summary of methods for prolonging the operating life of sensor nodes.

summarized in Figure 2.1 and will be briefly discussed next.

2.1.1 Wireless Power Transfer

Wireless power transfer (WPT) consists in the transmission of energy without any physical connection. As shown in Figure 2.2, this is done by connecting the power source to a transmitter circuit which transfers the energy through an electromagnetic (EM) field. This EM field is received at the other end of the system. The receiver circuit process the power and delivers it to the load.

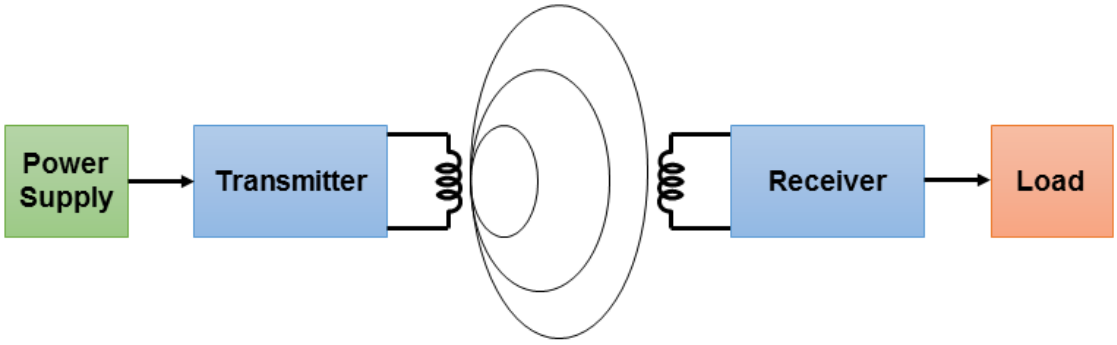

Figure 2.2: Block diagram of a Wireless Power Transfer system.

Wireless power transfer techniques are already used in commercial products (like electric toothbrushes and mobile devices) and their application to WSNs have been also proposed [41–43]. The most common WPT technique makes use of inductive coupling, in which an AC voltage is applied to a primary coil, generating a time-variant magnetic field that induces a voltage on a secondary

coil. This is a simple and very efficient technique [41]. However, transmission efficiency quickly decays with distance, and also the accurate alignment of the coils is required. These constraints limit the use of inductive coupling to applications where short distance and good alignment are guaranteed, like wearables and IMDs [44].

Another WPT technique consist in the transmission of energy through EM radiation, using dedicated radio frequency sources. Not only both information and power can be simultaneously transferred to the node [45–47], but also this technique works over larger distances than inductive coupling. However, transmission efficiency is still very low (less than 10%) and the transmitted power has to be kept under safe limits for humans. Therefore, the final power transferred to the load can still be very low. The WPT can also be realized through distributed laser charging (DLC) [48]. As shown in Figure 2.3, this approach could work in both indoor and outdoor scenarios, where DLC transmitters could be embedded on the building structure or transported with drones, respectively. This approach also has limited applicability due to the requirement of having a continuous line of sight and accurate alignment between the emitter and receiver. The use of drones also involves a very costly infrastructure.

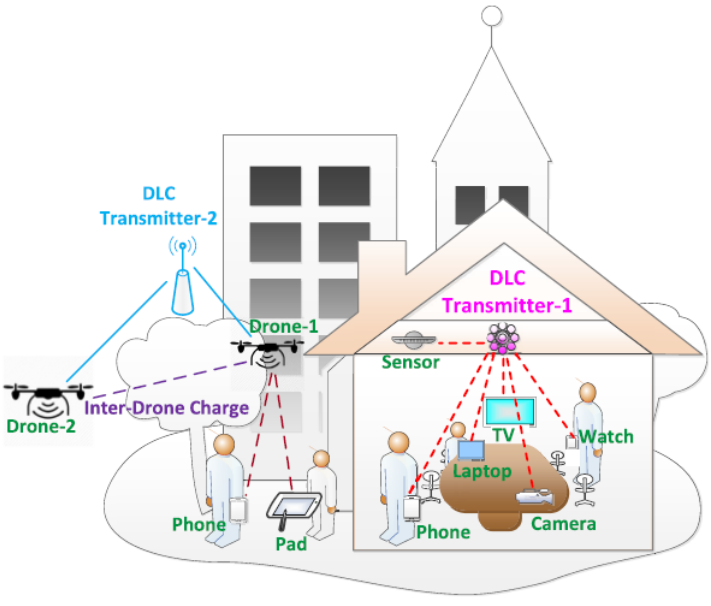

Figure 2.3: Different distributed laser charging (DLC) scenarios ©IEEE 2018 [48].

2.1.2 Ultralow-power Radio Architectures

Wireless sensor systems require an optimal use of the energy they have available. In that regard, ultralow-power (ULP) circuits can operate for extended periods of time, even when supplied from a limited power source. In recent years, a number of circuit architectures and design techniques that improve the energy utilization in an IoT device have been developed [49]. Energy efficient techniques have been proposed for the analog front-end circuits [50] and to reduce the leakage current in digital blocks of sensor nodes [51]. However, a main focus is given to the design of energy efficient radio systems for IoT [52], where researchers are proposing innovations at the block and system architecture level. The use of current-mode circuits [53] and wake-on radio receivers [54–56] are some examples. Others have proposed to reduce the power consumption of the communication system by replacing the phase-locked loop (PLL) and using instead digital calibration for the oscillator prior transmission [57]. These ULP radio architectures offer a promising solution to the limited lifetime of wireless sensors. However, most of the recent works make use of non-standard modulation techniques, architectures or communication protocols, which impedes their rapid adoption in the market.

2.1.3 Energy Conservation

Energy conservation techniques are focused in reducing the energy consumption of the sensor nodes. As wireless data transmission is the most power-hungry activity in sensor nodes, energy conservation techniques have been proposed to reduce the consumption related to the transfer of data. Among these are sleep/wake-up schemes [58], adaptive transmission schemes [59,60] and the development of energy efficient communication protocols [61]. Adaptive sampling in the analog frond-end is also proposed as an energy conservation scheme [62]. In Chapter 5 of this dissertation, a wireless sensor node for precision agriculture is presented, using a dynamic power management strategy that considers the changing rate of soil phenomena during the day. This strategy allows the system to establish an adaptive balance between energy consumption and the accuracy of its measurements.

2.1.4 Energy Harvesting

Energy harvesting (EH) is the process of capturing and converting freely available ambient energy into electric power useful to operate an electronic device [63]. Its main application is in stand-alone, ultra-low power systems, with low data transmission rate and heavily duty-cycled operation, where the use of batteries involves many drawbacks. EH has many advantages over Wireless Power Transfer, including the fact that it is environmentally friendly. Also, a variety of sources exist for the collection of energy (see Figure 2.4), which include ambient light, wind force, thermal gradients, radio frequency (RF) signals and mechanical vibrations.

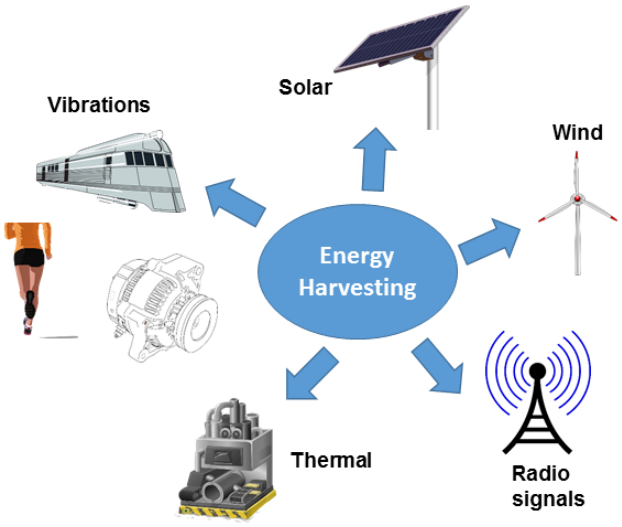

Figure 2.4: Possible man-made and natural energy harvesting sources.

EH can also be used in combination with energy conservation methods and new radio architectures [64] to prolong the battery life of the application and if possible, enable a batteryless operation. Therefore, EH techniques are suitable for a wide variety of applications in wearable devices, body area networks and wireless sensor networks [65–70].

The main disadvantage in the use of current EH techniques is that they are dependent on the availability of the energy source, which is not always guaranteed. The intermittent scavenging of

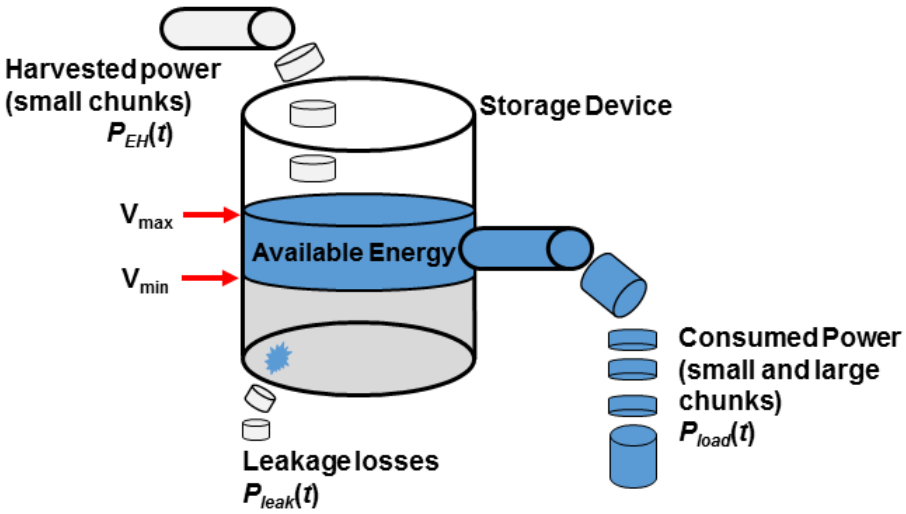

Figure 2.5: General idea of an EH-enabled system (adapted from [20]).

energy constraints the operation of the IoT system to a strict power budget, limiting its capacity. This is illustrated in Figure 2.5.

As shown in Figure 2.5, the EH system collects energy from the ambient source (many times in intermittent, small portions) and "pours" it in a storage device (SD). The more energy that is stored, the larger the voltage on the SD. A minimum of energy is necessary on the SD, below which its voltage (V_{min}) does not allow the correct operation of the load. Beyond that, any extra-harvested power is accumulated to be delivered when the load requires it. In a duty cycled system, the load is continuously draining a minimum of energy and suddenly demands large portions of power to perform an operation (sense, store and transmit data). Besides the energy consumed by the load, the storage device exhibit losses (leakage) due to its non-ideal construction. The energy available in the storage device is given by:

$$E_{av} = \int_0^t [P_{EH}(t) - P_{load}(t) - P_{leak}(t)]dt \tag{2.1}$$

From Equation 2.1, the system requires an energy balance in which the harvested power is at least equal to the power demanded by the load plus the losses. This would be called an energy-neutral operation. If this balance is broken, the SD is depleted and there is no energy available

to continue the safe operation of the system. To improve the system's performance, the following conditions are needed:

1. Increase the amount of power that is being harvested from the environment. There is continuous research in improving energy harvesters to increase their efficiency while reducing their size.

2. Reduce the system power consumption. As discussed above, several energy conservation techniques are under current investigation.

3. Reduce the losses in the system. Different technologies are available for the storage device, which are discussed in the following sections.

Therefore, more research work is still needed in terms of making reliable EH systems for IoT applications. With that consideration, this chapter analyzes the system architecture and individual components of a typical sensor node powered by energy harvesting. The power consumption requirements of sensor nodes is also evaluated, as well as the different technology options for energy harvesters and storage devices currently available. Then, the main design aspects of power management units (PMUs) for energy harvesting will be reviewed. The output power levels that have been reported in the most recent literature will be compared with the requirements of an IoT node. With this overview, an overall perspective is given of the progress that has been attained in PMUs for EH, and also of the opportunity areas that still can be explored.

2.2 Architecture of an IoT Sensor Node

Figure 2.6 shows a general IoT sensor node architecture. Four major sections can be identified: the sensing and processing unit, the power management unit, the wireless transmission unit, and the transducers unit, which includes both sensors and energy harvesting transducers. The node captures information from its environment through sensors, whose signals are filtered, amplified and then digitized by the front-end circuits. A low-power microcontroller unit (MCU) processes and stores the data. The wireless transmitter/receiver (RX/TX) unit is in charge of transferring data to other devices in the network. Various standards like Bluetooth Low-Energy (BLE), ZigBee or

Long-Range (LoRa) are commonly used for wireless communication. A more detailed comparison of the different wireless technologies is presented in Chapter 5 of this dissertation. In a common Internet of Things node, there is a power management unit (PMU) that converts the voltage coming from the energy storage element, and distributes a filtered and regulated supply to the whole system. The PMU is also in charge of presenting an efficient interface between the harvester and the storage device, making sure that there is a maximum transfer of energy from the harvester to the system. A more detailed description of PMUs for energy harvesting will occur later in this chapter.

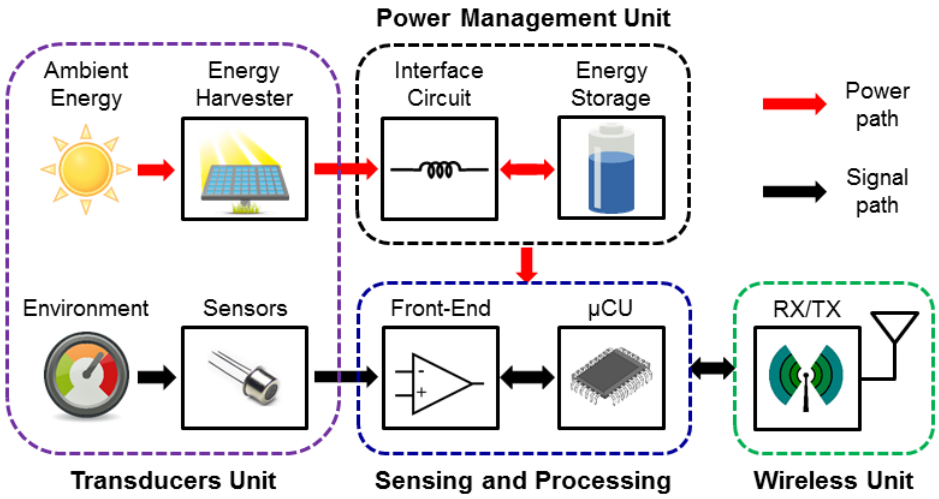

Figure 2.6: General system diagram of an Internet of Things sensor node.

Even when much progress has been already attained on the miniaturization of ultra-low-power (ULP) IoT sensor systems [71–73], still there are not many fully integrated solutions in the market [74], and state-of-art WSN applications are implemented with discrete-type components in a printed circuit board (PCB) [75–78]. That is why the power consumption requirements of a sensor node implemented with standard off-the-shelf commercial components will be analyzed.

A sample of commercial off-the-shelf components marketed for IoT applications is listed in Table 2.1, where typical active (I_{ACT}) and quiescent (I_Q) current consumption for each device is also shown. These devices exemplify all the blocks shown in the system diagram of Figure 2.6, and the sum of their current consumption is representative of the energy requirements of a wireless sensor node. The energy consumption distribution of a typical sensor node among its different elements is shown in Figure 2.7 [40].

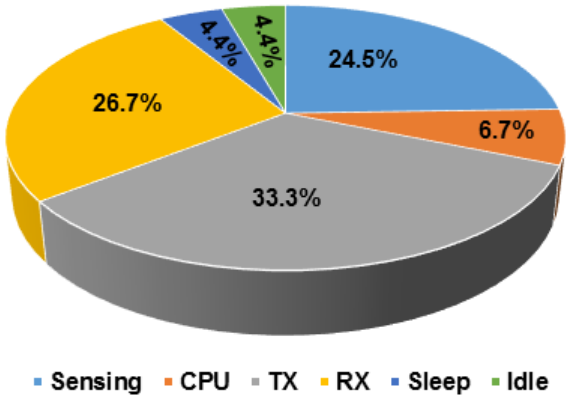

Figure 2.7: Energy consumption distribution in a typical sensor node (adapted from [40]).

From Table 2.1, it is seen that the average power consumed by a sensor node in standby operation could be within the range of 10's or 100's of microwatts. When the sensor is in active mode (performing sensing and transmission of data), the instantaneous consumption can increase p to several 100's of milliwatts.

2.2.1 Energy Harvesting Transducers

Ambient energy sources are almost present everywhere in the environment. Common sources used for IoT applications are solar radiation, thermal gradients, wind flow, mechanical vibrations and radio-frequency signals. The use of non-conventional sources such as microbial fuel cells have also been proposed in some instances. Table 2.2 presents a summary of these EH sources, their theoretical available power density and common transducers used for harvesting those sources.

Table 2.1: Sample commercial components for IoT applications.

Device	Company	Type	Quiescent Current	Active Current	Price (USD)
Sensors					
DRV5032	TI	Hall Effect Switch	NA	1.06 μA	1.32
STCN75	STM	Temperature	1 μA	125 μA	1.17
ADXL1003	ADI	Accelerometer	225 μA	1 mA	32.52
HDC1080	TI	Humidity	100 nA	710 nA	4.54
TDC1000	TI	Ultrasonic	610 nA	2.74 mA	4.95
OPT3001	TI	Ambient light	0.3 μA	1.8 μA	0.99
Sensing and Processing Unit					
MSP430F1491	TI	Microcontroller	1.6 μA	280 μA / MHz	5.21
PIC16F1619	Microchip	Microcontroller	50 nA	32 μA / MHz	1.56
LTC1563-2	ADI	Active filter	1 μA	8 mA	5.31
LPV542	TI	Dual Op-Amp	490 nA	NA	2.11
Communication ICs					
CC3120	TI	Wi-Fi Processor	4.5 μA	50 mA / 229 mA (RX / TX)	4.34
TR1000	Murata	916 MHz Transceiver	0.7 μA	3 mA / 12 mA (RX / TX)	5.95
XB24-AWI	Digi Int.	ZigBee RF Module	3 μA	50 mA / 45 mA (RX / TX)	19.00

Different companies commercialize energy harvesting transducers to convert the energy coming from the above-mentioned sources into electric power. In Table 2.3, the specifications of a sample number of commercial transducers are given. Table 2.3 also shows the instantaneous power that is generated by those devices, when they are subject under specific operating conditions.

From Table 2.3, it is appreciated that the instantaneous power that can be delivered by medium-

Table 2.2: Common ambient EH sources [22], [66].

Category	Power Source	Power Density	Transducer
Ambient light	Indoor light	10-100 μW/cm^2	PV cell
	Sunlight	1-100 mW/cm^2	
Mechanical	Human motion	1-10 μW/cm^2	Piezoelectric
	Machine vibrations	10-100 μW/cm^2	
	Wind	1-30 mW/cm^2	Wind turbine
Thermal	Human body	10-30 μW/cm^2	TEG
	Industrial heat	1-10 mW/cm^2	
Radio Frequency	GSM	0.1 μW/cm^2	Antenna
	Wi-Fi	1 μW/cm^2	
Biochemical	Bio-fuel	0.1-100 μW/cm^2	Fuel Cell

Table 2.3: Characteristics of commercial EH transducers.

Device	Type	Company	L x W x H (mm)	Power (mW)	Conditions	Cost (USD)
KXOB-22 -04X3	Solar	IXYS	22 x 7 x 1.8	20.1	Irradiance 100 mW/cm^2	3.3
MPT4.8-75 -KA	Solar	PowerFilm	90 x 73 x 0.57	240	Irradiance 100 mW/cm^2	5.95
AM-1815	Solar	Amorton	58 x 49 x 1.1	0.126	Indoor 200lux	6.39
TGP-651	Thermal	Micropelt	15 x 10 x 9.5	2.5	Hot side at 60 C	54.11
1MD-03-24	Thermal	RMT	3.8 x 4.8 x 0.9	10	Hot side at 55 C	NA
P-876-A12	Piezoelectric	PI Ceramic	61 x 35 x 0.5	0.3	1 Hz, R_L = 1 k	NA
PPA-1001	Piezoelectric	Mide	54 x 22 x 0.45	2.2	Acc. 2 g, 129 Hz, R_L = 1 k	36.73
T220-A4BR -1305XB	Piezoelectric	Piezo	32 x 13 x 0.51	17.1	Acc. 8 g, 420 Hz, R_L = 9 k	109.0

sized transducers is generally less than 100 mW. This power is significantly less than what is typically demanded by an IoT sensor nodes at peak points of active operation. That is why the system's power consumption has to be carefully designed, making sure that a balance occurs between the required energy by the circuits in active operation, and the average energy that is harvested in the idle periods of the system. Otherwise, different transducers with larger volume should be selected for the application, which in the end affects its final cost and form factor.

2.2.2 Energy Storage Devices

In wireless sensor nodes with energy harvesting, there is the need to store the harvested power in an energy storage device (SD). The SD is a critical component in the system and it should be carefully selected for each application. Typical storage devices used in sensor nodes are batteries and supercapacitors [66]. Both technologies offer different properties in terms of energy/density, current handling capabilities, and charge/discharge rates. The selection of one component over the other will make an impact in the final size, weight and lifetime of the application.

The main advantages of using rechargeable batteries over supercapacitors, is their lower self-discharge rate and higher energy densities. In that sense, batteries offer a more energy-dense solution, capable of delivering energy over long periods of time. However, these advantages come with very important limitations, such as a lower lifetime and reduced performance at low and high temperatures. Table 2.4 describe some important parameters for different rechargeable battery technologies.

Table 2.4: Parameters of rechargeable batteries [65], [66].

Type	**Cycle life**	**Charge time**	**Self-discharge /Month (%)**	**Rated voltage (V)**	**Temp. range (C)**	**Specific energy (Wh/kg)**	**Cost**
NiCd	1500	1-2 Hrs.	20	1.2	-40-60	50-60	Moderate
NiMH	300-500	2-4 Hrs.	30	1.2	-20-40	60-70	Moderate
Lead Acid	200-300	8-16 Hrs.	5	2	-20-60	30-50	Low
Li-ion	500-1000	2-4 Hrs.	10	3.6	-20-60	75-200	High
Alkaline	50	2-3 Hrs.	0.3	1.65	0-65	300-610	Moderate

In comparison, supercapacitor technology (see Table 2.5) offers a much higher recharge cycle life than batteries, and better performance at extreme temperature values. Supercapacitors can also operate over a broader range of voltage and currents than common rechargeable batteries. On the other hand, supercapacitors are limited by their low energy density and much higher self-discharge rates than batteries. That makes supercapacitors good candidates for delivering high instantaneous currents in short bursts of energy consumption.

Table 2.5: Parameters of commercial supercapacitors [65], [66].

Model	**Capacitance**	**Cycles**	**Leak current**	**Voltage**	**Specific energy**	**Temp. Range**	**Cost (USD)**
Maxwell PC10	10 F	500,000	0.04 mA	2.5 V	1.4 Wh/kg	-40 to 70	1.79
Maxwell BCAP035	350 F	500,000	0.45 mA	2.7 V	5.2 Wh/kg	-40 to 70	19.65
Elna DZ-2R5	4.7 F	NA	0.30 mA	2.5 V	NA	-25 to 70	3.93
AVX SCCS30	10 F	500,000	NA	3.0 V	4.0 Wh/kg	-40 to 65	3.44
Eaton TV1030	10 F	500,000	0.03 mA	3.0 V	NA	-40 to 65	6.89

2.3 Power Management Units for Energy Harvesting

The main function of the power management unit is to convert one power domain to another. Usually from one with input voltages that are incompatible with the required levels of the sensor node circuitry, to another that has the compatible voltage levels necessary for the required application. Figure 2.8 depicts the general architecture of a self-starting power management unit for energy harvesting [79]. The purpose of each block in the PMU is explained next.

The function of the start-up circuit, together with the undervoltage lockout (UVLO); is to

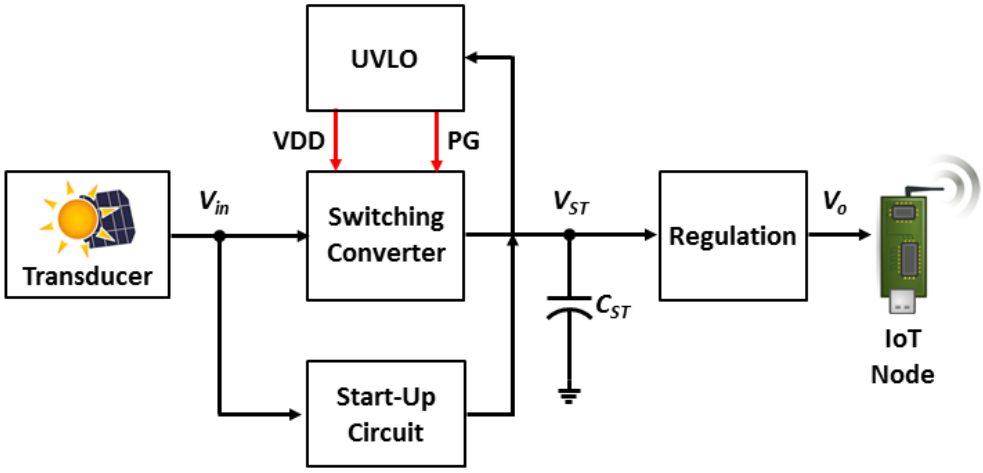

Figure 2.8: General PMU architecture used for energy harvesting [79].

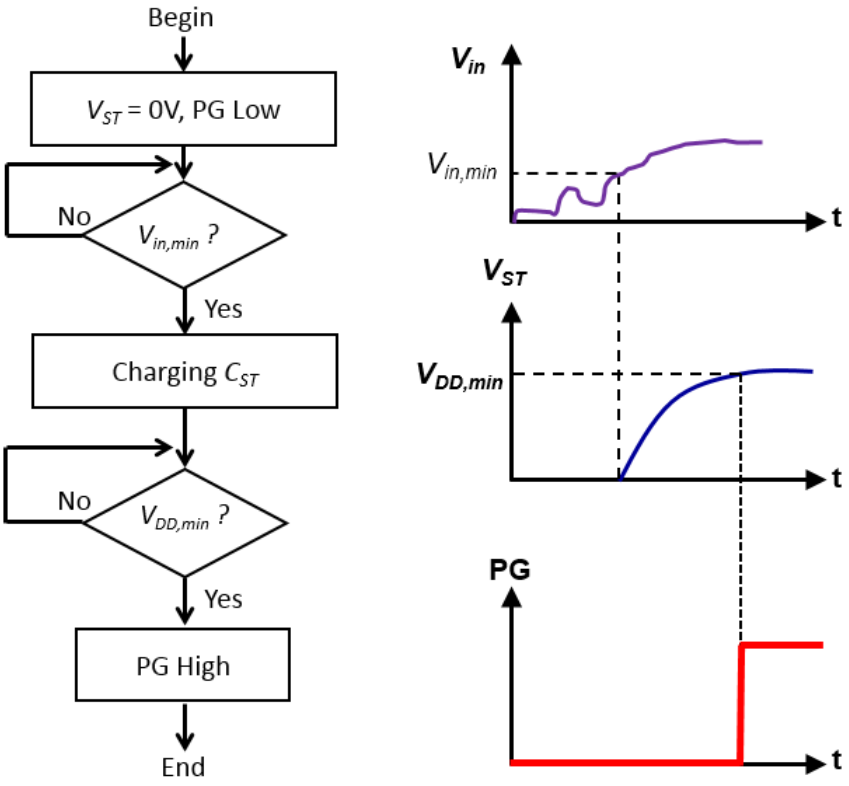

Figure 2.9: Start-up process in a PMU for energy harvesting.

allow the PMU to be able to start its operation even when no energy is stored in the system. This process is shown in Figure 2.9. The condition for the cold-start process to begin is to have a

minimum level of input voltage ($V_{in,min}$) available from the transducer. When that happens, the start-up circuit boost the voltage to charge the storage capacitor. During the start-up process, the UVLO is in charge of monitoring the magnitude of voltage in the storage device (V_{ST}). When the minimum value is reached for the system's operation, it sends a Power Good (PG) signal to the main converter, which now it can start its operation.

The start-up block can be implemented with a low-power secondary (or auxiliary) dc-dc converter like a Dickson charge pump [80, 81]. A discrete implementation of the start-up circuit, composed of a 3-stage oscillator (ring type) and a five-stage charge pump is shown in Figure 2.10 (similar to the one implemented in [80], but with an improved selection of components). The measurements of the start-up circuit are shown in Figure 2.11. As shown in that figure, the ring oscillator starts oscillating at a voltage as low as 390 mV. The minimum input at which the charge pump actually steps-up the voltage is 550 mV, with $V_{out} \approx 1$ V and a current consumption of 5.7 μA.

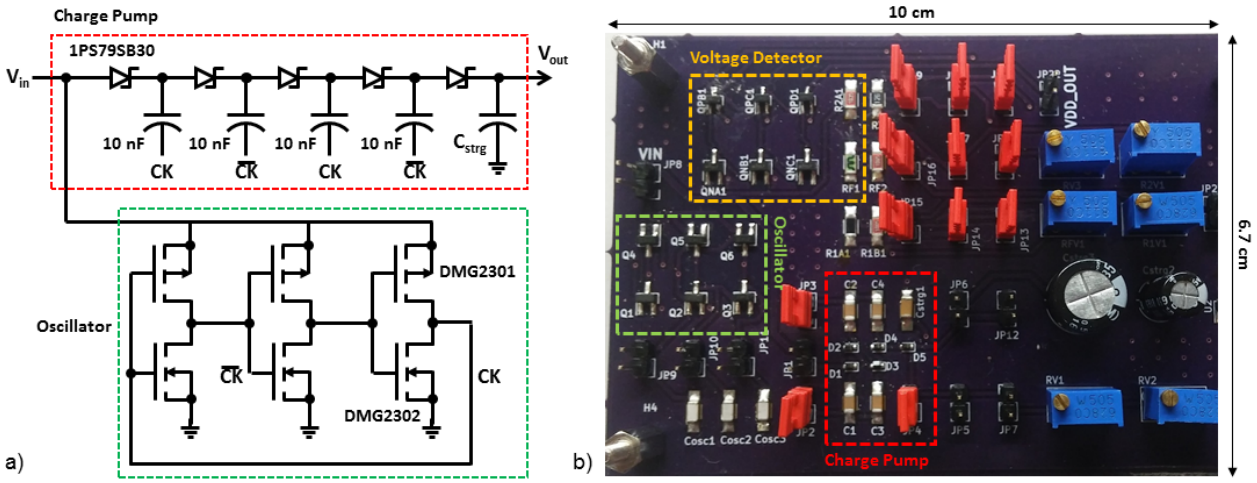

Figure 2.10: Start-up circuit: a) schematic, b) circuit board.

One of the objectives of the start-up circuit is to be able to kick-start the system from an input voltage as low as possible, with minimum current consumption. In the case of the discrete start-up circuit presented above, the 5.7 μA of current consumption is not suitable for very-low micro

power harvesting applications. Integrated implementations, however, may be able to start-up at similar input voltages, but with much lower current consumption. In Chapter 4 these concepts are explored in the design of the fully integrated energy harvesting combiner prototype.

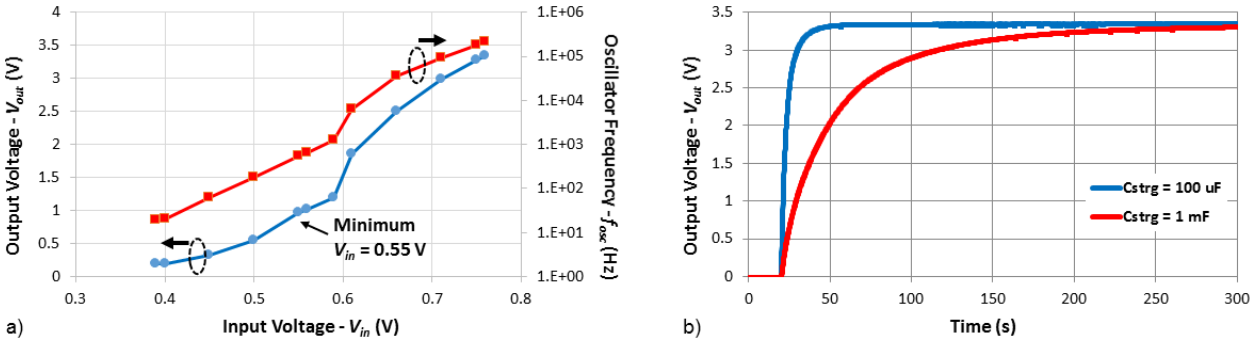

Figure 2.11: Start-up circuit measurements: a) Output voltage and oscillator's frequency versus input voltage, b) output voltage for V_{in} = 760 mV.

A discrete implementation of the UVLO circuit is also shown in Figure 2.12 [80]. At the beginning, in the UVLO circuit V_{CTRL} = V_{DD} = 0. V_{strg} (connected to the output of the charge pump) slowly increases with time. The UVLO circuit monitors when V_{strg} crosses the following thresholds:

$$V_{ON} = (1 + \frac{R_1}{R_H})V_T \tag{2.2}$$

$$V_{OFF} = (1 + \frac{R_L}{R_2})V_T \tag{2.3}$$

In the previous equations, V_T is the threshold voltage of the NMOS transistor, and R_H and R_L are given by:

$$R_H = \frac{R_2 R_F}{R_2 + R_F} \tag{2.4}$$

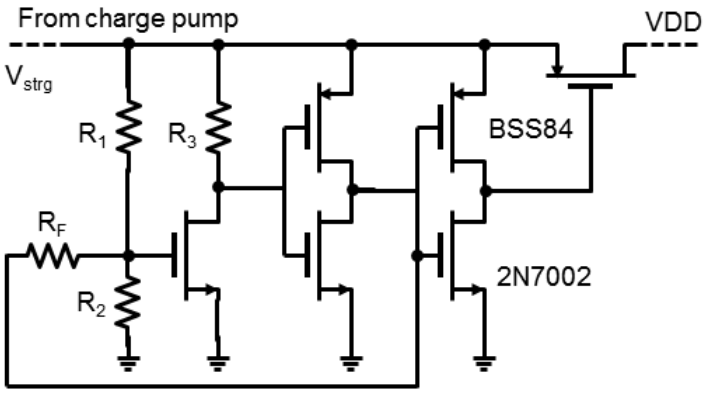

Figure 2.12: Voltage level detector circuit schematic.

$$R_L = \frac{R_1 R_F}{R_1 + R_F} \tag{2.5}$$

In the fabricated prototype (see Figure 2.10b), R_1 = 10 MΩ, R_2 = 15 MΩ, R_3 = 15.6 MΩ, and R_F = 64.8 MΩ. Figure 2.13 shows the measured signals of this UVLO. It can be seen that the PG signal initially stays low, and only gets raised high when the input voltage gets to a 3.28 V value. The PG voltage comes down again when the voltage at the input descends to 2.48 V. This gives a hysteresis value of 0.8 V.

Integrated implementations of the UVLO have been investigated in various works. The silicon area cost of the reported UVLOs is low ($\approx$ 250 μm^2), and they consume low currents in the order of 10's of nA. Therefore, the degradation of power conversion efficiency in the system is also low. However, the operation of these integrated UVLOs is based on leakage currents and transistor's threshold voltage. Therefore, they are heavily dependent on process variations. Normally, they require trimming after fabrication.

2.3.1 The Switching Converter

The main block in the power management unit is the switching converter. The switching converter (shown in Figure 2.14) is basically in charge first, of scaling up or down (depending on the type of harvester) the voltage from the transducer to a level suitable for the electronic circuits. Sec-

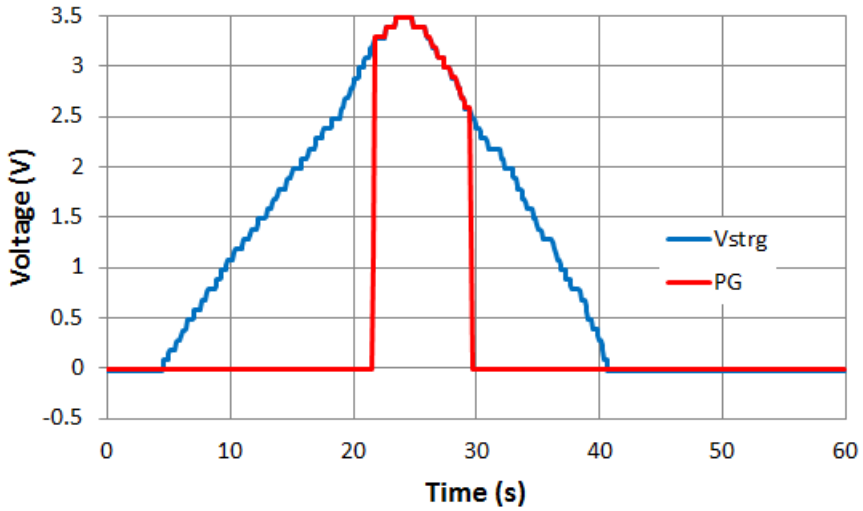

Figure 2.13: Measured input voltage and Power Good signal of the UVLO circuit from Figure 2.12.

ond, it should present to the energy harvesting device an equivalent input impedance that allows for the maximum transfer of power.

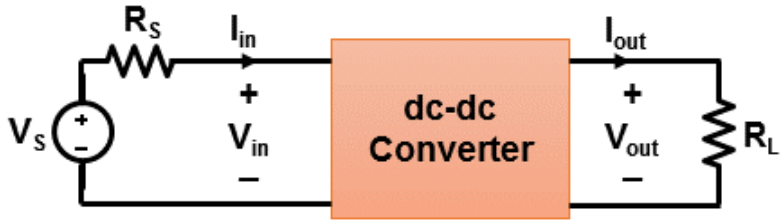

Figure 2.14: General operation of the switching converter in the PMU.

The converter works by temporally storing the energy coming from the input, into a storage component. This storage element can either be an inductor or capacitor. Then, the converter delivers that stored energy to its output. This cycle is repeated in time at a very fast rate (from kHz to MHz) in such a way that a specific output voltage is achieved. To be able to deliver to the load as much harvested power as possible, the converter must be highly efficient and have low power consumption. The expression for the converter efficiency is:

$$\eta = \frac{P_{out} - P_{loss} - P_{supply}}{P_{in}} \tag{2.6}$$

From Equation 2.6 we can see that the switching converter efficiency is reduced by conversion losses and the power consumed by the converter. Both factors of losses must be reduced as possible, especially because in EH applications the input power P_{in} can be extremely small.

The dc-dc converter can have a switched-capacitor (SC) [82–89] or switched-inductor (SI) [90–99] implementation. In previous works, it is shown that SI-based systems can harvest power starting from very low values [90]. Nevertheless, at the typical input power levels of energy harvesting; inductor-based converters require the use of a large external component [91], in order to operate with an acceptable conversion efficiency. This requirement at the end will increase the size and cost of the power management unit. On the other hand, switched-capacitor architectures allow a fully integrated implementation while showing an acceptable performance in terms of efficiency. In the fully integrated energy harvesting combiner presented in chapter IV, a SC implementation is chosen. Table 2.6 presents a summary of some EH systems published in the recent years.

2.3.2 Maximum Power Point Tracking Techniques

In order to achieve the maximum transfer of energy from the transducer to the storage element, the dc-dc converter not only needs to be highly efficient. It also must be able to perform maximum power point tracking (MPPT) for its input. Maximum power point tracking means that the input impedance seen at the switched converter input (R_{in}) creates the operating conditions that make the transducer deliver the maximum power possible under any circumstance. For a resistive harvester, R_{in} must match its equivalent output series resistance (R_{ser}). The switched converter should also be controlled in such a way that it also tracks the changes over time of the ambient conditions.

In this type of applications, inductive converters typically operate in Discontinuous Conduction Mode (DCM), due to the low current levels that are handled. In that case, R_{in} can be controlled by varying the switching frequency of the converter, through Pulse Frequency Modulation (PFM) [85, 92]. Switched-capacitor converters can have two-dimensional control over their equivalent

Table 2.6: Summary of published EH systems in the last years.

Ref.	Year	Type	Source	Process	Current	Min. Input	MPPT	PCE	Start-up	Max. Power
[90]	2010	Inductive	TEG	130 nm	-	20 mV	FOCV	80%	No	200 μW
[91]	2010	Inductive	PE	350 nm	-	-	SSHI	85%	No	32.5μW
[82]	2011	Capacitive	Solar	350 nm	400 nA	1 V	Hill-climbing	86%	No	80 μW
[92]	2013	Inductive	TEG	65 nm	20 μA	50 mV	No	73%	Yes	1.25 mW
[93]	2014	Inductive	TEG	500 nm	0.5 μA	20 mV	FOCV	61.2%	Yes	1.4 mW
[94]	2014	Inductive	PE	180 nm	0.5 μA	-	SSHI	86%	Yes	55 μW
[83]	2015	Capacitive	Solar	180 nm	-	1.1 V	Hill-climbing	86.4%	Yes	21 μW
[84]	2015	Capacitive	Solar	180 nm	-	1.0 V	Hill-climbing	88.7%	Yes	29 μW
[95]	2015	Inductive	Solar	180 nm	50 nA	70 mV	FOCV	76%	No	52 μW
[85]	2016	Capacitive	Solar	180 nm	1.2 μA	450 mV	Hill-climbing	81%	Yes	50 μW
[96]	2016	Inductive	PE	350 nm	0.52 μA	-	SSHI	79%	Yes	175 μW
[86]	2017	Capacitive	Solar	180 nm	467 nA	-	NFC	70%	No	833 μW
[87]	2017	Capacitive	Solar	65 nm	2.7 μA	-	No	53.3%	No	298 μW
[97]	2017	Inductive	PE	250 nm	4.8 μA	-	SSHI	85%	Yes	136 μW
[88]	2018	Capacitive	TEG	65 nm	-	150 mV	No	45 %	Yes	11.3 μW
[98]	2018	Inductive	TEG	180 nm	-	50 mV	FOCV	60%	Yes	400 μW
[89]	2018	Capacitive	TEG	130 nm	-	270 mV	FOCV	64%	No	500 μW
[99]	2019	Inductive	Solar	180 nm	-	70 mV	FOCV	89.9%	Yes	500 μW

input resistance by tuning the switching frequency and also reconfiguring their conversion ratio [84].

Several techniques to perform MPPT have been presented in the previous literature. One of them (shown in Figure 2.15) is called the fractional open circuit voltage (FOCV) method. This method requires the sampling of the open circuit voltage (V_{OC}) coming from the transducer, and then tuning the dc-dc converter input impedance until its input voltage is a fraction of the sampled voltage [79]. That is:

$$V_{in} = K_{MPPT} \cdot V_{OC} \tag{2.7}$$

The value of the K_{MPPT} constant will depend on the type of EH transducer that is being used, and has been empirically found to be ≈ 0.8 and 0.5 for photovoltaic (PV) and thermal harvesters, respectively.

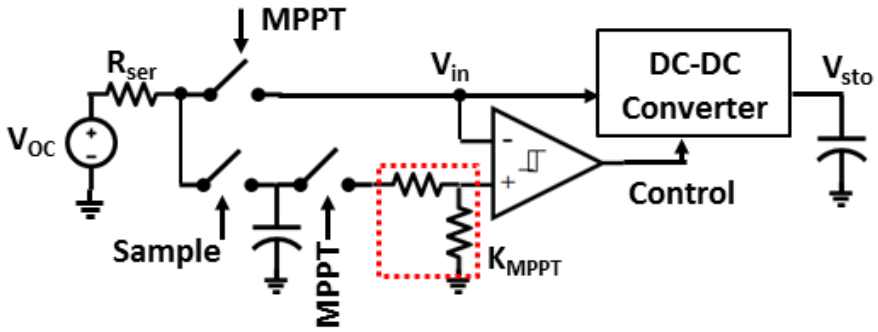

Figure 2.15: Fractional open circuit voltage method for MPPT [5].

Figure 2.16 depicts another MPPT method, which applies a hill-climbing algorithm. In this method, the output voltage V_{sto} is continuously monitored, while tuning the switching frequency (and conversion ratio) of the dc-dc converter. In this case, the algorithm searches for a global maximum in the output power for specific operating conditions of the transducer [84].

Finally, as shown in Figure 2.17 other works have proposed indirect time-based methods to per-

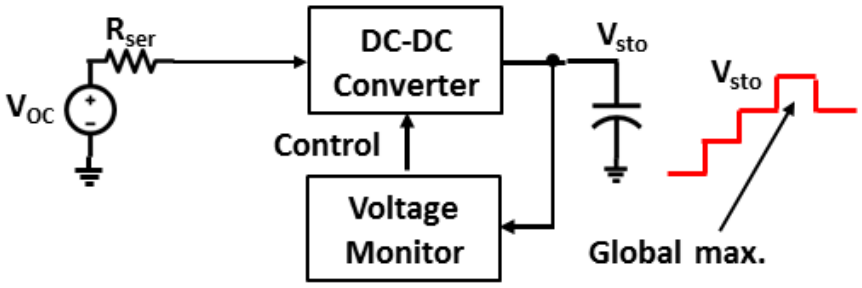

Figure 2.16: Hill-climbing algorithm method for MPPT [5].

form MPPT [83]; like measuring the time that it takes for the output voltage to charge the storage capacitor between two predefined levels. Table 2.7 summarizes the discussed MPPT techniques, contrasting their main advantages and disadvantages. Due to its relatively simple implementation and low power consumption, the FOCV is many times preferred in the most recent literature.

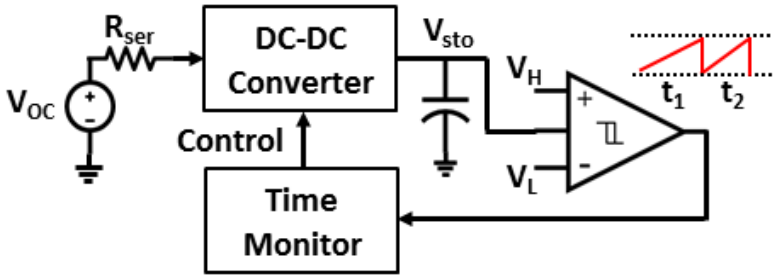

Figure 2.17: Time-based method for MPPT [5].

Figure 2.18 illustrates the progress over the last ten years in terms of available output power for several EH power management units. Often is hard to compare these results in a meaningful way due to the fact that most of the cited works don't follow a standard methodology in the characterization of their designs: transducers vary from one work to another, different test conditions (i.e. illumination, temperature gradient, mechanical acceleration) are used in the measurements, among other factors. However, a relatively fair comparison can be done by establishing a unifying criterion. For example, a common architecture has been selected for each type of transducer. Capacitive

Table 2.7: Comparison of different MPPT Methods.

Method	Advantages	Disadvantages
Fractional Open Circuit Voltage	Good trade-off between converted and consumed power.	Limited tracking accuracy.
Hill-Climbing Algorithm	Good tracking accuracy.	Continuous monitoring increases power consumption overhead
Indirect Time-Based	Good tracking accuracy and output voltage regulation.	Increased design complexity

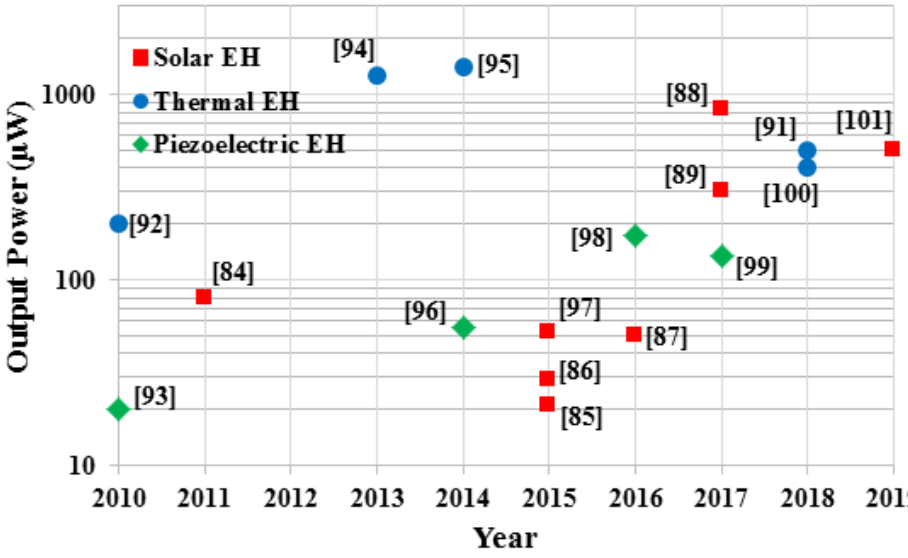

Figure 2.18: Evolution in time of obtained output power in energy harvesting PMUs [5].

and inductive based converters are used for solar and thermal harvesters, respectively; while the synchronized-switch harvesting on inductor technique is considered for piezoelectric transducers. With this basic criteria, it is possible to trace the evolution of a particular technique or topology over time, and observe how the particular contributions of each work advances circuit performance over time. From Figure 2.18 it can be seen that overall, there is a trend of increased available output power, and that state-of-the-art designs can already deliver from 100's of μW to a couple of mW of instantaneous power. These numbers satisfy the minimum requirements of consumed

energy in standby mode of a typical sensor node, but they are still far from the power consumption of the active modes of operation.

2.4 Conclusions

The recent developments obtained in system design for EH and ULP wireless transmitters play a key role in enabling many IoT applications, that in the past were not possible. However, there is still a long way to go over in terms of obtaining maximum extracted energy, high power conversion efficiency, and low-voltage operation. In the particular case of energy harvesting systems, improvements are still needed not only at the circuit level, but also in terms of transducer technology. Those improvements would enable system designers to comply with the power requirements of sensor nodes in the active modes of sensing and data transmission, without the need of recurring to heavy duty-cycled operation. Some of these issues are going to be explored in the following chapters of this dissertation.

3. OVERVIEW OF MULTISOURCE ENERGY HARVESTING ARCHITECTURES *

3.1 Introduction

The Internet of Things (IoT) is under constant development, and is being enabled by the latest research work from both industrial and academic communities. Among the many contributions in diverse areas such as sensor manufacturing, network protocols, and wireless communications, energy harvesting (EH) techniques stand out as a key enabling technology for the realization of batteryless IoT end-node systems. In this chapter of the dissertation an overview of the recent developments in circuit design for power management units (PMUs) is given, focusing mainly in the architectures and techniques required for energy harvesting from multiple sources. The chapter starts by discussing the need for PMUs capable of multisource energy harvesting. Then, an overview is given of different published works for multisource power harvesting, observing their main advantages and disadvantages and comparing their performance. Finally, some open areas of research in multisource harvesting are observed and relevant conclusions are given.

3.2 Energy Delivery Topologies for Power Management Units

Over the recent years, many power management units that harvest energy from single transducers have appeared. The most common selected sources of energy are light [100], thermal gradients [101], mechanical vibrations [102] and radio frequency signals [103]. However, it has been observed that due to ambient variations, single harvesting sources can exhibit long periods of energy shortage, which reduces their overall dependability [104]. As the main goal of a PMU is to provide a constant supply to its load, even when operating from irregular energy sources; the design of an autonomous system that relies on a single harvesting source can be quite challenging.

*Reprinted with permission from "Multiple Input Energy Harvesting Systems for Autonomous IoT End-Nodes" by J. Estrada-López, A. Abuellil, Z. Zeng, and E. Sánchez-Sinencio. *Journal of Low Power Electronics and Applications*, vol. 8, no. 1, p. 6, Mar. 2018. Copyright 2018 by the authors. Licensee MDPI, Basel, Switzerland.

In theory, a wireless sensor device is designed to collect data from its surrounding environment for a large period of time, ideally infinite. In order to do it, the system cannot consume more power than what it has available from the harvesting source. Otherwise, it will at the end completely deplete its storage device and stop its operation (see Figure 2.5 and associated discussion). If the energy consumption of the node is always less or equal than what is being harvested from the environment, then it can be said that it has achieved an energy neutral operation. In the literature, different topologies have been proposed for how the PMU performs energy delivery to its load [66]. Depending on the selected configuration, a specific energy management strategy would have to be required.

3.2.1 Power Management Unit Without Storage Device

A power management unit for EH can be implemented without the use of any device for energy storage. As shown in Figure 3.1, in this topology the switching converter supplies power to the load in a direct way, without any intermediary buffer (battery or supercapacitor). The PMU is supposed to fully satisfy the power requirements of the load only from ambient sources.

Figure 3.1: PMU topology with no storage devices.

This type of PMUs seem to have some advantages. First, their lifetime is not limited by the inefficiencies of the storage devices, which are inevitable. The dc-dc converter can provide maximum power tracking and regulate the output voltage at the same time. However, there are also some important limitations. First, a system without storage devices will operate only when there is energy available at the source. This means that only very limited activity is allowed to the load, and the system could be unable to operate for large periods of time. Second, as there is no place to

store any amount of excess energy that is coming from the environment, that energy is wasted. For this reason, the topology of Figure 3.1 is useful only for a short range of applications, like passive RFID tags that would be able to sense and transmit data only when they are requested to do so.

3.2.2 Battery-Assisted Power Management Unit

A battery-assisted power management unit (see Figure 3.2) has a battery as its main source of energy. The goal of this PMU topology is to use energy harvesting to extend the battery's lifetime, by reducing its usage as much as possible and therefore, making its replacement less frequent or not needed. In this system, the load is powered by the EH source whenever there is available ambient power. Any surplus energy from the transducer is stored in a secondary storage device, that could be either a supercapacitor or a rechargeable battery. During periods of energy shortage, the main battery would be the one that supplies energy to the load.

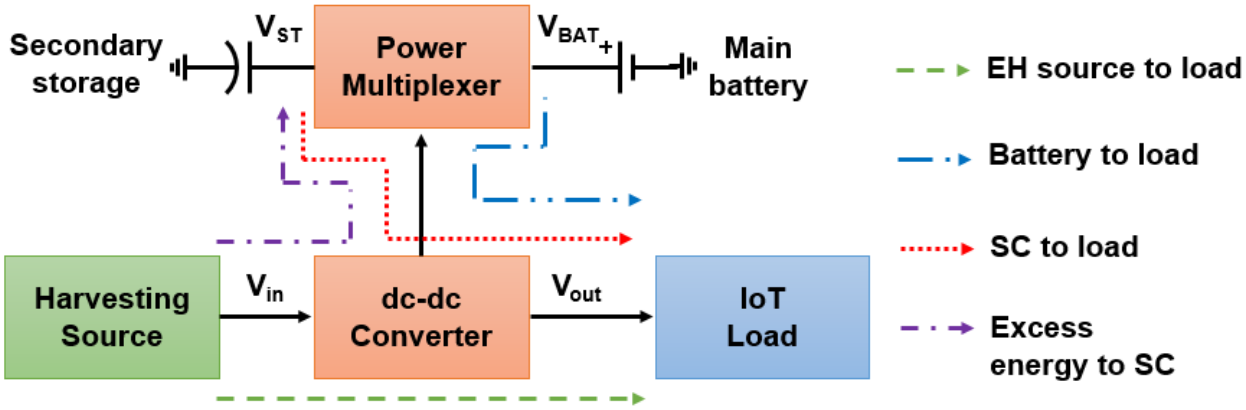

Figure 3.2: Battery assisted energy harvesting system.

The main advantage of this architecture is its reliability, because as long as the main battery is able to provide power, the system continues its operation even when there is no ambient energy to be harvested. The internal architecture of commercial products such as the LTC3107 [105], LTC3331 [106] from Analog Devices, the bq25505 [107] and bq25570 [108] from Texas Instruments, and the S6AE101A [109] from Cypress Semiconductor are based in this battery-assisted

topology.

3.2.3 Batteryless Power Management Units

The interest on batteryless energy harvesting systems is increasing more with time [22]. In a batteryless system (Figure 3.3), the EH transducer can be used to power the sensor node load directly. Any excess energy not required by the load can be accumulated in a storage device (SD), typically a supercapacitor. In the absence of ambient energy, the stored charge in the supercapacitor is used to sustain the operation of the load. As the system has no batteries to be replaced, the lifetime of the node is largely extended and limited only by the charging cycle life of the supercapacitor.

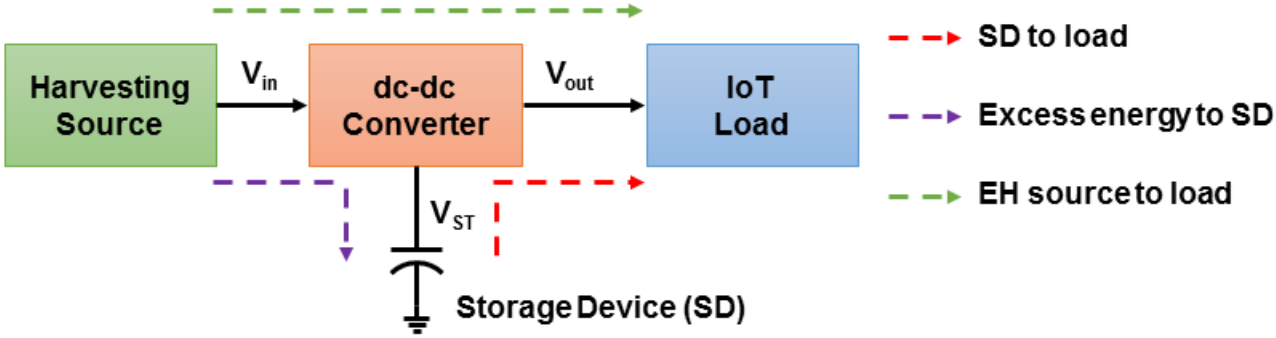

Figure 3.3: Batteryless energy harvesting system.

Batteryless systems require an adequate energy management method to avoid completely depleting the storage device and achieve operation with no interruptions. Both the supercapacitor and the energy harvesting transducer must be properly selected in order to ensure that they meet the voltage and current consumption requirements of the system. This energy management technique is discussed in the next section.

3.3 Duty cycled operation of wireless sensor nodes

As a way to reduce the average power consumption (P_{AVRG}) of a wireless sensor system, and achieve batteryless operation, they are commonly placed under duty-cycled activity. The transient

waveform of the voltage at the storage element (V_{ST}) of the power management unit under duty-cycled operation is shown in Figure 3.4, together with its transient power consumption. As shown, there are accumulation periods that occur during the low-power standby mode of the load. On that period, there is a minimum average power consumption ($P_{Q,T}$) produced by the standby and leakage currents of the electronic circuits and the storage device. The duration of this period depends on the available ambient energy. Once the maximum voltage at the storage element (V_{max}) is reached, the load is activated and data sensing and transmission is performed, producing a period of active power consumption $P_{ACTV,T}$. The charge in the storage element is allowed to be depleted down to a minimum voltage V_{min}, below which safe operation of the hardware cannot be guaranteed. If the storage and harvester elements are properly sized, the energy taken from the buffer while discharging from V_{max} to V_{min} is enough for the sensor nodes to perform its functions.

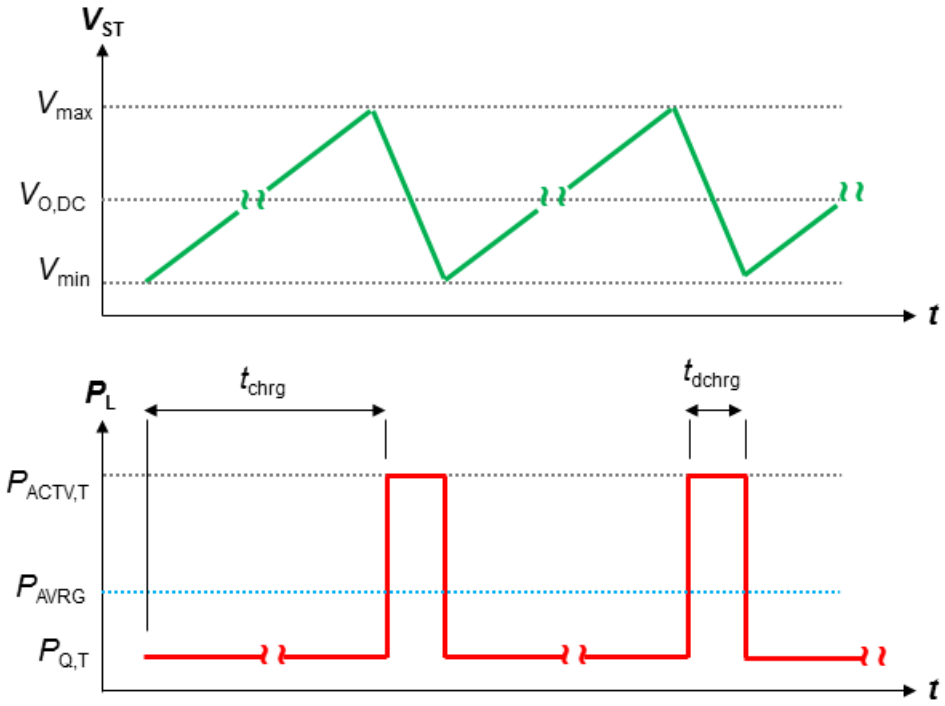

Figure 3.4: Transient waveforms of the voltage at the storage element (V_{ST}) and the power consumption of an IoT end-node in duty-cycled operation [104].

As already discussed, the operation of the IoT node should be carefully designed such that there is a balance on the energy required in the active mode, and the energy that is being supplied by the harvesting devices over the standby period. If designed properly, the storage element will not get completely depleted, and its voltage (V_{ST}) can be maintained within the minimum and maximum values required for the correct operation of the PMU. Taking Figure 3.4 as a reference, the minimum value of the storage capacitor (C_{ST}) needed to constrain the drop in the output voltage (when the system is in active mode) can be calculated using:

$$C_{ST,min} = \frac{I_{dchrg}}{V_{ST,max} - V_{ST,min}} \cdot t_{dchrg} \tag{3.1}$$

where I_{dchrg} is the total current consumed by the node in active operation, and t_{dchrg} is the duration of this mode. Both I_{dchrg} and t_{dchrg} are defined by individual specifications of the system's components. Observe that a constant discharging current is considered in Equation 3.1, and that this is just an approximation of actual behavior.

Once the minimum value of storage capacitance is known, the minimum required standby time (in minutes) to allow C_{ST} to be charged back again to its maximum voltage can be calculated as:

$$t_{chrg,min} = \frac{C_{ST,min} \cdot (V_{ST,max} - V_{ST,min})}{I_{chrg}} \cdot \frac{1}{60} \tag{3.2}$$

A simple example illustrates the previous design procedure. Let's assume a PMU delivers an output voltage of V_o = 3.3 V to an IoT sensor node system. This is a valid supply voltage for most off-the-shelf electronic components. If the PMU has an LDO in the regulation block (which is pretty common), there is a minimum voltage that is needed at the storage capacitance. This voltage can be estimated as:

$$V_{ST,min} = V_o + V_{DO} \tag{3.3}$$

where V_{DO} is the dropout voltage in the linear regulator. Assuming the use of a LP5907 regulator, then V_{DO} = 200 mV for an output current of 250 mA. That gives $V_{ST,min}$ = 3.5 V. The maximum

voltage allowed in the storage capacitor would be given by the maximum value that the LP5907 tolerates at its input, that is $V_{ST,max}$ = 5.5 V.

To calculate the minimum storage capacitance required in this example, we must know the duration of the active period in the sensor node (t_{dchrg}) and the total current that is being drawn during this time. From Table 2.1 we observe that the current drawn from the CC3120 Wi-Fi processor is the dominant value over all other components, so we assume $I_{dchrg} \approx 230\ m$A. If the active time is 10 ms, then:

$$C_{ST,min} = \frac{0.23A}{2V} \cdot 0.01s \approx 1.2mF \tag{3.4}$$

The system requires a minimum time in the standby mode, to allow the storage capacitor to be charged once again to its maximum value (see Figure 3.4). For this calculation, we will assume that the energy harvesting system is delivering a constant charging current of 100 μA. This has experimentally been found to be the approximate value for the charging current delivered by a low power PMU with 1.75 mW of input power [110], and will be used in our example. According to Equation 3.2, that makes $t_{chrg,min} \approx$ 24 s. This represents a heavily duty-cycled operation with D $\approx 0.04\%$. Also, observe that the total quiescent current consumption of the IoT node ($I_Q \approx$ 7.5 μA per Table 2.1) was neglected in the previous calculation, as well as the leakage current in the storage capacitor (estimated below 1 μA [110]). If we consider these extra current consumptions, the total charging time would have to increase its value by at least 10%.

Note that the above charging time calculation has considered a constant charging current approximation, and assumes that the necessary ambient conditions for the energy harvesters (i.e. minimum illumination, thermal gradient or kinetic energy) are always present during all the charging period. As shown in Figure 3.5, if there is any interruption on those conditions, the required charging time would have to be extended. This discussion highlights the importance of multisource energy harvesting for system reliability and performance. Finally, one important design aspect is that the total power consumption of the PMU circuitry should be negligible when compared to the power delivered to the load (particularly during standby mode). This imposes design constraints

for a PMU to operate in the regime of a few microwatts or even nanowatts. This in itself is also a very challenging design goal.

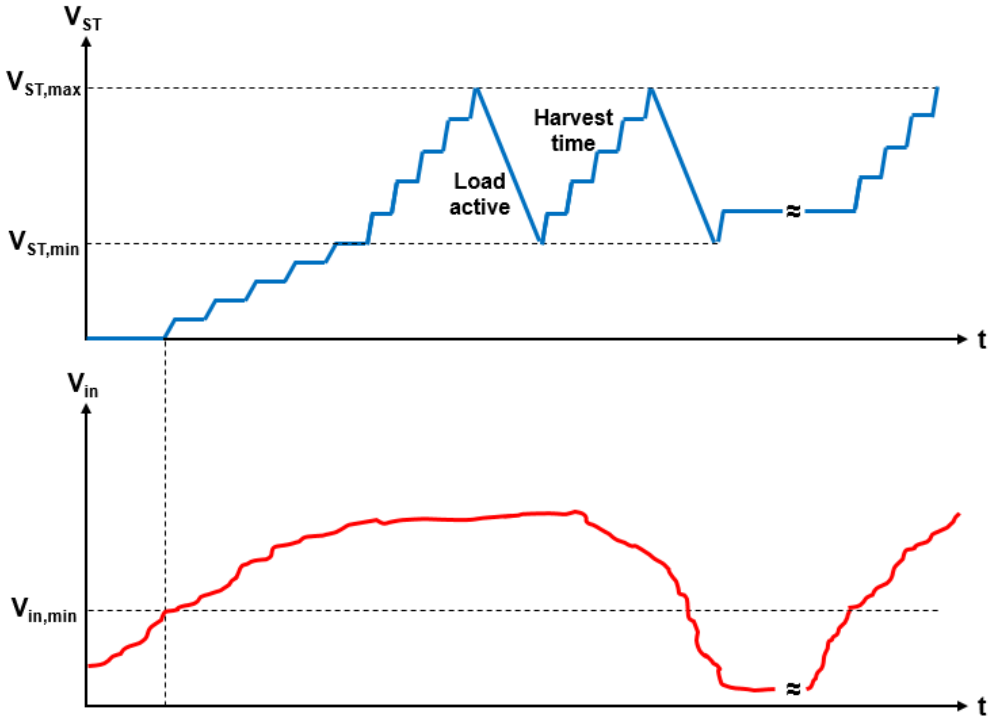

Figure 3.5: Extension of harvesting time between load activations due to absence of EH source.

3.4 Review of Multisource Energy Harvesting Techniques

In this section a review of published works on multiple-input energy harvesting is provided. The works are categorized according to common features and techniques, and presented in an order of increasing complexity of the topologies.

3.4.1 Simple methods for multisource energy harvesting

3.4.1.1 Complementary use of energy sources

The simplest method for multisource energy harvesting would be to mainly collect energy from a primary source, and then use a secondary transducer to only power up auxiliary circuits in the PMU. For example, the authors in [111] designed a two-input harvesting system for structural

health monitoring of aircrafts. As shown in Figure 3.6, in that work a thermoelectric generator was used as the main source of power for the sensor network circuitry, while a piezoelectric (PE) transducer was applied to charge a small capacitor (C_{bias}). This capacitor provided the supply voltage to the bias and reference circuits used by the active EH interface and regulation circuits.

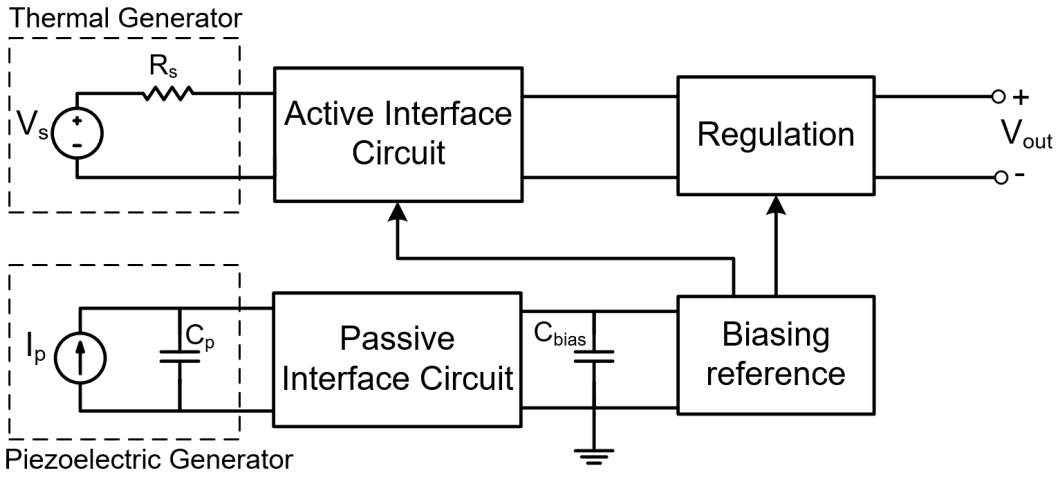

Figure 3.6: Simplified architecture for complementary use of energy harvesting sources [104].

With the approach shown in Figure 3.6, the PE generator allowed for the early biasing of the active interface circuits at the airplane's takeoff, when the power generated from the thermoelectric device is not enough to sustain the operation of the harvesting unit. Cold start-up of the system is then achieved through a passive interface and the complementary source of energy, eliminating the need of a battery. Note, however; that the described architecture does not really combine the energy coming from both sources to deliver it to the load. Also, the reported circuit lacked of a maximum power point tracking capability, which is a required feature to ensure maximum harvesting efficiency.

A complementary use of sources is also the approach taken in [112]. As shown in Figure 3.7, the PE harvester is utilized as a secondary source of energy to secure the cold start of the system, by adding its energy to the storage supercapacitor (SC). In this work, MPPT is performed only for

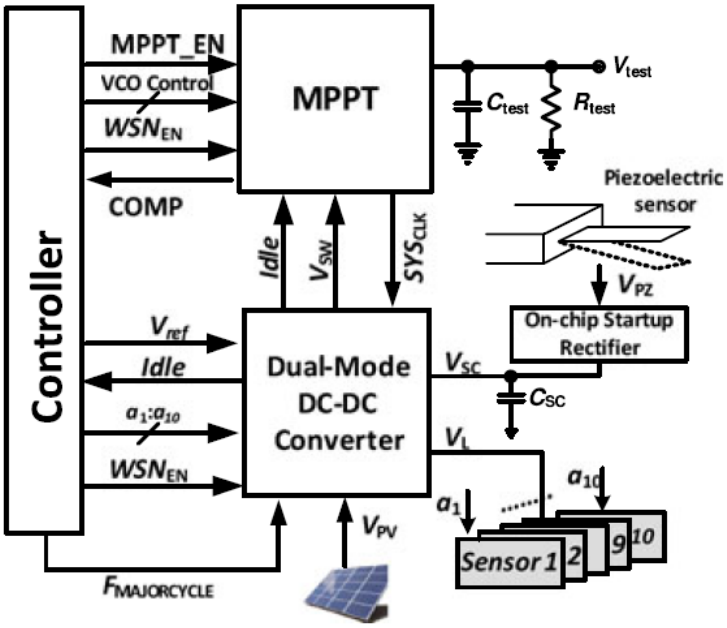

Figure 3.7: System architecture of a dual input EH system where the PE transducer is used as a complementary source of power for start-up ©IEEE 2018 [112].

the primary PV cell, but not for the piezoelectric device, which is less than an optimal solution.

3.4.1.2 Power ORing

A simple and effective way of harvesting the energy coming from multiple sources is through a Power ORing architecture, which consists in the parallel connection of all harvesters through diodes [113–116]. This is shown in Figure 3.8. Power ORing is also the internal topology of the commercial devices LTC3331 from Linear Technology [106] and CY39C811 [117] from Cypress Semiconductor, which is now obsolete.

The Power ORing topology, which is more suitable for an EH system implemented with discrete components, offers a modular approach, capable of supporting an arbitrary number of harvesting subsystems connected in parallel. The use of diodes in the Power ORing method also ensures a self-synchronized operation, reducing the complexity of the PMU control circuit. If needed, a dc-dc converter can further process and regulate the voltage at the storage element (V_{sc} and regulate the output voltage V_{out} according to the requirements of the load.

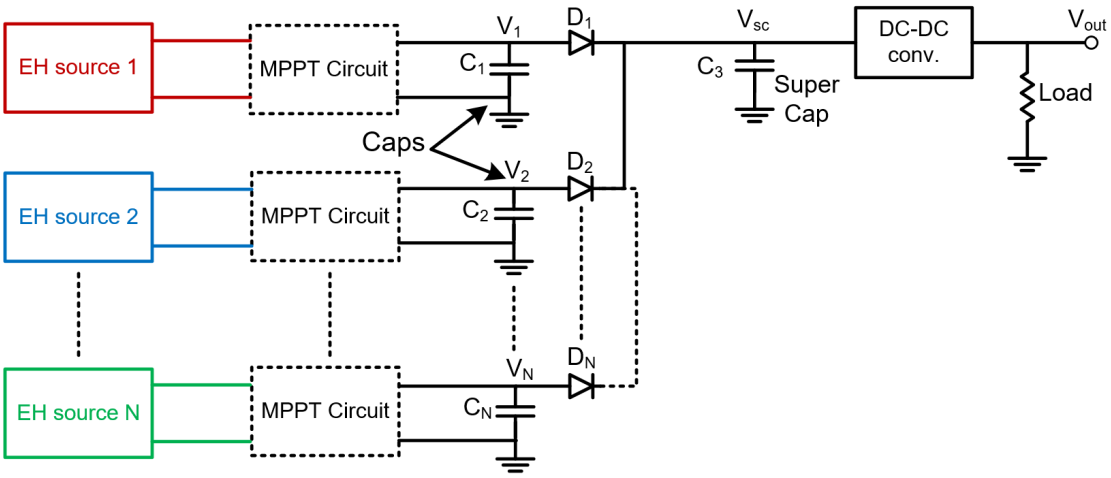

Figure 3.8: Power ORing architecture for multiple input energy harvesting [104].

As implemented in [114–116], each harvesting subsystem independently performs MPPT on its own transducer, which helps increasing the tracking efficiency for each harvester source. However, this approach increases significantly the size and cost of the final application, and comes with a significant overhead on its power consumption. Also, it is important to observe that, in the system of Figure 3.8; the energy coming from all the harvesters is not really added-up. Rather, only the largest input voltage from V_1, V_2 ... V_N is selected and delivered to the output. This strategy works well for harvesting scenarios where it is not expected that the transducers will be simultaneously delivering a significant amount of energy. However, the same scheme would offer a poor performance when multiple harvesters are at the same time delivering different but comparable levels of energy. These problems can be solved by eliminating the individual MPPT blocks, and controlling the dc-dc converter in such a way that the voltage at the storage capacitor (V_{sc}) ensures the maximum transfer of power from the parallel connection of harvesters [113]. However, this comes at the expense of losing tracking efficiency for each individual transducer, which gets worse for a large number of inputs [79].

3.4.1.3 Voltage Level Detection

With a more complex control scheme, the diodes in the circuit of Figure 3.8 can be replaced by voltage controlled switches, reducing the power losses associated to these devices. The turning-on of the switches can be synchronized according to different strategies. For example, in [118] a voltage level detection strategy is implemented, and the charging of a microbattery is taken from either the voltage generated by a thermal or an RF harvesting subsystem, depending on which one exhibits a higher value. In [119], a better approach is taken: each input is sequentially connected to the output for a predefined period of time, provided their voltage is higher than a specific threshold. The architecture for this approach is shown in Figure 3.9.

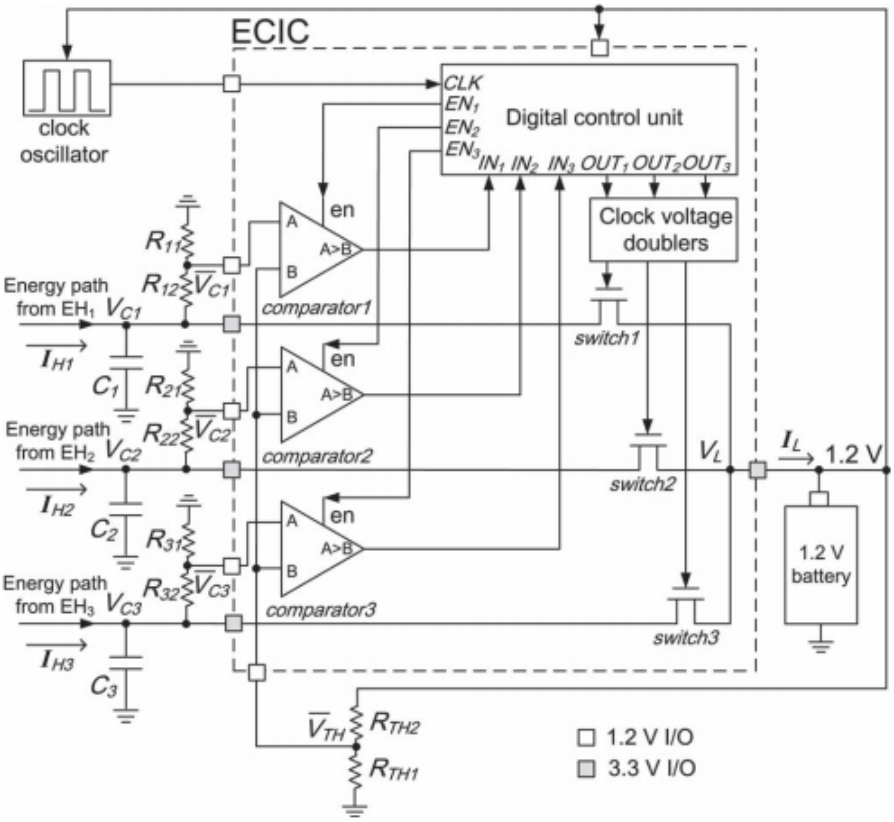

Figure 3.9: Voltage level detection architecture for an energy combiner ©IEEE 2015 [119].

Finally in [120], the operation of the control block also follows a voltage level-based criteria,

this time associated with the state-of-charge of the storage battery. When the voltages at the output of the harvesting subsystems are less than a preset voltage V_{max}, they are disconnected from the battery charging circuit till they charge up their corresponding output capacitors. The precise value of V_{max} would depend on the battery type that is being used. The battery charger is disconnected when the output voltages of the subsystems decrease below a certain minimum threshold, and then connected back again when any of the capacitors reach V_{max}.

The sequential nature of the algorithms proposed in [119, 120] implies that there is no simultaneous harvesting of the energy coming from the multiple inputs, and that there is a potential waste of available power. Specifically, if a minimum value is being established for connecting an input to the storage element, then this connection may never occur even when such input is delivering a significant amount of power, but below of the predefined threshold. Given the unpredictable variation of ambient energy sources, the voltage level detection approach has limited applicability.

3.5 Architectures for Multiple Source Energy Combining

One thing that was generally noted for all the above topologies is that none of them effectively combines or adds the energy coming from each input. However, in the literature different schemes have been proposed to perform the combination of energy. These are going to be discussed next.

3.5.1 Energy Combining Through Linear Regulators

As shown in Figure 3.10, all the energy coming from three different sources (inductive link, piezoelectric and photovoltaic cells) is added in current form, by connecting the output of individual linear regulators [121]. A single storage device (SSD external capacitor) is used to store the energy and stabilizing the LDOs. No battery charging mechanism is used in this scheme. The start-up mechanism (not shown in the Figure) occurs through a Power-on-Reset (POR) circuit: when the output voltage reaches a minimum value of 0.8 V, all the functional blocks are activated. The proposed architecture also allows to store the collected charges from each input in more than one output capacitor (MS1 to MS3). This multiple storage modes (determined by the control bits C1, C2 and C3), provides up to three different output voltage rails with independent regulation.

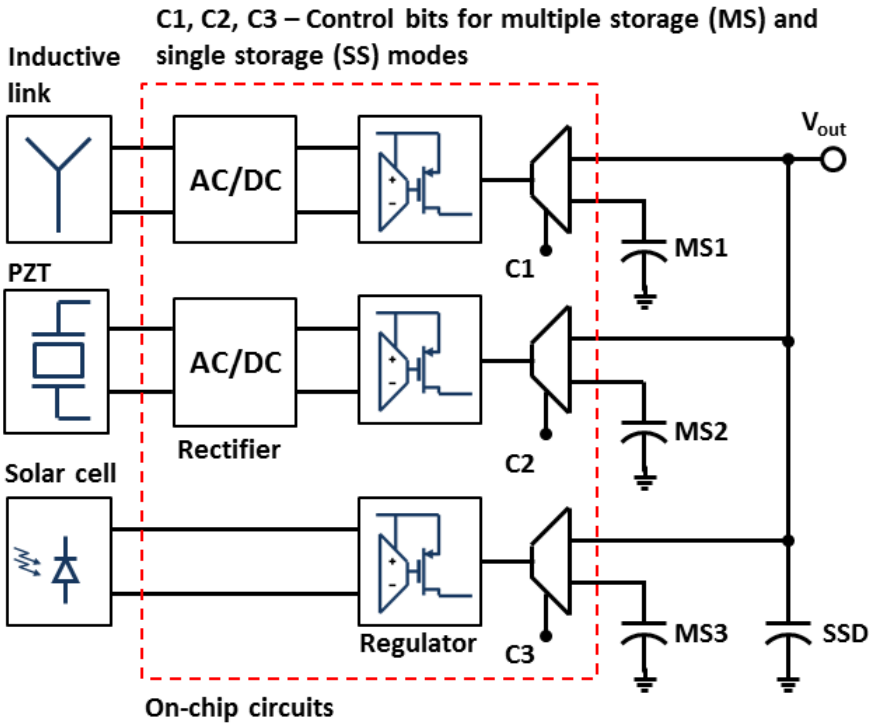

Figure 3.10: Simplified scheme of a multiharvested circuit architecture using linear regulators [121].

As observed, the circuit of Figure 3.10 is capable of concurrently harvesting energy from multiple sources, and requires of a simple control algorithm. However, the architecture requires of an LDO for each energy source, which compared with the switched-type of regulators, can be considered less efficient. Also, stabilization concerns limits the value of output capacitance that can be used, prohibiting the use of devices in the range of mF. Therefore, the number of practical uses for this kind of approach is rather limited.

3.5.2 Multiple-Input Boost Converters

Figure 3.11 shows a four input non-isolated boost switching converter that can be used for multisource energy harvesting [122]. This converter can also be seen as a modified Dickson charge pump, where each stage is fused with a boost converter. In this topology, energy is extracted from every input source and used to charge the capacitor of the following stage. A simple duty-cycle control can be used for output voltage regulation, according to the following equation:

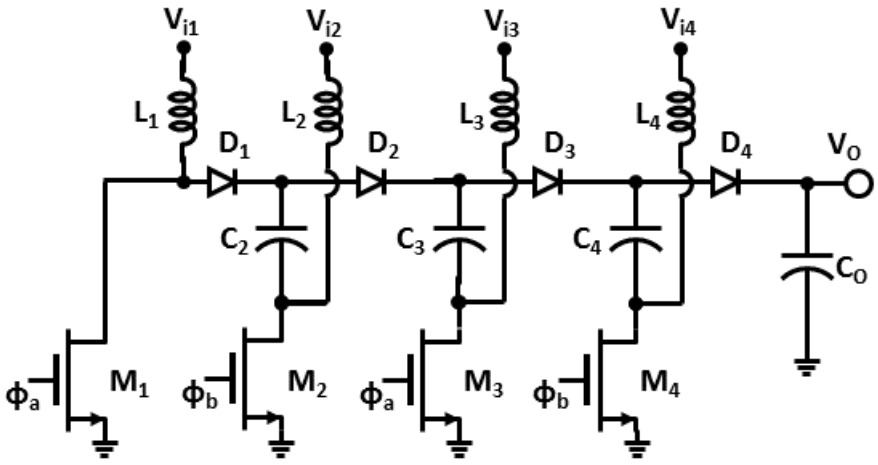

Figure 3.11: Non-isolated multiple input boost converter [122]).

$$V_O = \frac{V_{i1} + Vi3}{1 - D} + \frac{V_{i2} + Vi4}{D} \tag{3.5}$$

The converter shown in Figure 3.11 has nevertheless some important drawbacks. First of all, it requires of multiple inductors (one for each input), making it a bulky and expensive solution. Also, Equation 3.5 shows an opposite effect of the duty cycle on inputs 1 and 3, when compared with the effect on inputs 2 and 4. This means that a boosting ratio cannot be independently setup for each input source. Therefore, the switched converter still requires a regulation stage between its output and the load. Lastly, authors in [122] do not show if it is possible to implement any type of MPPT functionality on the converter.

3.5.3 Shared-Inductor DC-DC Converters

In the literature, buck-boost converters are commonly used in energy harvesting to create an impedance matching scheme for MPPT purposes, as their input impedance can be easily tuned via switching frequency control to create the required time-average input resistance. When multiple inputs are being considered, a single shared-inductor scheme can be used on the buck-boost converter to reduce the number of external components that are needed [123]. Figure 3.12 depicts a simplified schematic of this type of architecture [124], where 5 interface channels are given to AC

(piezoelectric) input types and 4 to DC (solar or thermal) input types. The complex controller in this topology allows all the inputs to have access to the single inductor, while at the same time ensuring that maximum transfer of power is obtained for each one of them.

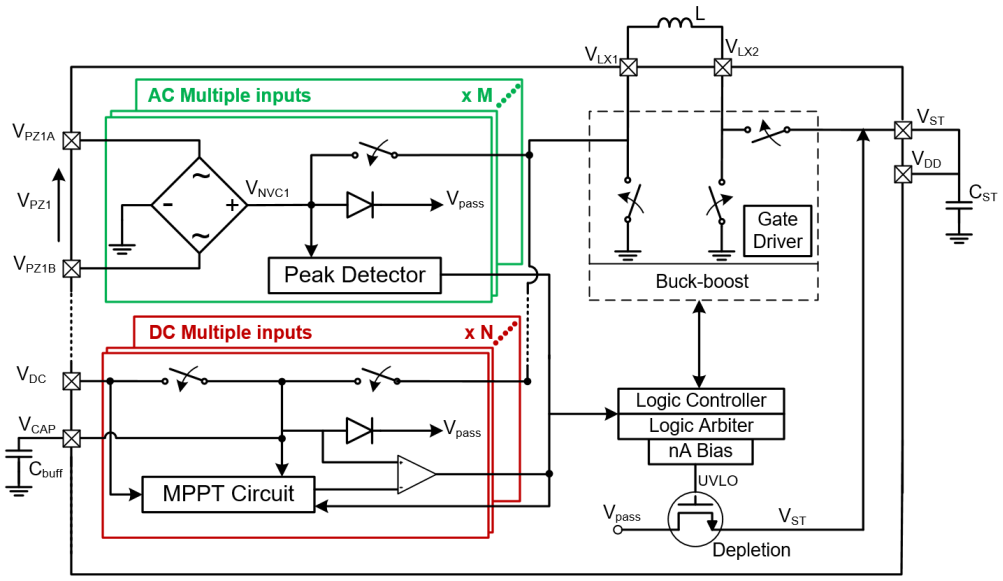

Figure 3.12: Buck-boost based energy combiner with shared inductor scheme [124].

In [124], a fractional open circuit voltage (FOCV) method is used for MPPT of the DC inputs. Open circuit conditions (OCC) are created by disconnecting each harvester from the interface, and then waiting for the voltage to restore to its open circuit value. Small capacitors are then used to sample and hold the voltage. In order to reduce the time required for the input voltage to reach the OCC, the input buffer capacitor (C_{buff}) is not directly connected to the harvester, but through an extra pin in the circuit (VCAP). Thus, 2 external pins per harvester are needed; as shown in Figure 3.12. This approach reduces the required sampling time down to 2 μsec, and the operation is repeated every 8 energy-extraction cycles of the boost converter (i.e. every 25 ms). This scheme allows following the variations of the input voltage, and reducing the wasted energy in the FOCV sampling process when the harvester is disconnected.

To regulate the access to the converter, an arbiter logic circuit was implemented, with preset

priorities fixed for each harvester type. Piezoelectric harvesters were set to the highest priorities as power can only be extracted when their output voltage reaches its maximum. Other type of harvesters (solar and TEG) were set to a lower priority, as their output power pattern is almost constant with time.

In the circuit of Figure 3.12, MPPT also requires the use of a comparator to control the switching speed in the boost converter, maintaining the harvester voltage close to the ideal OCC for maximum power extraction. Fast comparators are then needed to maintain good MPPT tracking accuracy, and they come with higher power consumption. In [125] this problem is solved by using a shared comparator for all input sources, and then tuning an oscillator to mimic the output of the comparator. The oscillator (one for each source) continues the MPPT operation, and the comparator is powered down to save power. With this strategy, power can be harvested even at the nanowatts level [125].

In [126], a structure similar to the one in Figure 3.12 is also used for multiple input harvesting. However, the MPPT algorithm is rather implemented with a time-multiplexing approach, and not priority-based as in the case of [124]. Rather, a microcontroller is used to monitor the MPPT process; seeking to maximize the $V_{in,i}^2\ N_i$ product, according to the following equation:

$$P_{in,i} = \frac{V_{in,i}^2}{R_{em}} = \frac{T_{CLK}}{8LN_T} \times V_{in,i}^2 N_i \tag{3.6}$$

In Equation 3.6, R_{em} is the emulated resistance of the boost converter, T_{CLK} is the switching period and L is the inductor's value. Also, N_i is the number of clock cycles given to the ith-input and N_T is the total number of clock cycles. The previous approach is similar to a hill-climbing algorithm, but with a simplified sensing scheme that doesn't require the measurement of current, as it is replaced by N_i as a parameter that reflects the average current extracted from the harvester.

The main disadvantage of the shared-inductor architecture is that, as the numbers of input sources are increased; the operation deviates from a truly concurrent energy harvesting, as all but one transducers are left disconnected. This effect can be reduced with a larger input buffer capacitor, as they store the energy while the harvester is disconnect but, as mentioned before;

it impacts the OC voltage settling time for the MPPT method. This in turn establish a tradeoff between tracking accuracy and harvesting efficiency.

3.5.4 Fully Integrated Switched-Capacitor Converter for Concurrent Energy Harvesting

It is well known that switched-capacitor (SC) circuits can be used to add voltages. The basic concept of a SC-based DC combiner is shown in Figure 3.13 [127]. The technique consists on converting a DC input into an AC form, then superimposing it on another DC input. By rectifying the resulting waveform, a DC output voltage can then be obtained. As shown in Figure 3.13, this process can be cascaded in a modular fashion to combine an arbitrary number of inputs.

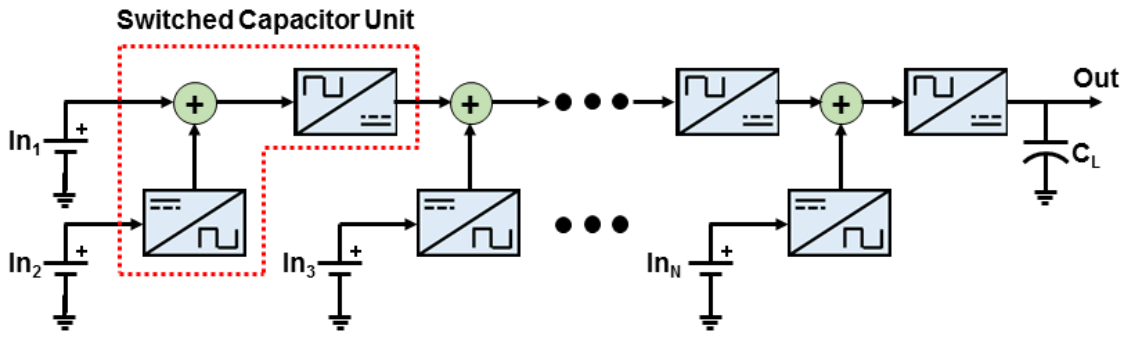

Figure 3.13: Basic concept of a switched capacitor based (i.e. fully integrated) DC power combiner for energy harvesting [104].

One implementation of the switched-capacitor unit for the DC combiner is shown in Figure 3.14 [127]. This circuit is capable of combining up to three DC sources, if they are available. In this topology, inputs *Source 1* and *Source 2* are converted into AC form using a pair of differential oscillators (I_0 and I_4). These oscillators are composed of thyristor-based delay cells, which makes them very low-power circuits. Then, with the help of drivers, the pulsed-shaped waveform are coupled to the intermediate nodes v_{i1} to v_{i4} through the capacitors C_1 to C_4. The peak-to-peak voltage of node pair v_{i1} and v_{i2} would be equal to *Source 1* + $Source_{IN}$, which is further rectified by the transistor pair M3-M4. Following the basic concept depicted in Figure 3.13, this resulting voltage is added in the node pair v_{i3} - v_{i4} to *Source 2*. If a large capacitor is connected at the output

node of the circuit, V_{OUT} will consist of a DC voltage equivalent to the sum of the three inputs.

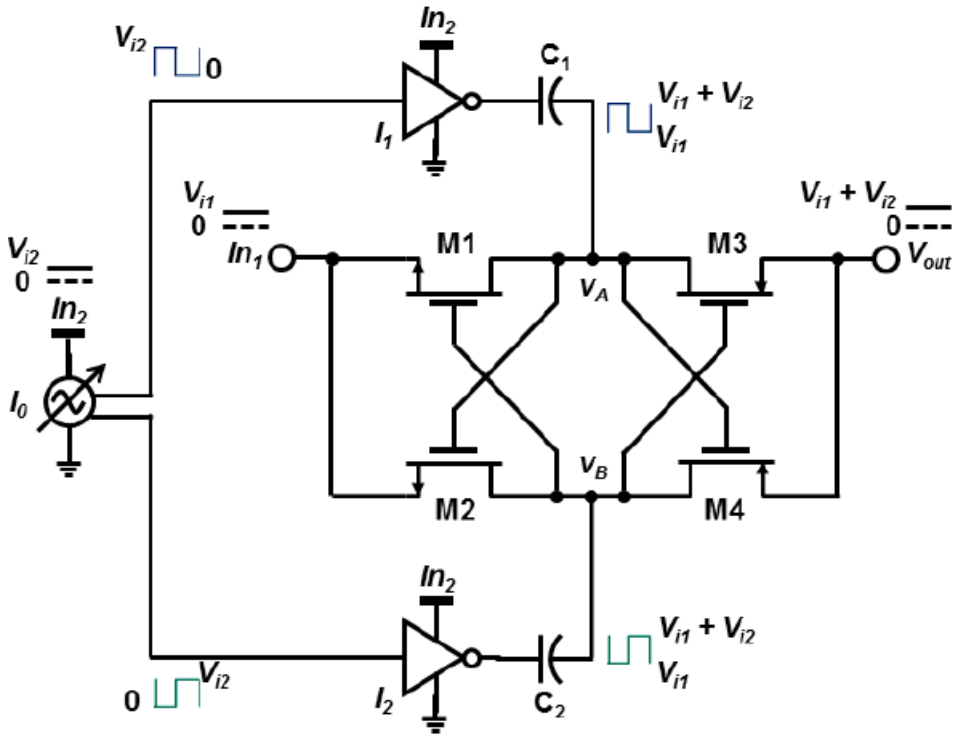

Figure 3.14: Two-input DC switched-capacitor combiner, which is used as a module for the architecture shown in Figure 3.13 [104].

The SC-based energy combiner of Figure 3.14 has several advantages over their inductor-based counterparts that where described in the previous subsection. First, it can be fully integrated, reducing the size and cost of the implementation. Also, the energy harvesting from multiple sources occurs in a concurrent way. There is not a multiplexing of inputs, imposed by the necessity of sharing a common resource as the single-inductor topology. As mentioned before, this multiplexing involves a trade-off between tracking accuracy and harvesting efficiency that is intensified by a larger number of inputs.

3.6 Performance Comparison of Multisource Energy Harvesting Architectures

In many cases it is difficult to compare the performance of different works found in the literature, especially when diverse technologies were used for each implementation. Most of the works also use different transducer models, so the value of total output power that is measured and reported will logically differ. However, in Table 3.1 a comparison is made on the performance of the various multisource energy harvesting topologies that were reviewed in this paper. We have rather focused on topological traits and capabilities, like being able to perform MPPT and battery charging operations. Peak efficiency can also be compared because it is a normalized quantity that is related to the architecture's complexity and serves as a standard figure of merit for PMUs. The input power (when available) at which the peak efficiency is measured is included as a reference. Another important figure-of-merit is the quiescent current consumption of each implementation, and it is also included on the comparison table.

3.7 Conclusions and Open Areas of Research

The IoT "revolution" has been the driving force for many research efforts in different areas of electronic circuits and computer systems. Energy harvesting techniques has been extensively investigated as they promise to be a key enabling technology for autonomous IoT end-nodes. In particular, multisource EH has demonstrated to be the best option for system reliability.

In recent years, different architectures have been proposed for harvesting energy from multiple inputs, each of them suitable for a particular application. The simpler schemes such as the Power ORing topology offer reduced system complexity and modularity, making them acceptable solutions when it is not expected that all the input sources will be delivering a significant amount of power at the same time. On the other hand, energy combining has been demonstrated with multiple input switched-inductor or switched-capacitor converter architectures. As observed in this chapter, the time-multiplexing nature of the shared-inductor scheme imposes a tradeoff between tracking accuracy and efficiency. In contrast, the SC approach offers concurrent energy addition with a fully integrated solution, but the functionality and performance of state-of-art designs can

Table 3.1: Comparison of multisource energy harvesting architectures.

Ref.	**Topology**	**Inputs**	**Type**	**Technology**	**MPPT**	**Battery Charging**	η_{peak}	P_{in}	**Quiescent Current**
[111]	Complementary	2	TEG PZT	HV 0.35 μm CMOS	No	No	82%	NA	300 nA
[114]	Power ORing	2	PV Wind	Discrete	Yes	Yes	82% (PV) 85% (wind)	NA	NA
[113]	Power ORing	2	PV TEG	Discrete	Yes	No	91%	392 μW	50 μA
[106]	Power ORing	2	DC AC	Commercial IC	No	Yes	90%	4 mW	950 nA
[117]	Power ORing	2	DC AC	Commercial IC	No	No	90%	NA	1.5 μA
[118]	Level Detect.	2	RF TEG	0.35 μm CMOS	No	Yes	50%	NA	70 μA
[119]	Level Detect.	3	DC	0.13 μ CMOS	No	Yes	95 %	85 μW	1.3 μA
[121]	LDO	3	RF, PZT PV	0.13 μm CMOS	No	No	85 %	7.3 mW	65 μA
[122]	Boost (multiple L)	2	DC	Discrete	No	No	NA	NA	NA
[124]	Shared L	9	TEG PZT RF PV	0.32 μm BCD	Yes	No	89.6 %	101 μW (TEG) 59 μW (PZT) 55 μW (PV)	NA
[125]	Shared L	3	PZT RF PV	0.18 μm CMOS	Yes	No	87%	20 μW	18 nA
[123]	Shared L	3	TEG PZT PV	0.35 μm CMOS	Yes	No	83% (PV) 58% (TEG) 79% (PZT)	NA	2.7 μA
[127]	SC	3	DC	0.13 μ CMOS	Yes (manual)	No	58.4%	600 μW	NA

still be improved. The reported architecture in [127] lacks an automatic MPPT control and battery charging functionality. The design of a complete integrated solution based on the SC unit block of Figure 3.14 (or other similar) is still to be investigated. A potential limitation inherent to the energy combiner scheme of Figure 3.13 would be the limited number of inputs that the system can accommodate, given a maximum Silicon area allocated to the converter. To increase the total number of inputs without increasing the area consumed by the integrated capacitors, some type of sharing scheme would have to be proposed. Also, algorithms could also be implemented for smart energy harvesting, where input sources can be selected depending on their available power. Intelligent battery-charging functionality, according to the levels of harvested power, is also an open area of research that has not been well explored. To date, none of these features have been found in state-of-the-art multisource harvesting architectures.

4. FULLY INTEGRATED MAXIMUM POWER TRACKING COMBINER FOR ENERGY HARVESTING IOT APPLICATIONS *

4.1 Introduction

The Internet of Things (IoT) continues to grow, thanks to the contributions of many enabling technologies. The design of ultra-low power (ULP) circuits and systems is one of them. With static power consumption on the order of μW's and even nW's, ULP systems enable IoT applications that can operate from a limited power source, such as a battery. However, some applications like portable biomedical systems and wireless sensor nodes require a very long operational life without the need of maintenance or battery replacement. In those cases, the use of alternative energy sources has been proposed as a way to extend battery life or even replace it completely [128].

Substantial research work has focused on the design of self-powered management units that harvest energy from individual sources such as light [129], heat [93], mechanical vibrations [91], and radio frequency signals [130]. However, none of these offer a constant source of power as a result of ambient variations, and they can even present indefinite periods of zero energy generation [131]. Considering their intermittent nature, trying to sustain the operation of a system with a single source might not provide an adequate solution. In contrast, harvesting power from various complementary sources offers a more reliable approach to ambient-powered applications [121].

In the literature, different approaches are proposed to combine the power from several sources [113, 114, 118, 119, 121, 123–127, 132]. Figure 4.1 depicts the most common architectures.

A simple method, shown in Fig. 4.1(a), consists in the parallel connection of all harvesters through a power ORing structure [113, 114]. A single dc-dc converter conditions the voltage at the storage element (V_{ST}) and provides maximum power point tracking (MPPT) to the output. This method offers a highly modular architecture that can be easily extended to any number of inputs. However, it is severely limited by its "winner-take-all" nature, in which the presence of a dominant

*Reprinted with permission from "A Fully Integrated Maximum Power Tracking Combiner for Energy Harvesting IoT Applications" by J. J. Estrada-López, A. Abuellil, A. Costilla-Reyes, M. Abouzied, S. Yoon and E. Sánchez-Sinencio. IEEE Trans. Industrial Electronics, DOI 10.1109/TIE.2019.2907449 ©IEEE 2019

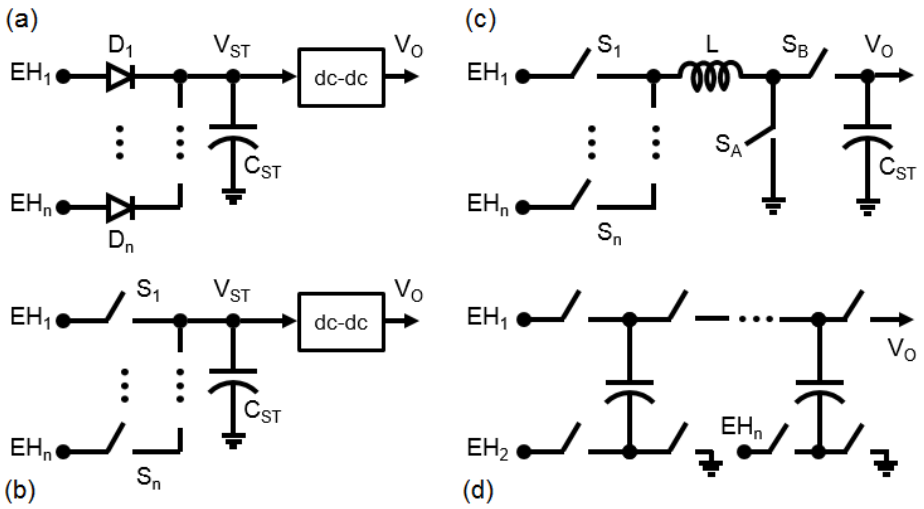

Figure 4.1: Methods of energy combining: (a) power ORing, (b) input multiplexing, (c) inductor sharing, and (d) switched capacitor-based [128].

source excludes the contribution from the other inputs [124]. Therefore, a true combination of energy is not achieved. Another drawback is the voltage drop on the conducting diodes, which represents a significant source of power loss, especially for low-voltage inputs.

Other works propose the input-multiplexing scheme of Fig. 4.1(b) [118, 119]. By using switches instead of diodes, the conduction losses are significantly reduced when compared with the ORing architecture. Different criteria can be used for input selection, which in the end affects the system's capacity to combine energy. In [118], a simple level detection technique is applied, where only the source with the highest voltage is allowed to charge the storage element (C_{ST}). This method is not different from the one shown in Fig. 4.1(a), and the energy from the other transducers is also wasted. A better solution is obtained when all the inputs that are larger than a threshold, are time-multiplexed and sequentially connected to C_{ST} [119]. That way, the combination of their energy is achieved. However, the system developed in [119] lacks of MPPT functionality, which is absolutely necessary if the maximum harvesting efficiency is desired.

As shown in Fig. 4.1(c), the level-based, time-multiplexed technique can also be incorporated into the structure of a multiple-input switched-inductor converter [123–126]. The inductor can be shared because the converter operates in the discontinuous conduction mode (DCM). Switched-

inductor converters in DCM can be very efficient at low-power levels and perform MPPT, but they require an external inductor that increases the size and cost of the solution. Time-multiplexing also yields loss of energy when the sources are disconnected from the circuit. This loss can be reduced if a storage capacitance is connected at every input [124]. However, this capacitance only increases area and cost.

Finally, as shown in Fig. 4.1(d), a switched-capacitor (SC) circuit can also be used for combining the energy from multiple sources [127, 132]. The main advantage of this approach is that it can constitute a fully integrated solution. It also allows concurrent energy combining, which eliminates time multiplexing [127]. However, the SC-based circuits in [127, 132] also have limitations. In [132], the SC circuit is used only to add the voltage from its two inputs, but maximum power point tracking was not provided for the transducers. In [127] the possibility of MPPT is demonstrated, but only performed manually in the lab. Also, the circuit in [127] suffers from reduced efficiency when weak inputs are present.

In this chapter, the design of a fully integrated, switched capacitor-based power combiner system for multisource energy harvesting (EH) is presented. This switched capacitor (SC) combiner incorporates automatic MPPT capability and a novel power-aware ranking strategy. Previous solutions use only voltage level-based techniques [118, 119, 126, 127] to select or disable their inputs. Others assign hard-coded priorities that cannot be changed after circuit fabrication [124]. Neither strategy guarantees the selection of inputs with maximum power, when they are characterized by the same open-circuit voltage. Different than those approaches, the proposed system applies a ranking scheme that is based not only on voltage levels, but also on the available power of the transducers. This is done by an efficient analog ranking circuit that allows the system to select and combine the sources according to their actual power. With this strategy, the system follows the changes in the inputs due to ambient variations, and maintains high power extraction.

A two-way energy storage approach has been implemented, where the inputs that are not being combined but still offer useful power, can be used to supply the combiner's circuitry. That way, longer self-sustained operation can be achieved. Furthermore, a new passive start-up scheme is also

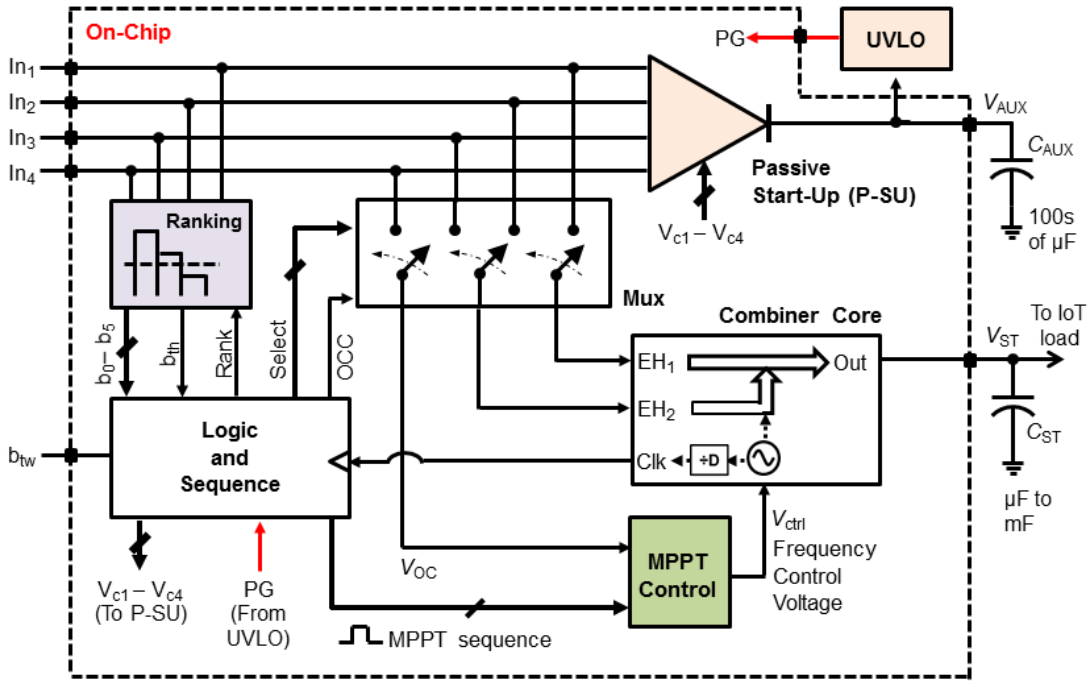

Figure 4.2: System level diagram of proposed multisource energy combiner [128].

proposed that selects the input with the largest voltage, but without using lossy diodes that slow down the start-up process. The system-level implementation and circuit-level design are discussed in the coming sections of this chapter.

4.2 System Level Architecture

The system level design of the proposed multisource energy combiner is presented in Figure 4.2. It is composed of the following blocks: passive start-up (P-SU), ranking and level detection, MPPT control, combiner core, multiplexer (Mux) and control logic. An external under-voltage lockout (UVLO) circuit is used to generate a power good (PG) signal that enables the system's operation. The design of UVLO circuits has been extensively covered in other works [24, 124, 125, 133]; therefore, it is not treated in this dissertation. For our purposes, a TPS3831 ultralow-power voltage monitor from Texas Instruments [134] was used as an UVLO circuit. Although it consumes a larger current (150 nA), it exhibits better accuracy ($\approx 1\%$) than integrated implementations.

As shown in Figure 4.2, a two-way energy storage architecture is implemented, using two

capacitors. The internal circuits of the combiner are supplied by the auxiliary capacitor C_{AUX}, while the bigger storage capacitance (C_{ST}) serves as the buffer to power the IoT load. Having a relatively small C_{AUX} makes the start-up process faster, while a big C_{ST} is able to meet the high-current demands of the load. The fractional open-circuit voltage (FOCV) method for MPPT was implemented, because it offers a good tradeoff between tracking accuracy and power consumption [124].

The system's operation follows the sequence described in the flowchart of Figure 4.3. At the beginning, when there is not enough stored energy to operate, the only functional block is the passive start-up. The P-SU selects the highest available input and provides a passive path to charge the auxiliary capacitor C_{AUX}. Once there is enough charge stored in C_{AUX} (i.e. $V_{AUX} \approx 1$ V), the UVLO raises the PG signal. With a high PG, the system enters active operation. A small waiting period (called t_{mppt}) is introduced before each sequence of ranking, selection and tracking of the inputs is updated. Considering the slow change that characterizes most ambient sources, a relatively low refresh rate (ms) for these operations is still enough to track voltage fluctuations in the energy harvesters [135] (harvesting efficiency is not affected) while at the same time saves dynamic power consumption in the associated circuitry. After the waiting period, the inputs are disconnected from the combiner core to reach the open circuit conditions (OCC).

Under the OCC period, the ranking circuit categorizes the inputs, and the results are given to the control logic in a digital word (b_0-b_5). Once the ranking operation is done, an MPPT sequence is initiated. The MPPT block samples the open circuit voltage (V_{OC}) of the input that is ranked first (V_{rank1}), and divides it by a factor of N. The value of N can be adapted to different types of harvesters (i.e., 2 for resistive sources and 1.3 for solar cells [135]). Then, the multiplexer selects two out of four inputs to connect to the combiner core. The frequency control voltage (V_{ctrl}) is varied by the MPPT control circuit until the maximum transfer of power is achieved (when voltage $V_{rank1} \approx V_{OC}/N$). After this sequence, the system starts harvesting and waits again for a period of t_{mppt} before updating the ranking and MPPT operations.

The temporary disconnection of the EH sources from the system during the OCC period (t_{occ})

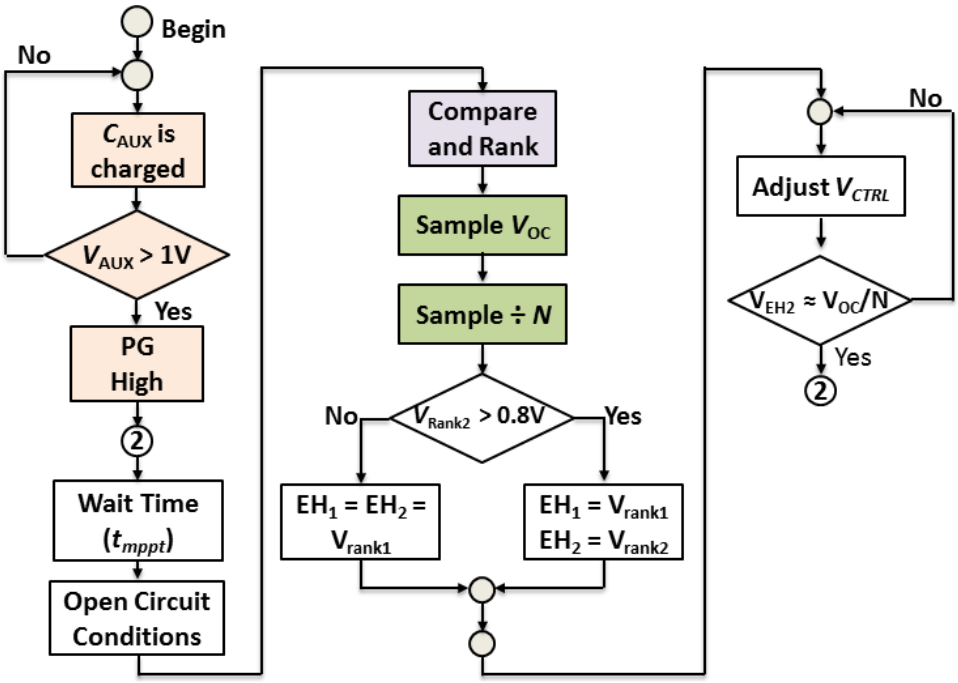

Figure 4.3: Control flow-chart of the energy harvesting system [128].

involves a loss of harvested energy. This loss in the system's efficiency can be roughly characterized by the following factor:

$$L_{occ} = 1 - \frac{t_{occ}}{t_{occ} + t_{mppt}} \tag{4.1}$$

The OCC period affects efficiency depending on its duration with respect to the time of effective harvesting t_{mppt} (when sources are connected to the system). Then, the disconnection losses can be made less than 1% if $t_{occ} \ll t_{mppt}$. However, t_{occ} should also be larger than the harvester's response time (t_{eh}), allowing it to effectively reach its V_{OC} before sampling. The OCC period should then follow the criterion:

$$t_{eh} < t_{occ} \ll t_{mppt} \tag{4.2}$$

In [124] and [135], an open circuit sampling period of 2 μs is used. As observed above, t_{mppt} is in the order of ms and in this design a t_{occ} of several μs is used. This would be able to accommodate

harvesters with comparable response time, while at the same time keeping the disconnection losses very low.

While the system is combining the two largest sources, they are disconnected from the P-SU circuit, so it cannot interfere with the harvesting process. This is done by asserting high the corresponding cut signals ($V_{c1} - V_{c4}$). Nevertheless, the start-up remains connected to the two remaining sources, meaning that they keep charging C_{AUX}. With this strategy, the energy of the four inputs (if available at the same time) can be exploited -even when only two of them are going through the combiner core.

As shown in Figure 4.3, the combiner performs a smart harvesting strategy that seeks to maintain the maximum power extraction possible. The ranking circuit not only categorizes the inputs, but also detects the voltage level of the second ranked source. If the V_{OC} of this source is less than 0.8 V ($b_{th} = 0$), the circuit will harvest energy only from V_{rank1}. This value means that in the case of N = 2, the input to the combiner is at least 0.4 V, which is the minimum voltage needed to operate with acceptable efficiency.

4.3 Circuit Level Design

4.3.1 Two-Input Combiner

The core energy combiner circuit is shown in Figure 4.4(a). It consists of a two-input SC converter, derived from traditional voltage-doubler structures [127, 136]. In this circuit, input EH_2 is converted into an alternating pulsed voltage by a differential low-power oscillator (I_3). Using drivers (I_1-I_2), the pulsed voltages are coupled to the intermediate nodes A and B. In [127, 137], it is shown that a charge transfer and accumulation process occurs at these nodes: the waveform with peak voltage EH_2 is superimposed to the dc-value of EH_1. The resulting waveform is rectified by the M_3-M_4 pair and being filtered by a load capacitance, finally appears at the output node as a dc-voltage equivalent to EH_1+EH_2. The addition of EH_1 and EH_2 through charge accumulation implies that a proportional amount of energy has been stored, resulting in the addition of power from these sources.

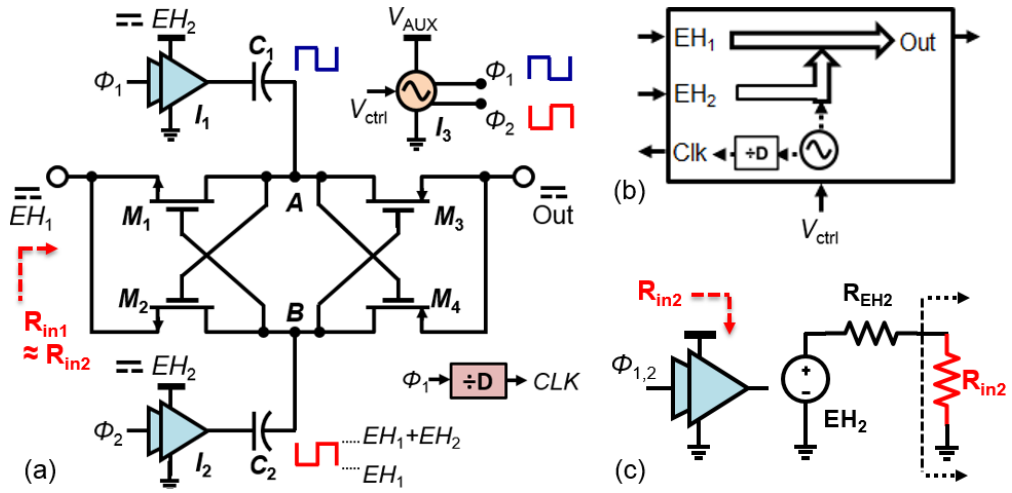

Figure 4.4: Two-input combiner core: (a) schematic, (b) symbol, (c) input resistance seen entering the buffer's supply terminal [128].

The steady-state operation of any SC converter can be modeled with the equivalent circuit shown in Figure 4.5(a) [138]. The model represents the open-circuit (ideal) gain $A = V_{out}/V_{in}$ of the converter. The resistances R_i and R_{out} model the losses of the circuit, which are dependent on the switching frequency and the converter's topology.

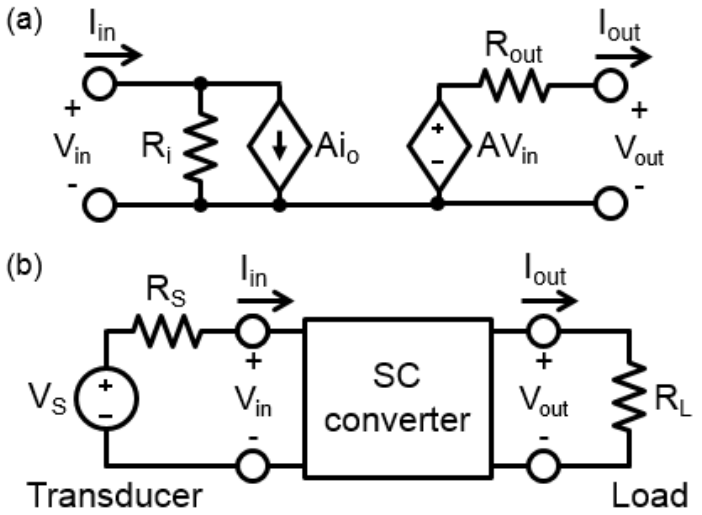

Figure 4.5: (a) Steady-state equivalent circuit model of a SC converter, (b) SC converter connected to transducer and load in EH system [128].

If the resistance of transistors M_1-M_4 is neglected, the output resistance of the SC circuit of Figure 4.4(a) is approximately given by [138, 139]:

$$R_{out,ssl} = \frac{\beta}{fC_t} \tag{4.3}$$

where f is the switching frequency, C_t = C_1 + C_2 is the total converter's capacitance, and β = 1/(1+α). The parameter α is the ratio of parasitic capacitance to total converter's capacitance C_{par}/C_t.

Equation 4.3 is valid only at low frequencies of operation and it is called the slow switching limit (SSL). At high frequencies, the output resistance is better modeled by:

$$R_{out} = \sqrt{R_{out,ssl}^2 + r_{on}^2} \tag{4.4}$$

where r_{on} is equal to the conduction losses of the MOS switches [127]. Eventually, at enough high frequency, R_{out} is constant and dominated by r_{on}. This is called the fast switching limit (FSL).

When the SC converter is connected to a harvester source and load (Figure 4.5(b)), it will demand a current I_{in} from the transducer. From Figure 4.5(a), this input current is given by:

$$I_{in} = \frac{V_{in}}{R_i} + \frac{A^2 V_{in}}{R_{out} + R_L} \tag{4.5}$$

The resistance R_i represents the input impedance of the converter at light (open circuit) load. Its value is typically high (in the MΩ range), so its contribution to the input current can be neglected [127, 138]. Then, the equivalent input resistance of the SC converter is R_{in} = V_{in}/I_{in} = (R_{out} + R_L)/A^2. A more detailed analysis [140, 141] can be used to show that:

$$R_{in} = \frac{1 + R_L/R_{out}}{(A^2 + \alpha) + \alpha R_L/R_{out}} \cdot R_{out} \tag{4.6}$$

Equation 4.6 takes into account the contributions to the input current of charging and discharging the converter's parasitic capacitances.

As shown in Figure 4.4(c), the input impedance R_{in2}, seen entering the buffer's terminal, can be set to match the source resistance R_{EH2}, by tuning the frequency of the oscillator. This is because, as expressed in Equation 4.6, the input resistance is proportional to R_{out}, which in turn is dependent on the switching frequency. Therefore, power tracking can be obtained by automatically adjusting f to reflect the necessary R_{in2} that matches the source resistance of the harvester. Figure 4.6 plots the theoretical (using Equation 4.6), simulated and measured dependence of R_{in2} with the oscillator's frequency, for an R_L in the kΩ range. The value of R_{in1} (seen at input EH_1) follows it closely. There is an experimental R_{in2} matching range of 450Ω−3kΩ. As it can be observed, there is a good agreement between the measured, simulated and analytical results.

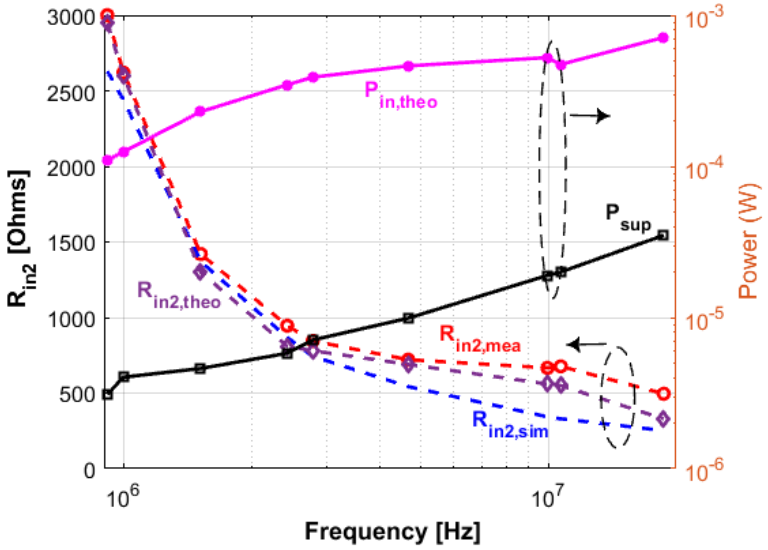

Figure 4.6: Input resistance, power consumption and theoretical harvested power of combiner circuit versus frequency [128].

From the model of Fig. 4.5, the available input power can be described with:

$$P_{in} = \frac{V_S^2 R_{in}}{(R_{in} + R_s)^2} \tag{4.7}$$

The maximum transfer of power occurs when R_{in} = R_s. Using Eq. 4.7, the theoretical input

power (assuming impedance matching) that the combiner would harvest is calculated and plotted in Fig. 4.6. This has been done considering that the combiner's inputs are at the minimum 0.4 V accepted by the circuit during harvesting. For comparison, the measured power consumption of the system P_{sup} (including logic, ranking, MPPT, and oscillator circuits) at V_{AUX} = 1 V is also shown.

For the SC converter of Fig. 4.4, power conversion efficiency (PCE) can be defined as [139]:

$$PCE = \frac{1}{1 + \alpha f C_t \frac{(R_L + R_{out})^2}{4R_L} + f C_t \frac{R_{out}^2}{R_L}} \tag{4.8}$$

This expression considers the losses due to R_{out} and parasitics, and shows the dependency of PCE to switching frequency (f) and the parasitic capacitance coefficient (α). Equation 4.8 shows that the PCE is limited by the α ratio which is process related. In a CMOS technology with MiM capacitors available, it is possible to obtain an α below 0.1. In that case, for a R_L = R_{out}, the third term in the denominator of Equation 4.8 will dominate (10×) the second term.

4.3.2 Passive Start-Up and Two-Way Storage Control

A commonly used start-up circuit for multiple inputs consist in the parallel connection of the harvesters with diodes [124]. This ORing topology is shown in Figure 4.7. This structure has the advanatge of automatically selecting the highest-input voltage. It also prevents backward current leakage effectively, isolating the harvesters from each other. In CMOS, the diodes can be implemented with MOS transistors or Schottky diodes (if the process allows it). The normally-on switches are implemented with depletion NMOS transistors [124].

However, the main disadvantage of the structure shown in Figure 4.7 is the associated voltage drop of the diodes, which increases the minimum start-up voltage by $V_{D,on}$. This in turn slows down the start-up process. The use of Schottky diodes and depletion devices also involves the use of costly extra-masks or discrete devices.

The proposed P-SU circuit shown in Figure 4.8 is used for the cold start-up of the harvesting system. This circuit eliminates the diode losses by using a tree-structure of cross-coupled PMOS

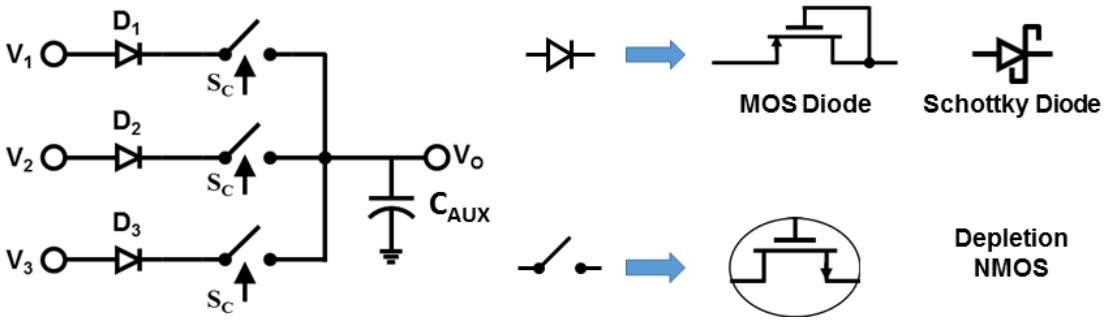

Figure 4.7: Power ORing topology commonly used for multisource passive start up implementation.

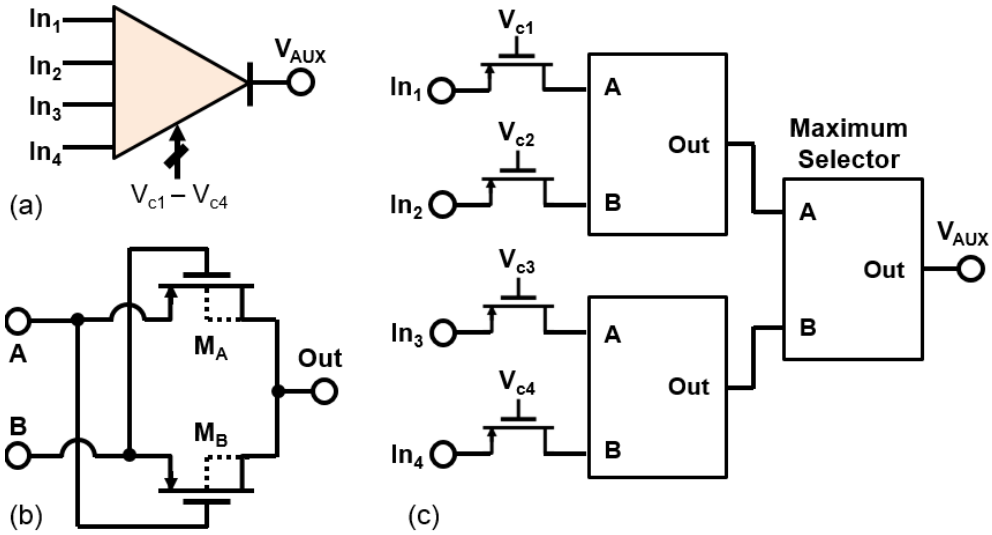

Figure 4.8: Passive start-up: (a) symbol, (b) maximum selector, c) architecture [128].

transistor pairs acting as maximum voltage selectors. Each stage selects its highest input and delivers it to the output. Therefore, V_{AUX} will consist of the highest of the four inputs. A minimum voltage difference of $V_{TH,P}$ between input pairs is needed to effectively connect the harvesters to capacitor C_{AUX}. This ensures the necessary V_{GS} to create a good-conducting transistor channel. Since the main goal of the system is to combine energy from harvesters of different nature, the probability of obtaining the same voltage on all of them at the same time is really low.

The start-up circuit turns to active mode once C_{AUX} accumulates enough charge to power up the system (at PG = 1). This is done by selectively turning off the PMOS transistors shown in Fig.

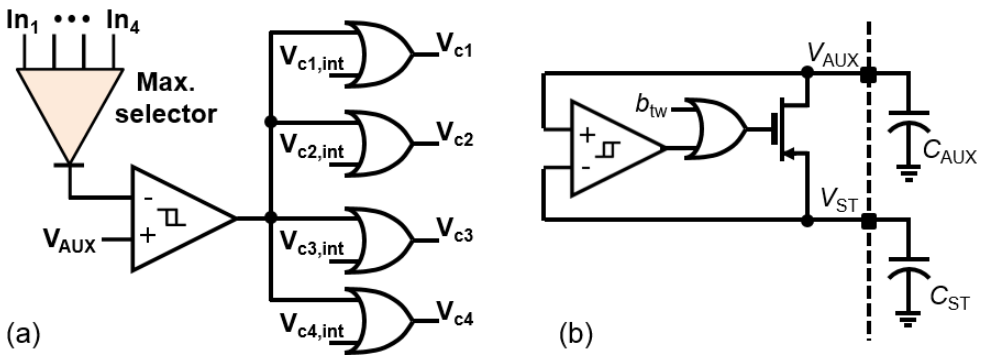

Figure 4.9: Control circuits for: (a) back-leak cut and (b) two-way storage [128].

4.8(c). These transistors are normally-on (closed) when the voltage at their gates is zero, but they can be opened by raising high the V_{c1}-V_{c4} signals. In the active mode the P-SU circuit performs the following functions:

1. *Continuous C_{AUX} Charging*: As mentioned before, once the ranking circuit selects the highest inputs and feeds them to the combiner, they are disconnected from the P-SU. The remaining inputs are left connected to keep replenishing C_{AUX} if energy is available. Even though no MPPT is done for these sources, they are still being used to power-up the circuitry, increasing overall system's efficiency.

2. *Back Leakage Elimination*: The maximum selector shown in Fig. 4.8(b) has a higher back current leakage than a conventional diode. If any of the non-combined inputs have a lower voltage than the C_{AUX}, a discharging path would be formed draining the capacitor. Therefore, the input switches need to be off when detecting that the maximum voltage generated by the harvesters is lower than V_{AUX}. To perform this function, a small-sized replica of the P-SU is connected to the inputs, while its output is compared with V_{AUX} (see Figure 7(a)). If V_{AUX} is larger than all inputs, the transistors are cut-off, eliminating the back current leakage.

Figure 4.10 shows the measured input and output voltages of the P-SU circuit. In this measurement, an external PG signal overrides the one generated by the UVLO; so both the P-SU selection of the largest input, and its active mode operation are distinguished. The capacitor C_{AUX} is also

disconnected. As shown, the output initially equals In_4. When In_2 is gradually increased, and its value surpasses In_4, it is selected as the output. When In_2 is decreased below In_4, the output once again picks In_4. Once the PG signal is set high, the circuit enters into active mode: In_4 is cut from the P-SU and V_{AUX} is equal to In_2 (the largest of the remaining inputs).

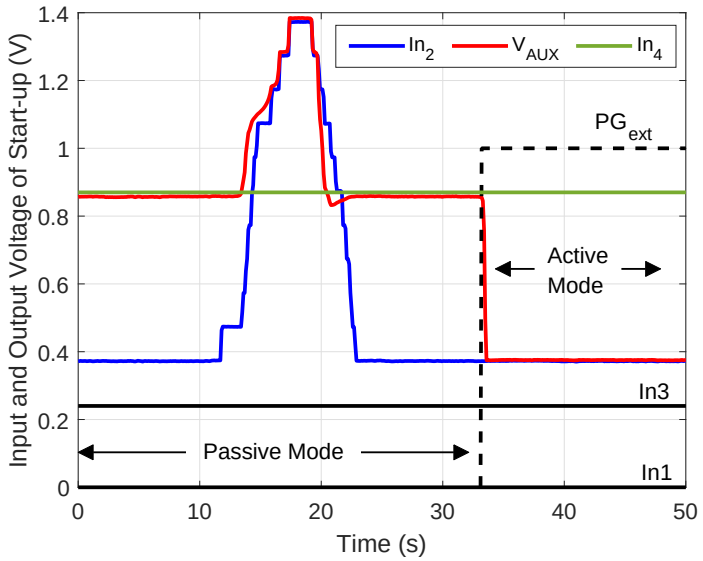

Figure 4.10: Acquired input and output voltages of the passive start-up circuit. The PG was overridden by an external signal [128].

Figure 4.9(b) shows the two-way storage control circuit that is active when PG = 1, and that can be externally controlled using the signal b_{tw}. When V_{ST} is larger than V_{AUX}, the comparator's output goes to zero. If the b_{tw} is externally set to zero, then C_{AUX} and C_{ST} will be short-circuited and the system would be self-powered through the sources that are being combined, independently of the power levels of the sources ranked 3 and 4. If the signal b_{tw} is set to logic-high, then no change occurs in the two paths, and the combiner's circuitry will be powered only by C_{AUX}. If the final application expects only one or two sources providing power concurrently, then b_{tw} should be set always low.

4.3.3 UVLO Circuit

As mentioned, the UVLO circuit was implemented in the prototype with a discrete component, the TPS3831 voltage monitor from Texas Instruments. The circuit is shown in Figure 4.11. The TPS3831 is connected to monitor the value of the auxiliary voltage V_{AUX}. When this voltage is $\approx$ 1 V, the PG signal (coming from the $\overline{Reset}$ pin) is raised high, indicating to the combiner system that it can start its harvesting process.

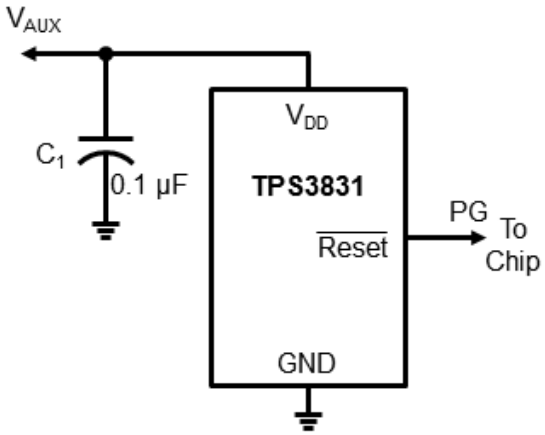

Figure 4.11: Undervoltage lockout circuit implemented with the TPS3831 voltage monitor.

Figure 4.12 presents the measurement of the input and output voltages of the UVLO circuit. In this test, voltage V_{AUX} is slowly increased while the UVLO monitors its value. It is observer that when $V_{AUX} \approx 1.14$ V, the PG signal goes high. From that moment on, the PG follows closely the value of V_{AUX}. When V_{AUX} decreases to 1.1 V, the PG goes down to 0 V again, which would turn off the combiner system circuits. The measured hysteresis is then 40 mV. The measured current consumption of the UVLO circuit is less than 200 nA.

4.3.4 Ranking Detector

As discussed in other sections, some works rely on measuring the open-circuit voltage (V_{OC}) of their inputs to enable or disable them in the harvesting process. However, the V_{OC} of a transducer

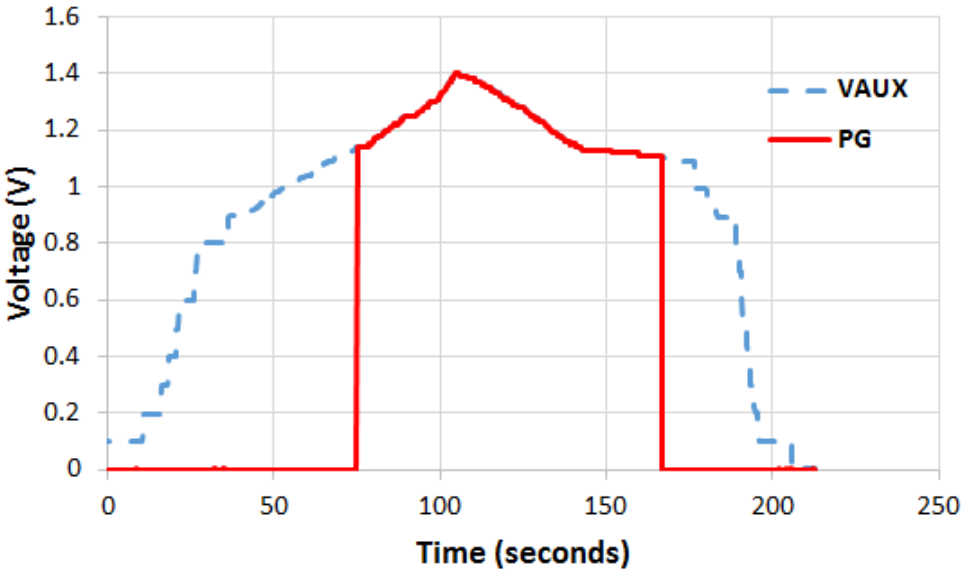

Figure 4.12: Measurement of input (V_{AUX}) and output (PG) voltages of the TPS3831 UVLO circuit.

alone does not reflect the amount of power it can deliver. Two harvesters with the same V_{OC} but different source resistance will deliver different power levels when current is drawn from them. At MPPT, the available power from the transducer is:

$$\mathrm{P}_{av,mpp} = \frac{(\mathrm{V}_{OC}/2)^2}{R_s} \tag{4.9}$$

which reduces for larger source resistance R_s.

To adequately categorize similar input sources according to their power levels, an amount of current can be extracted from them, and then measure the output voltage after the equivalent series resistance (see Fig. 4.13). The measured voltage V_{meas} = V_{OC} - $R_S I_{test}$ is proportional both to the open circuit value and the series resistance, offering a rough estimation of available power. The weaker transducers (the ones with large resistance) will exhibit the lowest output voltage under those test conditions.

The proposed power-based ranking is made by the common-gate comparator circuit shown in Fig. 4.14(a). Assuming that the same current flows through transistors M_2 and M_3, having $V_j < V_i$

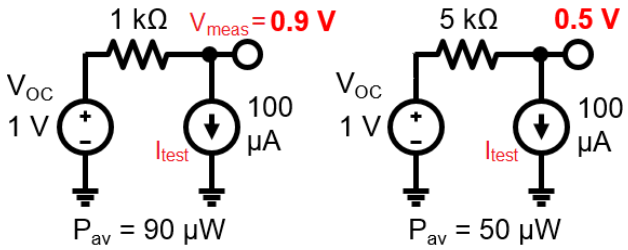

Figure 4.13: The effect of source resistance on the available power (P_{av}) of an energy harvester [128].

forces transistor M_2 into the triode region and $V_O \approx V_j$. The condition $V_j < V_i$ forces the current source's output transistor into the triode region and then $V_O \approx 0$. An inverting gain stage followed by a Schmitt trigger is used to sharpen the decision signal, translate it to the logic high level of V_{AUX}, and provide some noise immunity. For a precise comparison, a relatively large current (in the order of μAs) must be used for I_{test}. To reduce power consumption, the comparator is enabled only for a period of 450 to 610 ns (depending on process variations). This time is enough to allow the current-based comparator to response to the input voltages and obtain a valid comparison result. The Enable (En) signal is formed by a pulse generator as shown in Fig. 4.14(b). The size of the transistors and the bias currents has been selected to guarantee a maximum offset of $V_{OS} \approx 40$ mV under process variations in a Monte Carlo simulation ($<3\sigma$).

As shown in Fig. 4.14(c), the ranking operation requires comparing each input with the other three at the same time. Therefore six comparators in total are needed. As the comparators are disabled after the ranking process finishes, a latching circuit holds the results of each comparison. The latch pulse is generated by delaying the En signal (see Fig. 4.14(b)). The value of the delay has been designed to be less than the enable pulse period, but long enough to allow for the comparison to be completed before holding the data.

4.3.5 MPPT Control Circuit Design

The MPPT operation comes after the ranking process takes place, while the open circuit condition is still in effect. First, the V_{OC} of the harvester needs to be sampled and then divided by a factor of N. The circuit diagram and flowchart of the sample-and-divide circuit are shown in Fig.

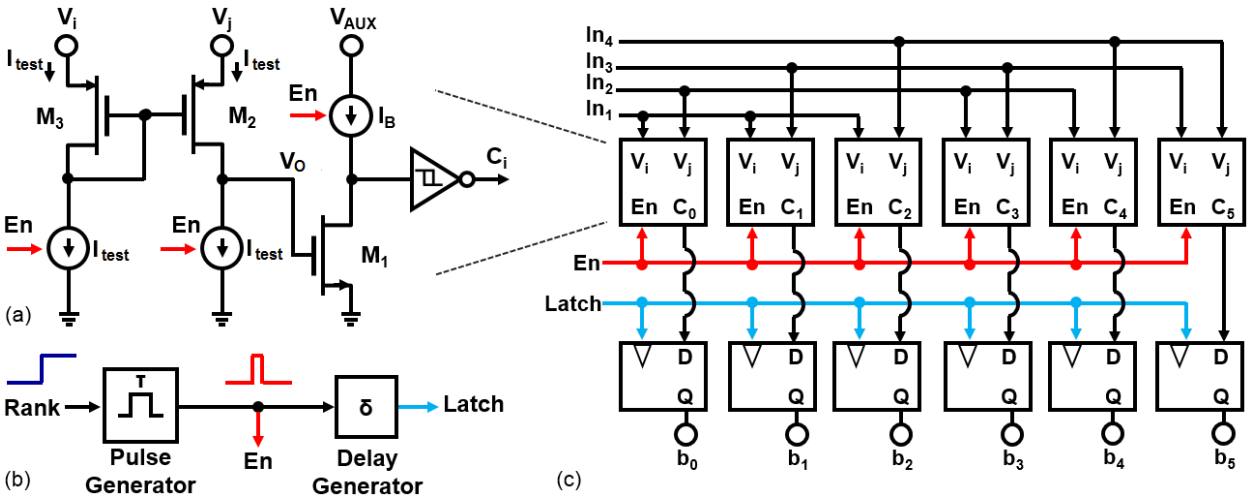

Figure 4.14: Ranking circuits: (a) current based comparator, (b) timing circuit, (c) four input ranking block [128].

4.15. A small capacitor C_{smp} is used to sample the open circuit voltage of the transducer. Then, using a reconfigurable capacitor C_{div}, that voltage is further divided by N. The value of N depends on the ratio of the two capacitors. As shown in the timing diagram, the $Sample$ and $Divide$ pulses are non-overlapping, which insures proper charge redistribution. The logic and sequence block provides these signals to the circuit.

With the slow-varying nature of typical harvesters, there is no need to constantly refresh the value of V_{OC}/N, which helps reduce the dynamic power consumption of all associated circuitry. However, this value needs to be held over a long period of time ($\sim$1 s), as a reference for the MPPT control circuit to lock and hold the point of maximum transfer of power. As leakage in the sampling capacitors and connected transistors is inevitable, the voltage on C_{div} will continuously drift over time, producing large errors and degrading tracking efficiency. A typical solution to this problem is to implement the sampling capacitors with big off-chip components (μF's) able to hold the voltage over time [108, 110]. This in turn increases the size and cost of the system.

Our proposed solution allows full integration of the sampling circuit and is shown in Figure 4.15. It consists of a series of two steps. First, a 4-bit flash ADC is enabled to generate a digital code that corresponds to the value of V_{OC}/N. To save power, the ADC circuitry is disabled after

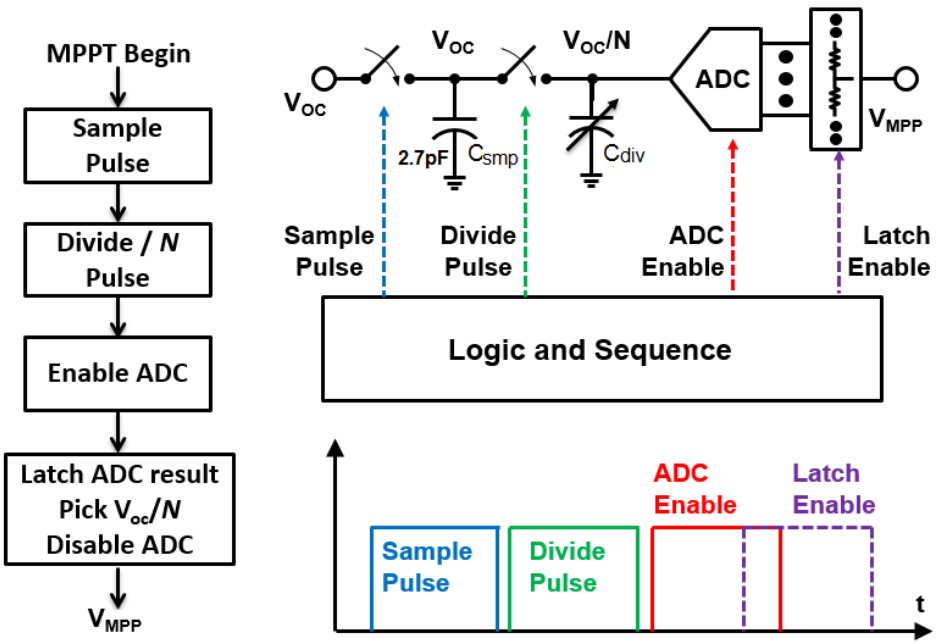

Figure 4.15: Sample, divide and MPPT reference generation circuit [128].

the conversion is done. Then, the digital code is used to create the reference voltage V_{MPP}, which is a quantized version of V_{OC}/N. This is done by previously latching the code and using it to pick the closest voltage to V_{OC}/N on a resistor string. This resistor string is in fact reused from the ADC circuitry. With this architecture, the reference voltage V_{MPP} is not affected by leakage and can be held for long periods of time. Even when some static current (1 μA) needs to be consumed in the resistor string, the use of a sampling capacitance of 2.7 pF allows a fully integrated implementation.

The circuit for V_{ctrl} generation is shown in Figure 4.16. It consists of a single comparator and an nA charge pump that slowly ramps up or down the control voltage for the oscillator. This in turn varies the input impedance of the combiner until both the harvester's voltage and the V_{MPP} are close to each other (within the hysteresis of the comparator which in simulations is $\approx$ 20 mV). Then, the maximum power transfer point is reached. Figure 4.16 also shows the steady-state waveforms of the circuit in time domain. In Figure 4.17, the measured input voltage of the combiner is shown when the MPPT is locked, with a ripple around the V_{MPP} of 23 mV.

The quantization error in the proposed MPPT control circuit will introduce losses in the actual

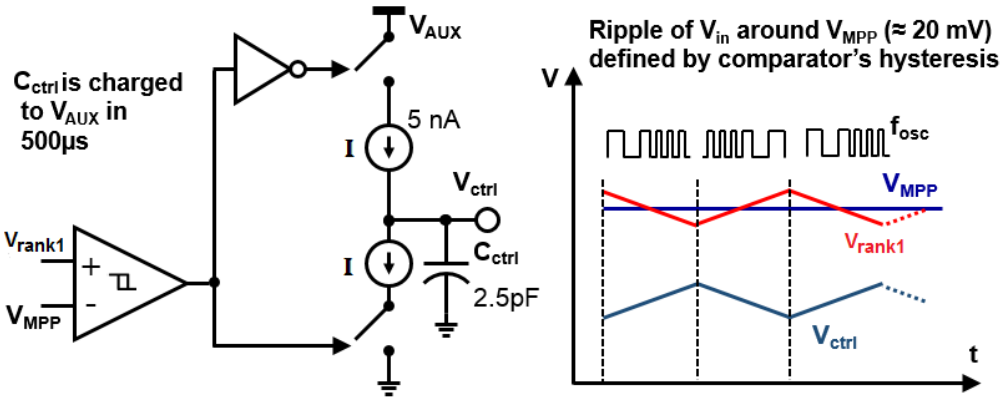

Figure 4.16: Circuit for V_{ctrl} generation and transient dynamics [128].

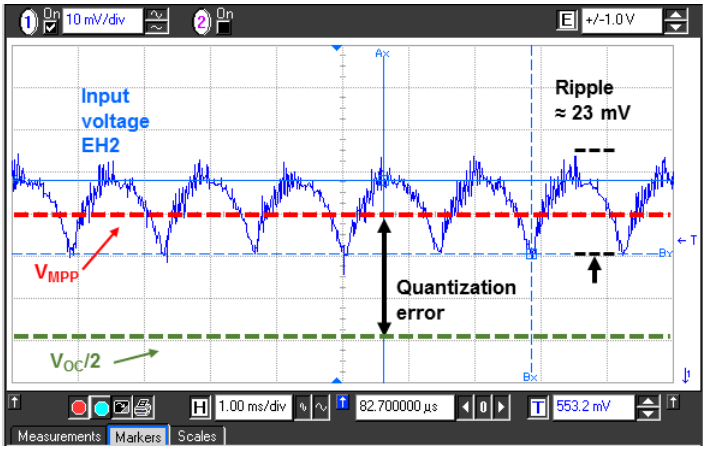

Figure 4.17: Acquired waveform of input to the combiner when MPPT is in process. The voltage shows a ripple of 23 mV [128].

harvested power, as the obtained V_{MPP} is not exactly equal to V_{OC}/N (see Fig. 4.17). The actual harvested input power, normalized to the maximum available power (Equation 4.9) can be shown to be:

$$\frac{P_{in}}{P_{av,mpp}} = 1 - \frac{\Delta^2}{(V_{OC}/2)^2} \tag{4.10}$$

The second term of Equation 4.10 represent the introduced losses, which are proportional to the voltage error Δ. The Δ is equal to the sum of the ADC's resolution and the observed ripple in the steady-state waveform. Figure 4.18 plots the resulting loss against the value of Δ, indicating

also what ADC resolution corresponds to these error values.

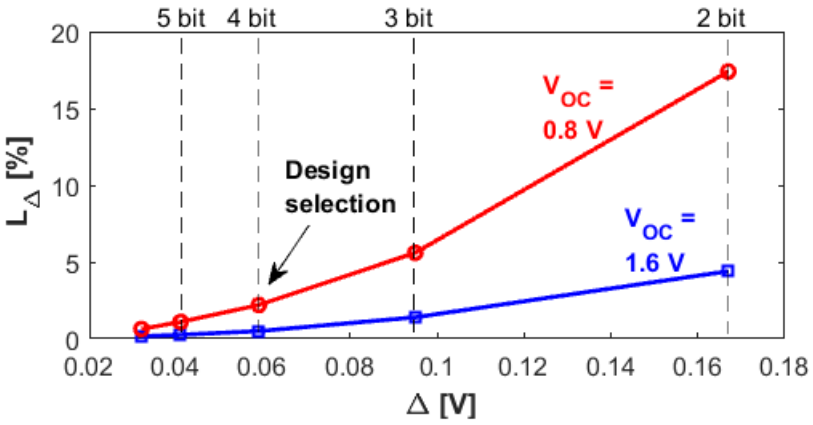

Figure 4.18: Power losses versus introduced error due to MPPT circuit operation [128].

As shown in Fig. 4.18, the losses decrease when reducing the error. For a measured ripple of 23 mV and a 4-bit ADC resolution, the losses are less than 3% for the worst-case of minimum V_{OC}. Although larger resolutions reduce the losses even more, the associated trade-off in area and extra power consumption does not justify it.

4.4 Measurement Results

4.4.1 Laboratory Setup

The energy combiner integrated circuit was fabricated using a 130 nm CMOS process. The chip photograph (with a silicon area of 0.48 mm^2) is shown in Fig. 4.19. The simplified laboratory experimental setup is shown in Fig. 4.20, as well as the test PCB. In the chip characterization, the voltage and currents at the inputs, C_{AUX}, C_{ST} and the load are monitored using digital multimeters (DMMs). Voltage waveforms, including those of EH_1 and EH_2 are captured with a digital oscilloscope. Voltage sources with a series resistance where used to emulate different types of harvesters. In this technology, the maximum tolerable voltage is 1.6 V when harvesting only from one input (under no load conditions). When two inputs are combined, the maximum voltage for each one is 0.8 V. The measured standby current consumption of the whole system is 1.95 μA.

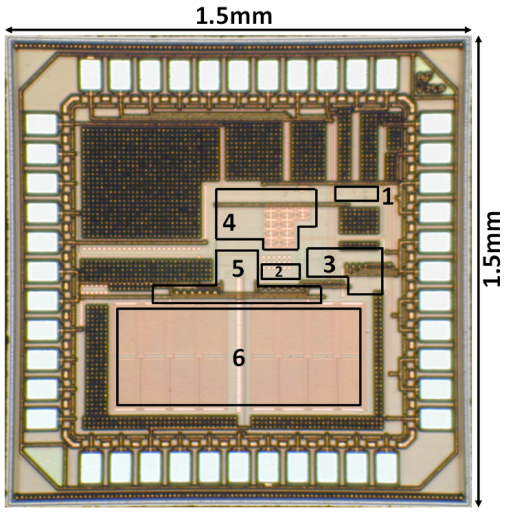

Figure 4.19: Chip photograph, showing (1) passive start-up, (2) control logic, (3) ranking circuit, (4) MPPT, (5) combiner and oscilator and (6) MiM capacitance.

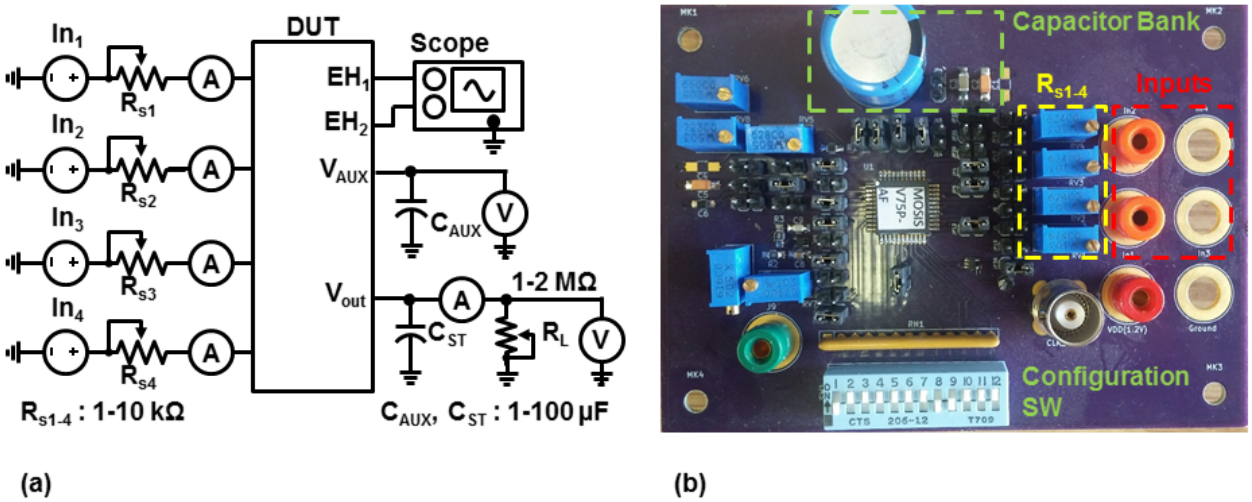

Figure 4.20: (a) Experimental laboratory setup for prototype characterization [128] (b) Printed Circuit Board.

4.4.2 Performance Characterization

The frequency of the control oscillator was measured for different supply voltages while varying the analog and digital controls. Results are plotted on Figure 4.21. The oscillation frequency can vary in a $30x$ range (from 560 kHz to 16.7 MHz). Figure 4.22 shows the transient operation

of the MPPT process when harvesting from one input source with $V_{OC} \approx 1.2$ V. The input voltage enters the OCC, when it goes from the level at MPPT to its open circuit value. The measured duration of the OCC period is 86 μs. The steady-state input voltage during the MPPT period is $\approx V_{OC}/2$, which corresponds to the optimal harvesting point.

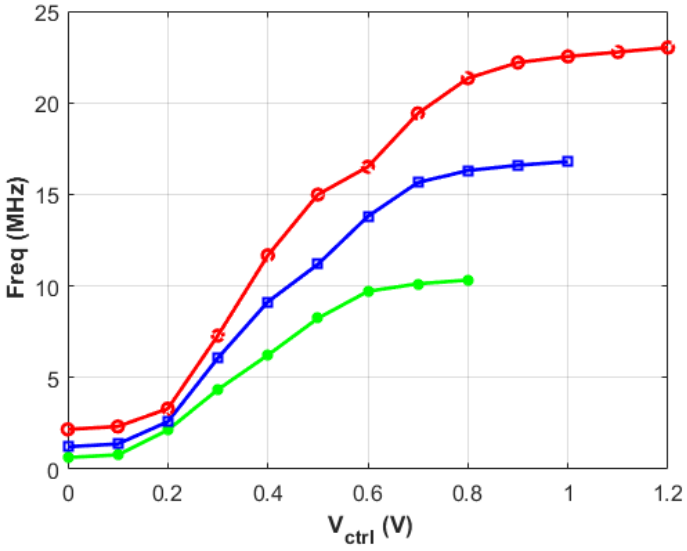

Figure 4.21: VCO output frequency range.

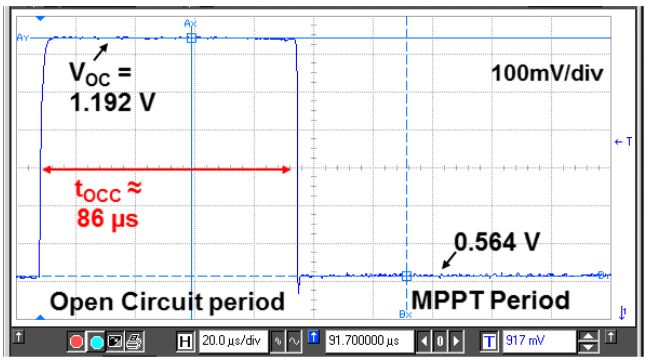

Figure 4.22: Transient measurements for input voltage waveform showing open circuit conditions and MPPT process [128].

In Fig. 4.23, the ratio of the OCC period with respect to the MPPT period is shown. As shown, the estimated efficiency loss due to source disconnection is less than 1%.

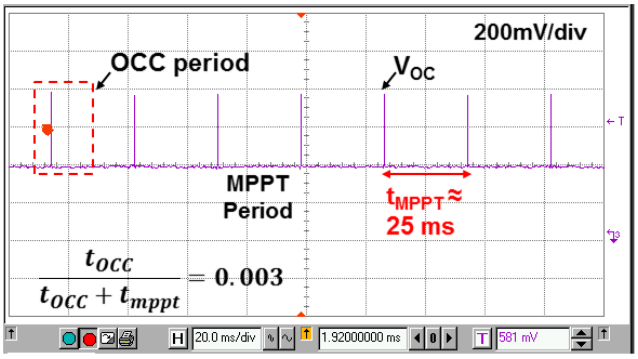

Figure 4.23: Ratio of open circuit period (t_{occ}) to harvesting period (t_{mppt}) [128].

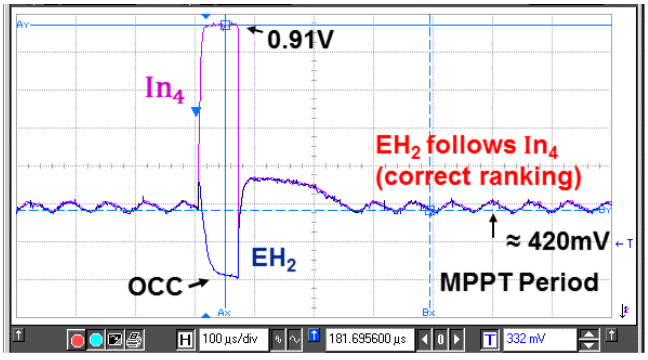

Figure 4.24: Input voltage and combiner input waveforms showing correct ranking.

In Fig. 4.24, two sources (V_{i1} = 1 V and V_{i4} = 0.91 V) are connected to the circuit. In that figure, both the lower source (In_4) and the input to the combiner (EH_2) are plotted. According to Fig. 4.3, as In_4 is larger than 0.8 V, it should be selected and connected to EH_2. The waveforms show an In_4 transition to OCC, while EH_2 drops because it is temporally disconnected from In_4. When OCC finishes, EH_2 then follows In_4, while MPPT occurs. The waveform demonstrates good

results for the ranking operation. The time the system takes to reach its MPP is approximately 200 μs.

Tracking efficiency can be defined as how close is the system to the peak power operating point, and can be calculated with [123, 141]:

$$\eta_{track} = \frac{V_{OC}/2 - \Delta\epsilon}{V_{OC}/2} \tag{4.11}$$

where $\Delta\epsilon$ is the difference between the ideal V_{OC}/2 and the real V_{in}. The η_{track} versus output power is measured, by varying the series resistance of each source at a fixed input voltage. Figure 4.25 plots the results. Tracking efficiency decreases at both low and high output powers, where the resistance to be matched is high and low, respectively. At both ends, the oscillator's output frequency varies with V_{ctrl} non-linearly and gets compressed, resulting in a coarser resolution for the equivalent resistance of the combiner. Power conversion efficiency (PCE) is measured for different loads and input voltages. The PCE is also shown in Fig. 4.25, compared with what is expected from Eq. 4.8. The power consumption of all the internal circuits was included as a loss factor in our PCE calculations. Figure 4.26 shows the power consumption distribution among internal circuits at the point of maximum efficiency.

Table 4.1 includes a performance summary for the multisource EH power combiner, compared with other state-of-the-art works. Our proposed system is the only one that performs concurrent EH and automatic MPPT with a fully integrated implementation. The system in [124] is able to harvest from more ambient sources, but it was implemented in a costly BCD technology and makes use of a discrete inductor.

A multiple input EH circuit was used to power up the system shown in Fig. 4.27. The system is composed of magnetic and light sensors and a PIC16F1619 ULP microcontroller (μC). This set can be used for different building and industrial automation applications. The sensors and μC in sleep mode consume less than 3 μA. The system is fed with a pair of solar cells (models SLMD121H09L and PowerFilm) and a 1.2 V battery. For demonstration purposes, a BQ25570 boost converter takes the combiner's output to deliver a regulated V_{DD} = 5 V. This regulation stage

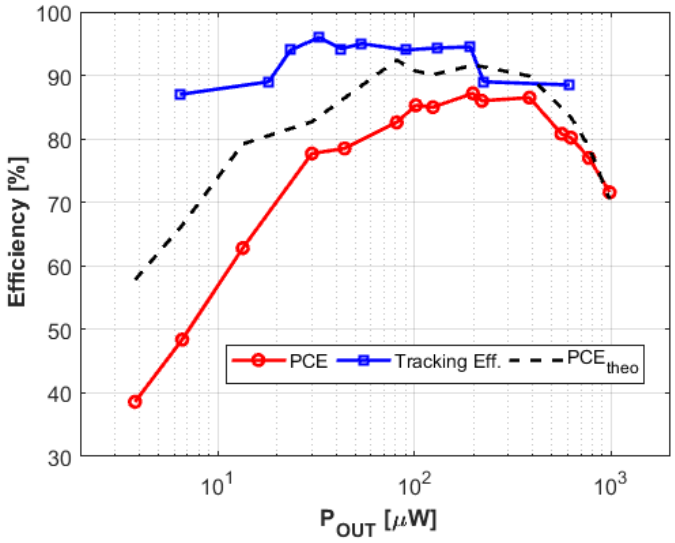

Figure 4.25: Measured tracking and power conversion efficiency (PCE) versus output power [128].

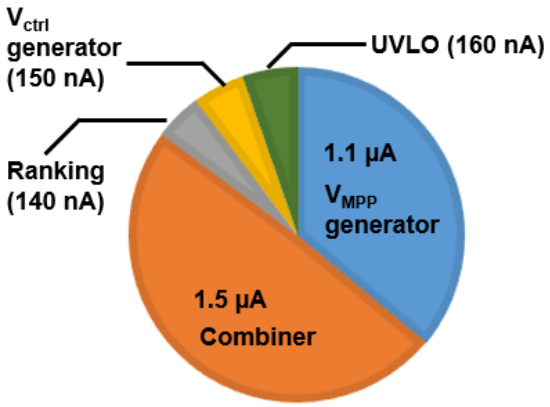

Figure 4.26: Distribution of total current consumption (3.05 μA) on internal circuits at 198 μW of output power and f = 1 MHz [128].

decrease the system's PCE by a factor of 0.85 to 0.9 depending on operating conditions [108]. The design of an integrated SC output regulator is considered as a future extension.

When the magnetic sensor of Figure 4.27 is activated, the μC awakes and compares the light sensor's output voltage with an internal reference. After storing the result, the μC returns to sleep mode. The process suddenly increases the load current by a few hundred of μA's. Figure 4.28 shows the output voltage from both the combiner (V_{ST}) and switched regulator (V_{DD}). Two

Table 4.1: Multisource Energy Harvesting Systems Comparison.

Ref.	Architecture	Inputs	Concurrent	MPPT	Input Range	Max. Output Power	Max. PCE	Tech.
[113]	Power ORing	2	No	Yes	0-10 V	621 μW	90 %	Discrete
[119]	Input multiplexing	3	No	No	1.46-3.3 V	300 μW	95 %	CMOS 130 nm
[124]	Inductive	9	No	Yes	0.1-1.0 V	2.12 mW	89.6%	BCD 0.32 μm
[125]	Inductive	3	No	Yes	>50 mV	100 μW	84 %	CMOS 180 nm
[132]	Capacitive+Ind.	2	Yes	No	N.A.	78 μW	74.5%	CMOS 250 nm
[127]	Capacitive	3	Yes	Manual	260-500 mV	354.4 μW	58.4 %	CMOS 130 nm
This Work	Capacitive	4	Yes	Yes	300-800 mV	981 μW	87.2%	CMOS 130 nm

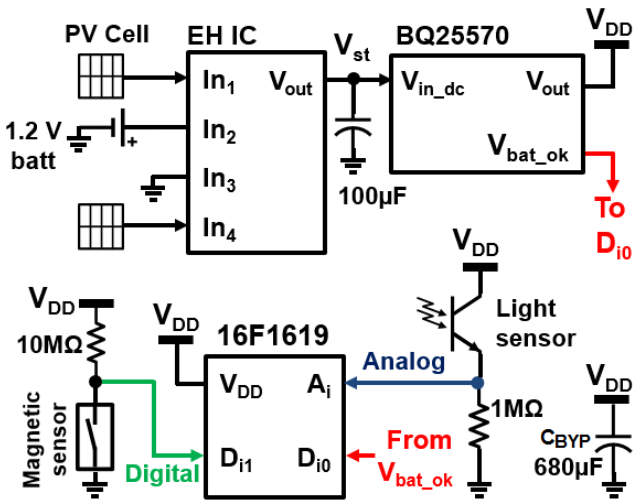

Figure 4.27: Energy harvesting system powering an μC and sensors [128].

cases are included: when the system is powered by the solar cells (indoor conditions illumination, V_{ST_PV}, V_{DD_PV}), and when it is powered by the battery (cells completely shaded, V_{ST_Batt}, V_{DD_Batt}). The system's operation is not affected by the drops in its supply voltage provided that it does not fall below the operating range of the μC and sensors, which is the case for the selected components. This test validates our combiner circuit in an application with typical features contained in an IoT system.

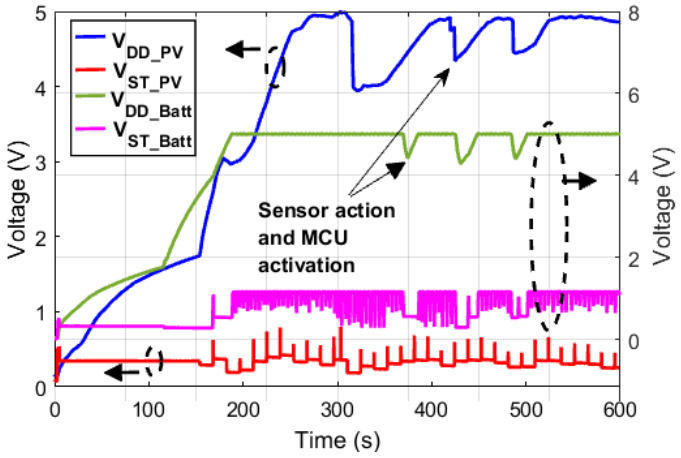

Figure 4.28: Transient measurements of combiner and regulator's output voltage. The V_{DD_PV} and V_{ST_PV} (V_{DD_Batt} and V_{ST_Batt}) correspond to the left (right) y-axis [128].

4.5 Conclusions

In this chapter, a multisource switched-capacitor based power combiner for IoT applications was presented. By automatically selecting the inputs with the highest available power, the system develops an optimal strategy for maximum harvested power. Moreover, the two-way storage architecture and proposed passive start-up circuit topology allows the use of the other inputs, when significant energy is still available from them. Also, the architecture of the converter and the proposed MPPT circuits permit a fully-integrated system with truly concurrent energy harvesting. None of the previous solutions integrate all these features. The performance in terms of power conversion efficiency and maximum output power compares favorably with other state-of-the-art single and multisource harvesting systems.

5. SMART SOIL PARAMETERS ESTIMATION SYSTEM USING AN AUTONOMOUS WIRELESS SENSOR NETWORK WITH DYNAMIC POWER MANAGEMENT STRATEGY *

5.1 Introduction

Precision agriculture (PA) is a term that makes reference to the application of information technology (IT) management systems to farming activities [142]. Historically, farmers have always recurred to traditional methods (like visual inspection) and their empirical experience to determine the state and conditions of their crops. However, with a precision agriculture system; farmers have access to valuable information that allows them to improve land utilization and efficiently use their limited resources. To begin with, they can avoid applying the same cultivation practices regardless of crop type and site conditions. They can also considerable reduce the wastage of pesticides, fertilizers and water used during cultivation periods. The resulting increase in quality and yield of crops with minimized environmental effects, make of the practice of PA an important contribution to achieve long-term sustainable farming [143].

5.1.1 Wireless Sensor Networks in Precision Agriculture

In the recent years, the field of precision agriculture has benefited from the evolution of wireless sensor networks (WSNs) and Internet-of-Things technologies [144]. Diverse WSN systems have been developed to solve problems related to farming. For example, in [145] a WSN was used to implement a cattle localization monitoring system, where Link Quality Indication (LQI) measurements where used to calculate the distance from fixed anchors to sensor nodes attached as ear-tags on cattle. In other works different WSN infrastructures are presented for automated irrigation systems, using conventional sensors buried in the ground [146–149] or digital images captured with a smart phone [150]. In [151], the operation of perpetual sensor motes to detect

*Reprinted with permission from "Smart Soil Parameters Estimation System Using an Autonomous Wireless Sensor Network With Dynamic Power Management Strategy" by J. J. Estrada-López, A. A. Castillo-Atoche, J. Vázquez-Castillo and E. Sánchez-Sinencio. IEEE Sensors Journal, vol. 18, no. 21, pp. 8913-8923, Nov. 2018. ©IEEE 2018

the presence of snails (an agricultural pest) is demonstrated, while in [152] a WSN is proposed for agrochemical dosage reduction. In [153, 154], sensor systems are implemented for the remote monitoring of honey bees' health in beehives. Finally, other works propose indoor and outdoor environmental monitoring systems, which could also have applications in gardens, greenhouses and on the field [76, 155–157]. A summary of these works is presented in Table 5.1. Overall, the main focus of these works has been the implementation of low-cost, energy efficient wireless systems to monitor real-time variables in different environments.

Although already significant progress has been achieved in PA applications, many open areas of opportunity for research still remain. For example, not all of the previous works demonstrate the possibility of perpetual operation of sensor nodes through energy harvesting (EH). There is also work needed in developing power management techniques that reduce the energy consumption in the sensor nodes, which in conjunction with EH is able to extend the network lifetime [149, 158].

The use of intelligent algorithms for data analysis and decision taking has also demonstrated potential application in PA. For example, the authors in [147, 150] use simple threshold detection to operate automated irrigation systems, while in [148] fuzzy logic is used to model the farmer's experience together with numerical soil and crop models. In [153] decision tree-based learning is used to describe the behavior of a beehive. In [159], machine learning with Bayesian methods are used to predict frost events in vineyards. Different studies [160–162] have also demonstrated the use of artificial neural networks (ANN) to estimate soil properties. However, as seen in Table 5.1, the use of ANN has not been extensively applied and in many of the works where they are proposed, no specific WSN implementations appeared. Therefore, the challenge still remains of developing cost-effective solutions for data monitoring and analysis with self-learning models that can infer relevant information from a limited set of measurements.

Table 5.1: Summary of WSN systems for precision agriculture.

Ref.	Year	Connectivity	Energy Harvesting	Battery Life	Sensors	Intelligence	Application
[149]	2018	ZigBee	No	65 days (2000 mAh)	Moisture	No	Precision irrigation
[157]	2018	-	Solar	4 days	Temperature, moisture	No	School garden
[76]	2018	BLE	No	1095 days (1000 mAh)	Temperature, humidity	No	Environment monitoring
[159]	2018	-	-	-	-	Bayesian methods	Frost prediction
[151]	2017	ZigBee	Solar	83 days (2000 mAh)	Capacitive	No	Pest detection
[149]	2017	IEEE 802.15.4	No	-	Temperature, humidity, moisture	Fuzzy logic	Precision irrigation
[156]	2017	ZigBee	No	2104 days (3400 mAh)	Temperature, humidity, acccelerometer	No	Disaster prevention
[154]	2017	ZigBee	No	75 hrs. (2300 mAh)	Temperature, humidity	No	Precision apiculture
[153]	2016	ZigBee	Solar	15 days (6600 mAh)	Temperature, humidity	Decision tree learning	Precision apiculture
[150]	2015	Wi-Fi	No	-	Smartphone camera	Threshold detection	Automated irrigation
[161]	2015	-	-	-	-	ANN	Soil P estimation
[147]	2014	ZigBee	Solar	-	Temperature, moisture, CO_2, O_2, NO_2	Threshold detection	Automated irrigation
[155]	2014	ZigBee	No	50 hrs. (350 mAh)	Temperature, humidity, O_2, CO_2, SO_2, NO_2	No	Environment monitoring

In this chapter, the design of a WSN-based system for precision agriculture is presented. The concept is illustrated in Figure 5.1. The system is composed of several low-cost, low-power consumption nodes, equipped with sensors, a microprocessor, a power management system and wireless communication devices. These sensor nodes should have a very long operative life without requiring any form of attendance. Temperature, humidity and conductivity of the soil are considered among the most basic and important variables to measure [144]. Typical WSN systems for agriculture have been designed to monitor such parameters, but only at one level below the ground's surface [147, 163, 164]. However, depending on the type of crop this approach can result in measurements with limited precision; because the soil conditions must be preferably monitored according to the root length of the plant [148, 165]. With that consideration, a new modular sensor node architecture is proposed to perform measurements at two different levels below ground, to accommodate various types of vegetables using the same hardware.

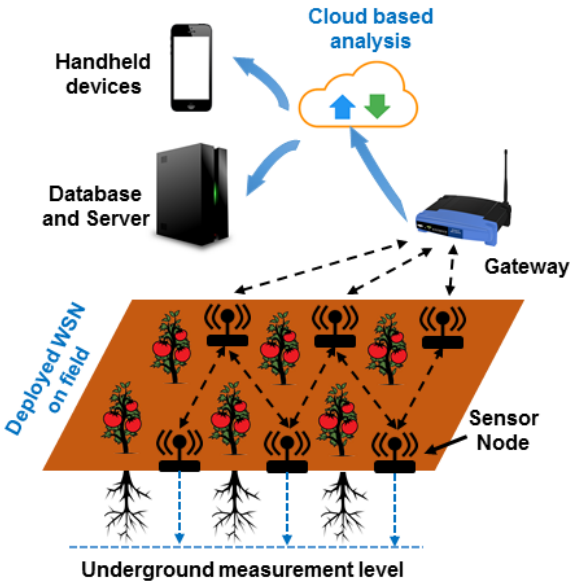

Figure 5.1: Conceptual WSN system for precision agriculture applications [142].

As shown in Figure 5.1, the sensor nodes communicate to the Internet through a gateway, using Machine-to-Machine (M2M) applications. Once the data is on the cloud, it can be further

analyzed to provide the user with meaningful information. Raw data is many time useless or requires significant effort to draw conclusions from it. Rather, farmers need information that helps them to take decisions and chose between different courses of action. In the proposed system, an artificial neural network is used to estimate the content of Phosphorus (P) in the ground. This nutrient plays a key role in soil fertility, but conventional methods used to monitor its value require extensive sampling of the soil and laboratory tests. All cloud services and data can then be easily accessed from any mobile device through a friendly user interface on the Internet.

Power consumption and battery life are to be considered in the design of any WSN system. This issue has been addressed through various steps. First, circuit design ensures that the elements of the sensor node demand the minimal current possible. Solar energy harvesting has also been adopted. The photovoltaic cell has been selected in order to achieve complete energy autonomy of the system, under specific weather conditions. Finally, to reduce the network's energy utilization, a dynamic power management (DPM) strategy is proposed to establish an adaptive balance between the accuracy of soil parameters measurements, and the required power of the wireless system. The DPM methodology considers the gradual change of the ground's microbial activity and organic content during the day and can be adapted to the soil features of different locations.

5.2 WSN System Architecture Design

In this section, the system architecture of the implemented wireless sensor network for precision agriculture is described.

5.2.1 Sensor Node Design

There are specific challenges involved when installing and working with wireless sensor systems in outdoor scenarios. Their design have to resist different weather conditions, and preferably be adaptable to diverse purposes (i.e. different crops). The proposed sensor node physical structure (illustrated in Fig. 5.2) has been designed taking into account such considerations. First, the whole system is enclosed in a waterproof Nylamid-Polymer housing coated with epoxy resin. Second, it has a modular construction that is composed of three sections. The top and bottom sections con-

tain sensors and signal conditioning circuits, while the middle section contains the ultra-low power microcontroller unit (MCU) with power management and wireless communication subsystems.

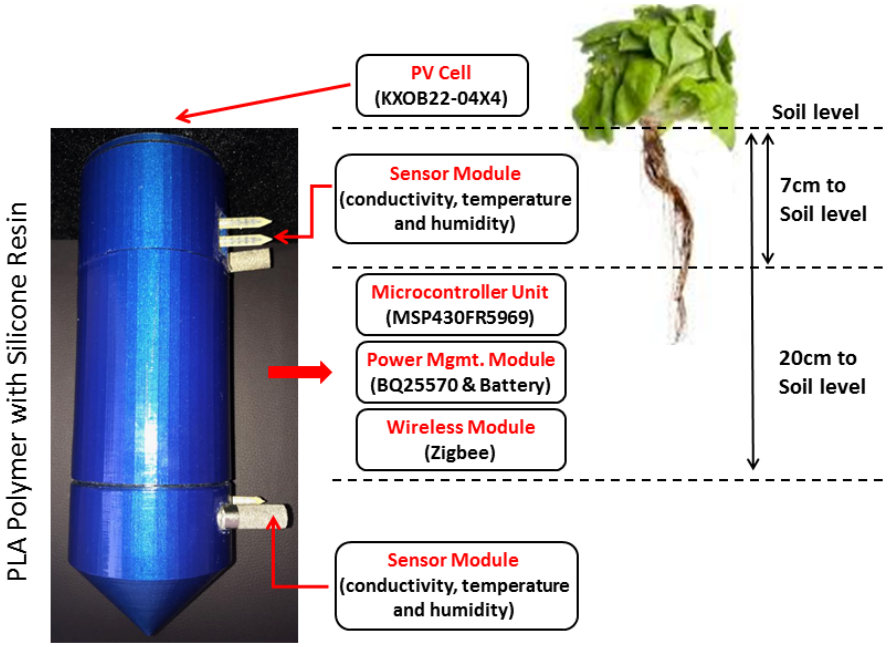

Figure 5.2: Sensor node physical structure [142].

As a proof of concept, the modular sensor node has been designed to perform measurements at 7 cm and 20 cm below ground. These levels accommodate different types of vegetables grown in the region. However, the structure can easily be adapted to other measurement levels, by changing only the height of the middle section. Figure 5.3 illustrates a simplified block diagram of the sensor node's electronic system. As the longest battery life is attained with small discharge currents, all the components have been selected to get the minimum consumption possible. The details of each subsystem is given next.

5.2.1.1 Sensors Module

The soil's temperature and humidity are acquired through the SHT10 sensor integrated circuit (IC) [166]. The SHT10 delivers a 12-bit digital output with a typical resolution of 0.05 % RH and 0.01 °C for humidity and temperature, respectively. It can be powered from a supply voltage

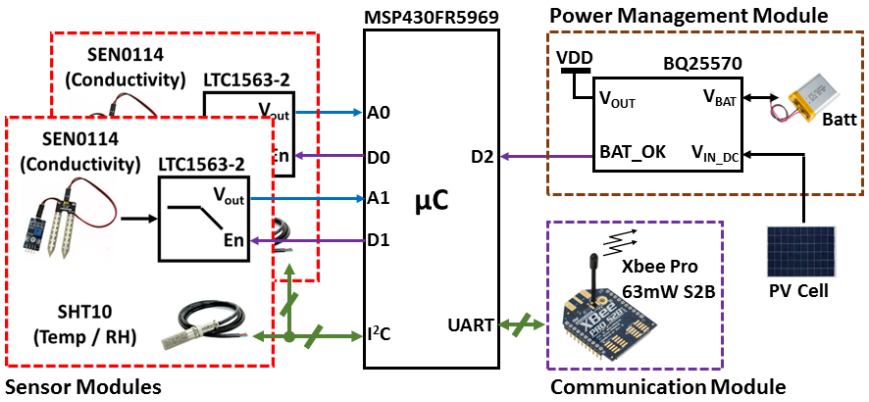

Figure 5.3: Sensor node circuit architecture [142].

range of 2.4 V to 5.5 V, consuming $0.9\ mA$ (typical) during operation and a maximum of 1.5 μA on sleep mode. To calibrate the temperature measurements, a Ti10 Fluke infrared camera was used to acquire the temperature at the two root levels of the plant. The obtained values were used as a comparison reference to the sensor's data. Figure 5.4 shows a view of the temperature measurement with the device placed in a laboratory crop pot.

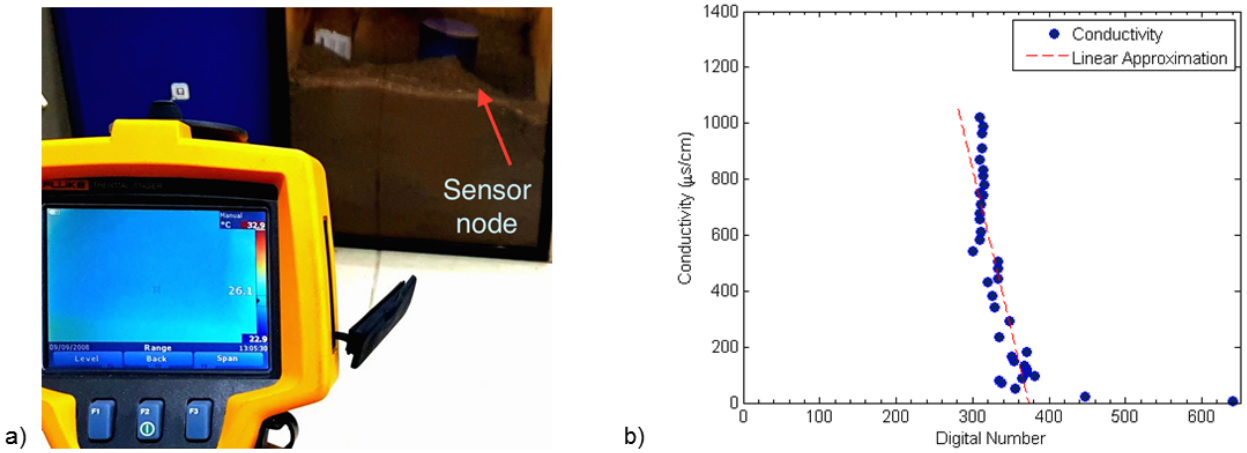

Figure 5.4: Sensor node calibration: a) Temperature measurements based on thermal camera, b) Soil conductivity [142].

The following equation is used to convert the digital readout data SO_T coming from the SHT10 to a calibrated temperature value:

$$T_{\circ\mathrm{C}} = d_1 + d_2 \cdot SO_T + d_{Ti10} \tag{5.1}$$

In Equation 5.1, $d_1 = -39.7$ °C, $d_2 = 0.04$ and $d_{Ti10} = 0.001$ °C, which represents the calibration offset of the infrared camera.

The nonlinearity of the humidity sensor can be compensated by converting the measured data as follows:

$$\%RH = c_1 + c_2 \cdot SO_{RH} + c_3 \cdot SO_{RH}^2 \tag{5.2}$$

where $c_1 = -2.0468$, $c_2 = 0.0367$, $c_3 = -1.5955 \times 10^{-6}$, and SO_{RH} is the humidity readout value. The humidity measurements also require temperature compensation by applying the following correction equation:

$$\%RH_C = (T_{\circ\mathrm{C}} - 25) \cdot (t_1 + t_2 \cdot SO_{RH}) + \%RH \tag{5.3}$$

where coefficients t_1 and t_2 have the corresponding values of 0.01 and 0.00008 and $\%RH_C$ is the temperature compensated relative humidity.

A low-cost conductivity sensor SEN0114 [167] is also incorporated into each sensor module. It consumes a current of 3.5 mA (typical) during operation. As the SEN0114 does not count with a sleep mode, an ADG819 single-pole, double-throw (SPDT) CMOS switch [168] is used to disconnected it from the supply and turn it off. The ADG819 has a maximum on-resistance of 0.7 Ω, maximum leakage current of 3 nA and current carrying capability of 200 mA. The conductivity signal is filtered at a 256 Hz cutoff frequency with the LTC1563-2 [169], an active 4th-order low-pass filter with Butterworth response. This IC incorporates a shutdown mode that reduces its current consumption down to 1 μA. Figure 5.5 shows the schematic circuit of the sensors module.

Soil conductivity plays a key role for crop quality estimation. However, uncertainties in the

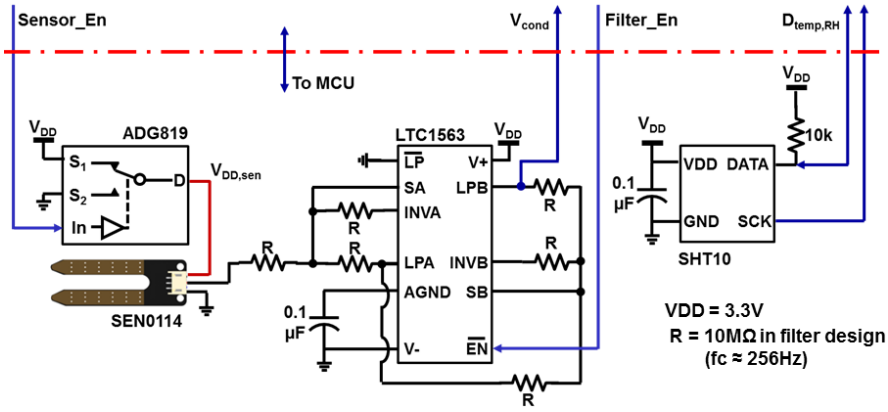

Figure 5.5: Circuit implementation of the sensors module.

measurements due to the variability of minerals and dry plant tissue make it necessary to calibrate this sensor for specific soil types in particular regions. A nonlinear approximation is implemented to estimate the data as a straight line. Figure 5.4(b) illustrates the calibration results. In this case, the conductivity was computed via a polynomial approximation with the following equation: $\sigma = -11.458x + 4275\,\mu$S/cm, where x is the digital number acquired by the analog-to-digital converter available in the microcontroller.

To ensure the accuracy of the data during system operation, the sensor nodes should be calibrated at the end of every crop cycle, with soil laboratory analysis employed as a reference. Other maintenance strategies can also be applied. For example, soil calibration samples can be taken once a month to ensure the quality of the sensor measurements and to verify their correct functioning [170]. Self-calibration strategies as the one reported in [171] can be considered as a future extension of this work.

5.2.1.2 Wireless Communication Module

Several technology options are available for the implementation of a wireless communication module in PA applications [31]. They can be broadly classified into Local Area Network and Low Power Wide Area (LPWA) technologies. The first category includes very well known and widely utilized technologies as ZigBee, Bluetooth Low-Energy (BLE) and Wi-Fi. LPWA technologies have been introduced in the recent years and would include options such as Narrowband

IoT (NB-IoT) and Long Range (LoRa). The main characteristics of these wireless communication technologies are shown in Table 5.1.

For PA applications, the technology that exhibits the best trade-off between power consumption and communication range should be selected. In terms of area coverage, LPWA technologies are good candidates. NB-IoT operates on the existing global system for mobile (GSM) and long-term evolution (LTE) networks, using licensed frequency bands. That means that it can share the LTE spectrum and even utilize the same type of equipment. LoRa operates in outlying regions without cellular network coverage, establishing private networks with specific quality and security requirements [172]. However, as shown in Figure 5.6, in terms of power consumption ZigBee and BLE have better performance than other technologies. In the case of ZigBee, it also shows an acceptable communication distance that makes it suitable for small-scale, low power consumption scenarios [144, 172], which is appropriate for PA applications. Therefore, for the purposes of our study the selected communication protocol for the energy harvesting powered sensor node is the IEEE 802.15.4 ZigBee.

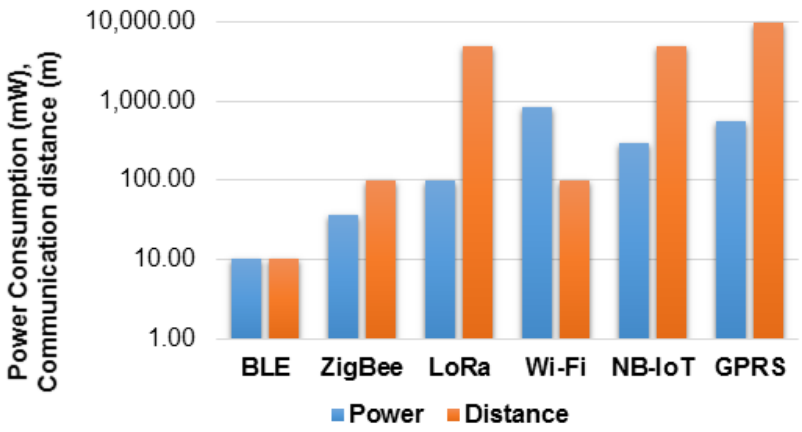

Figure 5.6: Comparison of power consumption and transmission range of various wireless technologies used in IoT PA applications (adapted from [144]).

The radio modem XBee PRO S2C [173] by Digi International is a low-cost, low-power data transceiver unit for wireless sensor networks. This module allows the creation of mesh networks

Table 5.2: Main characteristics of Wireless Communication Technologies (adapted from [144]).

Tech.	**Standard**	**Frequency Band**	**Modulation**	**Channel Bandwidth**	**Power Consump.**	**Data Rate**	**Range**	**Network Size**	**Cost**
ZigBee	IEEE 802.15.4	915 MHz / 2.4 GHz	BPSK / OQPSK	2 MHz	Low	250 kbps	100 m	65,000	Low
BLE	IEEE 802.15.1	2.4 GHz	GMSK	1 MHz	Ultra-low	1 Mbps	10 m	N.A	Low
Wi-Fi	IEEE 802.11a,b,g,n	2.4 GHz	BPSK / OQPSK	22 MHz	High	150 Mbps	100 m	32	High
GPRS	GSM++	900-1800 MHz	GMSK	200 kHz	Medium	170 kbps	1-10 km	1000	Medium
LoRa	IEEE 802.15.4g	869 / 915 MHz	GFSK	500 kHz	Low	50 kbps	5 km	10,000	Low
NB-IoT	LTE-M	700-900 MHz	QPSK	200 kHz	Low	200 kbps	1-10 km	10,000	Medium

based on the ZigBee mesh firmware, and operates with a power-down current that is less than 3.0 μA. The transmission power of the XBee PRO is $+18$ dBm, which according to the manufacturer's data, can reach distances of up to 1 mile (i.e., line-of-sight range) at a 250 $kbps$ maximum data rate.

5.2.1.3 Power Management Module

As shown in Figure 5.7, the power management and energy harvesting subsystem is composed of the BQ25570 boost charger and buck converter integrated circuit from TI [108], a KXOB22-04X3 monocrystalline photovoltaic (PV) module [174], and a 2000 mAh Li-Ion battery with nominal voltage of 3.7 V. The BQ25570 IC has a typical current consumption less than 500 nA and features an integrated boost battery charger capable of extracting power down to the μW-level from DC energy sources. The PV panel has been characterized with an open circuit voltage of 1.89 V and a short circuit current of 15 mA; furthermore, its voltage (current) at the maximum power point (MPP) is 1.5 V (13.38 mA) at standard irradiance conditions ($\approx$ 1000 W/m^2). The power management subsystem has been designed to deliver a regulated voltage of V_{DD} = 3.3 V to all the other modules of the sensor node, while keeping the maximum charging voltage to 4.2 V, and the minimum battery above 3.0 V.

5.2.1.4 Microcontroller Unit

The MSP430FR5969 is an ultra-low-power microcontroller platform with an internal architecture that offers an increased performance at lower energy budgets [175]. The MCU supports a wide supply voltage range (1.8 V to 3.6 V) and its 16-bit Reduced Instruction Set Computer (RISC) architecture includes seven low-power modes (LPM) that have been optimized to achieve extended battery life in energy-limited applications. The *active*, *standby* (LPM3), and *sleep* (LPM3.5) modes used in this application consume approximately 100 μA/MHz, 0.4 μA and 0.25 μA, respectively. All the electronics components of the sensor node are shown in Fig. 5.8.

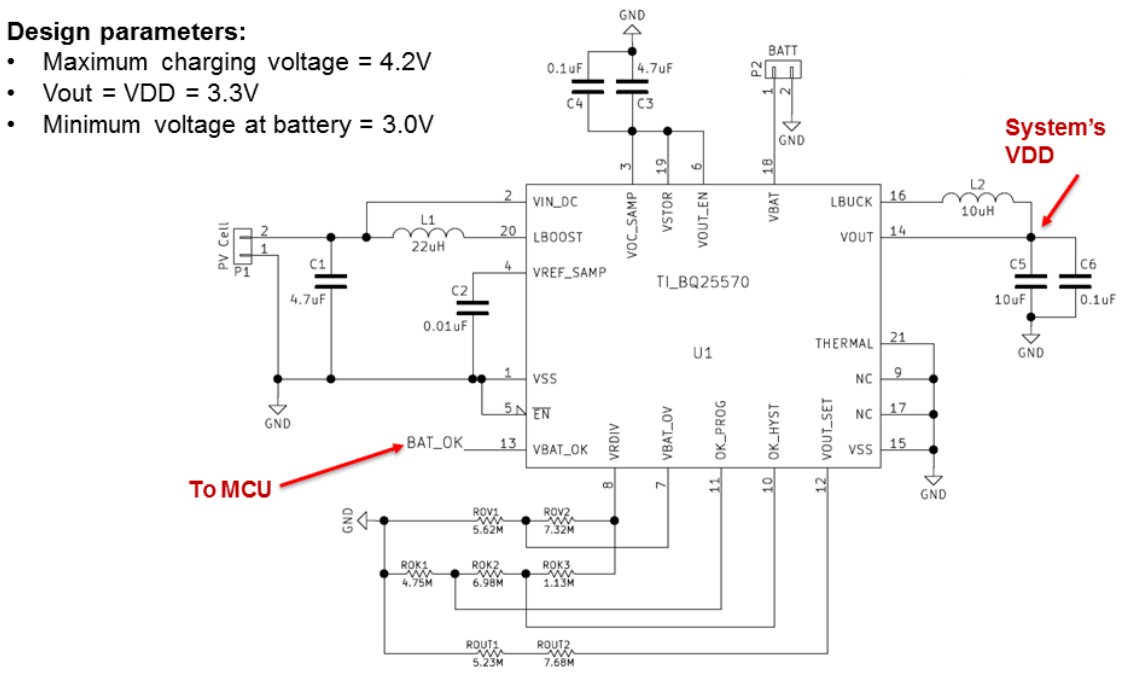

Figure 5.7: Power management module circuit.

5.2.2 Architecture of the WSN

Figure 5.9 represents the proposed platform's architecture model. As illustrated, the network is composed of three main elements: i) the designed sensor nodes integrated as "things" under an IoT paradigm, ii) a local gateway connected to the Internet to share the measured data with the cloud, and iii) a network infrastructure with IoT solutions that runs applications to analyze and manage data coming from the sensor nodes.

In local communication between nodes, the XBee radio modem (over IEEE 802.15.4) is used. The XBee-PRO S2 devices are configured in a ZigBee before they can transmit or receive data. Both Message Queue Telemetry Transport (MQTT) and Representational State Transfer (REST) protocols are used to transfer data in the form of messages from the sensor nodes to a gateway or server (BROKER). MQTT provides low-latency, small-packet sizes and a stable communication for resource constrained devices. Its bandwidth requirements are extremely low, and makes it very energy efficient [163]. REST is an architectural style that offers desirable properties such

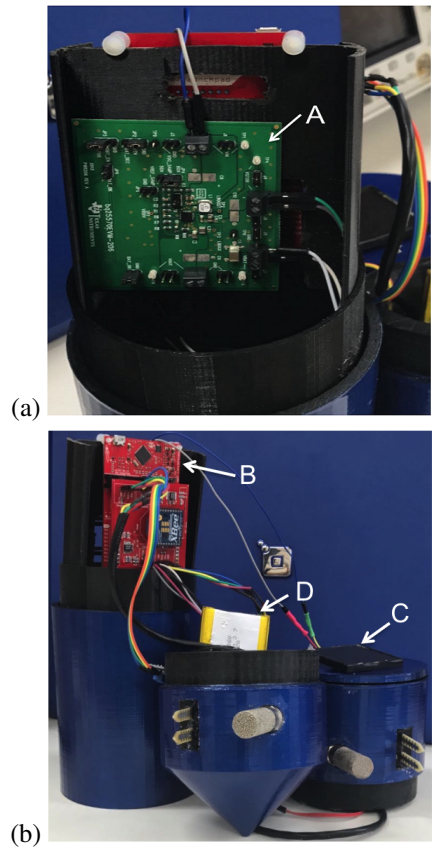

Figure 5.8: Sensor node prototype: (a) BQ25570 PMIC (A), (b) Ultra-low power MCU (B), Solar photovoltaic panel (C) and Li-Ion battery (D) [142].

as scalability and modifiability, enabling services to work on the Web. With the above described approach, the IoT-based network provides cloud services of data storage and analysis.

When powered on or being reset, the sensor node requests sensor-type information from devices connected to it. All sensors are assigned a unique *SensorID* to distinguish them from other types of devices, and each node is programmed with an unsigned 8-bit integer *NodeID* by the gateway. During normal operation of soil estimation, the node requests sensor data from the attached devices every 20 minutes. The sensor data packet consists of a header and data blocks. The header block contains packet length information indicating the type of data and destination as well as the DeviceIDs for each sensor attached to the node. After receiving data from the sensor, the node transmits a packet to the gateway. The Publish/Subscribe model used in MQTT is mapped to resource observers. PUT and GET operations on HTTP/REST are integrated on the MQTT broker.

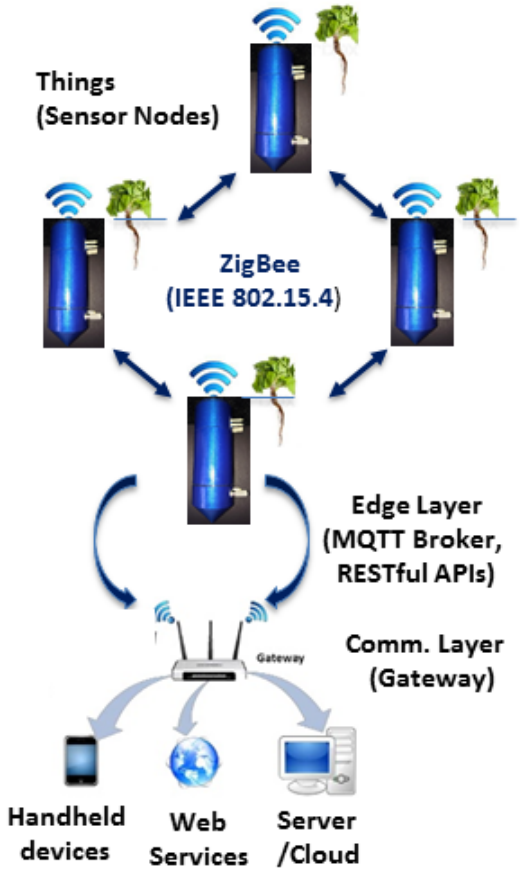

Figure 5.9: IoT & WSN system model [142].

5.3 Dynamic Power Management Strategy of the WSN

Power management is a very important issue in the design of efficient wireless sensor networks with prolonged operating life, and different energy-efficient techniques can be used in precision agriculture applications [144]. In this work, a dynamic power management (DPM) methodology has been implemented to minimize the overall energy consumed by the sensor nodes and increase the network lifetime. The result of the DPM strategy is a established trade-off between the energy efficiency and the accuracy of the WSN. The strategy is implemented both at circuit level in the sensor node, and at the system level in the operation of the network.

5.3.1 DPM at Circuit Level

The implemented strategy at the level of the sensor node consists in selectively turning on the system's components in a specific sequence, and to put all circuitry into *Sleep State* whenever possible [176]. This methodology allows saving battery power consumption and extends the life span of the node. The active operating states of the sensor node are called *Active Sensing* and *Active XBee* modes where data is respectively acquired and transmitted. There is also a *Standby* mode occurring between active states.

The circuit level DPM of the sensor node is described in Fig. 5.10, where each state is marked down with its most relevant current consumption and period duration. Transition times between states are also indicated in the model. All the values for currents and transition times have been taken from device datasheets. From Figure 5.10 it can be observed that the current consumption required by the communications module during the *Active XBee* transmission mode is dominant over any other component in the system. That is why the adopted strategy switches to a *Sleep State* mode from an *Active XBee* transmission mode. By doing so, there is a considerable reduction of the instantaneous current that is drawn from the battery, allowing the system to take advantage of the battery recovery effect as discussed in [176].

5.3.2 DPM at System Level

In a typical precision agriculture system, it is common that all the sensor nodes of the network are active at the same time throughout the day. However, various studies have demonstrated that the rates of different agriculture and soil phenomena can be significantly lower at nighttime than during daytime [165, 177–179]. For example, it has been shown that the daytime rates of both heterotrophic respiration (CO_2 efflux) and soil microbial activity (which in the form of phosphate-solubilizing bacteria improves P transfer from soil to plants) were consistently higher than their corresponding nocturnal values, with maximal rates occurring in the late afternoon [180–182]. Considering this gradual change of the soil microbial activity and organic content during the day, the proposed system-level DPM employs a spatial-temporal strategy for data acquisition. That is,

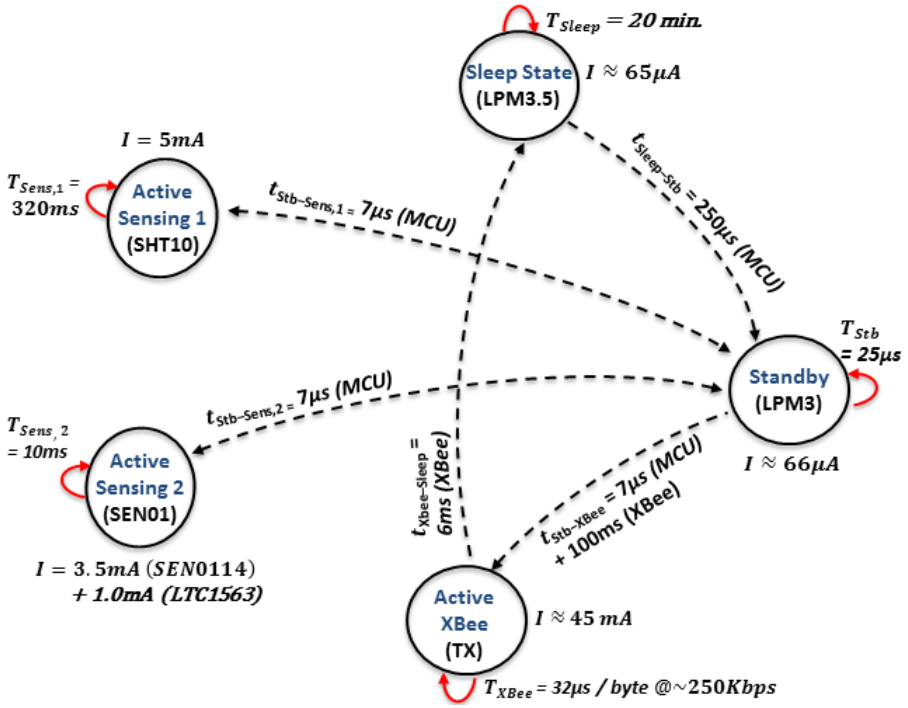

Figure 5.10: Dynamic power management model of the sensor node at circuit level [142].

we activate each node at a certain location during a specific time. Therefore, a dynamic trade-off between precision of the phosphorous estimation and the system's energy consumption is established. Also, package collisions are avoided due to less frequent transmissions, leading to a more efficient communication of the network.

Assume that the field of interest is a 2D rectangular region represented by a grid of $L \times W$ points, with a deterministic deployment of the sensor nodes that compose the network. A distance separating each pair of adjacent points equals one measurement unit (i.e., 1 meter). The proof-of-concept network considers a number (e.g. $N = 4$) of nodes deployed into the target region. Each device is placed within a rhombus pattern at (L_i, W_i) for $i = 1, ..., L; j = 1, ..., W$, as illustrated in Fig. 5.11, with labels P1 to P4.

Figure 5.12 shows the proposed adaptive DPM scheduling of the WSN system, which consist of four operational stages that correspond to the varying soil activity rates during a 24-hour period. The activation of a sensor on a specific time is represented by a colored box. The first stage (red

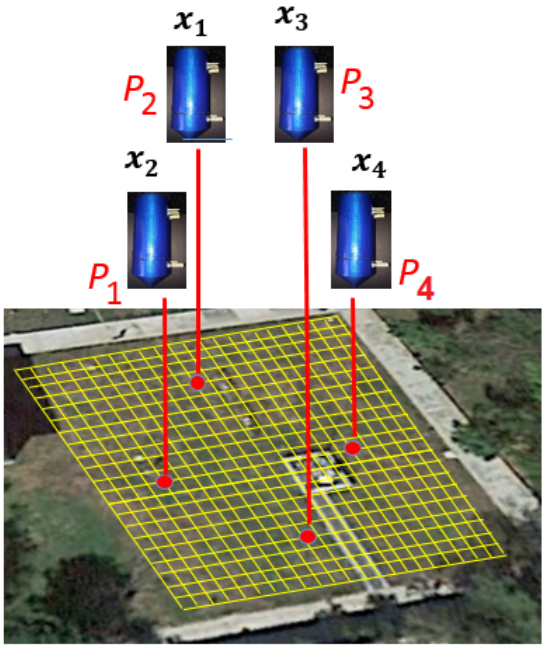

Figure 5.11: Sensor node deployment in test field [142].

color) considers the sequential activation of only one sensor node every 20 minutes during night hours (data acquisition rate for each node is every 80 minutes). In terms of the energy and quality tradeoff, the phosphorus estimation accuracy is barely affected at night, but the power consumption is reduced by 3.9% during that period.

Fused WSN and DPM: Daytime Schedule Strategy

Sensor Nodes	8:00 pm	8:20 pm	8:40 pm	9:00 pm	9:20 pm	...	6:00 am	6:20 am	6:40 am	...	8:00 am	8:20 am	8:40 am	9:00 am	9:20 am	...	12:00 pm	12:20 pm	...	3:20 pm	3:40 pm	4:00 pm	4:20 pm	4:40 pm	...	6:00 pm	6:20 pm	6:40 pm	...	8:00 pm	8:20 pm	8:40 pm	9:00 pm	9:20 pm	...
Sensor 1, Location P1*																																		
Sensor 2, Location P2						...				...						...			...					...				...						...
Sensor 3, Location P3																																		
Sensor 4, Location P4																																		
DPM Stages	1						2				3						4			3						2				1					

*Locations P1 to P4 ubicated in Faculty of Engineering, Autonomous University of Yucatan

Figure 5.12: DPM strategy at the system level. Each sensor node is activated in a specific sequence depending on the hour of the day [142].

In its second stage (black), the DPM strategy considers the gradual increase of soil activity rates

during day/night transitions. During these periods of time, the soil gets warmer and microbial activity is increased. Warmer temperatures and good levels of water content in the soil tend to hasten the microbial activity affecting its fertility [183, 184]. Parallel data measurements of two non-adjacent sensor nodes are then applied every 20 minutes (data acquisition rate of each node is every 40 minutes), which represents a good tradeoff between measurement accuracy and energy consumption, which at this stage is reduced by 2.5%.

The third (blue) and fourth (green) stages represent an increment in the accuracy of the measurements, by increasing the sampling rate of the system using three and four parallel sensor node measurements, respectively. We consider the third DPM stage as morning to early afternoon periods, when three adjacent sensors are turned on at a time (data acquisition rate of each node is sequentially adapted for one period of 40 minutes and three periods of 20 minutes as shown in Fig. 5.12). Finally, in the fourth stage, all sensor nodes are measuring at the same time every 20 minutes.

5.4 Soil Quality Estimation Algorithm

Phosphorus is a vital component of the plant's nucleic acids [185]. Consequently, it is considered to be a good predictor of the metabolic rates in plants and required for their growth and development processes [186]. However, the sorption/desorption of P in the soil depends on several factors, and its measurement is traditionally implemented with laboratory methods that need extensive and time-consuming labor. In [161], the use of an ANN to estimate soil phosphorus was explored, using diverse terrain and vegetation attributes extracted using the digital elevation model (DEM) and the NDVI indicator. However, the use of satellite images is not adequate to perform real-time monitoring. Therefore, in this work we propose to estimate the levels of P from basic soil parameters.

Recent research results indicate that plant's phosphorus content is linked to their respiration rates through a scaling relationship [185]. Other works also show that temporal variations of soil respiration can be explained by the interactions of its moisture and temperature [165]. Then, theoretically the level of P varies in the soil when changes occur in these variables. Therefore, in

this study an indirect measurement of P is proposed using the low-cost sensors integrated in the autonomous sensor node.

An artificial neural network (ANN) is a computational structure that can model the soil's content from different input measurements. The ANN is able to find significant correlations between soil parameters such as phosphorus, temperature, electrical conductivity and humidity. In the proposed system, a single feed-forward ANN model with one hidden layer is used. The ANN uses an adaptive procedure that recursively updates its network parameters. The learning process classifies the experimentally measured values of temperature, humidity and electrical conductivity to the hidden layer, and an optimization process maps the classified inputs to the phosphorus estimation output.

Each neuron output of the ANN can be mathematically represented as follows:

$$a = f\left[\sum_{i=1}^{n} x_i w_i + b\right] \tag{5.4}$$

where x_i represents the inputs, w_i is the weights, b is a bias and $f[\cdot]$ represents the activation function. The layers are interconnected and the weights are optimally computed using a cost function. The input to the hidden node is transformed by a nonlinear activation function, which is required to be monotonically increasing, bounded, continuous and differentiable. The activation function used in the network is the *logsigmoid* function as described in Equation 5.5.

$$f(x) = \frac{1}{1 + e^{-x}} \tag{5.5}$$

Figure 5.13 presents the developed ANN structure for P-estimation. As shown, the hidden layer classifies the features and nonlinearity behavior of the soil input data. A back propagation (BP) algorithm is employed to train the network by implementing the gradient descent (GD) method. In general, the sum-squared error is minimized in the optimization process or ANN training. In this learning process of the ANN model, 80% of the available data was selected to train the model,

whereas the remaining 20% was used to test the developed network. MATLAB® was used for designing and testing the ANN estimation model. A total of 32 soil samples were taken from off-grid at each position of the sensor nodes that where located on the field (7 cm and 20 cm depths). The Phosphorous content on those samples were extracted by laboratory analysis and compared with the values given by the ANN estimation. Table 5.3 presents a comparison between the laboratory analysis results and the ANN output estimation during a week. Laboratory test samples were acquired every second day at the same time (11 Hrs.) for fair comparative conditions. The experimental results indicate the high correlation between P-ANN estimated level and the laboratory samples.

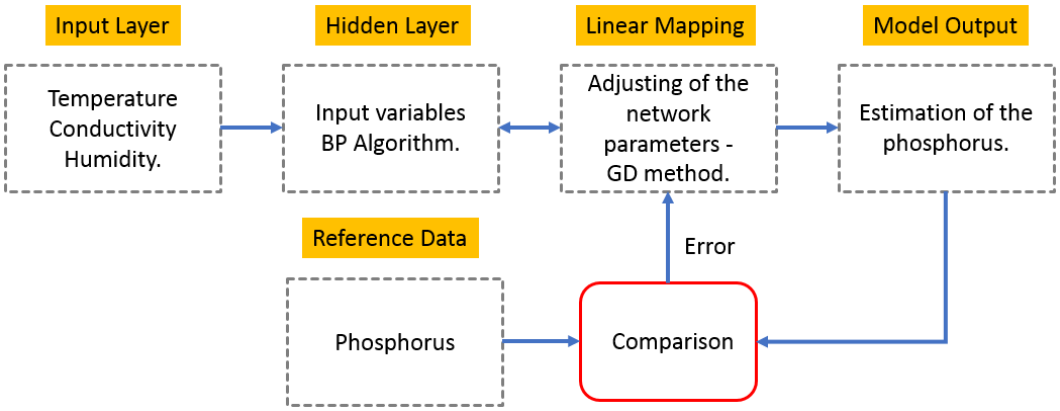

Figure 5.13: ANN feed-forward structure [142].

5.5 Experimental Results

The measured performance of the autonomous sensor node and the WSN system, in terms of its energy consumption and estimation accuracy is discussed next. A sample of the extracted spatial distribution maps that can be accessed through the Web interface is also shown.

5.5.1 Sensor Node Power Consumption

Power consumption is evaluated at the circuit level with the sensor node prototype, and at the system level with the WSN in view. A testbed was designed to test the node's power consumption

Table 5.3: Laboratory P Analysis and ANN Estimation Comparison [142].

Sensor Node	Phosphorous Content (mg/g) *							
	Day 1		Day 2		Day 3		Day 4	
	Lab.	Est.	Lab.	Est.	Lab.	Est.	Lab.	Est.
$P1_{7cm}$	4.855	4.871	4.521	4.794	4.915	4.758	4.418	4.016
$P1_{20cm}$	7.172	7.205	6.642	6.638	7.440	7.312	6.382	6.218
$P2_{7cm}$	4.630	4.625	4.462	4.468	4.918	4.891	4.016	4.115
$P2_{20cm}$	8.339	8.382	6.405	6.662	6.971	6.737	5.734	4.771
$P3_{7cm}$	1.103	1.204	1.043	0.933	1.154	0.943	1.011	0.937
$P3_{20cm}$	4.256	4.311	3.226	3.299	3.562	3.832	3.081	3.130
$P4_{7cm}$	9.861	9.799	9.279	9.378	10.32	10.25	9.067	9.172
$P4_{20cm}$	11.32	11.24	10.67	10.79	11.44	11.59	10.10	9.66

when actively measuring and transmitting data to the gateway. The ZigBee communication protocol was employed for communication between devices. Following the established DPM model at circuit level, a node state sequence is defined as shown in the timing diagram of Figure 5.14, where the duration of the T_{Sleep} varies according to the strategy described in the last section. The sequence that forms $T_{Sensing}$ corresponds to the DPM model of Fig. 5.10.

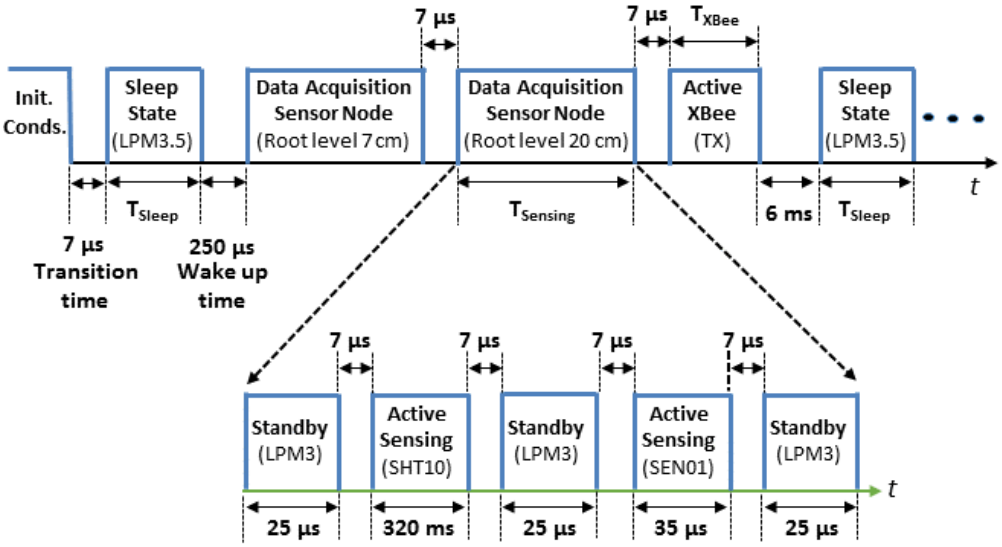

Figure 5.14: Timing diagram for sensor node data acquisition operation [142].

Figure 5.15 shows the real-time dynamic behavior of the node's power consumption, and Table 5.4 summarizes the measured values for all of the configuration states. The system's sleep mode has a current consumption of I_{Sleep} = 79.03 μA. Once the system wakes up, a sensing state is visualized that corresponds to the sensor modules activation for a period of $T_{Sensing}$= 320.14 ms, with a current consumption of $I_{Sensing}$ = 7.15 mA. Finally, the XBee transmission state requires I_{XBee} = 49.09 mA to send the data to the WSN in T_{XBee} = 6.1 ms.

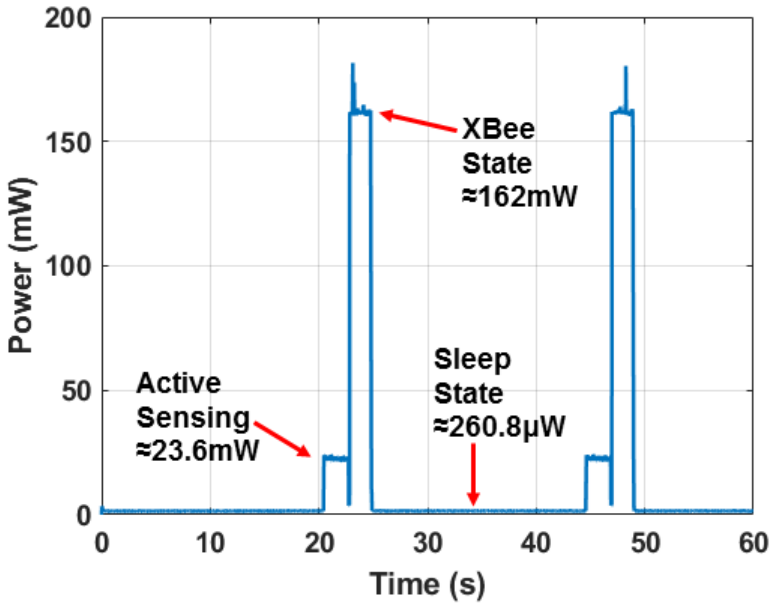

Figure 5.15: Measured transient power consumption of the sensor node prototype [142].

Table 5.4: Power Consumption Analysis [142].

Sensor node modules	Power Consumption
Sleep State MCU + Sleep Peripherals	260.8μW @ 79.03μA
Standby State MCU + Sleep Peripherals	343.3μW @ 104.3μA
Active Sensing (SHT10 + SEN0114)	23.6mW @ 7.15mA
Active XBEE	162mW @ 49.09mA

Knowing the node's current consumption for each state, it is possible to estimate the daily discharge (in mAh) that is taken from the battery [151]:

$$Q = 24 \cdot I_{Sleep} + [2 \cdot T_{Sensing} \cdot I_{Sensing} + T_{XBee} \cdot I_{XBee}] \cdot \frac{N}{360} \tag{5.6}$$

where N is the number of sensing and transmitting sequences during the day. If T_{Sleep} where a fixed period of 20 minutes (N = 72), that would signify a daily discharge from the battery of Q = 1.99 mAh. Considering a nominal capacity of 2000 mAh and 90% efficiency in the DC-DC converter of the power management IC [108], the estimated duration of the battery (without energy harvesting) would be of approximately 914 days. However, due to the implemented DPM at the WSN level, T_{Sleep} is variable during the day, reducing N for each node 39 times. This in turn extends the battery life for another 34 days.

Now, if we take a nominal battery voltage of $V_{BATT} = 3.7$ V, that means that the whole sensor node requires a total of 50.2 mWh per week to operate without interruption. Contemplating an average of five days of effective solar battery charging per week, with only three hours of irradiance at standard conditions (STC), this means that the instantaneous output power required from the PV panel during charging hours is 3.35 mW. The selected monocrystalline PV module for the sensor node has a value of $P_{MPPT} = 20.7$ mW [174] at a typical STC (i.e., $1000 W/m^2$ and a cell temperature of 25°C), which is ≈ 6 times the required power of the node. It can be concluded that the conditions for complete energy autonomy are met, meaning that perpetual operation is guaranteed without the need to manually recharge or replace the battery.

5.5.2 ANN Soil Estimation Accuracy

The WSN system was also tested with a small-scale autonomous network implemented as a proof-of concept in a 1500 m^2 rectangular field, located at the School of Engineering at the Autonomous University of Yucatan in Merida, Mexico. A grid of 2×2 points with a deterministic deployment of four sensor nodes was employed. The nodes coupled to the network comprise a rhombus pattern with four equal sides 20 meters long. Figure 5.11 shows sensors P1 to P4 located

at Lat. 21°2'55.94"N, Long. 89°38'34.76"O; Lat. 21°2'55.43"N, Long. 89°38'35.06"O; Lat. 21°2'55.38"N, Long. 89°38'34.53"O, and Lat. 21°2'55.82"N, Long. 89°38'34.30"O, respectively.

The back-propagation ANN model was tested using MATLAB®. The static (feed-forward) model was trained off-line and the sensor node measurements of soil temperature, humidity and conductivity at two different root levels are the data input to estimate the output, i.e., soil phosphorous. A high learning rate resulted in an increased accuracy of training and testing. However, a learning rate greater than one did not provide better results.

The implemented autonomous WSN system was also employed to analyze the tradeoff between a P estimation accuracy and the energy consumption of the network. The coefficient of determination (R-parameter) is used to evaluate the accuracy of the P estimation against laboratory observed values [187].

Figure 5.16 shows the obtained accuracy results for the four operational stages of the proposed adaptive DPM scheduling (see Fig. 5.14, for details). The experimental results indicate that a correlation exists between soil temperature, humidity and conductivity with its level of P. As shown by the R coefficient of determination in Fig. 5.16(a), sequential measurements performed by just one sensor node in the rhombus WSN pattern (i.e., Stage 1 in the adaptive DPM) presents only regular accuracy results.

The accuracy results using parallel sensor node measurements (Stage 2 to 4 of the adaptive DPM) are plotted in Figs. 5.16(b) to (d). The scatter plot data shows an increasing accuracy of the ANN-based P estimation model (data is closer to the straight line with an angle ≈ 45) when the number of sensor nodes measuring at the same time is augmented.

In terms of scalability, the WSN power consumption is analyzed for different numbers of sensor nodes as presented in Table 5.5. From the analysis, power reductions at circuit (i.e., per sensor node) and at the WSN system level were obtained, according to the proposed DPM strategy. Good correlation results between the soil's P and the variability of the field conditions were achieved with our ANN-based intelligent soil condition estimation. However, the accuracy of the ANN-based estimation is related to the N number of sensor nodes in the network, and therefore; the

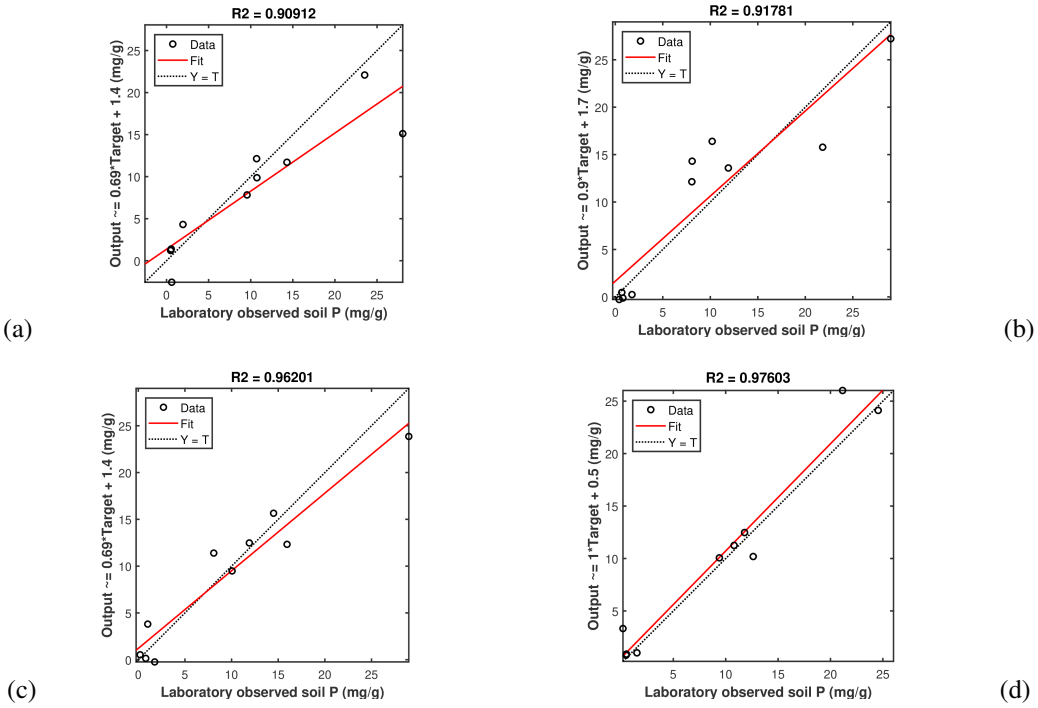

Figure 5.16: Scatter plots (a) to (d) of the laboratory observed versus ANN-based estimated values of soil P using DPM stages 1 to 4, respectively [142].

system's power consumption. In this regard, a fused WSN system with an adaptive dynamic power management methodology was implemented for energy-efficient operation of the WSN. Our measurements indicate that with only $N = 4$ sensor nodes, we achieved coefficient of determination results of up to 0.97603, with a power reduction of 3.67% per node, which means an extension of battery-life (without energy harvesting) of approximately 34 days.

Table 5.5: Power Comparison Analysis of the Proposed WSN [142].

Number of Sensor Nodes (N)	WSN Power Consumption		Power Reduction Per Node
	With DPM Strategy (Stage 1)	Without DPM Strategy (Stage 2)	
1	7.37 mWh @ 1.97 mAh	7.37 mWh @ 1.97 mAh	-
4	7.105 mWh @ 1.92 mAh	29.48 mWh @ 7.88 mAh	3.9%
8	7.06 mWh @ 1.908 mAh	58.96 mWh @ 15.76 mAh	4.2%
12	7.04 mWh @ 1.904 mAh	88.46 mWh @ 23.64 mAh	4.47%
16	7.063 mWh @ 1.902 mAh	117.92 mWh @ 31.52 mAh	4.61%

5.5.3 Spatial distribution maps of soil parameters

A simple web-based supervision system was developed for on-line visualization of the measured data. Figure 5.17 shows an example of the achieved maps for the measured data in the test-field. A spline interpolation technique was used for the generation of spatial distribution maps of each soil parameter.

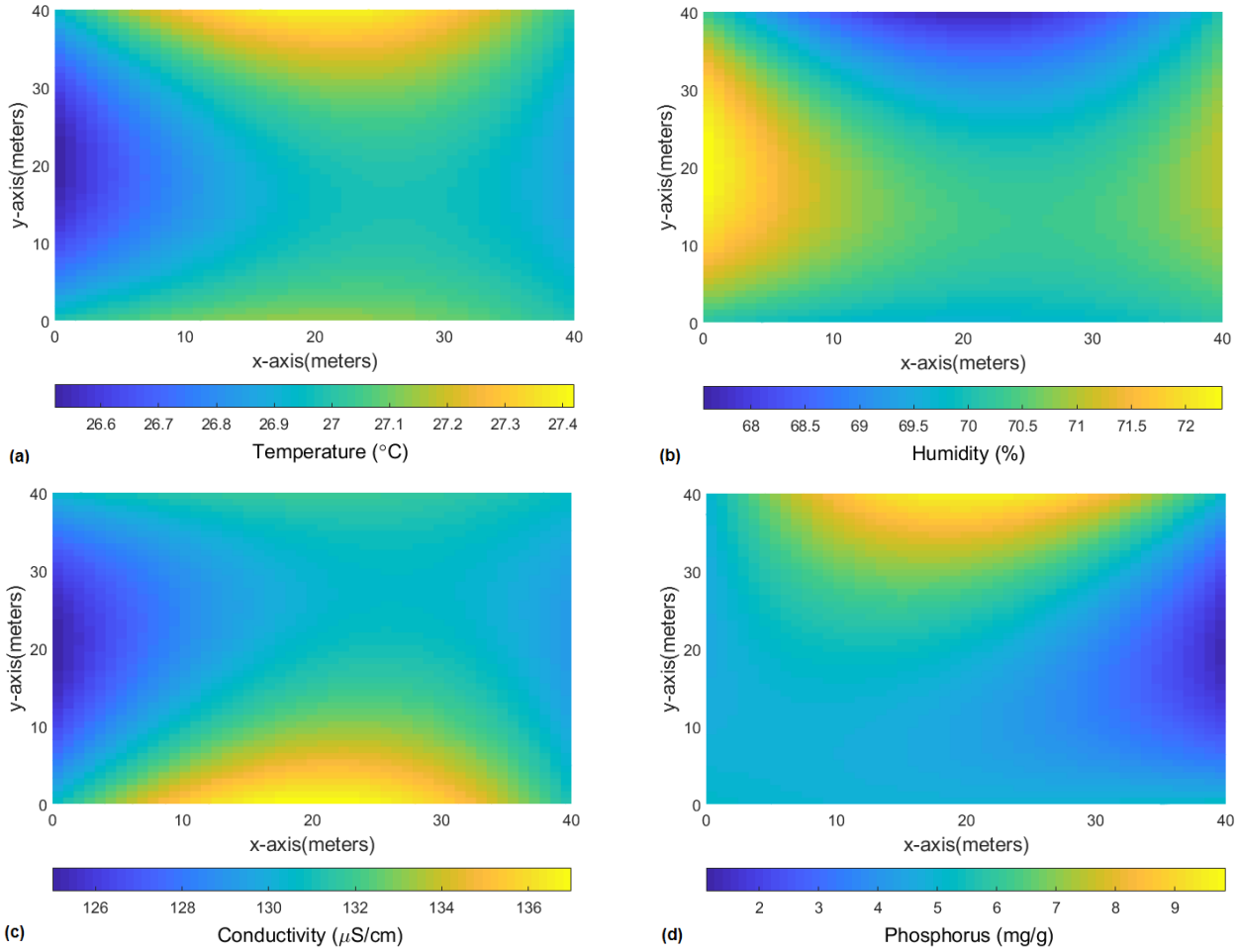

Figure 5.17: Spatial distribution maps of (a) temperature, (b) humidity, (c) conductivity and (d) phosphorus at 7cm plant root levels [142].

Figure 5.18 shows a sample of the system's user interface as seen on an Android hand-held device, where the acquired temperature values on both plant root sections of the node are plotted.

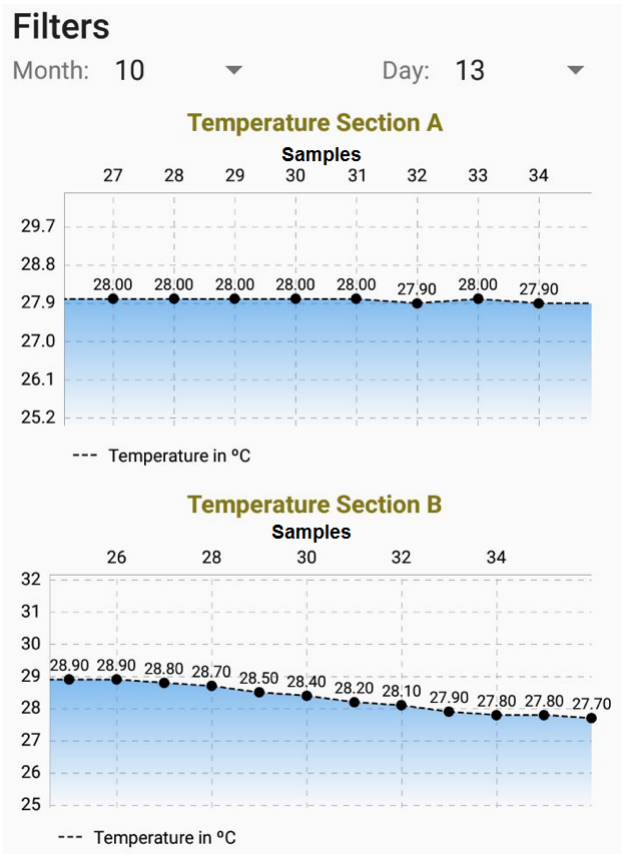

Figure 5.18: User interface displaying temperature over time measurements [142].

The web application also allows selection of the desired sensor node variable and displays an image of the corresponding map. With this scheme, the user can analyze the behavior of the soil conditions at the two different root-levels. All information is stored in the cloud.

5.6 Conclusions

This chapter presents the design of an autonomous sensor node prototype for precision agriculture. This ultra-low-power system is integrated with energy harvesting and is operated with an adaptive dynamic power management strategy that establishes an energy-accuracy balance. This strategy considers that soil respiration rates during the day are affected by temperature, humidity and conductivity changes, and are therefore linked to other biological activities. A Wireless Sensor Network with $N = 4$ nodes deployed in a rhombus pattern is proposed for the intelligent estimation of soil parameters. After basic parameters are measured by the nodes, an artificial neural network

is used to analyze the data and estimate the level of phosphorus in the soil, generating real-time spatial distribution maps of soil parameters at two different root-levels. Experimental results indicate that the WSN achieves a good accuracy in the estimation of phosphorus levels with a power reduction of 3.67% per node. The proposed WSN with DPM strategy can be adapted to solve precision agriculture problems with different types of crops and agricultural regions.

6. DESIGN AND FABRICATION OF A 3-D PRINTED LIGHT CONCENTRATOR FOR SOLAR THERMOELECTRIC ENERGY HARVESTING BASED WIRELESS SENSOR NODES

6.1 Introduction

The recent progress on ultra-low power (ULP) electronic circuits has enabled new research opportunities in wireless sensor networks (WSN) and related applications. These networks of wireless sensors are envisioned to be deployed everywhere, performing a variety of functions and communicating through the Internet [14]. To be economically viable, however; sensor nodes should have very low manufacturing and operational costs, for which power autonomy is absolutely essential. If a system does not depends on a battery to operate, it could in theory be maintenance free and run for as long the electronic components show reliable operation.

Battery-less systems require to harness energy from the environment to be able to operate [21,40]. To date, solar energy is considered one of the most important renewable resources that are available, and photovoltaic (PV) cells are commonly used to harvest that type of energy. However, even when PV technology keeps continuously improving, other critical issues are also emerging. For example, the raw materials used for high-efficiency PV cells are scarce, and the manufacturing complexity of these devices impact their life cycle cost [188]. Therefore, the use of alternative solar energy conversion technologies is still of interest.

Thermoelectric generators (TEGs) are commonly used to collect energy from dissipated heat in industry plants [189, 190] or from body heat in wearable sensors [191, 192]. However, some research works has also shown their potential to be used as an economically viable alternative for converting solar energy [193]. A solar thermoelectric generator (STEG) is a solid-state device that can convert the energy from the sun into electric energy through the Seebeck effect. Basically, STEGs operate by absorbing sunlight, which generates a temperature gradient over the thermoelectric generator, which in turn generates electricity. STEGs have received considerable research

attention and a good number of theoretical and computer simulation studies have appeared in the literature to address their modeling, design and performance optimization [194–199].

This chapter of the dissertation presents the design of an inexpensive concentrating solar thermoelectric generator system to power wireless sensor nodes, using commercial TEG modules. Figure 6.1 illustrates the STEG design concept. The chapter is organized as follows: First it will discuss the general structure of a solar thermoelectric generator and its main components. The design and fabrication of a solar concentrated STEG prototype that can be easily assembled and adapted to different scenarios is presented in the following section. Then, measurement results of the STEG prototype will be shown. A final section summarizes the obtained results and concludes this chapter.

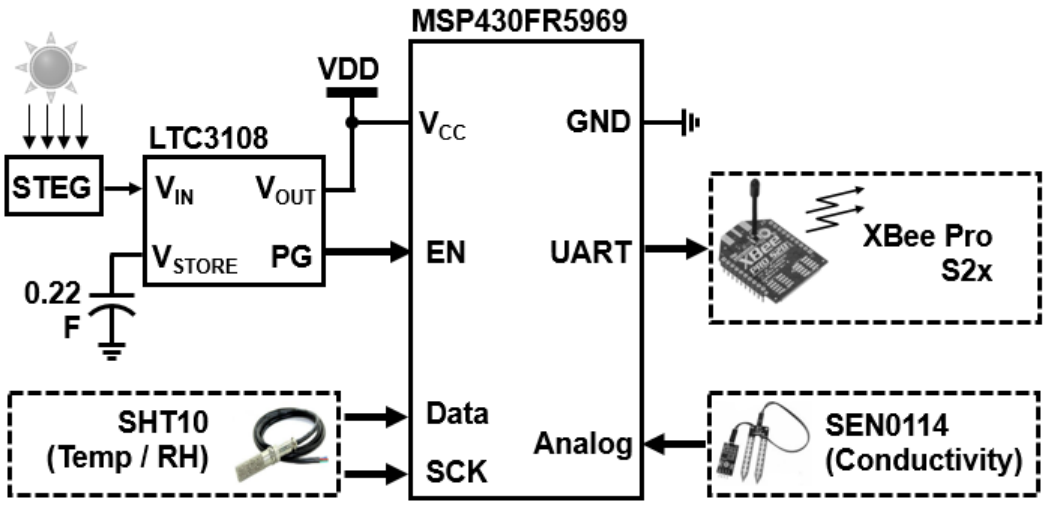

Figure 6.1: Conceptual STEG prototype for IoT-based precision agriculture applications

6.2 Solar Thermoelectric Generator Structure

As shown in Figure 6.2, a solar thermoelectric generator consists of three main components or subsystems: a solar concentrator, the thermoelectric generator itself, and a cooling (or heat management) mechanism. The final efficiency of the STEG will depend, first, on how efficiently the sunlight is converted to heat (which depends on the concentration system). Second, it will also

depend on the conversion efficiency (from heat to electricity) of the thermoelectric device. The output power of the STEG is affected by how well the heat is dissipated in the cold side of the TEG. In typical TEG modules, there is a very short distance (thickness) between the hot and cold sides of the device (3-4 mm). This narrow distance might limit the temperature gradient that can be created, so at the end, this process is related to the cooling system. For these reasons, each one of the components is described next.

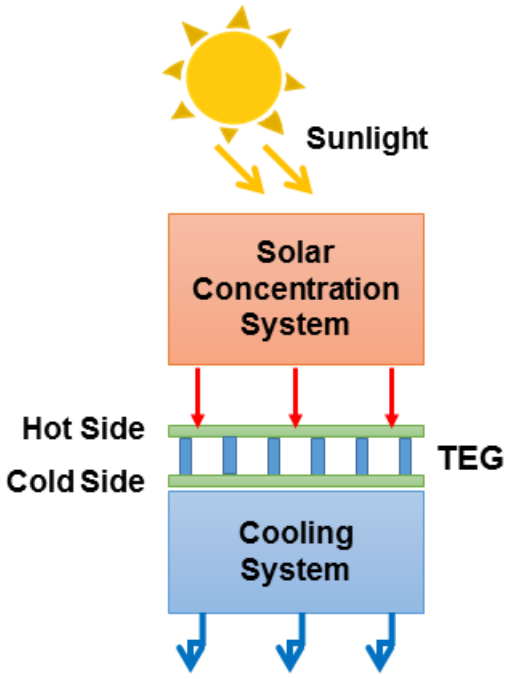

Figure 6.2: General STEG structure

6.2.1 Solar concentration system

The purpose of the solar concentration subsystem is to allow the hot side of the thermoelectric generator to absorb as much as possible of the incident solar energy. The solar concentrator can be implemented through different mechanisms. For example, the authors in [200] make use of a parabolic reflector, to direct the sunlight onto a fixed focal spot. Another approach that can be taken is to optically concentrate the solar radiation on the TEG, through the use of lenses. It has

been demonstrated that this latter approach allows the STEG to operate at higher temperatures [193, 201].

Other research works also propose the thermal coupling of the TEG's hot side to a selective absorber surface. This surface is designed to have maximum absorption at the solar spectrum. With a selective absorber, most of the incident solar energy effectively contributes towards raising the hot-side's temperature [193, 200–202]. However, the use of a selective absorber increases both the cost and manufacturing complexity of the STEG system. For example, the absorber in [202] was made using an aluminum substrate coated through a magnetron sputtering technique. This type of machinery is expensive at with costly maintenance. Therefore, other cost-effective alternatives should be considered, as the authors in [164] did, where a simple aluminum flat-panel was used as the solar absorber.

In the STEG structure, most of the heat losses occur through air convection. It has been proved that enclosing the device inside a vacuum reduces those losses [193, 201–203]. However, this option also raises significantly the complexity of the STEG manufacturing, and its maintenance cost. For that reason, the implementation of a vacuum chamber will be avoided in the proposed prototype.

6.2.2 Thermoelectric generator

A thermoelectric generator creates an electric potential as a response to a temperature gradient between two dissimilar semiconductor materials (p-type and n-type). The magnitude of the generated open-circuit voltage (V_{oc}) is given by the Seebeck effect, as expressed by the following equation:

$$V_{OC} = (S_p - S_n)(T_h - T_c) \tag{6.1}$$

In Equation 6.1, $(S_p - S_n)$ accounts for the difference in the Seebeck coefficients (in units of V/K) of the materials, while T_c and T_h represent the temperatures at the cold and hot sides of the thermoelectric module, respectively.

The conversion efficiency of an ideal TEG device is mainly determined by its operating temperatures and the material's figure of merit $ZT = (S^2\sigma/k)T$, where T is the ambient temperature, k and σ are the thermal and electrical conductivities, respectively, and S is the Seebeck coefficient. The efficiency of the TEG is given by:

$$\eta_{TE} = \frac{T_h - T_c}{T_h} \frac{\sqrt{1 + \overline{ZT}} - 1}{\sqrt{1 + \overline{ZT}} + \frac{T_c}{T_h}} \tag{6.2}$$

In Equation 6.2, $\overline{ZT}$ represents the effective (or average) figure of merit of the material between both temperatures. From Equation 6.2, we can see that the efficiency of the TEG can be improved both by increasing the temperature difference between both sides, or by improvements on the thermoelectric material itself. For that reason, [201] proposes the use of custom-made segmented thermoelectric legs, composed of skutterudite and doped bismuth telluride elements. The segmentation of the n-type and p-type legs enabled the hot side temperature reach up to 600 °C, while at the same time maintaining the cold side at 25 °C. The authors in [204] also propose the use of segmented materials, but with a combination of asymmetrical TEG legs. Nevertheless, even when some works propose the use of specially designed and manufactured thermoelectric generators, it has been demonstrated that commercial off-the-shelf thermoelectric modules can be used for the same purpose, which helps reducing the final cost of the system. This is the approach proposed here.

6.2.3 Cooling system

A key challenge in the design of the STEG is creating a significant temperature gradient across the TEG module. Therefore, an effective cooling mechanism is needed. This mechanism can have either a passive or an active implementation. In the past, the use of some sort of water cooling has demonstrated to be effective in hybrid PV-TEG systems [188, 205]. The use of active cooling with spray water is also proposed and assessed in [199]. However, the use of this type of structures will constraint the STEG application to a very limited set of scenarios. Also, an active spray system requires energy to operate, which makes it unfeasible in micropower harvesting systems.

On the other hand, passive cooling with heat sinks can be implemented, without constraining the applicability of the STEG design, and with reduced penalty in power efficiency. In the proposed STEG prototype, the TEG module container has also been specially designed to keep the cold side temperature low. This design is described in the following section.

6.3 Design of the Solar Thermoelectric Generator System

A low-cost prototype of the STEG-based sensor node system has been implemented with poly-lactic acid (PLA) polymer silicone resin as the base material. Figure 6.3 illustrates the system's mechanical architecture. It is composed of three main sections: the Fresnel lens, the TEG container module, and the wireless sensor node module. Figure 6.3 also illustrates how the whole system looks like when the STEG is attached to the sensor module described in Chapter V. Each subsection of the STEG-based sensor node system is described next.

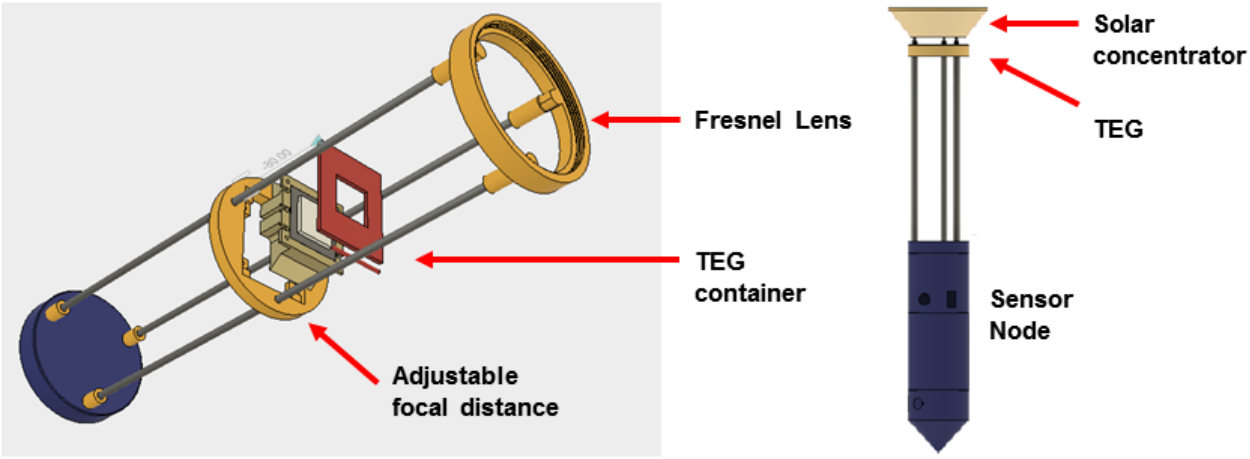

Figure 6.3: STEG-based sensor node prototype architecture.

6.3.1 Fresnel Lens

As shown on Figure 6.3, the optical polycarbonate lens is located on the top part of the solar thermoelectric generator structure. The Fresnel lens consist of a series of concentric grooves etched into plastic. The grooves on the surface of the Fresnel lens act as a solar heat collector, by refracting

the sun rays in a common focal length and concentrating the heat on one side of the TEG. The Fresnel lens offer several advantages when it is compared with conventional curved surface lenses. For example, it has a thinner, lightweight construction. Also, its low-cost makes it ideal for the solar concentrator design proposed in this chapter.

6.3.2 Thermoelectric Container Module

The thermoelectric container is a subsection of the STEG prototype that can be conveniently moved up or down. That means that the distance of the TEG to the Fresnel lens can be adjusted to adapt the STEG to different sunlight conditions, making the design adaptable to a diversity of regions. The container also incorporates a mechanical design with heat-transfer holes drilled in its base. These holes allow the creation of a better differential temperature (Δ°C) in the thermoelectric module, increasing its power generation.

A standard off-the-shelf CP60333 module is used in the STEG, which exhibits a high operating temperature range of up to 80 °C. A passive aluminum heat sink and thermal insulation are used to maintain the cold side of the TEG closer to the ambient temperature. The thermal insulation is composed of silicone rubber filled with ceramic, which ensures a good Δ°C between both sides of the TEG. This insulation component is employed around the TEG module.

Figure 6.4 illustrates a transversal cut view of the TEG container. The figure describes the component's integration of the container: TEG, thermal insulation and the heat sink.

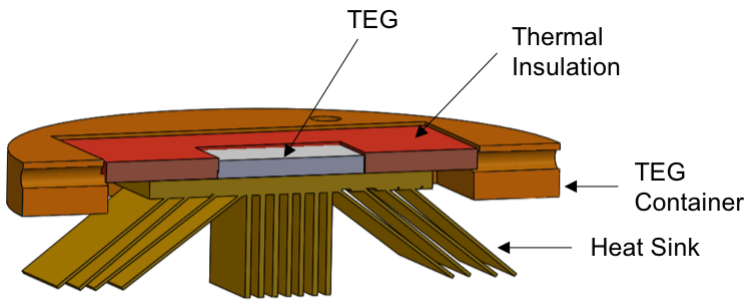

Figure 6.4: Transversal-cut view of the TEG container.

6.3.3 Sensor Node

The sensor node section has been designed for agricultural applications. It is capable to perform measurements of temperature, electrical conductivity and humidity of the soil at two levels below the ground's surface. The basic sensor node design was presented in Chapter V of this dissertation. This sensor node was adapted to the proposed STEG prototype, as shown in Figure 6.3. The measured current consumption of the node at both sleep and active states of operation is shown in Figure 5.15. As illustrated in Figure 6.1, an energy harvester circuit based on the LTC3108 integrated circuit is implemented. The LTC3108 provides a complete power management solution for low-output voltage transducers, such as thermoelectric generators. The main output of the LTC3108 has been programmed to give 3.3V, and a 0.22F supercapacitor is used to store the harvested energy. An MSP430FR5969 microcontroller is selected for its wide voltage range supply of 1.8 to 3.6V.

6.4 Experimental Results

A prototype of the STEG was fabricated and its performance was characterized in the field. A photograph of the fabricated structure is shown in Figure 6.5. The first step in the STEG characterization, is measuring the temperature at three locations: 1) the top side of the thermoelectric module, 2) the heat sink attached to the cold side of the TEG, and 3) the ambient temperature next to the prototype. The measurements were performed using a Ti10 Fluke infrared camera, as shown in Figure 6.6. These measurements were performed every four minutes for a duration of 2 hours, starting at noon time.

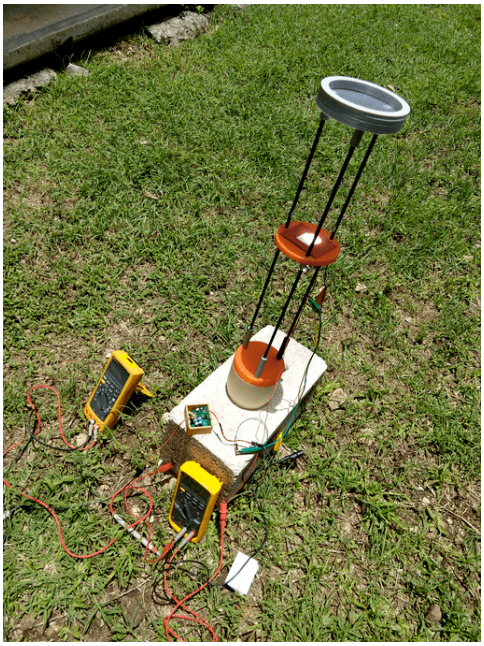

Figure 6.5: Photograph of the STEG prototype

Figure 6.6: STEG characterization using temperature measurements.

The measured temperatures at the hot and cold sides of the TEG are shown in Figure 6.7. The corresponding values of the thermoelectric module's open-circuit voltage (with no loading) are

shown in Figure 6.8. It can be observed from Figures 6.7 and 6.8 that there is a peak temperature difference obtained between the cold and hot sides of the TEG is ≈ 77 °C, resulting in a maximum output voltage of $V_{OC} \approx 150\ mV$.

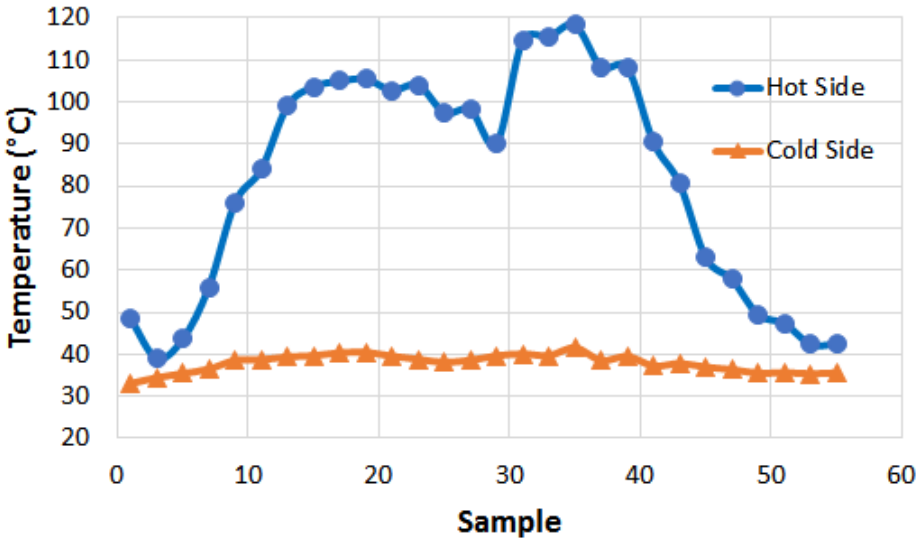

Figure 6.7: Temperature measured at different points in the STEG system.

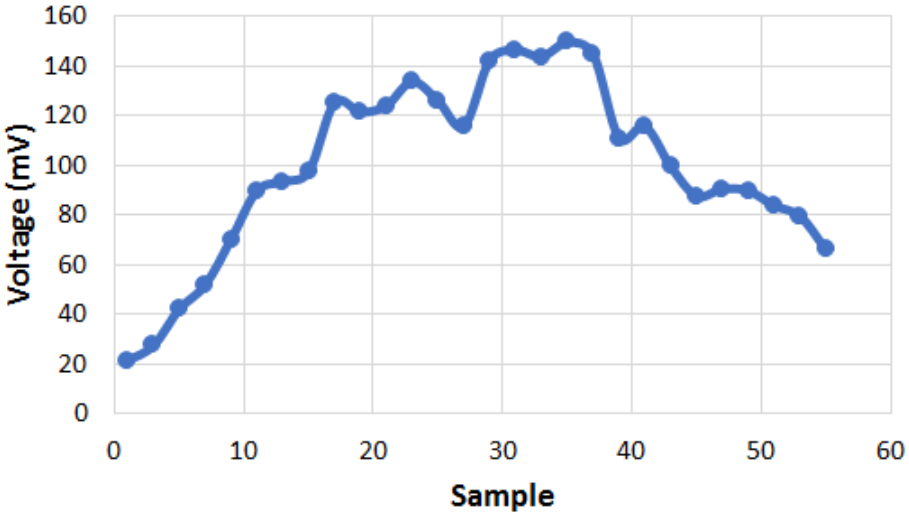

Figure 6.8: Measured output voltage (no loading) of the TEG module.

Table 6.1: Maximum output power generated by the STEG at different temperature gradients.

Temperature gradient (°C)	**Output Power (μW)**
15	100
20	126.6
40	326.7
50	901

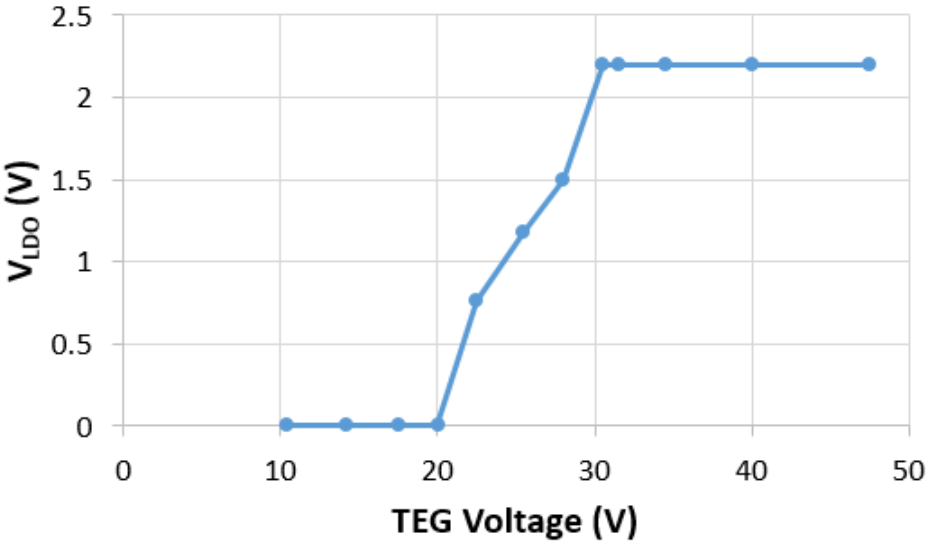

Figure 6.9: Output voltage of the LDO in the LTC3108 with varying TEG voltage.

The maximum instantaneous power generated by the STEG was measured, under different loading conditions and for various temperature gradients. The results are presented in Table 6.1. It was generally observed that the output power reaches a maximum when the load resistance is $R_L \approx 4\ \Omega$. In Figure 6.9, the measured value for the LDO output voltage of the LTC3108 dc-dc converter with the TEG voltage is shown. It is observed that the LTC3108 is able to produce a regulated output voltage from 30 mV of input from the TEG.

6.5 Conclusions

In this chapter of the dissertation, a novel prototype for a STEG-based energy harvesting system is presented. The proposed STEG architecture is based on a low-cost manufacturing process and a commercial off-the-shelf thermoelectric module. The prototype was fabricated (3-D printed) and characterized experimentally. On a sunny day, the STEG creates a maximum differential temperature of 77°C, with an open circuit output voltage of 150 mV, and delivering up to 1 mW of instantaneous power. These conditions permitted the cold-start operation of the LTC3108 harvesting IC. The measurement results show that the STEG can generate enough power to prolong the operation lifetime of a wireless sensor node designed for precision agriculture applications.

7. SCALABLE MULTIPLE-INPUT SYNCHRONOUS ELECTRIC CHARGE EXTRACTION PIEZOELECTRIC ENERGY HARVESTING

7.1 Introduction

Due to the recent evolution in wireless sensor technologies and IoT applications, there is a increased demand of electronic products that are characterized by a long operating lifetime. Designers are looking to reduce the dependency on batteries and are recurring to different methods in order to achieve the desired extended operation. Among different options, the harvesting of energy from the environment is considered as the most viable candidate to substitute the battery as the main power source of these systems. The conversion of kinetic energy to electric power has also been demonstrated as a promising solution in scenarios where there is a strong presence of mechanical vibrations. As shown in Figure 7.1, a vibration energy harvesting system is generally conformed by three sections: a transducer structure, a circuit interface (AC-DC power converter) and an energy storage device.

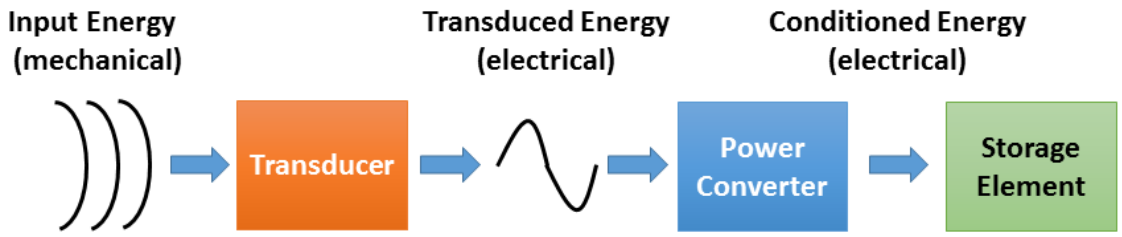

Figure 7.1: Block diagram of a typical vibrational energy harvesting system.

There are various forms of converting the mechanical energy coming from vibrations, including the use of electromagnetic (EM), electrostatic and piezoelectric (PE) transducers [206, 207]. From all of these options, the latter seems to be the most advanced technology, and there is already a lot of developed work related to the modeling, design and characterization of PE transducers. There are also different piezoelectric commercial devices available in the market (see Chapter 2 for a

couple of examples). Piezoelectric harvesters provide the second highest power density ($\approx$ 250 μW/cm^3) from the different harvesters that are used in the literature, so a lot of specific attention has been given to them.

7.1.1 PE Materials and Structures

The electrical power generation capacity of PE materials have been already extensively investigated [208–210]. A summary of characteristics for common piezoelectric materials is presented in Table 7.1. The electromechanical coupling coefficient k is a key parameter because it quantifies the transducer's capacity for energy conversion. Also, the mechanical quality factor Q_m is related to the losses of the transducer's mechanical structure. The figure of merit that quantifies the capacity of a material for mechanical to electrical energy conversion is given by [210]:

$$FOM_{EH} = k^2 Q_m \tag{7.1}$$

Table 7.1: Electromechanical Properties of Common Piezoelectric Materials

Piezoelectric Material	**Coupling Coefficient (k)**	**Mechanical Quality Factor (Q_m)**	**Characteristics**
PZT ceramics	Low to medium (0.5 - 0.7)	High (100 - 1000)	Brittle, low stress
PVDF	Low (0.2)	Low (10)	Flexible
Quartz	Very low (0.1 - 0.2)	Very high (10^4 - 10^6)	Expensive

From Table 7.1, it can be seen that the properties of lead zirconate titanate (PZT) hard ceramics are the most adequate to harvesting purposes: they show a high mechanical quality factor and a moderate coupling coefficient [210]. The main disadvantage of PZT ceramics is that they are

brittle, and generally tolerate low levels of stress before breaking. On the other hand, Polyvinylidene fluoride (PVDF) polymers, although having low figures of merit, are mechanically flexible and therefore they allow for energy harvesting in certain applications where a flexible transducer is needed, such as from shoes insoles or harnessing energy from the waves under the sea [211].

PE transducers can be fabricated in different structures and with various shapes and dimensions [210,211]. For example, Figure 7.2 shows an hexagonal foil or membrane laminate fabricated with PVDF material, that was used as a shoe insole to harvest energy from human walking [211]. The most common geometry for harvesting energy from vibrations, however, would be the rectangular cantilever beam with PZT inserts, as shown in Figure 7.3 [210–212]. This is the geometry that is found in most of the literature. The cantilever construction is characterized by having low resonance frequencies, which can be reduced even more with the addition of a tip-mass to the structure. The capacity of resonating at a particularly low frequency makes it adequate to harvest energy from common human and machine generated vibrations.

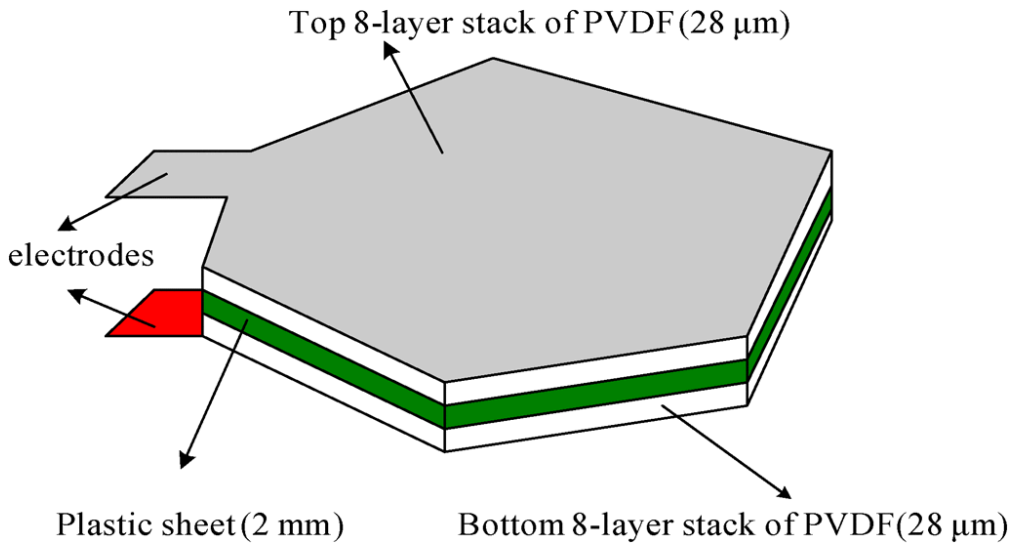

Figure 7.2: PVDF foil used for energy harvesting from shoes ©IEEE 2010 [211].

The main disadvantage of using PE transducers to harvest kinetic energy is the already mentioned fact that these devices are naturally prone to resonate at an specific frequency. At this

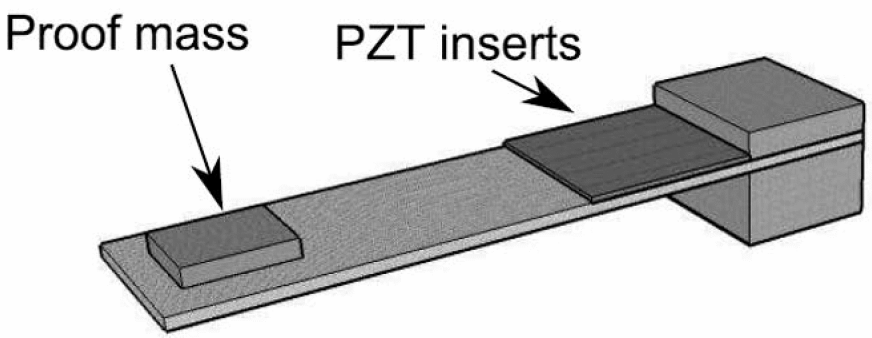

Figure 7.3: PZT PE cantilever beam for energy harvesting ©IEEE 2008 [212].

resonance frequency, the PE transducer produces the largest output power possible. However, the magnitude of the converted energy (from mechanical to electrical) quickly decays as the vibrating frequency deviates from that resonance value. In previous works it has also been observed that a trade-off exists between the operating bandwidth of the PE harvesters and the energy that can be extracted from it.

In certain scenarios, the PE transducer can be tuned to vibrate at the frequency of the input mechanical vibrations. That is the case, for example, of harvesting energy from the vibrations of industrial electric machinery. Nevertheless, it is known that most of the mechanical excitations that are produced by human movements are random in nature. Therefore, they contain a wide band frequency spectrum. With that consideration, some researches has recurred to different techniques in order to enable the harvesting of energy from wide band mechanical vibrations. From those works, it has been proved that the existing trade-off between bandwidth and harvested energy of PE harvesting systems are relaxed when using various piezoelectric transducers in a single harvester structure [213–215].

The use of an array of PE transducers, however, raises the need of a special interface circuit that is capable of collecting and processing the voltages that are coming from multiple elements at the same time. Several systems have been proposed to such effect and are reviewed next.

7.1.2 Previous Works in Energy Harvesting from Multiple PE elements

There are some published works that already deal with the problem of harvesting from multiple PE transducers. In [216] an array of up to 9 elements were connected in parallel to a single standard full-wave rectifier (FWR) followed by a supercapacitor. As it will be discussed in the coming sections, the FWR is the PE interface with least energy extraction capability. It also was shown in [216] that simply connecting the elements in parallel does not necessarily produce the perfect addition of their currents, resulting in a waste of more than 30% of the generated energy. It is important to observe that that was the case for elements vibrating at the same frequency. Results can be worse when the PE harvesters are responding to different mechanical excitations.

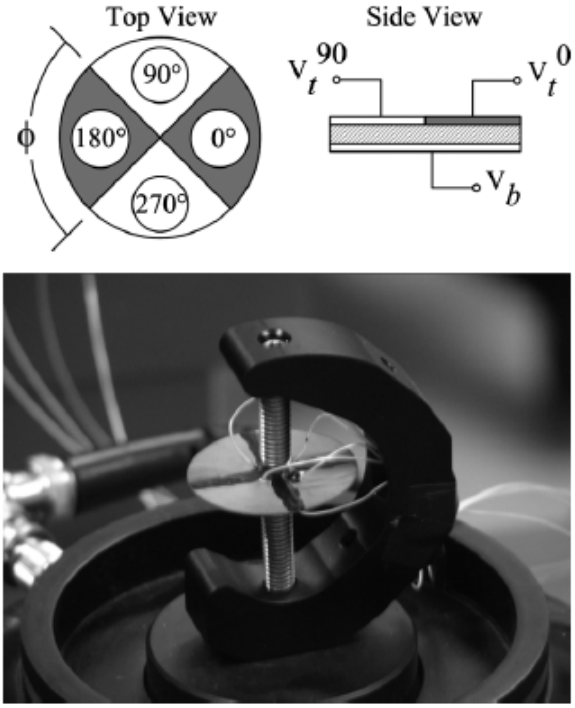

Figure 7.4: Custom-made PE disk used in [217] ©IEEE 2009.

The authors in [217] propose a CMOS full-wave rectifier with integrated peak selection, which is capable of harvesting from a custom-made PE disk that generates more than one output voltage.

The shape of the PE disk is shown in Figure 7.4. The FWR rectifier that was proposed, however, requires of input voltages with an specific phase shift of 90°, and therefore provides an interface only to the non-standard PE disk shape.

In [218], several circuits for multisource PE energy harvesting are designed and analyzed, but all of them require an inductor for each input. This is obviously a suboptimal solution in terms of components count, cost and volume for a harvesting system. Finally, [219, 220] propose a single non-linear interface scheme that can be shared with multiple PE devices. However, in both works the prototype implementations where made with discrete components. That is why, in [219] a system power consumption of up to 30 μW is measured, which is not suitable for micro-harvesting or weak mechanical vibrations. In [220], a lower consumption was achieved, but the proposed circuit topology recurs to a flyback transformer topology. Flyback transformers are bulky, therefore their solution goes against the advantages of recurring to a single-inductor reuse scheme (which is saving area and cost).

In this chapter of the dissertation, a scalable circuit interface for multi source PE harvesting is proposed. This interface can be fully integrated with the exception of a single external inductor component that is shared by all harvesters.

7.2 Processing Techniques for PE Energy Harvesting

7.2.1 PE Transducer Modeling

The PE cantilever structure shown in Figure 7.3 can be adequately modeled by the simple resonator shown in Figure 7.5, composed of a spring, mass and damper. The mass M represents the rigid mass of the cantilever, K_E the structural stiffness, and the damper C_V the mechanical losses. In the figure, F is the externally applied force, u is the mass displacement of the cantilever, and V is the output voltage generated by the transducer.

The following dynamic equations link the mechanical variables (which are dependent on the physical parameters of the structure) to the electrical output variables:

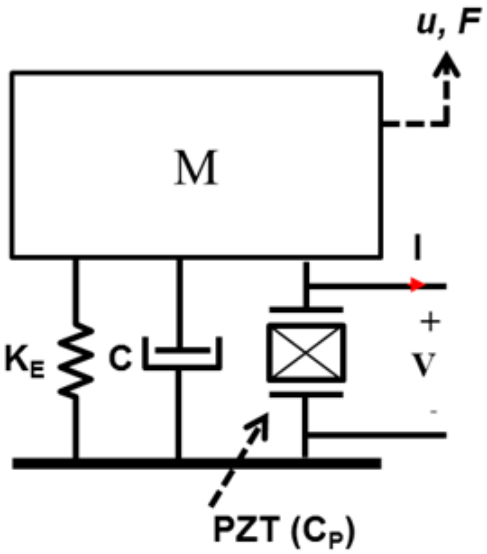

Figure 7.5: Simple model for resonant excitation of a PE transducer.

$$M\ddot{u} + C\dot{u} + K_E u = F - \alpha V \tag{7.2}$$

$$I = \alpha\dot{u} - C_P\dot{V} \tag{7.3}$$

Equations 7.2 and 7.3 can be called the motion and electrical equations, respectively, where α is the force factor and C_P is the electrical capacitance in the transducer. For circuit simulation purposes, the equivalent electrical circuit of Figure 7.6 can be used to represent the PE transducer. In that figure, the left side represents the mechanical behavior of the transducer, i.e. the voltages and currents correspond to forces and velocities, respectively. The right side models the electrical parameters of the device: the PE output capacitance (C_P) and the electrical losses (R_P). The transformer in the middle of the circuit models the transduction mechanism, reflecting the electromechanical coupling of the PE element.

In the model of Figure 7.6, the following equations describe the relationship of the circuit elements to the physical variables of Figure 7.5:

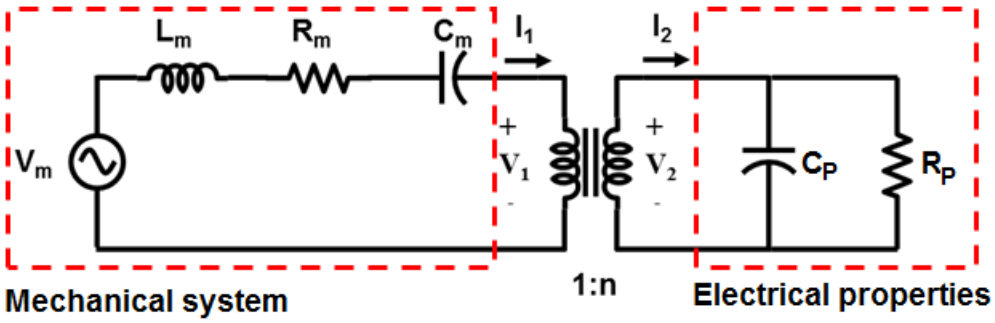

Figure 7.6: Electrical equivalent circuit of the PE generator.

$$V_m = m\ddot{u} \tag{7.4}$$

$$L_m = m \tag{7.5}$$

$$R_m = C \tag{7.6}$$

$$C_m = 1/K_E \tag{7.7}$$

If the PE transducer has a relatively low coupling coefficient (as is the case of most devices fabricated with PZT material), then the transformer in Figure 7.6 has a high turns ratio, meaning that the loading at the secondary side does not affect the current in the primary side (which corresponds to the proof mass' velocity). In other words, the electrical damping is very low. In that case, the element can be substituted with a current-controlled current source as shown in Figure 7.7. The model can further be simplified to the simple circuit shown in Figure 7.7 when the device is operating at or very close to its resonance frequency.

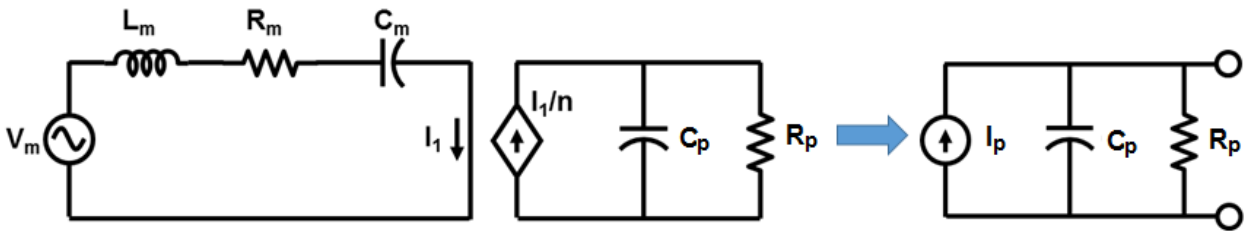

Figure 7.7: Circuit model of a PE generator with low electromechanical coupling.

7.2.2 PE Energy Harvesting Interfaces

In the recent years, several circuit interfaces have been proposed for PE energy harvesting [221–224]. The main challenges and concerns in all this works has been:

- Provide efficient rectification of the AC input voltage.
- Reduce the quiescent power consumption of the interface.
- Increase the final converted and extracted energies of the system.
- Realize independency of the harvested power from the load connected the interface circuit.
- Provide output voltage conditioning (smoothing, regulation and level conversion of the output voltage)

A revision of the most common interfaces that have been used is provided in the following section.

7.2.3 PE Harvesting with Complex Impedance Matching

Considering the capacitive nature of a PE transducer, the maximum power that can be harvested occurs when the device is presented with a complex matching (i.e. inductive) load. This case is described in Figure 7.8. In that Figure, the current generated by the PE transducer is $i_p(t)$ = $I_P$sin(ωt). It can be proved that the matching inductor value that provides maximum power extraction from the PE harvester is:

$$L_{eq} = \frac{1}{\omega^2 C_P} \tag{7.8}$$

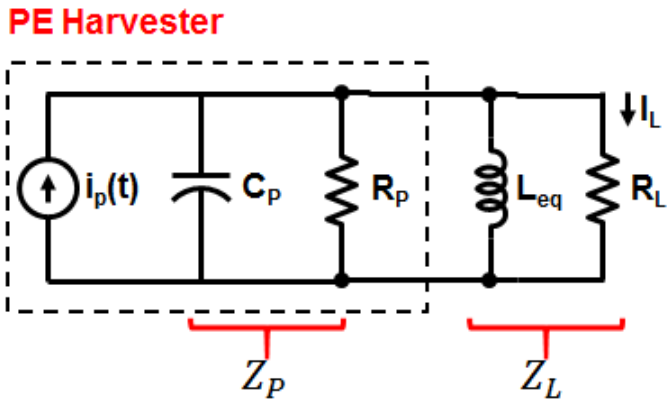

Figure 7.8: Piezoelectric harvester with complex impedance matching.

At those matching conditions, and if R_L = R_P, then the maximum output power is given by:

$$P_{max,match} = \frac{I_P^2 R_P}{8} \tag{7.9}$$

An example calculation can be done with the following parameters of a commercial PE transducer: R_P = 600 $k\Omega$, C_P = 120 nF, f_P = 225 Hz and I_P = 40.7 μA. With that conditions, the open-circuit output voltage of the harvester is V_P = 2.4 V and its output power $P_{max,match}$ = 124.24 μA. To realize those previous conditions, an inductor value of 4.2 H is required. As it can be seen, these operating conditions cannot be physically implemented, because the required inductor implementation is not feasible. However, as that is the ideal maximum power that can be extracted from the transducer, the value of $P_{max,match}$ is kept as a reference for evaluating the performance of other approaches.

7.2.4 Full-Wave Rectifier Circuit

The simplest interface circuit for PE harvesting, would be the full-wave rectifier (FWR) shown in Figure 7.9. If we assume that the storage capacitance C_{strg} is large enough when compared with C_P, the voltage at the output of the rectifier V_{rect} can be considered a constant value. The waveforms for the current and voltage of the PE harvester are shown in Figure 7.10. As shown, the PE voltage $V_P(t)$ must be larger than the voltage at the storage element by 2 times the voltage drop of the diodes (V_D), in order for the diodes to conduct and the harvester being able to deliver charge to the output (from time t_1 to time t_2). That means that a large portion of the PE current (shown with the shaded region) is waste in charging only the PE capacitance (from t_0 to t_1). This behavior severely limits the amount of power that can be harvested with the FWR circuit.

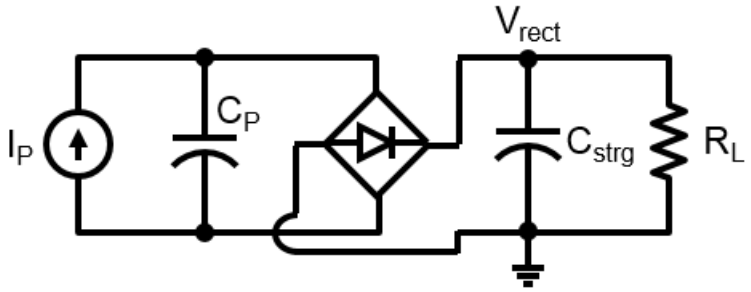

Figure 7.9: Full-Wave Rectifier for PE energy harvesting.

It has been shown that the output power that can be extracted with the FWR circuit is given by [223]:

$$P_{o,fwr} = \frac{2}{\pi} I_P V_{rect} [1 - \frac{V_{rect} + 2V_D}{V_{rect}}] \tag{7.10}$$

This power has a maximum value (see Figure 7.11) that occurs when V_{rect} = V_P/2 - V_D (basically half the value of the peak open-circuit voltage V_P). To that effect, maximum power extraction circuits has to be implement, that make sure that the right value of V_{rect} is the storage capacitance,

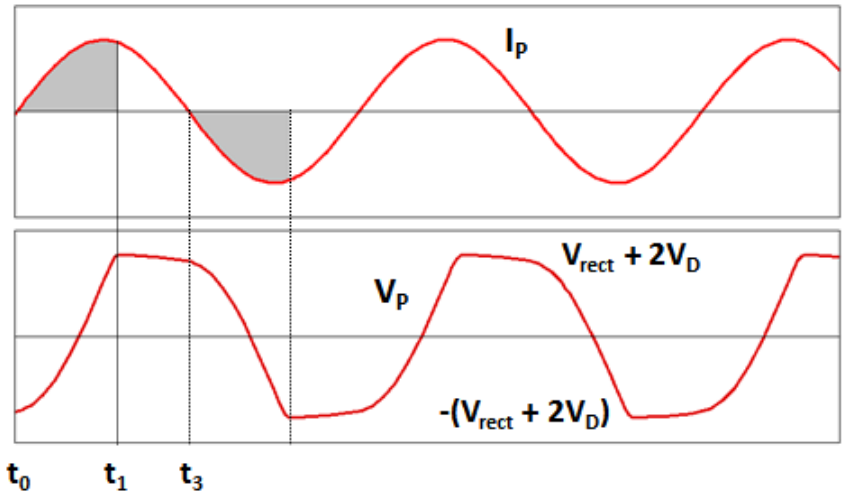

Figure 7.10: Simulated waveforms for the FWR PE harvesting circuit.

tracking the changes in amplitude of V_P [225–227]. The maximum power is given by the following expression:

$$P_{max,fwr} = \frac{1}{2\pi}(1 - \frac{2V_D}{V_P})^2(\frac{I_P^2}{\omega C_P}) \tag{7.11}$$

If the same parameters of the example given in the previous section are considered, the maximum extracted power is $P_{max,fwr}$ = 15.54 μW when ideal diodes are considered. That is only a 12.51$\%$ of the total power when using a matching load. The real extracted power is less when actual diodes are considered. For that reason, many works propose non-linear, resonant harvesting techniques to increase or enhance the power that can be extracted from PE devices.

7.2.5 Synchronized Switch Harvesting on Inductor Technique

Several non-linear, resonant techniques have been proposed in the literature, including the parallel and serial synchronized switch harvesting on inductor (P-SSHI and S-SSHI respectively). The circuit for the P-SSHI is shown in Figure 7.12, and the waveform for the PE voltage in Figure 7.13 [223].

The idea of the P-SSHI technique, is to close the switch when the piezoelectric current changes polarity. This coincides when the PE transducer is in its maximum point of deflection, as well as

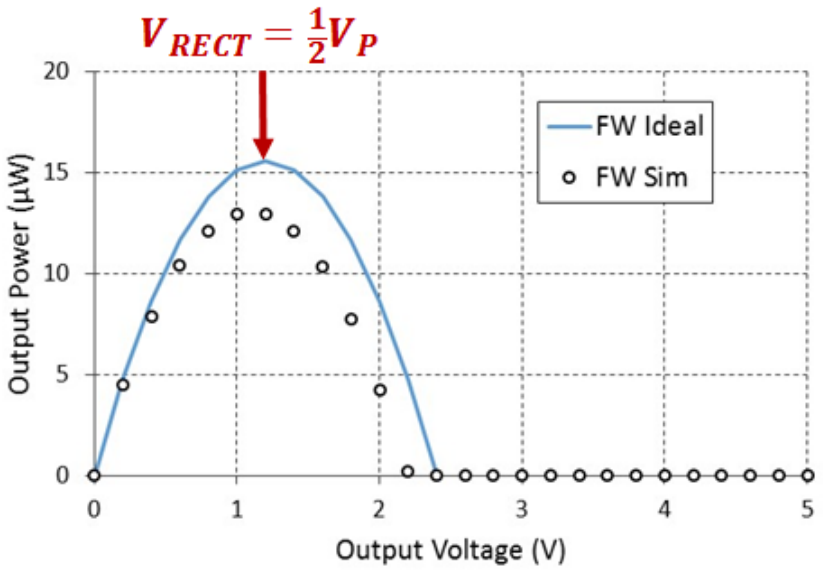

Figure 7.11: Theoretical (ideal) and simulated (with BAT54 Schottky diodes) power of the FWR circuit.

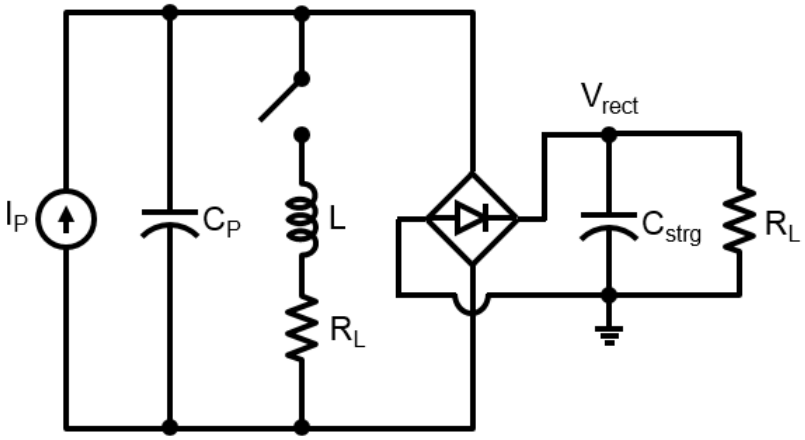

Figure 7.12: Parallel SSHI circuit topology.

the voltage V_P. When the switch closes, the inductor L resonates with the PE capacitance, and a voltage inversion is produced. This voltage inversion reduces the amount of current that is wasted charging C_P, hence more power can be extracted from the harvester [94, 228]. The maximum output power that can be extracted with the P-SSHI technique is given by [223]:

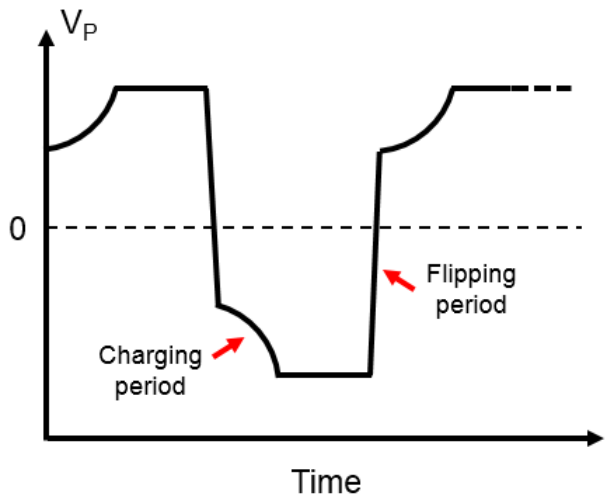

Figure 7.13: Waveform of the PE output voltage in the P-SSHI circuit.

$$P_{max} \approx [1 - \frac{\pi}{2Q}\frac{V_D}{V_{PO}}](\frac{2Q}{\pi^2})(\frac{I_p^2}{\omega C_P}) \tag{7.12}$$

where V_{PO} is the open-circuit voltage of the harvester and Q is the quality factor of the inductor. This maximum power extraction occurs when the rectifier has an output voltage of:

$$V_{rect} = \frac{V_{PO}}{1-\gamma} - V_D \tag{7.13}$$

In the previous equation, the parameter γ is expressed as:

$$\gamma \approx e^{(-\frac{\pi}{2Q})} \tag{7.14}$$

In terms of power extraction, both the P-SSHI and S-SSHI offer up to 10$\times$ improvement with respect to the standard FWR approach [228], even with modest values of inductor's quality factor. However, these techniques are not good for low-voltage EH, and they still exhibit load dependency [222]. Also, as shown with Equation 7.13, they also require tracking the magnitude of vibration, in such a way that the maximum power extraction is always ensured.

Other non-linear harvesting techniques include the Double Synchronized Switch Harvesting

(DSSH) [212] and Synchronous Electric Charge Extraction (SECE) [229]. Each one of these techniques offer their own advantages and disadvantages, which are summarized in Table 7.2. The DSSH and SECE techniques offer moderate power improvement ($5\times$) but they are more suitable for low-voltage harvesting and offer load independency [222]. From those two options, SECE is the most suitable for multisource harvesting, which is going to be explained next.

Table 7.2: Classification of common non-linear PE harvesting techniques.

Technique Name	**Low voltage harvesting**	**Load Independency**	**Circuit complexity**	**Power Improvement**
FWR	Poor	Poor	Good	-
P-SSHI	Poor	Poor	Moderate	≈ 10
S-SSHI	Moderate	Poor	Moderate	≈ 10
DSSH	Moderate	Good	Poor	≈ 5
SECE	Moderate	Good	Moderate	≈ 4

7.2.6 Synchronous Electric Charge Extraction

As mentioned before, one problem of the energy transfer approaches such as S-SSHI and P-SSHI is that the transducer has a direct connection to the inductor and also to the load. Therefore, there is an induced mechanical damping on the PE transducer that occurs when extracting energy from it. This is particularly a problem in the case of PE structures with high electromechanical coupling. The undesired outcome of those methods is then that the harvested power is heavily dependent on the connected load. The Synchronous Electric Charge Extraction (SECE) method alleviates this problem because by structural design, it isolates the PE device from the load for most of the vibration period. That means that the impedance seen by the transducer is almost constant, making the extraction process less sensitive to the load. It has also been proved that

the harvested power with SECE method is four times greater than with the simple impedance adaptation approach [230].

In the SECE method, a nonlinear approach is taken where the electrical charge extraction from the PE device occurs when the absolute value of the energy stored in its output capacitance is at its maximum. This coincides with the point of maximum deflection of the cantilever beam. The SECE basic architecture is shown in Figure 7.14, where it can be seen that is topologically similar to a buck-boost converter, but with different control algorithm.

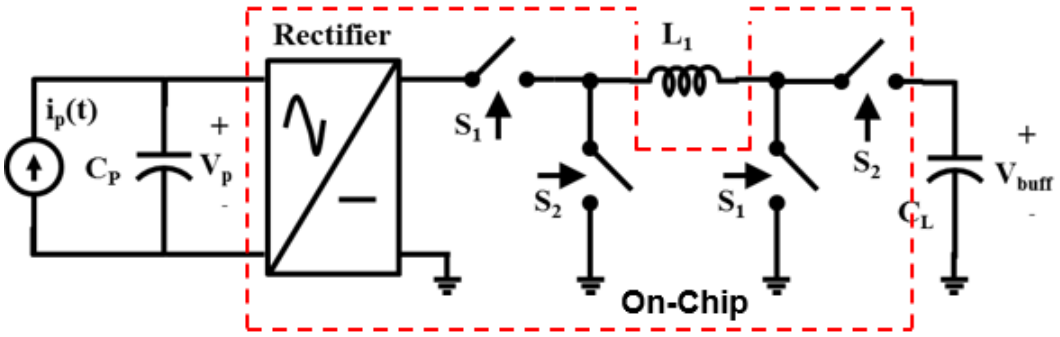

Figure 7.14: SECE basic architecture.

In Figure 7.15 the main voltage and current waveforms of the SECE circuit are shown, describing its operation. As it can be seen, the switch pairs S_1 and S_2 are open most of the time during the vibration period. Therefore, the inductor current is ideally zero during that time. When the PE transducer reaches its maximum point of deformation, its output voltage V_P reaches its maximum. At that moment the switches S_1 are closed (during period P_1) and the inductor L_1 is charged. At the same time, the PE capacitance C_P is discharged meaning that V_P rapidly decreases to zero. When V_P reaches zero, I_{L1} peaks at its maximum value. The control circuit has to detect that point, where it opens S_1 and closes S_2 (period P_2), transferring the energy that was accumulated in the inductor to the storage capacitor. The voltage V_{buff} is then increased by a certain amount because the load capacitance is charged. The sum of periods 1 and 2 is equal to the time τ_L. From

Figure 7.15, another advantage of the SECE technique is appreciated: it is a self-adaptive method because it automatically follows the displacement peaks of the transducer.

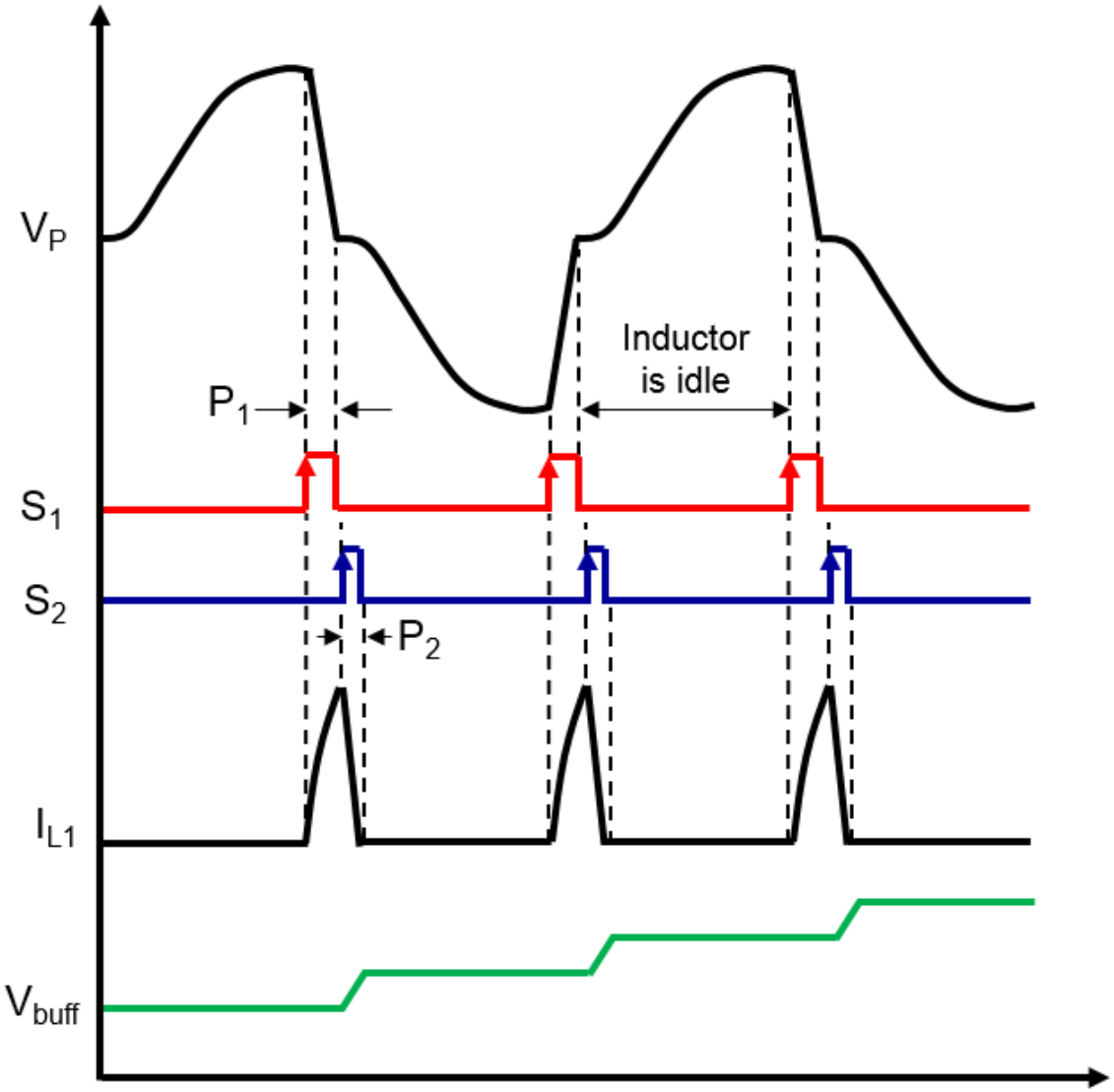

Figure 7.15: SECE basic waveforms.

7.2.7 Synchronous Electric Charge Extraction for Multiple Inputs

Observe that in the single-input SECE operation of Figure 7.15, the charge extraction time is significantly less than the complete signal period. That means that in the operation of the SECE

circuit, the inductor lies idle for most of the vibration period. This fact opens the opportunity to adapt the SECE technique to several inputs with multiple energy harvesters. Figure 7.16 shows such scheme for a two-input system. It is important to notice that thanks to the SECE operation, no interaction or coupling exist between the harvesting devices themselves or the load. This method also recurs to an inductor re-use scheme, which means that no extra-cost is added in terms of external components and PCB area.

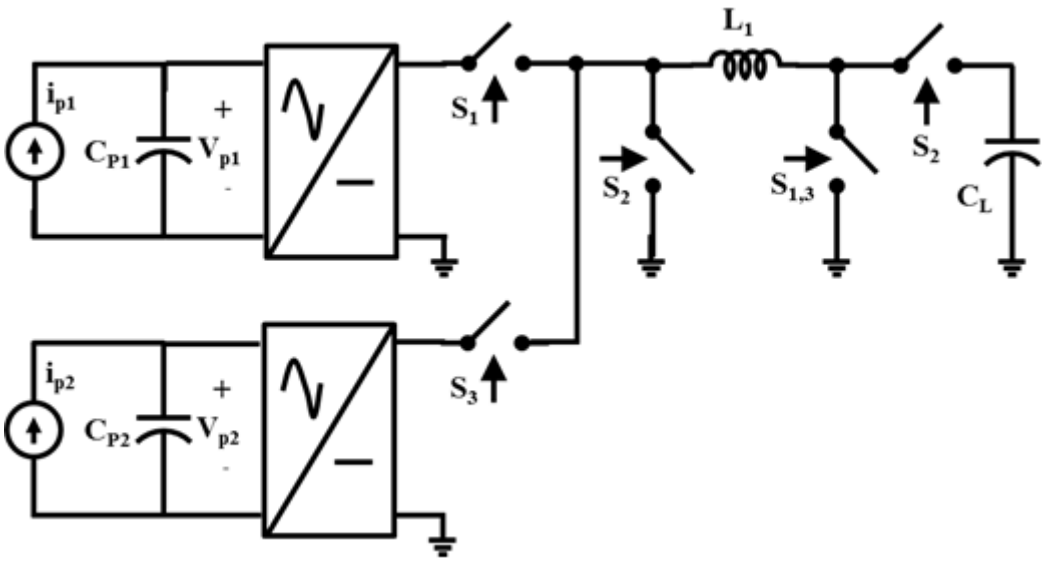

Figure 7.16: SECE architecture extended to two inputs.

The possibility of having multiple inputs with the SECE technique, enables then the energy harvesting from a multisource, wide-band array of PE transducers. As mentioned before, this approach has already been taken in [219, 220], where both implementations were made with discrete components. In this work, an integrated multi source PE harvesting circuit is proposed, with minimum use of external components. It is designed in a CMOS 130 nm process. The implemented multisource PE system is described next.

7.3 Proposed Multisource SECE Energy Harvesting System

7.3.1 System Architecture

The proposed architecture for the scalable multisource PE energy harvesting system is shown in Figure 7.17. The main idea is having a single SECE core interface for multiple PE transducers, with its own digital control circuit and storage device. The transducers are connected in parallel through its own rectifier. The SECE interface output is connected to a SC circuit to up-convert the voltage. As future work, the SC converter can be controlled to regulate its output to the load. The system can be made scalable by replicating several SECE circuits operating in an independent fashion, and summing up their respective output voltage V_{buff} through a multi-input switched-capacitor (SC) converter. In the designed prototype, a two-input SC converter was implemented, but the system can be scaled-up with many SECE sub circuits as inputs the SC converter has. The circuit design for the proposed system will be described in the following sections.

7.3.2 Circuit Design

7.3.2.1 Enhanced Rectifier

As shown in Figure 7.17, each SECE interface has a rectifier for each one of its inputs. The rectifiers are implemented with a combination of passive and active rectification circuits. The passive rectifier allows for a "cold" start of the system, while the active rectifier increases the AC-DC conversion efficiency once the system is in active operation. The passive rectifier is implemented with the Negative Voltage Converter (NVC) shown in Figure 7.18 [229]. The NVC consists of cross-coupled NMOS and PMOS transistor pairs. Even when the NVC topology requires a minimum input of V_{th} to have an output voltage, it has the advantage of being self-controlled and presenting negligible voltage drop once the transistors are conducting. The NVC transistor sizes has been designed for a voltage drop less than 50 mV at the maximum load current.

The system's power conversion efficiency is severely degraded with the use of only passive rectifiers. As shown in the simulation of Figure 7.19, the relatively high "turn-on" voltage of the NVC causes a significant "waste" of extracted charge in the PE capacitor. Even when the

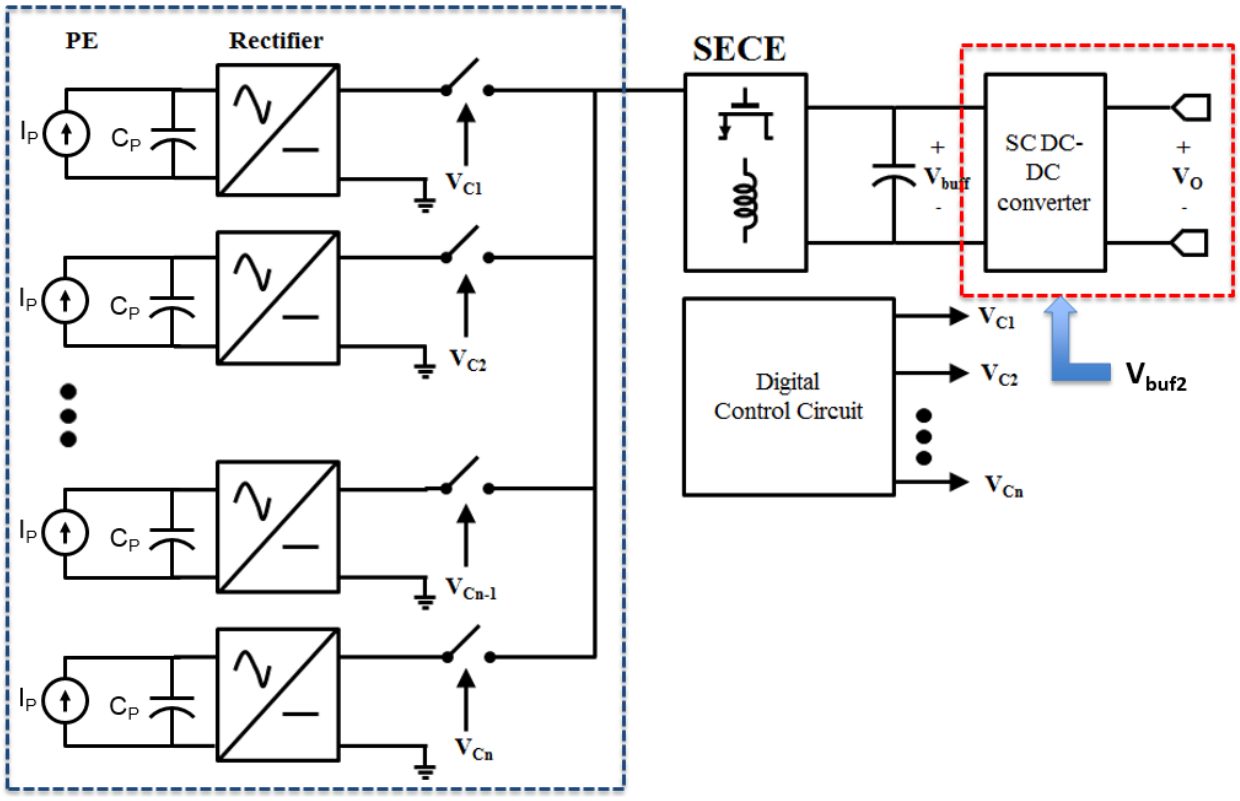

Figure 7.17: Proposed multi-input SECE architecture.

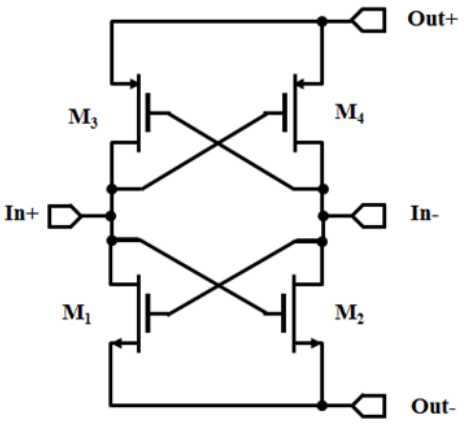

NVC design sizes

Device	Size (µm/µm)
M_1	(10/0.18) x 100
M_2	(10/0.18) x 100
M_3	(10/0.18) x 100
M_4	(10/0.18) x 100

Figure 7.18: Negative voltage converter used for passive rectification.

obtained performance is better than using external discrete Schottky diodes, the required minimum threshold voltage in the MOS transistors has the effect that the PE output voltage during SECE operation cannot reach 0 V. This means that the peak value is degraded from 2.0 V to 1.63 V,

reducing the harvested power. The degradation in terms of harvested power with the NVC passive rectifier is presented in Figure 7.20, where it can be seen that using only the NVC circuit, the total harvested power would be only 53.2 % of the total available power. The relatively constant performance for the output voltage range in this figure confirms that the SECE circuit performance is independent of the voltage at the load capacitance.

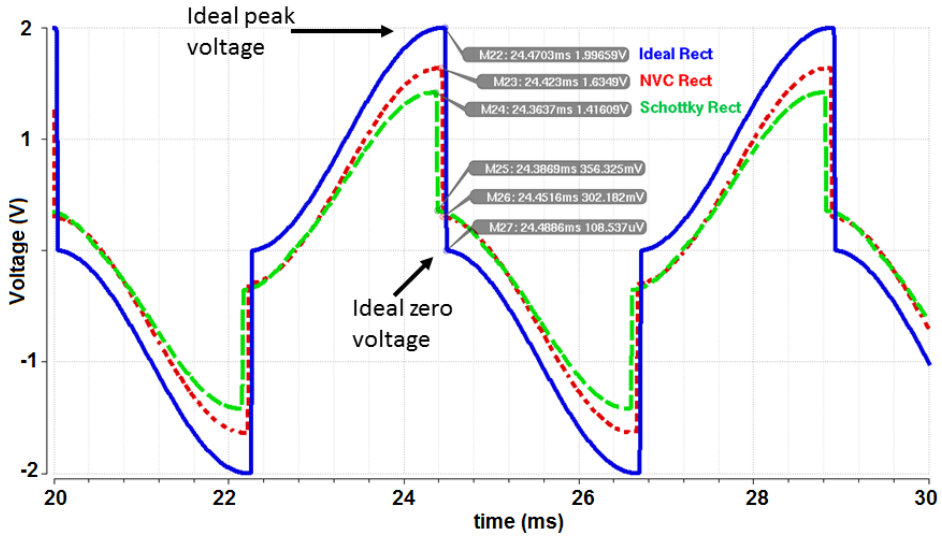

Figure 7.19: Negative voltage converter simulation against ideal and Schottky rectifier.

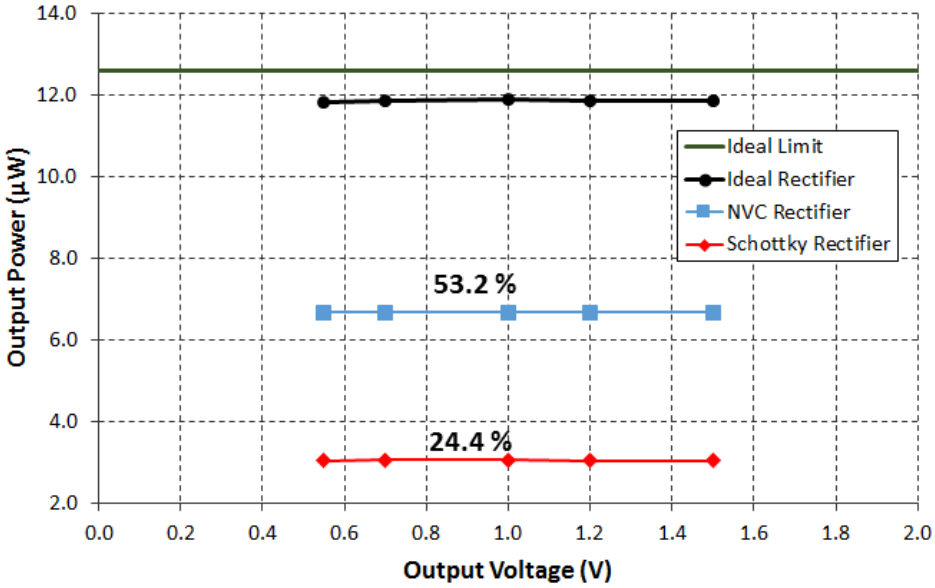

Figure 7.20: Degradation of harvested power with the use of only passive rectifiers.

To solve this problem, an active rectifier circuit can be used, as in [124]. The active rectifier is a parallel circuit that is enabled once there is a constant input of power, and it helps to reduce the losses due to the passive rectifier threshold voltage. The active rectifier design and its control circuit are shown in Figure 7.21. The control circuit detects the polarity of the input voltage and activates the corresponding transistors (M_1/M_4 or M_2/M_3) to produce a positive output all the time (i.e. full-wave rectification) [124]. As this is an auxiliary circuit to the passive NVC, the transistor sizes can be relaxed in order to save chip area and reduce parasitic capacitances (which increases losses). The improvement produced by the use of the active rectifier is shown in the simulation of Figure 7.22. The PE voltage at the rectifier's output now reaches a peak value that is 50 mV close to the ideal, and during charge extraction drops down to only 2.5 mV.

7.3.2.2 Detector Circuits

The SECE control system requires several detector circuits in order to operate. As seen in the waveforms of Figure 7.15, the peak or maximum of the PE voltage must be detected (after rectification), in order to start the charge extraction from the transducer (i.e. period 1 of the process). The chosen peak detector is shown in Figure 7.23 [231]. In this circuit, the PE voltage is compared with

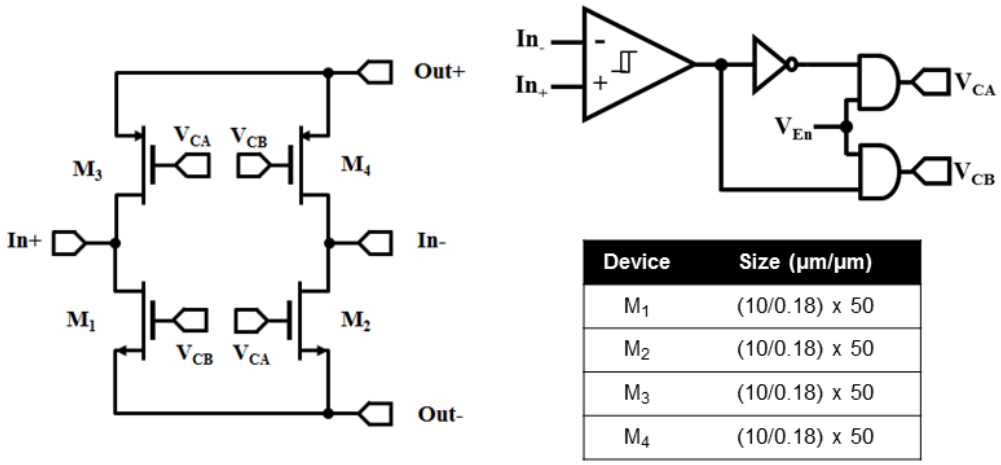

Device	Size (µm/µm)
M_1	(10/0.18) x 50
M_2	(10/0.18) x 50
M_3	(10/0.18) x 50
M_4	(10/0.18) x 50

Figure 7.21: Active rectifier design and its control circuit.

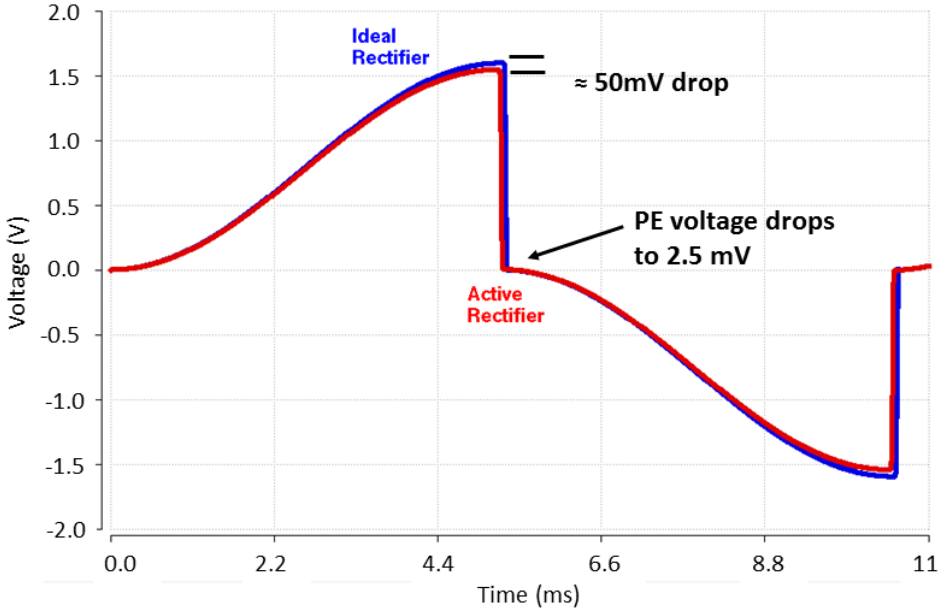

Figure 7.22: PE output voltage waveform after active rectifier starts operation.

a delayed version of itself. While the voltage is increasing, V_{rect} is always larger than its delayed version, therefore the output voltage of the comparator is low. When V_{rect} reaches its maximum value and starts decreasing, its delayed version will turn to be larger. When this is detected by the comparator, its output voltage is turned high. A pulse generator is used at the output of the detector to generate the necessary change of state in the digital control circuit.

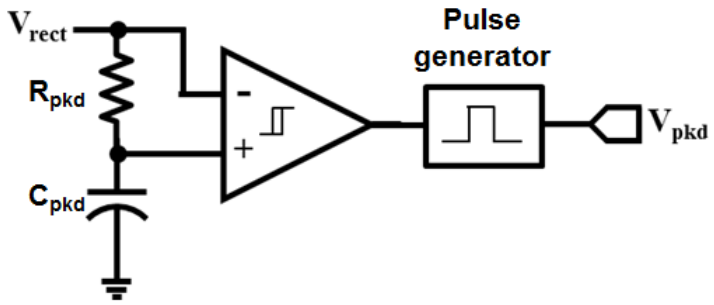

Figure 7.23: Peak detector used in the SECE interface control circuit.

In the operation of the SECE core circuit, a zero crossing detector is necessary to identify when the PE capacitor has been completely discharged or that its voltage reaches close to zero (which corresponds to the peak of the inductors current). To detect this event, the simple comparator circuit presented in Figure 7.24 is used.

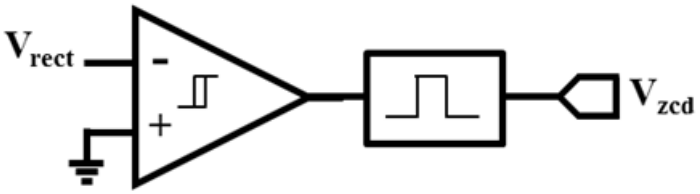

Figure 7.24: Zero crossing detector circuit.

Finally, the SECE process finishes once the inductor have been discharged in the buffer capacitor, and its current has reached zero. If the connection between the inductor and capacitor is not interrupted, they would keep resonating an the capacitor would start discharging over the inductor, which is undesirable. So, a circuit is used to detect any reverse current in the capacitor, opening the output switch when the discharge from the inductor to the storage capacitance has finished. The circuit shown in Figure 7.25 is used for that purpose, which can be basically described as an active-diode circuit.

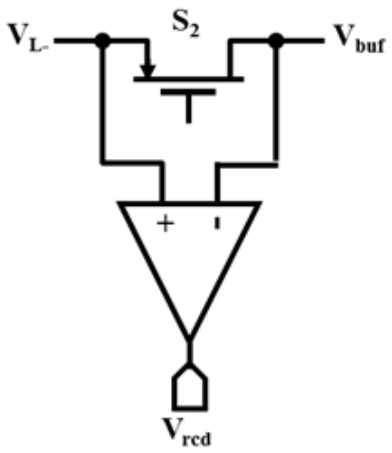

Figure 7.25: Simple active-diode detector used in the SECE interface.

7.3.2.3 Selection of the Inductor's Value

The value of the inductance affects both the "extraction" time as well as the power conversion efficiency. The extraction time is given by:

$$T_n = \frac{\pi}{2}\sqrt{LC_P} \tag{7.15}$$

which is a quarter of the resonating frequency. As it is seen from the previous equation, the lower the inductance value, the shorter the extraction time. However, as the same charge is extracted independently of the value of the extraction time, the peak current increases when reducing T_n. The larger that current, more losses occur in the charge extraction process. This effect is shown in Figure 7.26. Inductor values of 1.0 mH and 300 μH exhibit 1.76 and 3.98 $\%$ of loss with respect to a 10 mH component. The selected inductor for the system prototype is a 10 mH Panasonic ELC18B inductor, with R_{DC} = 3.9 Ω, maximum dc current of 360 mA.

7.3.2.4 Dual-input Switched Capacitor Converter

The implemented PE harvesting system includes a SC converter with two inputs. The converter, which is based on the general structure presented in [232], is shown in Figure 7.27 below. It is composed of two flying capacitors (C_1 and C_2) and eleven switches.

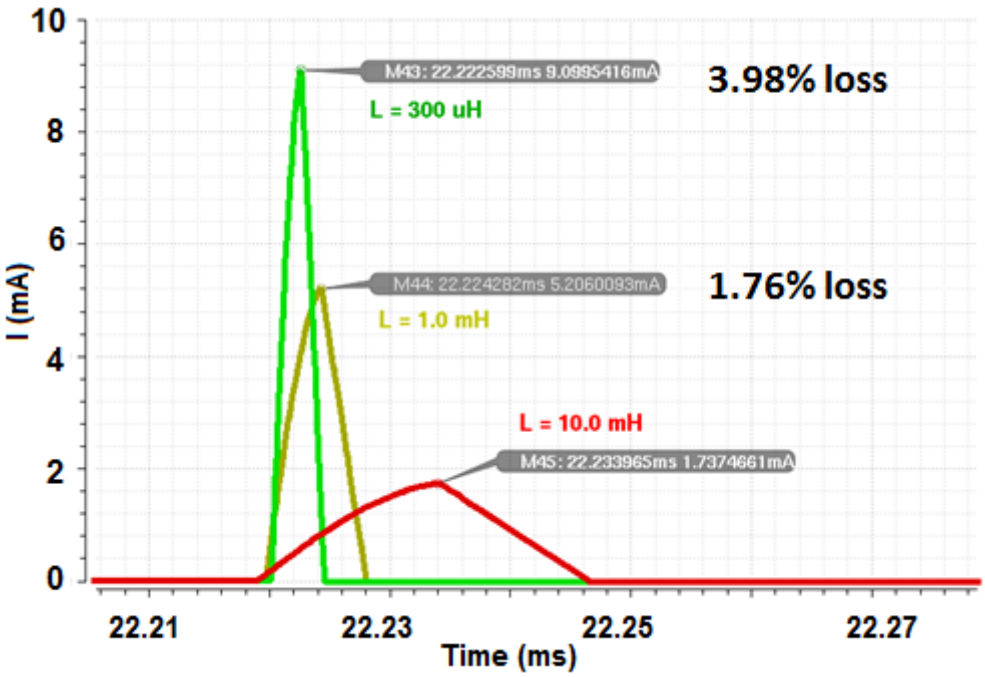

Figure 7.26: Inductor current for different inductance values.

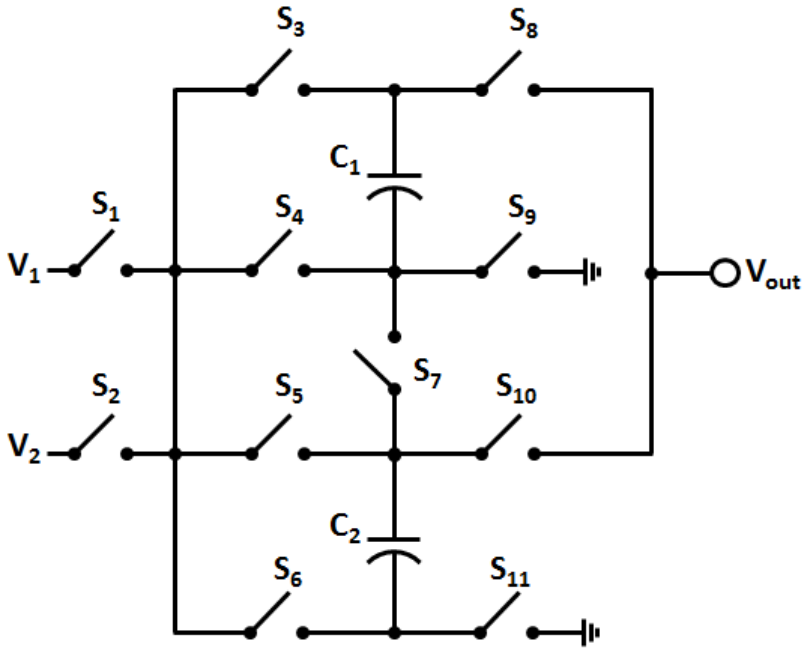

Figure 7.27: Switched capacitor converter implemented in the fabricated prototype.

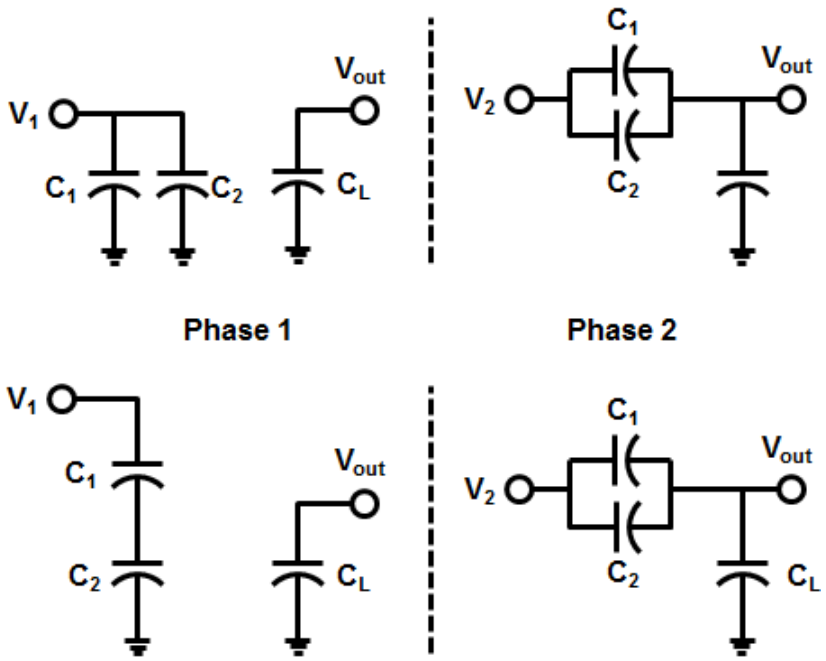

Figure 7.28: Switched capacitor configuration per phases for conversion ratios of V_1+V_2 (top) and $0.5V_1$+V_2 (bottom).

The converter operates by interleaving its inputs, one per phase of the switching clock [232]. That way, it is able to combine both inputs, delivering their added power to the output. Depending on the desired conversion ratio, each switch is activated in a different fashion per phase. Figure 7.28 shows the switch configurations for two possible conversion ratios that were implemented in the control circuit of the converter.

7.4 Results of the Multi-source PE Harvesting System

The multiple input piezoelectric harvesting system was designed and fabricated in a CMOS 130 nm standard process. The microphotograph of the fabricated chip and the test PCB are shown in Figure 7.29. This section presents the simulated and measured results of the prototype design.

7.4.1 Performance of the SC Converter

The switched-capacitor dc-dc converter performance was experimentally characterized. Its efficiency and output voltage was obtained while changing its load and switching frequency. The experimental efficiency and output voltage versus load power are shown in Figures 7.30 and 7.31.

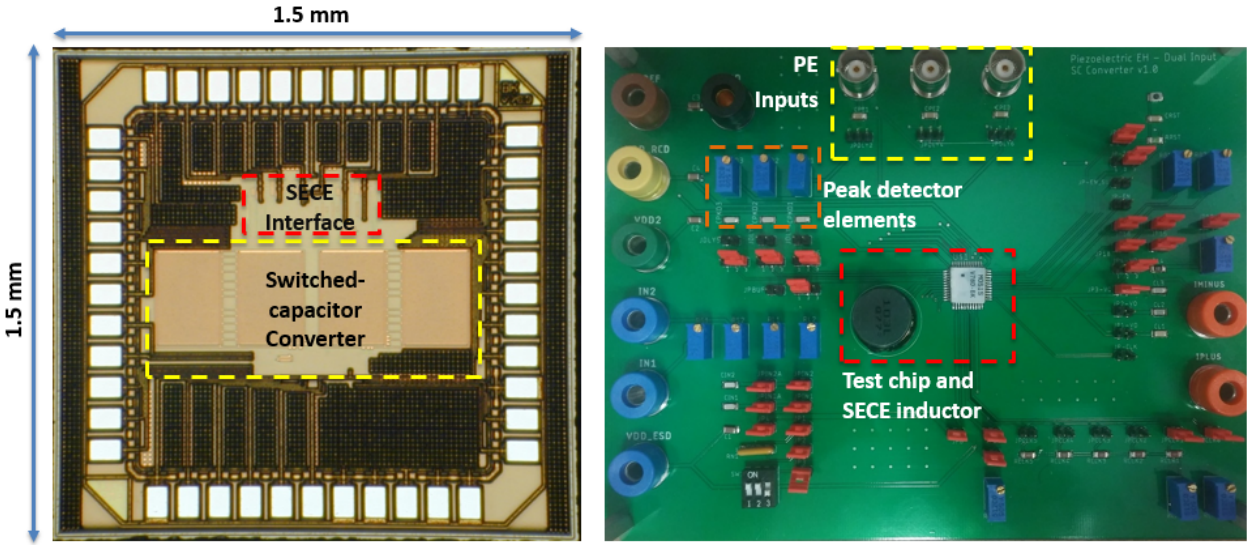

Figure 7.29: Microphotograph of the SECE piezoelectric chip prototype and test PCB.

Each figure presents the performance of a different conversion ratio. From those figures, it can be observed that at higher switching frequencies, the converter is capable of delivering larger output powers with better efficiency. It is also capable of sustaining its output voltage for more demanding current loads. However, at those switching frequencies the performance at low output power is low, because the switching losses are high.

To use this switched-capacitor converter at the output of the PE harvesting system, the experimental results indicate that switching frequencies below 500 kHz are adequate to obtain the higher efficiency possible.

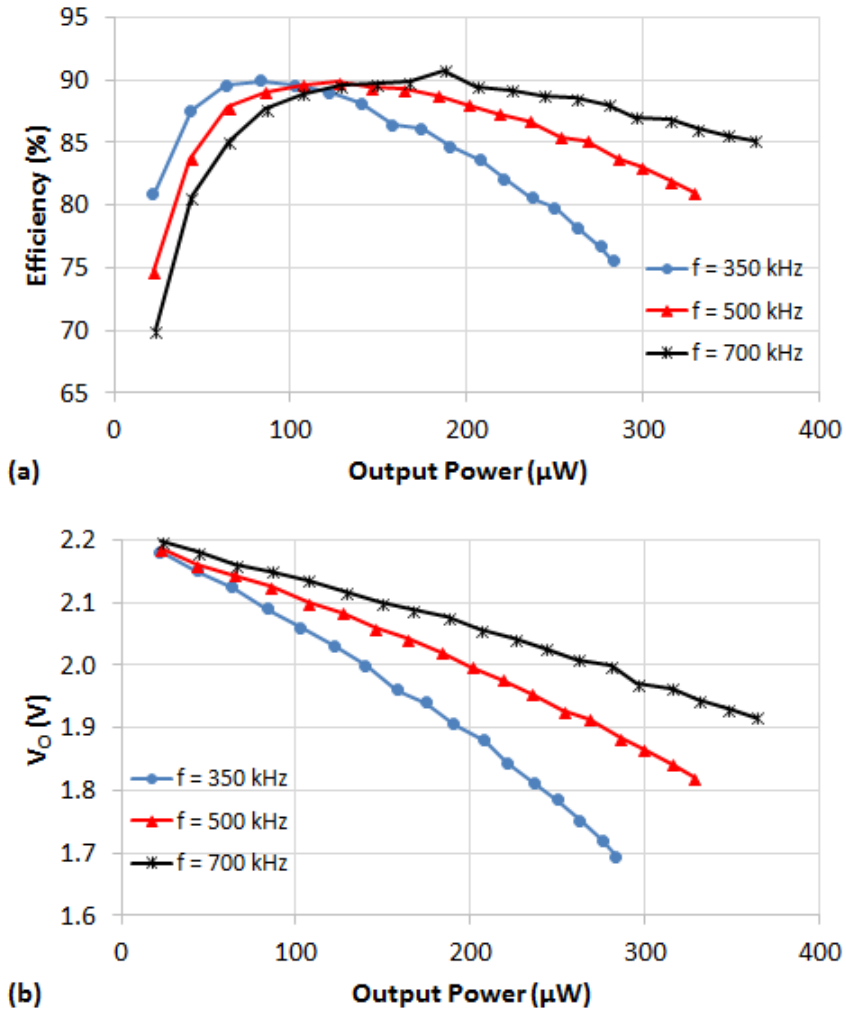

Figure 7.30: (a) Efficiency performance and (b) output voltage for the SC converter with $V_O = V_1 + V_2$

7.4.2 Performance of the PE Harvesting System

The piezoelectric energy harvesting system has been tested in simulation and measurements. The PE harvesters have been modeled in the simulation using the simplified circuit at resonance shown in Figure 7.7. A capacitance C_P = 120 nF is used in the simulation, which is the reported value for the V25W piezoelectric transducer from Mide, vibrating at 130 Hz. A piezoelectric current with peak value of I_P = 49 μA is used, which corresponds to an open-circuit peak voltage of $V_{PO} \approx 500\ m$V (the maximum input voltage admitted by the system is 0.6 V, due to technological

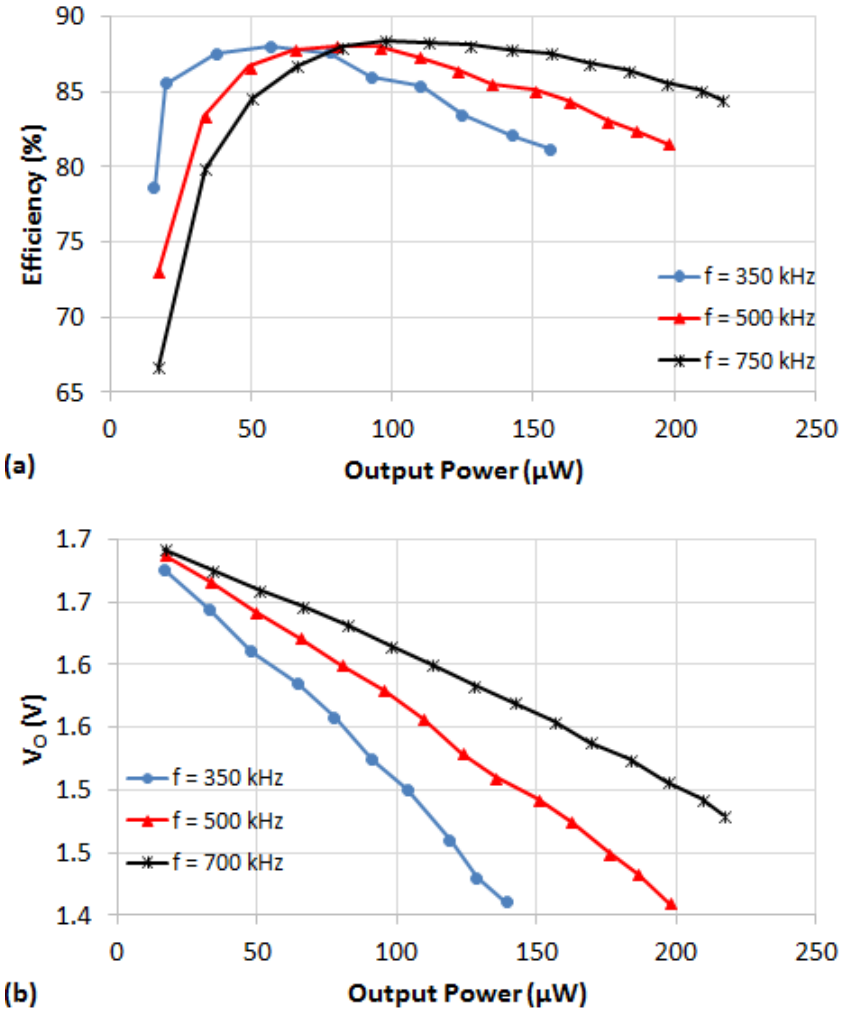

Figure 7.31: (a) Efficiency performance and (b) output voltage for the SC converter with $V_O = 0.5V_1 + V_2$

restrictions). A buffer capacitance of C_{buff} = 500 μF is used in the test setup.

The simulated waveforms of the piezoelectric harvesters is shown in Figure 7.32. In the simulation, it can be seen how the capacitance C_P is quickly discharged when the voltage waveform reaches its peak value, according to SECE operation. In the simulation it can also be observed that, due to the SECE mechanism, the PE voltage in steady-state reaches a peak value of two-times the open circuit voltage (i.e. $\approx$ 1 V).

Figure 7.33 shows the simulated signals for the output of the NVC rectifiers (top) and the Enable signal that indicates the start of a charge extraction cycle. The Enable signal goes down

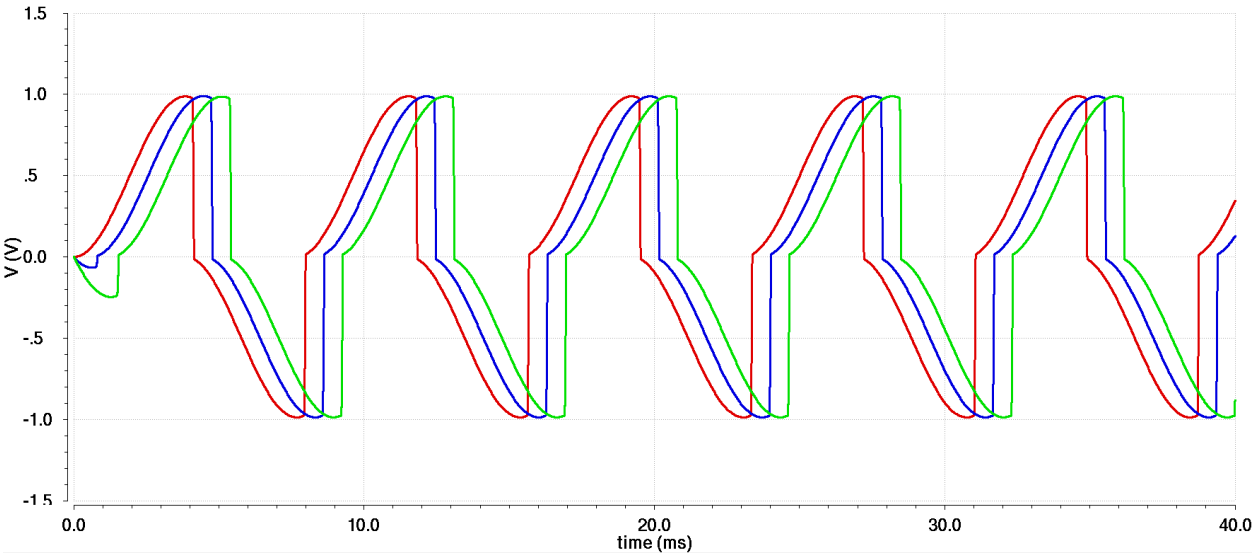

Figure 7.32: Simulated voltage waveforms of PE input voltages in steady-state of the SECE system.

each time the peak voltage of an input is detected. The inductor's current is also shown in Figure 7.33, reaching a peak value of 3.25 mA, together with the voltage at the buffer capacitor, which increases every time a charge extraction process is made. The voltage V_{buff} starts at 1.2 V at t = 0 and increases approximately 2.6 mV in 40 ms.

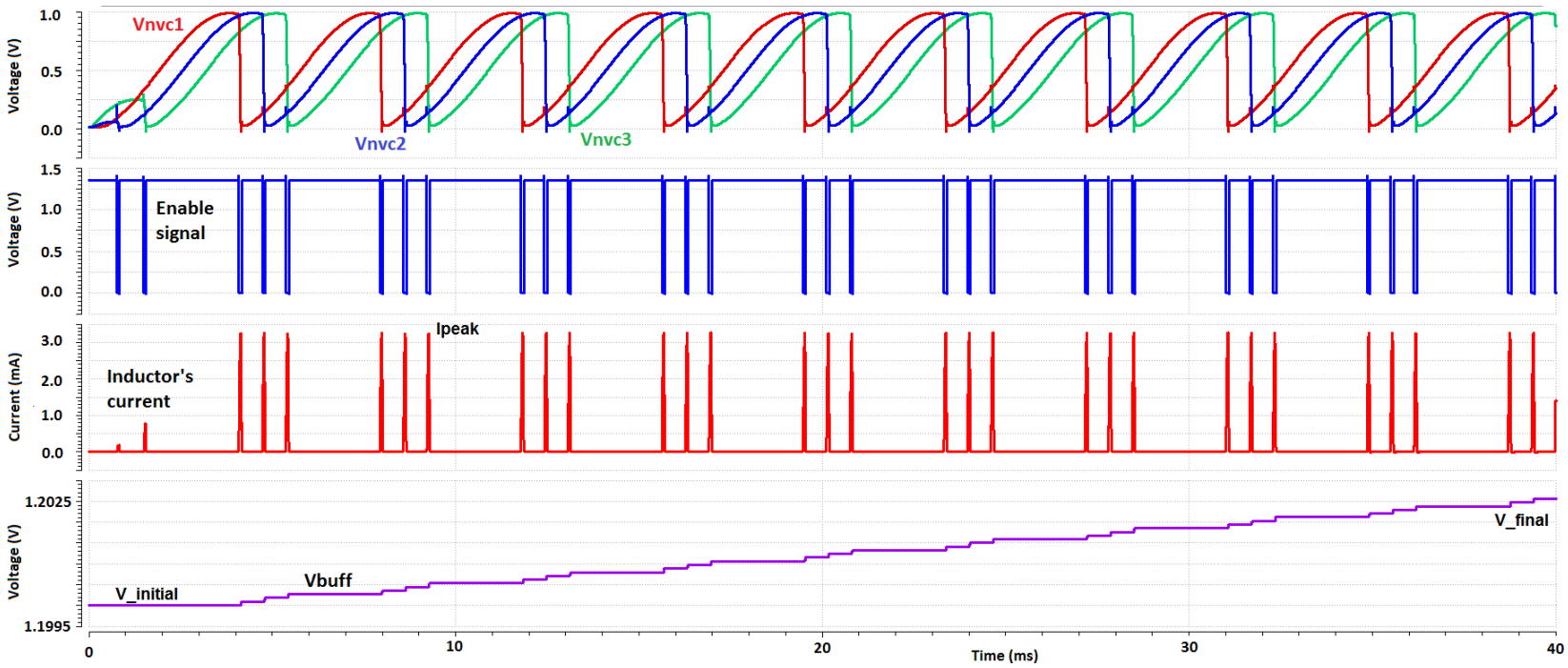

Figure 7.33: Simulation signal waveforms of multisource PE harvesting system with three inputs.

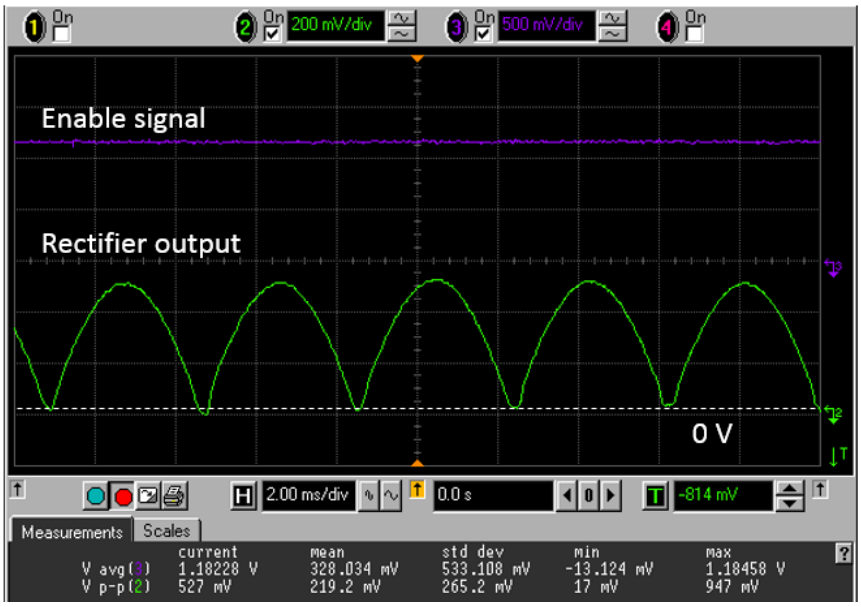

Figure 7.34: Output of NVC enhanced rectifier with sinusoidal input.

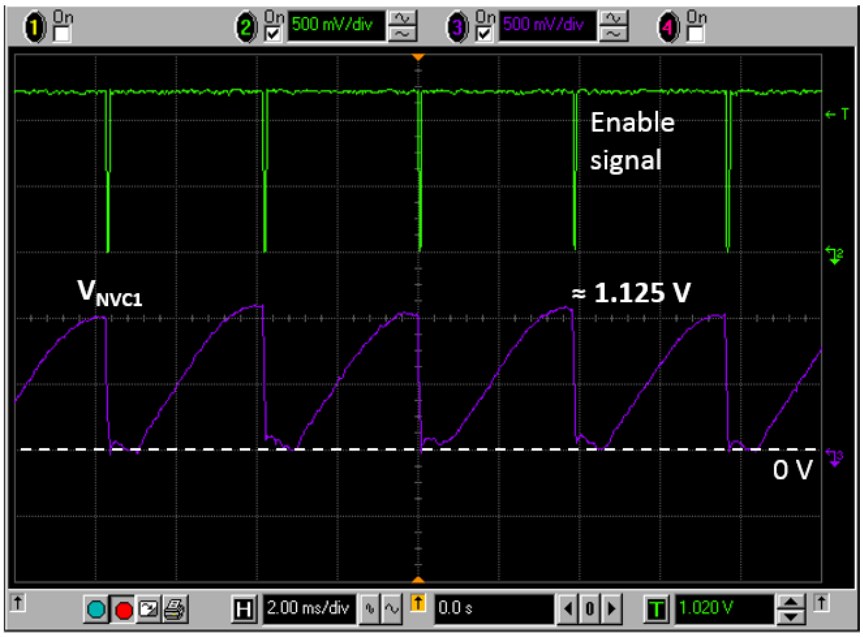

Figure 7.35: SECE rectified PE voltage (one input).

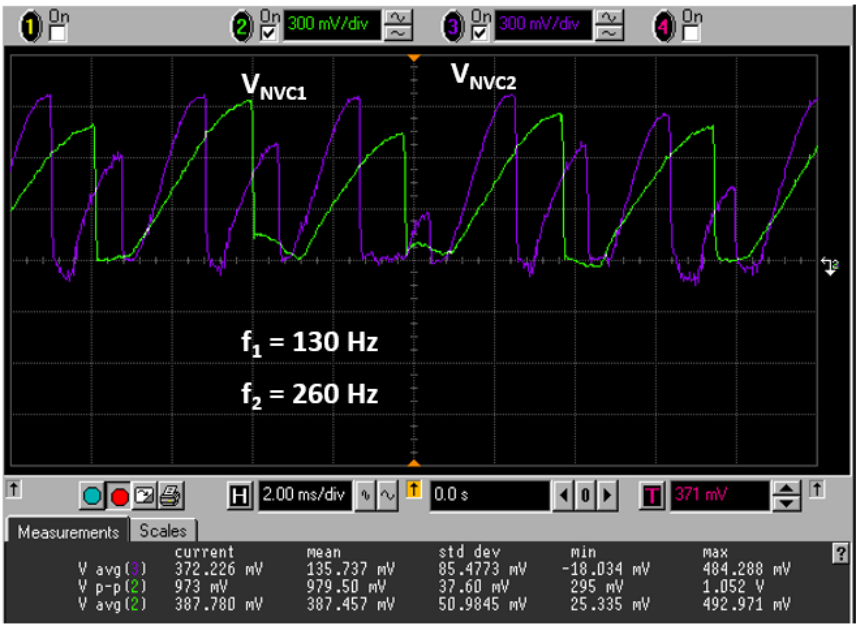

Figure 7.36: SECE rectified PE voltages (two inputs).

Figure 7.34 shows the measured waveforms of the Enable signal and the output of one NVC rectifier with PE input voltage of $\approx$ 520 mV peak with the SECE system disabled. The Enable signal does not change its state and the NVC output has the well-known form of a full-wave rectified sinusoidal voltage. Figure 7.35 shows the same waveforms once the SECE system is enabled. The Enable signal goes down every time a peak is detected in the PE voltage, initiating the charge extraction process. As it can be seen, due to the charge extraction process, the PE voltage reaches now a peak value of approximately the double of the original input. Figure 7.36 presents the operation of the charge extraction of the system with two inputs with different frequency. The first input has a frequency of f_1 = 130 Hz, while f_2 = 260 Hz.

In [231], it is demonstrated that, in the SECE technique, the ideal (zero losses) output power that is extracted from each piezoelectric input is equal to:

$$P = \frac{I_P^2}{\pi^2 f C_P} \tag{7.16}$$

With the PE inputs used in the test setup, that means that for each input there should be an

output power of 15.59 μW, giving a total of 46.78μW. The energy that was transfered to the buffer capacitor in Figure 7.33 is given by:

$$E_{buff} = \frac{1}{2}(C_{buff})(V_{final}^2 - V_{initial}^2) \tag{7.17}$$

The energy can then be calculated for a 400 μF capacitor:

$$E_{buff} = \frac{1}{2}(400 \times 10^{-6})(1.2026^2 - 1.2^2) = 1.53\mu J \tag{7.18}$$

The transfered energy corresponds to an average power of 1.53$\times$ 10^{-6}/40$\times$ 10^{-3} = 38.25 μW over the 40 ms period. The total power consumption of the system is 2.99 μW, less than 1 μW per input. The efficiency of the PE system can be estimated as:

$$\eta = \frac{P_{out}}{P_{in} + P_{consmp}} \tag{7.19}$$

The final efficiency of the system is:

$$\eta = \frac{38.25}{46.78 + 2.99} = 76.9\% \tag{7.20}$$

Table 7.3 below summarizes the performance of the PE harvesting system.

7.5 Conclusions

The current trends on mobile electronic devices and wireless communication for IoT applications are vigorously pushing forward to obtain increased operating life of systems. Energy harvesting has proved as a viable solutions alternative to the use of batteries, but they require efficient interface circuits for maximum power extraction at minimum cost. This chapter of the dissertation has focused on energy harvesting from piezoelectric elements. An interface circuit was presented that harvests power from three vibrating sources. The proposed system collect 38 μW of power from these sources with an efficiency of 76.9$\%$, consuming only 996 nW for each input. Future work should include mechanical testing with real multiple transducers and creating the peripheral

Table 7.3: Comparison of PE harvesting systems.

Parameter	**[227]**	**[94]**	**[219]**	**[220]**	**This Work**
Process	0.35 μ BCD	0.18 μ	Discrete	Discrete	0.13 μm
Extraction Method	MPPT	P-SSHI	SECE	SECE	SECE
Input Voltage	1 - 7 V	-	20 V	34 V	0.6 V
Output Power	33 μW - 10 mW	50 μW	300 μW	300.8 μW	38.25 μW
Inputs	1	1	3	2	3
Maximum Efficiency	80%	86%	74%	83%	76.9%

circuits for self-starting operation. This can be done with auxiliary passive rectifier and practical UVLO circuits as the ones that has been presented in Chapter 2 and Chapter 4. The proposed system therefore, has open opportunities for future improvements and research.

8. SUMMARY AND FUTURE WORK

This dissertation discussed the most important challenges involved in the design of wireless sensors for modern Internet of Things applications. The discussion highlighted in particular the need of extending the operating lifetime of IoT nodes, in order to satisfy the technological trends and the expected market growth for IoT products in a sustainable manner. Among different options, the use of alternative sources of energy (other than batteries) and power management strategies have demonstrated an enormous potential toward the implementation of sensor node systems that operate without batteries. The discussion highlighted the main motivations for the research that is presented in this work. In that direction, this dissertation presented different circuit and system solutions for energy harvesting and Internet of Things applications.

The first part of the dissertation presented a new circuit architecture for a fully-integrated, multiple-input, switched-capacitor based energy harvesting system. This four-input architecture automatically selects the two sources with the largest available power, and simultaneously harvest from them. The selection is done with a proposed efficient analog ranking circuit. The design of a maximum power point tracking architecture is also proposed and demonstrated, that allows the full integration of the open circuit voltage sampling circuit. The proposed system was fabricated in a 0.13 μm CMOS technology. The measured results demonstrate a peak tracking efficiency of 96%. The experimental peak power conversion efficiency was 87.2% at an output power of 198 μW. The maximum measured output power with an efficiency still larger that 70% was 981 μW. A test done with a sensor system also validates the operation of the combiner circuit in an IoT application-like circuit.

The second part of this work was directed toward the implementation of autonomous wireless sensor nodes for precision agriculture applications. First, the design of a low-power wireless sensor node system with energy harvesting was investigated. Experimental results demonstrate that under typical environmental conditions, the sensor node exhibits complete energy autonomy. Sustained only with a 2000 mAh battery the sensor node can continuously operate over 914 days

(2.5 years). A proposed dynamic power management strategy extends the battery another 34 days. This performance guarantees that the sensor node will not require any maintenance for the whole growth cycle of common crops, even without energy harvesting. The sensor node also exhibits an innovative modular design adaptable to the characteristics (i.e. root length) of different crops. The design of a solar thermoelectric generator (STEG) prototype for energy harvesting from the environment was also presented. The STEG demonstrated the capability of generating a temperature gradient of up to 77°C, with a V_{OC} of 150 mV and power generation that is larger than 900 μW.

The research presented in this work can be further extended into different directions. First, building upon the proposed multisource energy combiner system, a solution can be developed that includes output voltage regulation and battery charging capability, achieving an universal fully integrated solution for systems that harvest energy from multiples sources. The application of the energy combiner system into the design of the proposed wireless sensor network is contemplated, where more than one source could be available to feed the sensor node. The most natural selection would be the solar cell and STEG investigated in this dissertation, but other potential sources, such as harvesting energy from the wind force and from plants can also be investigated. These latter options are also suitable sources for a sensor node located at outdoor scenarios, like in precision agriculture or environmental monitoring applications.

REFERENCES

[1] A. D. Rayome, “How the term ‘Internet of Things’ was invented,” *TechRepublic*, July 2018. Available: https://www.techrepublic.com/article/how-the-term-internet-of-things-was-invented/.

[2] S. Dodson, “The internet of things,” *The Guardian*, October 2003. Available: https://www.theguardian.com/technology/2003/oct/09/shopping.newmedia/.

[3] N. Gershenfeld, R. Krikorian, and D. Cohen, “The internet of things,” *Scientific American*, vol. 291, pp. 76–81, October 2004.

[4] L. Atzori, A. Iera, and G. Morabito, “The Internet of Things: A survey,” *Computer Networks*, vol. 54, pp. 2787–2805, October 2010.

[5] J. J. Estrada-López, A. Abuellil, A. Costilla-Reyes, and E. Sánchez-Sinencio, “Technology enabling circuits and systems for the internet-of-things: An overview,” in *2018 IEEE International Symposium on Circuits and Systems (ISCAS)*, pp. 1–5, 2018.

[6] Advantech Co., "3G IoT Wireless Sensor Node with 6-ch DI, 2-ch DO, and 1-port RS-485," WISE-4470-S250 datasheet, September 2018. Available: https://www.advantech.com/.

[7] Monnit Corp., "Monnit Wireless Temperature Sensor - Commercial Coin Cell Powered," MNS-9-W1-TS-ST datasheet, January 2019. Available: https://www.monnit.com/.

[8] Phase IV Engineering Inc., "Phase IV’s Breakthrough Wireless Sensors: Leap Sensors Streamline the Development of Customized Industrial IoT Systems and Smart Products," LEAP sensors white paper, December 2018, Rev. 3.4. Available: https://www.phaseivengr.com.

[9] K. J. Singh and D. S. Kapoor, “Create your own Internet of Things: A survey of IoT platforms,” *IEEE Consumer Electronics Magazine*, vol. 6, pp. 57–68, April 2017.

[10] A. Zanella, N. Bui, A. Castellani, L. Vangelista, and M. Zorzi, "Internet of things for smart cities," *IEEE Internet of Things Journal*, vol. 1, pp. 22–32, February 2014.

[11] S. C. Mukhopadhyay, "Wearable sensors for human activity monitoring: A review," *IEEE Sensors Journal*, vol. 15, pp. 1321–1330, March 2015.

[12] B. P. L. Lo, H. Ip, and G. Yang, "Transforming health care: Body sensor networks, wearables, and the internet of things," *IEEE Pulse*, vol. 7, pp. 4–8, January 2016.

[13] V. C. Gungor, G. P. Hancke, *et al.*, "Industrial wireless sensor networks: Challenges, design principles, and technical approaches," *IEEE Transactions on Industrial Electronics*, vol. 56, pp. 4258–4265, October 2009.

[14] A. Al-Fuqaha, M. Guizani, M. Mohammadi, M. Aledhari, and M. Ayyash, "Internet of Things: A survey on enabling technologies, protocols, and applications," *IEEE Communications Surveys Tutorials*, vol. 17, pp. 2347–2376, Fourthquarter 2015.

[15] J. Lin, W. Yu, N. Zhang, X. Yang, H. Zhang, and W. Zhao, "A survey on Internet of Things: Architecture, enabling technologies, security and privacy, and applications," *IEEE Internet of Things Journal*, vol. 4, pp. 1125–1142, October 2017.

[16] P. Sethi and S. R. Sarangi, "Internet of Things: architectures, protocols, and applications," *Journal of Electrical and Computer Engineering*, vol. 2017. Article ID 9324035, 25 pages, 2017. https://doi.org/10.1155/2017/9324035.

[17] L. Columbus, "2017 roundup of Internet of Things forecasts," *Forbes*, December 2017. Available: https://bit.ly/2TVvHzx.

[18] J. A. Stankovic, "Research directions for the Internet of Things," *IEEE Internet of Things Journal*, vol. 1, pp. 3–9, February 2014.

[19] M. Weyrich and C. Ebert, "Reference architectures for the Internet of Things," *IEEE Software*, vol. 33, no. 1, pp. 112–116, 2016.

[20] B. Calhoun and D. Wentzloff, "Ultra-low power wireless SoCs enabling a batteryless IoT," in *2015 IEEE Hot Chips 27 Symposium (HCS)*, pp. 1–45, August 2015.

[21] R. J. M. Vullers, R. V. Schaijk, H. J. Visser, J. Penders, and C. V. Hoof, "Energy harvesting for autonomous wireless sensor networks," *IEEE Solid-State Circuits Magazine*, vol. 2, pp. 29–38, Spring 2010.

[22] F. Yahya, C. Lukas, and B. Calhoun, "A top-down approach to building battery-less self-powered systems for the Internet-of-Things," *Journal of Low Power Electronics and Applications*, vol. 8, no. 2, p. 21, 2018.

[23] B. Haug, "Wireless sensor nodes can be powered by temperature gradients; no batteries needed: Harvesting energy from thermoelectric generators," *IEEE Power Electronics Magazine*, vol. 4, pp. 24–32, December 2017.

[24] G. Yang, B. H. Stark, S. J. Hollis, and S. G. Burrow, "Challenges for energy harvesting systems under intermittent excitation," *IEEE Journal on Emerging and Selected Topics in Circuits and Systems*, vol. 4, no. 3, pp. 364–374, 2014.

[25] R. G. Cid-Fuentes, A. Cabellos-Aparicio, and E. Alarcón, "Area model and dimensioning guidelines of multisource energy harvesting for nano–micro interface," *IEEE Internet of Things Journal*, vol. 3, no. 1, pp. 18–26, 2016.

[26] C. Ding, N. Liu, Y. Wang, J. Li, S. Heidari, J. Hu, and Y. Liu, "Multisource indoor energy harvesting for nonvolatile processors," *IEEE Design & Test*, vol. 34, no. 3, pp. 42–49, 2017.

[27] O. B. Akan, O. Cetinkaya, C. Koca, and M. Ozger, "Internet of hybrid energy harvesting things," *IEEE Internet of Things Journal*, vol. 5, no. 2, pp. 736–746, 2018.

[28] H. Yetgin, K. T. K. Cheung, M. El-Hajjar, and L. H. Hanzo, "A survey of network lifetime maximization techniques in wireless sensor networks," *IEEE Communications Surveys & Tutorials*, vol. 19, no. 2, pp. 828–854, 2017.

[29] D. Metcalf, S. T. Milliard, M. Gomez, and M. Schwartz, "Wearables and the internet of things for health: wearable, interconnected devices promise more efficient and comprehensive health care," *IEEE Pulse*, vol. 7, no. 5, pp. 35–39, 2016.

[30] H. Baali, H. Djelouat, A. Amira, and F. Bensaali, "Empowering technology enabled care using IoT and smart devices: A review," *IEEE Sensors Journal*, vol. 18, no. 5, pp. 1790–1809, 2018.

[31] T. Ojha, S. Misra, and N. S. Raghuwanshi, "Wireless sensor networks for agriculture: The state-of-the-art in practice and future challenges," *Computers and Electronics in Agriculture*, vol. 118, pp. 66–84, October 2015.

[32] M. Ayaz, M. Ammad-uddin, I. Baig, *et al.*, "Wireless sensor's civil applications, prototypes, and future integration possibilities: A review," *IEEE Sensors Journal*, vol. 18, no. 1, pp. 4–30, 2017.

[33] M. Raza, N. Aslam, H. Le-Minh, S. Hussain, Y. Cao, and N. M. Khan, "A critical analysis of research potential, challenges, and future directives in industrial wireless sensor networks," *IEEE Communications Surveys & Tutorials*, vol. 20, no. 1, pp. 39–95, 2017.

[34] A. B. Noel, A. Abdaoui, T. Elfouly, M. H. Ahmed, A. Badawy, and M. S. Shehata, "Structural health monitoring using wireless sensor networks: A comprehensive survey," *IEEE Communications Surveys Tutorials*, vol. 19, pp. 1403–1423, Thirdquarter 2017.

[35] J. F. Rohan, M. Hasan, S. Patil, D. P. Casey, and T. M. Clancy, "Energy storage: battery materials and architectures at the nanoscale," in *ICT-Energy-Nanoscale energy management concepts towards Zero-Power Information and Communication Technology*, Intech, 2014.

[36] A. Valenzuela, "Energy harvesting for no-power embedded systems," October 2008. ed: Texas Instruments. Available: http://www.ti.com/.

[37] C. Alippi, G. Anastasi, M. Di Francesco, and M. Roveri, "Energy management in wireless sensor networks with energy-hungry sensors," *IEEE Instrumentation & Measurement Magazine*, vol. 12, no. 2, 2009.

[38] T. Rault, A. Bouabdallah, and Y. Challal, "Energy efficiency in wireless sensor networks: A top-down survey," *Computer Networks*, vol. 67, pp. 104–122, July 2014.

[39] A. A. Babayo, M. H. Anisi, and I. Ali, "A review on energy management schemes in energy harvesting wireless sensor networks," *Renewable and Sustainable Energy Reviews*, vol. 76, pp. 1176–1184, September 2017.

[40] F. Engmann, F. A. Katsriku, J.-D. Abdulai, K. S. Adu-Manu, and F. K. Banaseka, "Prolonging the lifetime of wireless sensor networks: A review of current techniques," *Wireless Communications and Mobile Computing*, vol. 2018. Article ID 8035065, 23 pages, 2018. https://doi.org/10.1155/2018/8035065.

[41] L. Xie, Y. Shi, Y. T. Hou, and A. Lou, "Wireless power transfer and applications to sensor networks," *IEEE Wireless Communications*, vol. 20, no. 4, pp. 140–145, 2013.

[42] F. Engmann, J.-D. Abdulai, and J. Q. Azasoo, "Enhancing the reliability of WSN through wireless energy transfer," in *International Conference on Computational Science and Its Applications*, pp. 610–618, Springer, 2016.

[43] C. Wang, J. Li, Y. Yang, and F. Ye, "Combining solar energy harvesting with wireless charging for hybrid wireless sensor networks," *IEEE Transactions on Mobile Computing*, vol. 17, pp. 560–576, March 2018.

[44] K. Noh, J. Amanor-Boadu, M. Zhang, and E. Sánchez-Sinencio, "A 13.56-MHz CMOS active rectifier with a voltage mode switched-offset comparator for implantable medical devices," *IEEE Transactions on Very Large Scale Integration (VLSI) Systems*, vol. 26, pp. 2050–2060, October 2018.

[45] K. Huang and E. Larsson, "Simultaneous information and power transfer for broadband wireless systems," *IEEE Transactions on Signal Processing*, vol. 61, no. 23, pp. 5972–5986, 2013.

[46] D. Mishra, S. De, S. Jana, S. Basagni, K. Chowdhury, and W. Heinzelman, "Smart RF energy harvesting communications: Challenges and opportunities," *IEEE Communications Magazine*, vol. 53, no. 4, pp. 70–78, 2015.

[47] S. Bi, C. K. Ho, and R. Zhang, "Wireless powered communication: Opportunities and challenges," *IEEE Communications Magazine*, vol. 53, no. 4, pp. 117–125, 2015.

[48] Q. Zhang, W. Fang, Q. Liu, J. Wu, P. Xia, and L. Yang, "Distributed laser charging: A wireless power transfer approach," *IEEE Internet of Things Journal*, vol. 5, no. 5, pp. 3853–3864, 2018.

[49] T. Jang, G. Kim, B. Kempke, M. B. Henry, N. Chiotellis, C. Pfeiffer, D. Kim, Y. Kim, Z. Foo, H. Kim, *et al.*, "Circuit and system designs of ultra-low power sensor nodes with illustration in a miniaturized GNSS logger for position tracking: Part I - analog circuit techniques," *IEEE Transactions on Circuits and Systems I: Regular Papers*, vol. 64, no. 9, pp. 2237–2249, 2017.

[50] P. Harpe, H. Gao, R. v. Dommele, E. Cantatore, and A. H. M. van Roermund, "A 0.20mm^2 3 nW signal acquisition IC for miniature sensor nodes in 65 nm CMOS," *IEEE Journal of Solid-State Circuits*, vol. 51, pp. 240–248, January 2016.

[51] T. Jang, G. Kim, B. Kempke, M. B. Henry, N. Chiotellis, C. Pfeiffer, D. Kim, Y. Kim, Z. Foo, H. Kim, *et al.*, "Circuit and system designs of ultra-low power sensor nodes with illustration in a miniaturized GNSS logger for position tracking: Part II data communication, energy harvesting, power management, and digital circuits," *IEEE Transactions on Circuits and Systems I: Regular Papers*, vol. 64, no. 9, pp. 2250–2262, 2017.

[52] A. Burdett, "Ultra-low-power wireless systems: Energy-efficient radios for the Internet of Things," *IEEE Solid-State Circuits Magazine*, vol. 7, no. 2, pp. 18–28, 2015.

[53] O. Elsayed, J. Zarate-Roldan, A. Abuellil, F. A. Hussien, A. Eladawy, and E. Sánchez-Sinencio, "Highly linear low-power wireless RF receiver for WSN," *IEEE Transac-*

tions on Very Large Scale Integration (VLSI) Systems, pp. 1–10, January 2019. doi: 10.1109/TVLSI.2018.2890093.

[54] N. E. Roberts and D. D. Wentzloff, "A 98nW wake-up radio for wireless body area networks," in *Radio Frequency Integrated Circuits Symposium (RFIC), 2012 IEEE*, pp. 373–376, IEEE, 2012.

[55] R. Piyare, A. L. Murphy, C. Kiraly, P. Tosato, and D. Brunelli, "Ultra low power wake-up radios: A hardware and networking survey," *IEEE Communications Surveys & Tutorials*, vol. 19, no. 4, pp. 2117–2157, 2017.

[56] D. Giovanelli, B. Milosevic, D. Brunelli, and E. Farella, "Enhancing Bluetooth low energy with wake-up radios for IoT applications," in *2017 13th International Wireless Communications and Mobile Computing Conference (IWCMC)*, pp. 1622–1627, IEEE, 2017.

[57] J. Zarate-Roldan, A. Abuellil, M. Mansour, O. Elsayed, F. A. Hussien, A. Eladawy, and E. Sánchez-Sinencio, "0.2-nJ/b fast start-up ultralow power wireless transmitter for IoT applications," *IEEE Transactions on Microwave Theory and Techniques*, vol. 66, pp. 259–272, January 2018.

[58] R. C. Carrano, D. G. Passos, L. C. S. Magalhães, and N. Célio Vinicius, "Survey and taxonomy of duty cycling mechanisms in wireless sensor networks.," *IEEE Communications Surveys and Tutorials*, vol. 16, no. 1, pp. 181–194, 2014.

[59] G. Dai, J. Qiu, P. Liu, B. Lin, and S. Zhang, "Remaining energy-level-based transmission power control for energy-harvesting wsns," *International Journal of Distributed Sensor Networks*, vol. 8, no. 5, p. 934240, 2012.

[60] X. Ju, W. Liu, C. Zhang, A. Liu, T. Wang, N. Xiong, and Z. Cai, "An energy conserving and transmission radius adaptive scheme to optimize performance of energy harvesting sensor networks," *Sensors*, vol. 18, no. 9, p. 2885, 2018.

[61] D. Purkovic, M. Hönsch, and T. R. M. K. Meyer, "An energy efficient communication protocol for low power, energy harvesting sensor modules," *IEEE Sensors Journal*, vol. 19, no. 2, pp. 701–714, 2019.

[62] C. Alippi, G. Anastasi, M. Di Francesco, and M. Roveri, "An adaptive sampling algorithm for effective energy management in wireless sensor networks with energy-hungry sensors," *IEEE Transactions on Instrumentation and Measurement*, vol. 59, no. 2, pp. 335–344, 2010.

[63] C. Lu, V. Raghunathan, and K. Roy, "Efficient design of micro-scale energy harvesting systems," *IEEE Journal on Emerging and Selected Topics in Circuits and Systems*, vol. 1, no. 3, pp. 254–266, 2011.

[64] O. Elsayed, M. Abouzied, V. Vaidya, K. Ravichandran, and E. Sánchez-Sinencio, "An ultralow-power RF wireless receiver with Rf blocker energy recycling for IoT applications," *IEEE Transactions on Microwave Theory and Techniques*, vol. 66, pp. 4927–4942, November 2018.

[65] K. S. Adu-Manu, N. Adam, C. Tapparello, H. Ayatollahi, and W. Heinzelman, "Energy-harvesting wireless sensor networks (EH-WSNs): A review," *ACM Transactions on Sensor Networks (TOSN)*, vol. 14, no. 2, p. 10, 2018.

[66] M. Prauzek, J. Konecny, M. Borova, K. Janosova, J. Hlavica, and P. Musilek, "Energy harvesting sources, storage devices and system topologies for environmental wireless sensor networks: A review," *Sensors*, vol. 18, no. 8, p. 2446, 2018.

[67] A. Omairi, Z. H. Ismail, K. A. Danapalasingam, and M. Ibrahim, "Power harvesting in wireless sensor networks and its adaptation with maximum power point tracking: current technology and future directions," *IEEE Internet of Things Journal*, vol. 4, no. 6, pp. 2104–2115, 2017.

[68] S. M. Demir, F. Al-Turjman, and A. Muhtaroğlu, "Energy scavenging methods for WBAN applications: a review," *IEEE Sensors Journal*, vol. 18, no. 16, pp. 6477–6488, 2018.

[69] F. K. Shaikh and S. Zeadally, "Energy harvesting in wireless sensor networks: A comprehensive review," *Renewable and Sustainable Energy Reviews*, vol. 55, pp. 1041–1054, March 2016.

[70] S. Seneviratne, Y. Hu, T. Nguyen, G. Lan, S. Khalifa, K. Thilakarathna, M. Hassan, and A. Seneviratne, "A survey of wearable devices and challenges," *IEEE Communications Surveys Tutorials*, vol. 19, pp. 2573–2620, Fourthquarter 2017.

[71] Y. Zhang, F. Zhang, Y. Shakhsheer, J. D. Silver, A. Klinefelter, M. Nagaraju, J. Boley, J. Pandey, A. Shrivastava, E. J. Carlson, A. Wood, B. H. Calhoun, and B. P. Otis, "A battery-less 19μW MICS/ISM-band energy harvesting body sensor node SoC for ExG applications," *IEEE Journal of Solid-State Circuits*, vol. 48, pp. 199–213, January 2013.

[72] A. Roy, A. Klinefelter, F. B. Yahya, X. Chen, L. P. Gonzalez-Guerrero, C. J. Lukas, D. A. Kamakshi, J. Boley, K. Craig, M. Faisal, S. Oh, N. E. Roberts, Y. Shakhsheer, A. Shrivastava, D. P. Vasudevan, D. D. Wentzloff, and B. H. Calhoun, "A 6.45μW self-powered SoC with integrated energy-harvesting power management and ULP asymmetric radios for portable biomedical systems," *IEEE Transactions on Biomedical Circuits and Systems*, vol. 9, pp. 862–874, December 2015.

[73] Y. Pu, C. Shi, G. Samson, D. Park, K. Easton, R. Beraha, A. Newham, M. Lin, V. Rangan, K. Chatha, D. Butterfield, and R. Attar, "A 9-mm2 ultra-low-power highly integrated 28-nm CMOS SoC for Internet of Things," *IEEE Journal of Solid-State Circuits*, vol. 53, pp. 936–948, March 2018.

[74] PsiKick Inc., "Overcoming the Battery Obstacle to Ubiquitous Sensing - Finally," PsiKick white paper, 2018. Available: https://www.psikick.com/.

[75] X. Yue, M. Kauer, M. Bellanger, O. Beard, M. Brownlow, D. Gibson, C. Clark, C. MacGregor, and S. Song, "Development of an indoor photovoltaic energy harvesting module for autonomous sensors in building air quality applications," *IEEE Internet Things Journal*, vol. 4, no. 6, pp. 2092–2103, 2017.

[76] L. Lombardo, S. Corbellini, M. Parvis, A. Elsayed, E. Angelini, and S. Grassini, “Wireless sensor network for distributed environmental monitoring,” *IEEE Transactions on Instrumentation and Measurement*, vol. 67, no. 5, pp. 1214–1222, 2018.

[77] Texas Instruments, "Humidity and Temperature Sensor Node for Sub-1GHz Star Networks Enabling 10+ Year Coin Cell Battery Life," TIDA-00484 datasheet, September 2018. Available: http://www.ti.com/.

[78] Texas Instruments, "Industrial wireless condition monitoring reference design," TIDA-010012 datasheet, December 2018. Available: http://www.ti.com/.

[79] A. Romani, M. Tartagni, and E. Sangiorgi, “Doing a lot with a little: Micropower conversion and management for ambient-powered electronics,” *IEEE Computer*, vol. 50, no. 6, pp. 41–49, 2017.

[80] D. Masotti, A. Costanzo, P. Francia, M. Filippi, and A. Romani, “A load-modulated rectifier for RF micropower harvesting with start-up strategies,” *IEEE Transactions on Microwave Theory and Techniques*, vol. 62, pp. 994–1004, April 2014.

[81] D. Rozgić and D. Marković, “A miniaturized 0.78-mW/cm2 autonomous thermoelectric energy-harvesting platform for biomedical sensors,” *IEEE Transactions on Biomedical Circuits and Systems*, vol. 11, pp. 773–783, August 2017.

[82] J. Kim, J. Kim, and C. Kim, “A regulated charge pump with a low-power integrated optimum power point tracking algorithm for indoor solar energy harvesting,” *IEEE Transactions on Circuits and Systems II: Express Briefs*, vol. 58, pp. 802–806, December 2011.

[83] X. Liu and E. Sánchez-Sinencio, “An 86% efficiency 12 μW self-sustaining PV energy harvesting system with hysteresis regulation and time-domain MPPT for IOT smart nodes,” *IEEE Journal of Solid-State Circuits*, vol. 50, pp. 1424–1437, June 2015.

[84] X. Liu and E. Sánchez-Sinencio, “A highly efficient ultralow photovoltaic power harvesting system with MPPT for internet of things smart nodes,” *IEEE Transactions on Very Large Scale Integration (VLSI) Systems*, vol. 23, pp. 3065–3075, December 2015.

[85] X. Liu, L. Huang, K. Ravichandran, and E. Sánchez-Sinencio, "A highly efficient reconfigurable charge pump energy harvester with wide harvesting range and two-dimensional MPPT for internet of things," *IEEE Journal of Solid-State Circuits*, vol. 51, pp. 1302–1312, May 2016.

[86] S. Mondal and R. Paily, "On-chip photovoltaic power harvesting system with low-overhead adaptive MPPT for IoT nodes," *IEEE Internet of Things Journal*, vol. 4, pp. 1624–1633, October 2017.

[87] J. Li, J.-s. Seo, I. Kymissis, and M. Seok, "Triple-mode, hybrid-storage, energy harvesting power management unit: Achieving high efficiency against harvesting and load power variabilities," *IEEE Journal of Solid-State Circuits*, vol. 52, no. 10, pp. 2550–2562, 2017.

[88] H. Yi, J. Yin, P.-I. Mak, and R. P. Martins, "A 0.032-mm2 0.15-V three-stage charge-pump scheme using a differential bootstrapped ring-VCO for energy-harvesting applications," *IEEE Transactions on Circuits and Systems II: Express Briefs*, vol. 65, no. 2, pp. 146–150, 2018.

[89] S. Yoon, S. Carreon-Bautista, and E. Sánchez-Sinencio, "An area efficient thermal energy harvester with reconfigurable capacitor charge pump for IoT applications," *IEEE Transactions on Circuits and Systems II: Express Briefs*, vol. 65, pp. 1974–1978, December 2018.

[90] E. J. Carlson, K. Strunz, and B. P. Otis, "A 20 mV input boost converter with efficient digital control for thermoelectric energy harvesting," *IEEE Journal of Solid-State Circuits*, vol. 45, pp. 741–750, April 2010.

[91] Y. K. Ramadass and A. P. Chandrakasan, "An efficient piezoelectric energy harvesting interface circuit using a bias-flip rectifier and shared inductor," *IEEE Journal of Solid-State Circuits*, vol. 45, no. 1, pp. 189–204, 2010.

[92] P. Weng, H. Tang, P. Ku, and L. Lu, "50 mV-input batteryless boost converter for thermal energy harvesting," *IEEE Journal of Solid-State Circuits*, vol. 48, pp. 1031–1041, April 2013.

[93] S. Carreon-Bautista, A. Eladawy, A. N. Mohieldin, and E. Sánchez-Sinencio, "Boost converter with dynamic input impedance matching for energy harvesting with multi-array thermoelectric generators," *IEEE Transactions on Industrial Electronics*, vol. 61, no. 10, pp. 5345–5353, 2014.

[94] E. E. Aktakka and K. Najafi, "A micro inertial energy harvesting platform with self-supplied power management circuit for autonomous wireless sensor nodes," *IEEE Journal of Solid-State Circuits*, vol. 49, pp. 2017–2029, September 2014.

[95] G. Chowdary and S. Chatterjee, "A 300-nW sensitive, 50-nA DC-DC converter for energy harvesting applications," *IEEE Transactions on Circuits and Systems I: Regular Papers*, vol. 62, no. 11, pp. 2674–2684, 2015.

[96] S. Du, Y. Jia, C. D. Do, and A. A. Seshia, "An efficient SSHI interface with increased input range for piezoelectric energy harvesting under variable conditions," *IEEE Journal of Solid-State Circuits*, vol. 51, no. 11, pp. 2729–2742, 2016.

[97] L. Wu, X. Do, S. Lee, and D. S. Ha, "A self-powered and optimal SSHI circuit integrated with an active rectifier for piezoelectric energy harvesting," *IEEE Transactions on Circuits and Systems I: Regular Papers*, vol. 64, pp. 537–549, March 2017.

[98] M. Chen, H. Yu, G. Wang, and Y. Lian, "A batteryless single-inductor boost converter with 190 mv self-startup voltage for thermal energy harvesting over a wide temperature range," *IEEE Transactions on Circuits and Systems II: Express Briefs*, 2018. doi: 10.1109/TCSII.2018.2869328.

[99] G. Saini and M. S. Baghini, "A generic power management circuit for energy harvesters with shared components between the MPPT and regulator," *IEEE Transactions on Very Large Scale Integration (VLSI) Systems*, vol. 27, pp. 535–548, March 2019.

[100] N. Khosro Pour, F. Krummenacher, and M. Kayal, "Fully integrated solar energy harvester and sensor interface circuits for energy-efficient wireless sensing applications," *Journal of Low Power Electronics and Applications*, vol. 3, pp. 9–26, February 2013.

[101] A. Richelli, S. Comensoli, and Z. M. Kovacs-Vajna, “A dc/dc boosting technique and power management for ultralow-voltage energy harvesting applications,” *IEEE Transactions on Industrial Electronics*, vol. 59, pp. 2701–2708, June 2012.

[102] T. Oh, S. K. Islam, M. Mahfouz, and G. To, “A low-power CMOS piezoelectric transducer based energy harvesting circuit for wearable sensors for medical applications,” *Journal of Low Power Electronics and Applications*, vol. 7, p. 33, December 2017.

[103] A. Bertacchini, L. Larcher, M. Maini, L. Vincetti, and S. Scorcioni, “Reconfigurable RF energy harvester with customized differential PCB antenna,” *Journal of Low Power Electronics and Applications*, vol. 5, pp. 257–273, November 2015.

[104] J. Estrada-López, A. Abuellil, Z. Zeng, and E. Sánchez-Sinencio, “Multiple input energy harvesting systems for autonomous iot end-nodes,” *Journal of Low Power Electronics and Applications*, vol. 8, p. 6, March 2018.

[105] Analog Devices, "Ultra-Low Voltage Energy Harvester and Primary Battery Life Extender," LTC3107 datasheet, 2013. Available: https://www.analog.com/.

[106] Analog Devices, "Nanopower Buck-Boost DC/DC with Energy Harvesting Battery Charger," LTC3331 datasheet, 2014. Available: https://www.analog.com/.

[107] Texas Instruments, "Ultra Low-Power Boost Charger With Battery Management and Autonomous Power Multiplexer for Primary Battery in Energy Harvester Applications," BQ25505 datasheet, August 2013. Available: http://www.ti.com/.

[108] Texas Instruments, "Nano power boost charger and buck converter for energy harvester powered applications," BQ25570 datasheet, March 2013. Available: http://www.ti.com/.

[109] , 2018. Cypress Semiconductor, "Energy Harvesting PMIC for Wireless Sensor Node," S6AE101A datasheet, October 2018. Available: https://www.cypress.com/.

[110] S. Carreon-Bautista, L. Huang, and E. Sánchez-Sinencio, “An autonomous energy harvesting power management unit with digital regulation for IoT applications,” *IEEE Journal of Solid-State Circuits*, vol. 51, no. 6, pp. 1457–1474, 2016.

[111] C. Vankecke, L. Assouère, A. Wang, P. Durand-Estèbe, F. Caignet, J. Dilhac, and M. Bafleur, "Multisource and battery-free energy harvesting architecture for aeronautics applications," *IEEE Transactions on Power Electronics*, vol. 30, pp. 3215–3227, June 2015.

[112] M. R. Elhebeary, M. A. Ibrahim, M. M. Aboudina, and A. N. Mohieldin, "Dual-source self-start high-efficiency microscale smart energy harvesting system for IoT," *IEEE Transactions on Industrial Electronics*, vol. 65, no. 1, pp. 342–351, 2018.

[113] Y. K. Tan and S. K. Panda, "Energy harvesting from hybrid indoor ambient light and thermal energy sources for enhanced performance of wireless sensor nodes," *IEEE Transactions on Industrial Electronics*, vol. 58, pp. 4424–4435, September 2011.

[114] D. Carli, D. Brunelli, L. Benini, and M. Ruggeri, "An effective multi-source energy harvester for low power applications," in *Design, Automation & Test in Europe Conference & Exhibition (DATE), 2011*, pp. 1–6, IEEE, 2011.

[115] H. Li, G. Zhang, R. Ma, and Z. You, "Design and experimental evaluation on an advanced multisource energy harvesting system for wireless sensor nodes," *The Scientific World Journal*, vol. 2014. Article ID 671280, 13 pages, 2014. https://doi.org/10.1155/2014/671280.

[116] F. Deng, X. Yue, X. Fan, S. Guan, Y. Xu, and J. Chen, "Multisource energy harvesting system for a wireless sensor network node in the field environment," *IEEE Internet of Things Journal*, vol. 6, pp. 918–927, February 2019.

[117] Cypress Semiconductor, "Ultra Low Power Buck PMIC Solar/Vibrations Energy Harvesting," CY39C811 datasheet, October 2018. Available: https://www.cypress.com/.

[118] H. Lhermet, C. Condemine, M. Plissonnier, R. Salot, P. Audebert, and M. Rosset, "Efficient power management circuit: From thermal energy harvesting to above-IC microbattery energy storage," *IEEE Journal of Solid-State Circuits*, vol. 43, no. 1, pp. 246–255, 2008.

[119] T. Kang, S. Kim, C. Hyoung, S. Kang, and K. Park, "An energy combiner for a multi-input energy-harvesting system," *IEEE Transactions on Circuits and Systems II: Express Briefs*, vol. 62, no. 9, pp. 911–915, 2015.

[120] J. Amanor-Boadu, M. A. Abouzied, S. Carreon-Bautista, R. Ribeiro, X. Liu, and E. Sánchez-Sinencio, "A switched mode li-ion battery charger with multiple energy harvesting systems simultaneously used as input sources," in *Circuits and Systems (MWSCAS), 2014 IEEE 57th International Midwest Symposium on*, pp. 330–333, IEEE, 2014.

[121] J. Colomer-Farrarons, P. Miribel-Catala, A. Saiz-Vela, and J. Samitier, "A multiharvested self-powered system in a low-voltage low-power technology," *IEEE Transactions on Industrial Electronics*, vol. 58, no. 9, pp. 4250–4263, 2011.

[122] L. Colalongo, D. Dotti, A. Richelli, and Z. M. Kovács-Vajna, "Non-isolated multiple-input boost converter for energy harvesting," *Electronics Letters*, vol. 53, no. 16, pp. 1132–1134, 2017.

[123] S. Bandyopadhyay and A. P. Chandrakasan, "Platform architecture for solar, thermal, and vibration energy combining with MPPT and single inductor," *IEEE Journal of Solid-State Circuits*, vol. 47, no. 9, pp. 2199–2215, 2012.

[124] M. Dini, A. Romani, M. Filippi, V. Bottarel, G. Ricotti, and M. Tartagni, "A nanocurrent power management IC for multiple heterogeneous energy harvesting sources," *IEEE Transactions on Power Electronics*, vol. 30, no. 10, pp. 5665–5680, 2015.

[125] G. Chowdary, A. Singh, and S. Chatterjee, "An 18 nA, 87% efficient solar, vibration and RF energy-harvesting power management system with a single shared inductor," *IEEE Journal of Solid-State Circuits*, vol. 51, no. 10, pp. 2501–2513, 2016.

[126] C. Shi, B. Miller, K. Mayaram, and T. Fiez, "A multiple-input boost converter for low-power energy harvesting," *IEEE Transactions on Circuits and Systems II: Express Briefs*, vol. 58, no. 12, pp. 827–831, 2011.

[127] M. A. Abouzied, H. Osman, V. Vaidya, K. Ravichandran, and E. Sánchez-Sinencio, "An integrated concurrent multiple-input self-startup energy harvesting capacitive-based DC adder combiner," *IEEE Transactions on Industrial Electronics*, vol. 65, pp. 6281–6290, August 2018.

[128] J. J. Estrada-López, A. Abuellil, A. Costilla-Reyes, M. Abouzied, S. Yoon, and E. Sánchez-Sinencio, "A fully integrated maximum power tracking combiner for energy harvesting iot applications," *IEEE Transactions on Industrial Electronics*. Accepted on March 2019. 10.1109/TIE.2019.2907449.

[129] H. Shao, C.-Y. Tsui, and W.-H. Ki, "The design of a micro power management system for applications using photovoltaic cells with the maximum output power control," *IEEE Transactions on Very Large Scale Integration (VLSI) Systems*, vol. 17, no. 8, pp. 1138–1142, 2009.

[130] V. H. Duong, N. X. Hieu, H. S. Lee, and J. W. Lee, "A battery-assisted passive EPC Gen-2 RFID sensor tag IC with efficient battery power management and RF energy harvesting," *IEEE Transactions on Industrial Electronics*, vol. 63, pp. 7112–7123, November 2016.

[131] A. A. Blanco and G. A. Rincón-Mora, "Energy-harvesting microsensors: Low-energy task schedule & fast drought-recovery design," in *Proc. IEEE Midwest Symp. Circuits Syst.*, (Abu Dhabi, UAE), pp. 1–4, October 2016.

[132] N. J. Guilar, R. Amirtharajah, P. J. Hurst, and S. H. Lewis, "An energy-aware multiple-input power supply with charge recovery for energy harvesting applications," in *2009 IEEE International Solid-State Circuits Conference - Digest of Technical Papers*, pp. 298–299,299a, February 2009.

[133] C. Carvalho and N. Paulino, "Start-up circuit for low-power indoor light energy harvesting applications," *Electronics Letters*, vol. 49, pp. 669–671, May 2013.

[134] Texas Instruments, "Ultralow power, supply voltage monitor," TPS383x datasheet, July 2015. Available: http://www.ti.com/.

[135] M. Dini, A. Romani, M. Filippi, and M. Tartagni, "A nanocurrent power management IC for low-voltage energy harvesting sources," *IEEE Transactions on Power Electronics*, vol. 31, no. 6, pp. 4292–4304, 2016.

[136] D. Maksimovic and S. Dhar, "Switched-capacitor DC-DC converters for low-power on-chip applications," in *Proc. 30th Annu. IEEE Power Electron. Spec. Conf.*, vol. 1, (Chaleston, SC), pp. 54–59, 1999.

[137] M.-D. Ker, S.-L. Chen, and C.-S. Tsai, "Design of charge pump circuit with consideration of gate-oxide reliability in low-voltage CMOS processes," *IEEE Journal of Solid-State Circuits*, vol. 41, pp. 1100–1107, May 2006.

[138] A. Cabrini, S. Gregori, and G. Torelli, "Integrated charge pumps: a generalised method for power efficiency optimisation," *IET Circuits, Devices & Systems*, vol. 10, no. 1, pp. 12–19, 2016.

[139] P. Favrat, P. Deval, and M. J. Declercq, "A high-efficiency CMOS voltage doubler," *IEEE Journal of Solid-State Circuits*, vol. 33, no. 3, pp. 410–416, 1998.

[140] G. Palumbo, D. Pappalardo, and M. Gaibotti, "Charge-pump circuits: power-consumption optimization," *IEEE Transactions on Circuits and Systems I: Fundamental Theory and Applications*, vol. 49, no. 11, pp. 1535–1542, 2002.

[141] S. Yoon, S. Carreon-Bautista, and E. Sánchez-Sinencio, "An area efficient thermal energy harvester with reconfigurable capacitor charge pump for IoT applications," *IEEE Transactions on Circuits and Systems II: Express Briefs*, vol. 65, no. 12, pp. 1974–1978, 2018.

[142] J. J. Estrada-López, A. A. Castillo-Atoche, J. Vázquez-Castillo, and E. Sánchez-Sinencio, "Smart soil parameters estimation system using an autonomous wireless sensor network with dynamic power management strategy," *IEEE Sensors Journal*, vol. 18, pp. 8913–8923, November 2018.

[143] R. Bongiovanni and J. Lowenberg-Deboer, "Precision Agriculture and Sustainability," *Precision Agriculture*, vol. 5, pp. 358–387, August 2004.

[144] H. Jawad, R. Nordin, S. Gharghan, A. Jawad, and M. Ismail, "Energy-efficient wireless sensor networks for precision agriculture: A review," *Sensors*, vol. 17, no. 8, p. 1781, 2017.

[145] J. I. Huircán, C. Muñoz, H. Young, L. Von Dossow, J. Bustos, G. Vivallo, and M. Toneatti, "Zigbee-based wireless sensor network localization for cattle monitoring in grazing fields," *Computers and Electronics in Agriculture*, vol. 74, no. 2, pp. 258–264, 2010.

[146] R. W. Coates, M. J. Delwiche, A. Broad, and M. Holler, "Wireless Sensor Network with Irrigation Valve Control," *Computers and electronics in Agriculture*, vol. 96, pp. 13–22, August 2013.

[147] J. Gutiérrez, J. F. Villa-Medina, A. Nieto-Garibay, and M. A. Porta-Gándara, "Automated irrigation system using a wireless sensor network and GPRS module," *IEEE Transactions on Instrumentation and Measurement*, vol. 63, pp. 166–176, January 2014.

[148] F. Viani, M. Bertolli, M. Salucci, and A. Polo, "Low-cost wireless monitoring and decision support for water saving in agriculture," *IEEE Sensors Journal*, vol. 17, pp. 4299–4309, July 2017.

[149] R. G. Vieira, A. M. da Cunha, L. B. Ruiz, and A. P. de Camargo, "On the design of a long range WSN for precision irrigation," *IEEE Sensors Journal*, vol. 18, pp. 773–780, January 2018.

[150] J. G. Jagüey, J. F. Villa-Medina, A. López-Guzmán, and M. A. Porta-Gándara, "Smartphone irrigation sensor," *IEEE Sensors Journal*, vol. 15, pp. 5122–5127, September 2015.

[151] D. García-Lesta, D. Cabello, E. Ferro, P. López, and V. M. Brea, "Wireless sensor network with perpetual motes for terrestrial snail activity monitoring," *IEEE Sensors Journal*, vol. 17, pp. 5008–5015, August 2017.

[152] F. Viani, M. Bertolli, and A. Polo, "Low-cost wireless system for agrochemical dosage reduction in precision farming," *IEEE Sensors Journal*, vol. 17, pp. 5–6, January 2017.

[153] F. Edwards-Murphy, M. Magno, P. M. Whelan, J. O'Halloran, and E. M. Popovici, "b+ WSN: Smart beehive with preliminary decision tree analysis for agriculture and honey bee health monitoring," *Computers and Electronics in Agriculture*, vol. 124, pp. 211–219, June 2016.

[154] S. Gil-Lebrero, F. Quiles-Latorre, M. Ortiz-López, V. Sánchez-Ruiz, V. Gámiz-López, and J. Luna-Rodríguez, "Honey bee colonies remote monitoring system," *Sensors*, vol. 17, no. 1, p. 55, 2017.

[155] A. Kumar and G. P. Hancke, "Energy efficient environment monitoring system based on the IEEE 802.15.4 standard for low cost requirements," *IEEE Sensors Journal*, vol. 14, pp. 2557–2566, August 2014.

[156] H.-C. Lee, K.-H. Ke, Y.-M. Fang, B.-J. Lee, and T.-C. Chan, "Open-source wireless sensor system for long-term monitoring of slope movement.," *IEEE Transactions on Instrumentation and Measurement*, vol. 66, no. 4, pp. 767–776, 2017.

[157] P. Lopez-Iturri, M. Celaya-Echarri, L. Azpilicueta, E. Aguirre, J. Astrain, J. Villadangos, and F. Falcone, "Integration of autonomous wireless sensor networks in academic school gardens," *Sensors*, vol. 18, no. 11, p. 3621, 2018.

[158] T. Ruan, Z. J. Chew, and M. Zhu, "Energy-aware approaches for energy harvesting powered wireless sensor nodes," *IEEE Sensors Journal*, vol. 17, pp. 2165–2173, April 2017.

[159] A. L. Diedrichs, F. Bromberg, D. Dujovne, K. Brun-Laguna, and T. Watteyne, "Prediction of frost events using machine learning and iot sensing devices," *IEEE Internet of Things Journal*, vol. 5, no. 6, pp. 4589–4597, 2018.

[160] H. Jiang and W. R. Cotton, "Soil moisture estimation using an artificial neural network: a feasibility study," *Canadian Journal of Remote Sensing*, vol. 30, pp. 827–839, October 2004.

[161] A. Keshavarzi, F. Sarmadian, E.-S. E. Omran, and M. Iqbal, "A neural network model for estimating soil phosphorus using terrain analysis," *Egyptian Journal of Remote Sensing and Space Science*, vol. 18, pp. 127–135, July 2015.

[162] D. D. Alexakis, F.-D. K. Mexis, A.-E. K. Vozinaki, I. N. Daliakopoulos, and I. K. Tsanis, "Soil moisture content estimation based on sentinel-1 and auxiliary earth observation products. a hydrological approach," *Sensors*, vol. 17, no. 6, p. 1455, 2017.

[163] F. Ferrández-Pastor, J. García-Chamizo, M. Nieto-Hidalgo, J. Mora-Pascual, and J. Mora-Martínez, “Developing ubiquitous sensor network platform using internet of things: Application in precision agriculture,” *Sensors*, vol. 16, no. 8, p. 1141, 2016.

[164] P. C. Dias, F. J. O. Morais, M. B. de Morais França, E. C. Ferreira, A. Cabot, and J. A. S. Dias, “Autonomous multisensor system powered by a solar thermoelectric energy harvester with ultralow-power management circuit,” *IEEE Transaction on Instrumentation and Measurement*, vol. 64, pp. 2918–2925, November 2015.

[165] Z. Hu, S. Liu, and X. Liu, “Soil respiration and its environmental response varies by day/night and by growing/dormant season in a subalpine forest,” *Scientific Reports*, vol. 6, p. 11, November 2016.

[166] Sensirion, "Humidity and Temperature Sensor IC," SHT1x datasheet, December 2011. Available: https://www.sensirion.com/en/.

[167] DFRobot, "Gravity: Analog Soil Moisture Sensor For Arduino," SEN0114 datasheet, May 2017. Available: https://www.dfrobot.com/.

[168] Analog Devices, "1.8 V to 5.5 V, 2:1 Mux/DPDT Switch," ADG819 datasheet, May 2012. Available: https://www.analog.com/.

[169] Analog Devices, "Active RC, 4th Order Lowpass Filter Family," LTC1563 datasheet, Rev. A 2005. Available: https://www.analog.com/.

[170] N. Kotamäki, S. Thessler, J. Koskiaho, A. O. Hannukkala, H. Huitu, T. Huttula, J. Havento, and M. Järvenpää, “Wireless in-situ sensor network for agriculture and water monitoring on a river basin scale in southern finland: Evaluation from a data users perspective,” *Sensors*, vol. 9, no. 4, pp. 2862–2883, 2009.

[171] B. Fishbain and E. Moreno-Centeno, “Self calibrated wireless distributed environmental sensory networks,” *Scientific reports*, vol. 6, p. 24382, April 2016.

[172] Y. Song, J. Lin, M. Tang, and S. Dong, “An internet of energy things based on wireless LPWAN,” *Engineering*, vol. 3, no. 4, pp. 460–466, 2017.

[173] Digi International Inc., "XBee/XBee-PRO S2C ZigBee RF Module," RF Module User Guide, March 2019. Available: https://www.digi.com/.

[174] Ixys Corp., "IXOLAR High Efficiency SolarBIT," KXOB22-04X3 datasheet, August 2011. Available: http://www.ixys.com/.

[175] Texas Instruments, "Mixed-Signal Microcontrollers," MSP430FR59xx datasheet, March 2017. Available: http://www.ti.com/.

[176] F. Salvadori, M. de Campos, P. S. Sausen, R. F. de Camargo, C. Gehrke, C. Rech, M. A. Spohn, and A. C. Oliveira, "Monitoring in industrial systems using wireless sensor network with dynamic power management," *IEEE Transactions on Instrumentation and Measurement*, vol. 58, pp. 3104–3111, September 2009.

[177] J. Burrell, T. Brooke, and R. Beckwith, "Vineyard computing: sensor networks in agricultural production," *IEEE Pervasive Computing*, vol. 3, pp. 38–45, January 2004.

[178] H. Wei, X. Chen, G. Xiao, B. Guenet, S. Vicca, and W. Shen, "Are variations in heterotrophic soil respiration related to changes in substrate availability and microbial biomass carbon in the subtropical forests?," *Scientific Reports*, vol. 5, p. 11, December 2015.

[179] F. E. Moyano, S. Manzoni, and C. Chenu, "Responses of soil heterotrophic respiration to moisture availability: An exploration of processes and models," *Soil Biology and Biochemistry*, vol. 59, pp. 72 – 85, April 2013.

[180] W. Song, S. Chen, B. Wu, Y. Zhu, Y. Zhou, Q. Lu, and G. Lin, "Simulated rain addition modifies diurnal patterns and temperature sensitivities of autotrophic and heterotrophic soil respiration in an arid desert ecosystem," *Soil Biology and Biochemistry*, vol. 82, pp. 143 – 152, March 2015.

[181] Z. Fan and C. Liang, "Significance of microbial asynchronous anabolism to soil carbon dynamics driven by litter inputs," *Scientific Reports*, vol. 5, p. 7, April 2015.

[182] L. Taneva and M. A. Gonzalez-Meler, "Distinct patterns in the diurnal and seasonal variability in four components of soil respiration in a temperate forest under free-air co_2 enrichment," *Biogeosciences*, vol. 8, no. 10, pp. 3077–3092, 2011.

[183] W. Wang, R. Dalal, P. Moody, and C. Smith, "Relationships of soil respiration to microbial biomass, substrate availability and clay content," *Soil Biology and Biochemistry*, vol. 35, no. 2, pp. 273 – 284, 2003.

[184] D. Hillel, *Environmental Soil Physics: Fundamentals, Applications, and Environmental Considerations*. San Diego: Academic Press, 1998.

[185] Z. Wang, H. Huang, J. Deng, and J. Liu, "Scaling the respiratory metabolism to phosphorus relationship in plant seedlings," *Scientific Reports*, vol. 5, p. 5, November 2015.

[186] L. O. Hedin, "Physiology: Plants on a different scale," *Nature*, vol. 439, pp. 399–400, January 2006.

[187] J. Wösten, Y. A. Pachepsky, and W. J. Rawls, "Pedotransfer functions: bridging the gap between available basic soil data and missing soil hydraulic characteristics," *J. Hydrology*, vol. 251, no. 3, pp. 123 – 150, 2001.

[188] D. Narducci and B. Lorenzi, "Challenges and perspectives in tandem thermoelectric and photovoltaic solar energy conversion," *IEEE Transactions on Nanotechnology*, vol. 15, no. 3, pp. 348–355, 2016.

[189] S. Dalola, V. Ferrari, M. Guizzetti, D. Marioli, E. Sardini, M. Serpelloni, and A. Taroni, "Autonomous sensor system with power harvesting for telemetric temperature measurements of pipes," *IEEE Transactions on Instrumentation and Measurement*, vol. 58, no. 5, pp. 1471–1478, 2009.

[190] J. Chen, J. Klein, Y. Wu, S. Xing, R. Flammang, M. Heibel, and L. Zuo, "A thermoelectric energy harvesting system for powering wireless sensors in nuclear power plants," *IEEE Transactions on Nuclear Science*, vol. 63, no. 5, pp. 2738–2746, 2016.

[191] V. Leonov, "Thermoelectric energy harvesting of human body heat for wearable sensors," *IEEE Sensors Journal*, vol. 13, no. 6, pp. 1–8, 2013.

[192] Y. Wu, Z. Yang, F. Lin, and W. Xu, "Towards batteryfree and wireless sensing for personalized ultraviolet exposure monitoring," *IEEE Sensors Journal*, vol. 18, no. 13, pp. 5515–5521, 2018.

[193] P. Cheruvu, V. P. Kumar, and H. C. Barshilia, "Experimental analysis and evaluation of a vacuum enclosed concentrated solar thermoelectric generator coupled with a spectrally selective absorber coating," *International Journal of Sustainable Energy*, vol. 37, no. 8, pp. 1–17, 2017.

[194] L. L. Baranowski, G. J. Snyder, and E. S. Toberer, "Concentrated solar thermoelectric generators," *Energy & Environmental Science*, vol. 5, no. 10, pp. 9055–9067, 2012.

[195] D. Kraemer, K. McEnaney, M. Chiesa, and G. Chen, "Modeling and optimization of solar thermoelectric generators for terrestrial applications," *Solar Energy*, vol. 86, no. 5, pp. 1338–1350, 2012.

[196] M. Olsen, E. Warren, P. Parilla, E. Toberer, C. Kennedy, G. Snyder, S. Firdosy, B. Nesmith, A. Zakutayev, A. Goodrich, *et al.*, "A high-temperature, high-efficiency solar thermoelectric generator prototype," *Energy Procedia*, vol. 49, pp. 1460–1469, 2014.

[197] S. Su and J. Chen, "Simulation investigation of high-efficiency solar thermoelectric generators with inhomogeneously doped nanomaterials," *IEEE Transactions on Industrial Electronics*, vol. 62, no. 6, pp. 3569–3575, 2015.

[198] R. Lamba, S. Manikandan, and S. Kaushik, "Performance analysis and optimization of concentrating solar thermoelectric generator," *Journal of Electronic Materials*, vol. 47, no. 9, pp. 5310–5320, 2018.

[199] M. Ge, Z. Wang, L. Liu, J. Zhao, and Y. Zhao, "Performance analysis of a solar thermoelectric generation (STEG) system with spray cooling," *Energy Conversion and Management*, vol. 177, pp. 661–670, December 2018.

[200] R. Amatya and R. Ram, "Solar thermoelectric generator for micropower applications," *Journal of Electronic Materials*, vol. 39, no. 9, pp. 1735–1740, 2010.

[201] D. Kraemer, Q. Jie, K. McEnaney, F. Cao, W. Liu, L. A. Weinstein, J. Loomis, Z. Ren, and G. Chen, "Concentrating solar thermoelectric generators with a peak efficiency of 7.4%," *Nature Energy*, vol. 1, no. 11, p. 16153, 2016.

[202] K. Sudharshan, V. P. Kumar, and H. C. Barshilia, "Performance evaluation of a thermally concentrated solar thermo-electric generator without optical concentration," *Solar Energy Materials and Solar Cells*, vol. 157, pp. 93–100, December 2016.

[203] D. Kraemer, B. Poudel, H.-P. Feng, J. C. Caylor, B. Yu, X. Yan, Y. Ma, X. Wang, D. Wang, A. Muto, *et al.*, "High-performance flat-panel solar thermoelectric generators with high thermal concentration," *Nature Materials*, vol. 10, no. 7, p. 532, 2011.

[204] H.-B. Liu, J.-H. Meng, X.-D. Wang, and W.-H. Chen, "A new design of solar thermoelectric generator with combination of segmented materials and asymmetrical legs," *Energy Conversion and Management*, vol. 175, pp. 11–20, November 2018.

[205] D. Yang and H. Yin, "Energy conversion efficiency of a novel hybrid solar system for photovoltaic, thermoelectric, and heat utilization," *IEEE Transactions on Energy Conversion*, vol. 26, no. 2, pp. 662–670, 2011.

[206] D. Kwon, G. A. Rincon-Mora, and E. O. Torres, "Harvesting ambient kinetic energy with switched-inductor converters," *IEEE Transactions on Circuits and Systems I: Regular Papers*, vol. 58, pp. 1551–1560, July 2011.

[207] G. D. Szarka, B. H. Stark, and S. G. Burrow, "Review of power conditioning for kinetic energy harvesting systems," *IEEE Transactions on Power Electronics*, vol. 27, no. 2, pp. 803–815, 2012.

[208] C.-N. Xu, M. Akiyama, K. Nonaka, and T. Watanabe, "Electrical power generation characteristics of PZT piezoelectric ceramics," *IEEE Transactions on Ultrasonics, Ferroelectrics, and Frequency Control*, vol. 45, no. 4, pp. 1065–1070, 1998.

[209] S. R. Platt, S. Farritor, and H. Haider, "On low-frequency electric power generation with pzt ceramics," *IEEE/ASME Transactions on Mechatronics*, vol. 10, pp. 240–252, April 2005.

[210] E. Lefeuvre, G. Sebald, D. Guyomar, M. Lallart, and C. Richard, "Materials, structures and power interfaces for efficient piezoelectric energy harvesting," *Journal of Electroceramics*, vol. 22, pp. 171–179, February 2009.

[211] A. Khaligh, P. Zeng, and C. Zheng, "Kinetic energy harvesting using piezoelectric and electromagnetic technologies - state of the art," *IEEE Transactions on Industrial Electronics*, vol. 57, pp. 850–860, March 2010.

[212] M. Lallart, L. Garbuio, L. Petit, C. Richard, and D. Guyomar, "Double synchronized switch harvesting (dssh): a new energy harvesting scheme for efficient energy extraction," *IEEE Transactions on Ultrasonics, Ferroelectrics, and Frequency Control*, vol. 55, pp. 2119–2130, October 2008.

[213] M. Ferrari, V. Ferrari, M. Guizzetti, D. Marioli, and A. Taroni, "Piezoelectric multifrequency energy converter for power harvesting in autonomous microsystems," *Sensors and Actuators A: Physical*, vol. 142, no. 1, pp. 329–335, 2008.

[214] W. Al-Ashtari, M. Hunstig, T. Hemsel, and W. Sextro, "Enhanced energy harvesting using multiple piezoelectric elements: theory and experiments," *Sensors and Actuators A: Physical*, vol. 200, pp. 138–146, October 2013.

[215] X. Cui, M. Teng, and J. Hu, "PSPICE-based analyses of the vibration energy harvester system with multiple piezoelectric units," *Canadian Journal of Electrical and Computer Engineering*, vol. 38, no. 3, pp. 246–250, 2015.

[216] J. Colomer-Farrarons, P. Miribel-Catala, A. Saiz-Vela, M. Puig-Vidal, and J. Samitier, "Power-conditioning circuitry for a self-powered system based on micro PZT generators in a 0.13-μm low-voltage low-power technology," *IEEE Transactions on Industrial Electronics*, vol. 55, pp. 3249–3257, September 2008.

[217] N. J. Guilar, R. Amirtharajah, and P. J. Hurst, "A full-wave rectifier with integrated peak selection for multiple electrode piezoelectric energy harvesters," *IEEE Journal of Solid-State Circuits*, vol. 44, pp. 240–246, January 2009.

[218] H. Xia and R. Chen, "Design and analysis of a scalable harvesting interface for multi-source piezoelectric energy harvesting," *Sensors and Actuators A: Physical*, vol. 218, pp. 33–40, October 2014.

[219] A. Romani, M. Filippi, and M. Tartagni, "Micropower design of a fully autonomous energy harvesting circuit for arrays of piezoelectric transducers," *IEEE Transactions on Power Electronics*, vol. 29, pp. 729–739, February 2014.

[220] S. Boisseau, P. Gasnier, M. Perez, C. Bouvard, M. Geisler, A. B. Duret, G. Despesse, and J. Willemin, "Synchronous electric charge extraction for multiple piezoelectric energy harvesters," in *2015 IEEE 13th International New Circuits and Systems Conference (NEWCAS)*, pp. 1–4, June 2015.

[221] R. D'hulst, T. Sterken, R. Puers, G. Deconinck, and J. Driesen, "Power processing circuits for piezoelectric vibration-based energy harvesters," *IEEE Transactions on Industrial Electronics*, vol. 57, pp. 4170–4177, December 2010.

[222] D. Guyomar and M. Lallart, "Recent progress in piezoelectric conversion and energy harvesting using nonlinear electronic interfaces and issues in small scale implementation," *Micromachines*, vol. 2, pp. 274–294, June 2011.

[223] J. Dicken, P. D. Mitcheson, I. Stoianov, and E. M. Yeatman, "Power-extraction circuits for piezoelectric energy harvesters in miniature and low-power applications," *IEEE Transactions on Power Electronics*, vol. 27, pp. 4514–4529, November 2012.

[224] F. G. Dell'Anna, T. Dong, P. Li, Y. Wen, Z. Yang, M. R. Casu, M. Azadmehr, and Y. Berg, "State-of-the-art power management circuits for piezoelectric energy harvesters," *IEEE Circuits and Systems Magazine*, vol. 18, pp. 27–48, Thirdquarter 2018.

[225] C. Lu, C. Tsui, and W. Ki, "Vibration energy scavenging system with maximum power tracking for micropower applications," *IEEE Transactions on Very Large Scale Integration (VLSI) Systems*, vol. 19, pp. 2109–2119, November 2011.

[226] I. M. Darmayuda, Y. Gao, M. T. Tan, S. Cheng, Y. Zheng, M. Je, and C. Heng, "A self-powered power conditioning IC for piezoelectric energy harvesting from short-duration vibrations," *IEEE Transactions on Circuits and Systems II: Express Briefs*, vol. 59, pp. 578–582, September 2012.

[227] M. Shim, J. Kim, J. Jeong, S. Park, and C. Kim, "Self-powered 30 μw to 10 mw piezoelectric energy harvesting system with 9.09 ms/v maximum power point tracking time," *IEEE Journal of Solid-State Circuits*, vol. 50, pp. 2367–2379, October 2015.

[228] Y. K. Ramadass and A. P. Chandrakasan, "An efficient piezoelectric energy harvesting interface circuit using a bias-flip rectifier and shared inductor," *IEEE Journal of Solid-State Circuits*, vol. 45, pp. 189–204, January 2010.

[229] T. Hehn, F. Hagedorn, D. Maurath, D. Marinkovic, I. Kuehne, A. Frey, and Y. Manoli, "A fully autonomous integrated interface circuit for piezoelectric harvesters," *IEEE Journal of Solid-State Circuits*, vol. 47, pp. 2185–2198, September 2012.

[230] E. Lefeuvre, A. Badel, C. Richard, and D. Guyomar, "Piezoelectric energy harvesting device optimization by synchronous electric charge extraction," *Journal of Intelligent Material Systems and Structures*, vol. 16, pp. 865–876, October 2005.

[231] D. Kwon and G. A. Rincon-Mora, "A 2-μm bicmos rectifier-free AC-DC piezoelectric energy harvester-charger IC," *IEEE Transactions on Biomedical Circuits and Systems*, vol. 4, pp. 400–409, December 2010.

[232] G. Pillonnet, A. Andrieu, and E. Alon, "Dual-input switched capacitor converter suitable for wide voltage gain range," *IEEE Journal on Emerging and Selected Topics in Circuits and Systems*, vol. 5, pp. 413–420, September 2015.

APPENDIX A

PAPER CONTRIBUTIONS

- **J. J. Estrada López**, A. Abuellil, A. Costilla-Reyes, M. Abouzied, S. Yoon and E. Sánchez-Sinencio, "A Fully Integrated Maximum Power Tracking Combiner for Energy Harvesting IoT Applications," *IEEE Transactions on Industrial Electronics*, Accepted on March 03, 2019.

- **J. J. Estrada López**, A. A. Castillo-Atoche, J. Vázquez-Castillo and E. Sánchez-Sinencio, "Smart Soil Parameters Estimation System Using an Autonomous Wireless Sensor Network With Dynamic Power Management Strategy," *IEEE Sensors Journal*, vol. 18, no. 21, pp. 8913-8923, 1 Nov.1, 2018.

- **J. Estrada López**, A. Abuellil, Z. Zeng and E. Sánchez-Sinencio, "Multiple Input Energy Harvesting Systems for Autonomous IoT End-Nodes," *Journal of Low Power Electronics and Applications,*, vol. 8, no. 1, p. 6, Mar. 2018.

- **J. J. Estrada López**, A. Abuellil, A. Costilla-Reyes and E. Sánchez-Sinencio, "Technology Enabling Circuits and Systems for the Internet-of-Things: An Overview," *2018 IEEE International Symposium on Circuits and Systems (ISCAS)*, Florence, 2018, pp. 1-5.

- Z. Zeng, **J. J. Estrada López**, M. Abouzied and E. Sánchez-Sinencio, "A Reconfigurable Rectifier with optimal Loading Point Determination for RF Energy Harvesting from - 22 dBm to - 2 dBm," *Transactions on Circuits and Systems II: Express Briefs*, doi: 10.1109/TCSII.2019.2899338.

- A. Costilla-Reyes, A. Abuellil, **J. J. Estrada López**, S. Carreon-Bautista and E. Sánchez-Sinencio, "Reconfigurable System for Electromagnetic Energy Harvesting with Inherent Activity Sensing Capabilities for Wearable Technology," *IEEE Transactions on Circuits and*

Systems II: Express Briefs, doi: 10.1109/TCSII.2018.2884613.

- A. Abuellil, **J. J. Estrada López**, A. Vighnesh, A. Costilla-Reyes, Z. Zeng and E. Sánchez-Sinencio, "Multiple-Input Harvesting PMU with Enhanced Boosting Scheme for IoT Applications," *IEEE Transactions on Industrial Electronics*, **Under Review**.